Numerical Simulation of Multiphase Flows: Level-Set Techniques

Centre Tecnològic de Transferència de Calor
Departament de Màquines i Motors Tèrmics
Universitat Politècnica de Catalunya

Néstor Vinicio Balcázar Arciniega
Doctoral Thesis

Numerical Simulation of Multiphase Flows: Level-Set Techniques

Néstor Vinicio Balcázar Arciniega

TESI DOCTORAL

presentada al

Departament de Màquines i Motors Tèrmics
E.T.S.E.I.A.T.
Universitat Politècnica de Catalunya

per a l'obtenció del grau de

Doctor per la Universitat Politècnica de Catalunya

Terrassa, Setembre, 2014

Numerical Simulation of Multiphase Flows: Level-Set Techniques

Néstor Vinicio Balcázar Arciniega

Directors de la Tesi

Dr. Assensi Oliva Llena
Dr. Oriol Lehmkuhl
Dr. Joaquim Rigola

Tribunal Qualificador

Dr. Carlos D. Pérez-Segarra
Universitat Politècnica de Catalunya

Dr. José Fernández Seara
Universidad de Vigo

Dr. Francisco J. Rey Martínez
Universidad de Valladolid

Now this is not the end.
It is not even the beginning of the end.
But it is, perhaps, the end of the beginning.
Winston Churchill

Agradecimientos

Quedo profundamente agradecido con el Prof. Assensi Oliva, director de Centro Tecnológico de Transferencia de Calor (CTTC), por su confianza y por haberme dado la oportunidad de integrarme como doctorando al CTTC, y emprender un trabajo de investigación en un tópico apasionante como lo es el flujo multifásico, en un ambiente científico excelente.

Un especial agradecimiento a los directores de la presente tesis doctoral, Prof. Assensi Oliva, Prof. Oriol Lehmkuhl y Prof. Joaquim Rigola por direccionar mi trabajo, por su apoyo académico al proporcionarme valiosas ideas y por el soporte instrumental brindado para que éste trabajo cumpla con las rigurosas expectativas científicas de una tesis doctoral.

Me gustaría también agradecer de forma general a los Profesores e Investigadores del CTTC, de quienes he podido enriquecerme intelectualmente, sea asistiendo a sus clases o mediante cada diálogo académico establecido en el transcurso de éstos años.

Un especial agradecimiento para el Prof. Oriol Lehmkuhl quien siempre ha estado dispuesto a brindar críticas constructivas de mis manuscritos científicos, su guía académica ha sido invalorable durante el desarrollo de los nuevos métodos numéricos orientados a resolver las complejidades del flujo multifásico. Muchas gracias a Lluis Jofre, con quién he trabajado en la extensión del código de C++ de TermoFluids para incorporar la nueva librería de cómputo de flujos multifásicos, bajo la cuidadosa coordinación del Prof. Oriol Lehmkuhl. Muchas gracias al Prof. Jesús Castro por sus sugerencias en el ámbito de la modelización de las fuerzas de tensión superficial.

También deseo agradecer a todos mis compañeros del CTTC quienes han hecho que mi estancia en la UPC sea una experiencia fructífera acompañada de crecimiento académico, cultural y personal, especialmente a Daniel M., Sergio M., Óscar A. y Ahmed H. con quienes he tenido una mayor oportunidad de interactuar. Muchas gracias a Octavi P. y Jorge C. por su ayuda en la solución de problemas informáticos. Mi agradecimiento a Deniz K. quién hizo de nexo entre el CTTC y mi persona, previa mi llegada a Barcelona, para respaldar tanto mi postulación a las becas MAEC-AECID como las gestiones burocráticas asociadas al visado de estudios. De igual manera, quisiera agradecer al Prof. Juan Toledo y Prof. Celso Romero de la UTPL en Ecuador por las cartas de recomendación académica que respaldaron mi postulación a la beca doctoral antes mencionada.

Un especial agradecimiento a mis padres, hermanos y familiares, por su apoyo y comprensión durante éstos cinco años de ausencia.

Ésta lista no pretende ser exhaustiva y faltaría espacio para expresar mi gratitud a todas las personas que han colaborado para que ésta tesis llegue a buen término, por lo que anticipo mis disculpas ante cualquier omisión que será de carácter involuntario.

Contents

Contents

Abstract

This thesis aims at developing a numerical methodology suitable for the numerical simulation (DNS) of free surface and interfacial flows in order to be used on basic research, and in industrial applications. At the same time, the study of such multiphase flows can be an opportunity for gaining insight into the complex hydrodynamics and interfacial physics associated with them.

To accomplish these goals, the mathematical formulation of two-phase flows with interfaces are incorporated through the so called one fluid formulation. Moreover, the conservative level-set method for capturing the interface between two fluids is combined with a variable density projection scheme to simulate incompressible two-phase flows on unstructured meshes. All equations are discretized by using a conservative finite-volume approximation on a collocated grid arrangement. A high order scheme based on a flux limiter formulation, is adopted for approximating the convective terms, while the diffusive fluxes are centrally differenced. Gradients are computed by the least-squares approach, whereas physical properties are assumed to vary smoothly in a narrow band around the interface to avoid numerical instabilities. Finally, the numerical method is validated against classical advection test and two-phase flow examples including topology changes.

After presenting the general methodology and code validation of the conservative level-set method, the numerical methodology is applied to study the gravity driven bubble flow in a vertial duct. Unlike the cases presented in the first part, a periodic boundary condition is applied in the vertical direction, in order to mimic a channel of infinite length. First, the shape and terminal velocity of a single bubble which rises in a quiescent liquid are calculated and validated against experimental results reported in the literature. Then, different initial arrangements of bubble pairs were considered to study its hydrodynamic interaction. Finally, the gravity-driven bubbly flow is explored in a periodic vertical pipe including the coalescence of multiple bubbles. The results show that the conservative level-set approach is able to accurately capture the deformation of the interface on simulations of bubbly flows, and can remain numerically stable for a wide range of Morton and Reynolds numbers. Moreover, conservation properties are shown to be excellent, while accuracy remains satisfactory even for the most complex flows.

In the third part of this thesis, a methodology is presented for interface capturing in two-phase flows with surface tension effects by combining volume-of-fluid with level-set methods. While the volume-of-fluid transport relies on a robust and accurate polyhedral library for interface capturing, geometrical properties of interface (curvature) are calculated by using a level-set function, which is reconstructed through an iterative geometrical procedure. The method is validated on 2D and 3D test cases reported in the scientific literature. The simulations reveal that numeri-

15

cal schemes afford qualitatively similar results to those obtained by the conservative level-set method. Mass conservation is shown to be excellent, while geometrical accuracy remains high even for the most challenging cases involving topology changes.

In the fourth part of the thesis a novel multiple marker level-set method is presented. This method is deployed to perform numerical simulation of deformable fluid particles without numerical coalescence of their interfaces, which is a problem inherent to standard interface tracking methodologies (e.g. level-set and volume of fluid). Each fluid particle is described by a separate level-set function, thus, different interfaces can be solved in the same control volume, avoiding artificial and potentially unphysical coalescence of fluid particles. Therefore, bubbles or droplets are able to approach each other closely, within the size of one grid cell, and can even collide. The proposed algorithm is developed in the context of the conservative level-set method, whereas, surface tension is modeled by the continuous surface force approach. The pressure-velocity coupling is solved by the fractional-step projection method. For validation of the proposed numerical method, the gravity-driven impact of a droplet on a liquid-liquid interface is studied; then, the binary droplet collision with bouncing outcome is examined, and finally, it is applied on simulation of gravity-driven bubbly flow in a vertical column. The study of these cases contributed to shed some light into physics present in bubble and droplet flows.

Chapter 1

Introduction

1.1 Background and Motivation

Multiphase flow denotes a large class of problems which encompasses a host of different technological contexts, a wide spectrum of different scales and a broad range of scientific and engineering disciplines [11, 4]. Therefore, a precise definition is difficult to formulate, and whether a certain situation should be considered as a multiphase flow problem depends more of the point view [11]. Thus, in the context of this thesis, the term multiphase flow will be used to refer to any two-phase flow consisting of immiscible fluids separated by a clearly differentiated interface.

The flow of two-phases is ubiquitous. Numerous examples can be found in nature and industry, for example, in energy production (see Fig. 1.1a), unit operations in chemical engineering, waste water treatment, agriculture, among other environmental, geophysical and engineering situations. Specific applications include off-shore oil production, the nuclear steam supply system of a power plant where steam is produced in a reactor vessel and then used in a turbine-generator [8], bubble reactors, flotation, fermentation, liquid-liquid extraction, distillation columns, combustion of liquid fluids, spray drying, two-phase heat exchangers, heat transfer by boiling and many others [14]. Examples of multiphase flows in nature include the exchange of heat and mass transfer between oceans and the atmosphere where bubbles and droplets play an important role, volcanic explosions, rainfall, hailstones, clouds and others [16]. Therefore, the importance of understanding and controlling the behaviour of multiphase flows cannot be overstated.

A persistent theme throughout the study of multiphase flows is the need to model and predict the detailed behavior of those flows and the phenomena that they manifest [4]. However, many challenging problems have to be addressed in order to get successful models of this kind of flows. A frequent feature of multiphase flow problems is the complexity arising from the mutual interaction of many subsystems such as bubbles or droplets immersed in a fluid [11]. In addition, intrinsic physical mech-

anisms present in multiphase flows contribute to their complexity, for instance solid-liquid-gas contact lines, the transition between gas-liquid flow regimes, turbulence and others [11]. One of the major difficulties is that the geometry of the interfaces is not know and cannot be determined a priory, but is rather a part of the solution [8]. For example, in a bubbly flow, it is not possible to know a priory whether bubbles will be distributed uniformly in the liquid or the bubbles will coalesce and flow in the center of the pipe while a liquid film will be formed on the wall [8]. In this regard, basically, there are three ways in which such models can be explored: (1) experimentally, through laboratory-sized models equipped with appropriate instrumentation, (2) theoretically, using mathematical equations and models for the flow, and (3) computationally, using the power and size of modern computers to address the complexity of the flow [4].

The complexity of multiphase flow limits the usefulness of exact analytical methods to problems under restricted conditions, for instance bubbles and droplets in Stokes flow, linear inviscid waves and small oscillations of bubbles and droplets [16]. Moreover, it may be even difficult to set up a multiphase flow experiment in a laboratory with the necessary degree of control, for instance the bubble coalescence or a precise characterization of the bubble size [11]. Thus, the need for numerical solutions of the governing equations of multiphase flow is justified.

1.2 Computational methods for simulation of multiphase flows

Limitation in theoretical and experimental investigations has made computational multi-fluid dynamics (CMFD) one of the major means of modelling multiphase flow problems. There are multiple approaches for the numerical simulation of multiphase flows, for instance: Eulerian-Eulerian (E-E) method, Eulerian-Lagrangian (E-L) method and Direct Numerical Simulation (DNS). In the E-E method (or two-fluid model) both the continuous phase and the dispersed phase, such as particles, bubbles, and droplets, are treated as interpenetrating continuous media, occupying the same space as does the continuous phase with different velocities and volume fractions for each phase. The structure of the Eulerian-Eulerian models is well developed, but the closure relationships (particularly for three dimensional problems) are still a long way from being satisfactory [9, 3, 18, 19, 7]. In the E-L method, or discrete particle method, the continuous fluid phase is formulated in the Eulerian mode, while the position and the velocity of the dispersed phase, particles, or bubbles, is traced in the Lagrangian mode by solving Lagrangian motion equations. The closure relationship for the interaction forces between phases requires to be provided in the E-L method [19, 7], thus, empirical information is needed to perform simulations in

Figure 1.1: Some applications of the conservative level-set method [1] formulated in the present thesis for modelling of two-phase flows: (**a**) Simulation of an oscillating water column (OWC) device used to recover energy from the rise and fall of water caused by waves in the sea. (**b**) Simulation of gravity-driven bubbly flow in a vertical pipe.

this framework. Due the increase in computational power, Direct Numerical Simulation (DNS) of the Navier-Stokes equations coupled with interface capturing methods (e.g. level-set, volume-of-fluid, front tracking) has became important in characterizing details of the complex multiphase flow field. In this method the grid size is commonly much smaller than the object size of the dispersed phase, and the moving interface can be represented by implicit or explicit schemes in the computational domain. The velocity field of the fluid phase is obtained by solving the Navier-Stokes equation considering the interfacial forces, such as surface tension [19, 7]. Indeed, regarding the computational approach the main emphasis of this thesis is on the most fundamental level of modelling, namely the Direct Numerical Simulation (DNS) of multiphase flows. This field has advanced considerably in the past decade due to the advances in numerical simulation techniques and computer hardware [6]. Indeed, modern computers can now study the dynamics in great detail and these simulations yield unprecedented insight [16].

The use of a single set of governing equations to describe the flow of two fuids separated by a common interface requires the accurate tracking of the interface. This is usually done by advecting a marker function (e.g. signed distance function, color function, etc.) which takes one value in one fluid and another value in the other fluid. Advecting the marker function in such a way that it remains sharp at the interface is one of the most challenging problems of modern computational fluid dynamics. It has proven particularly difficult to accurately simulate these flows, which can be attributed to (i) the fact that the interface separating the fluids needs to be tracked accurately without introducing excessive computational smearing, (ii) the necessity to account for surface tension force [6].

1.2.1 Direct Numerical Simulation at the CTTC

The Heat and Mass Transfer Technological Center (CTTC) of the Technical University of Catalonia (UPC) is a research group dedicated to academic, research, innovation and technology transfer in the heat and mass transfer and fluid dynamic field, together with their application to thermal systems and equipments. The CTTC research activities are focused on one basic research line dedicated to the mathematical formulation, numerical resolution and experimental validation of heat and mass transfer phenomena. Some issues in this line are: natural and forced convection, turbulence modelling (RANS, LES and DNS), combustion, two-phase flow, solid-liquid phase change, radiation, porous media, numerical algorithms and solvers, general purpose CFD codes, high performance computing HPC (parallelisation), aerodynamics, etc. A second research line involves the application of the acquired know-how from the basic studies mentioned above to the thermal and fluid dynamic optimization of thermal system and equipment. Please, the reader is refered to [20] for detailed information of the CTTC.

CTTC facilities include a HPC Beowulf cluster called Joan Francesc Fernández (JFF) that has been used in this thesis to perform most of the parallel calculations. It has 128 cluster nodes, each node has 2 AMD Opteron Quad Core processors with 8 Gigabytes of RAM memory and linked with an infiniband DDR 4X network interconnection between nodes with latencies of 2.6 microseconds with a 20Gbits/s bandwidth. The cluster has also 40 cluster nodes, each node has 2 AMD Opteron with 16 Cores for each CPU linked with 64 Gigabytes of RAM memory and an infiniband QDR 4X network interconnection between nodes with latencies of 1.07 microseconds with a 40Gbits/s bandwidth. In these two groups of HPC Clusters, there is a total of 2304 CPUs.

Regarding to the development of numerical methods to perform Direct Numerical Simulation (DNS) of single phase flows, [24] presented a general symmetry-preserving discretization method for the DNS of turbulent, incompressible flows of Newtonian fluids. In addition, regularization modelling of turbulent flows was developed to carry out simulations on loosely coupled parallel computers. These numerical methods were used in DNS of a differentially heated air-filled cavity. Following this philosophy, [21] developed a numerical methodology suitable for the DNS and large-eddy simulation (LES) of turbulent flows in order to be used on complex geometries. Here, a mathematical formulation, conservative spatial discretization on unstructured grids and time integration scheme for solving the Navier-Stokes equations were presented. These numerical methods were applied on the study of turbulent flows past bluff bodies, such as: the flow past a sphere, the flow past a circular cylinder and the flow past a NACA 0012 airfoil. Regarding to numerical simulation of two-phase flows, important efforts have been carried out, for instance, [22] presented a free surface model based on a volume-of-fluid conservation equation. This model was applied to perform detailed simulations of absorption processes with presence of surfactants on two-dimensional cartesian meshes. [23] performed the numerical analysis of the thermal and fluid-dynamic behaviour of the two-phase flow in conducts, based on a quasi-homogeneous model, and the two-fluid model [9]. The aforementioned works are some examples related to DNS of single phase flows, and numerical modelling of two-phase flow, deployed recently at the CTTC. However, further steps are needed to perform Direct Numerical Simulations of Multiphase Flows. Therefore, in this work, the know- how developed at the CTTC on DNS of single phase flows, is extended to include new numerical methods to treat discontinuities in physical properties, interface capturing techniques (e.g. level-set methods [1]) and modelling of the surface tension forces. This thesis is an effort to contribute in this challenging task.

21

1.3   Objectives of this thesis

The numerical simulation of multiphase flows is a powerful tool for investigating and understanding the multiphase flows and to provide insight on the physics of free surface and interfacial flows such as bubble and droplet dynamics, ocean wave motion, among others. The advances in computational fluid dynamics (CFD) and its extension to multi-fluid flows called computational multi-fluid dynamics (CMFD) together with the increasing capacity of parallel computers have made possible to tackle such complex problems by using high performance numerical techniques such as direct numerical simulation (DNS).

DNS is an important research area in modern CMFD. In this sense, DNS has a key role for improving the understanding of the multiphase phenomena and for using this technique for the simulation of flows in complex geometries. On the other hand, results from DNS can be very useful for developing better Eulerian-Eulerian and Eulerian-Lagrangian models. Since now most of the DNS methods reported in the literature have been restricted to cartesian meshes and academic configurations. The reasons are mainly due to the limited computational resources and because the standards algorithms are very complex to be efficiently implemented on unstructured grids. Considering the actual state-of-the-art in multiphase flow modelling and numerical simulation methods, the main objectives of this thesis are:

- To develop a suitable formulation for the DNS of two-phase flows with moving interface boundaries on collocated unstructured grids. The numerical method will be based in the level-set method for interface capturing, and specially care is taken to address the mass conservation error present in standard formulations.

- The use of this formulation might allow the advance in the understanding of the physics of multiphase flows, specifically related to bubble and droplet dynamics by means of the numerical simulations of gravity-driven and surface-tension driven interfacial flows. The framework developed will be also applicable to free surface flow problems.

- A third objective is related to develop an interface capturing method suitable for simulation of bubble and droplet flows without numerical coalescence of interfaces, which is an artifact present in standard interface tracking formulations (e.g. level-set and volume-of-fluid methods).

In order to achieve these objectives, a conservative finite-volume discretization of the Navier-Stokes/Level-set equations has been proposed in the framework of collocated unstructured grids. The resulting code allows the high-performance computing of two-phase flow problems with moving interface boundaries using millions of

control volumes on parallel computers. Taking in account the ability of unstructured meshes to create grids around complex geometries, this code is used to simulate complex fluid dynamics on geometries not explored yet. Moreover a novel multiple marker approach here proposed in the framework of the conservative level-set method allows to simulate bubble and droplet flows without numerical coalescence.

1.4 Outline of the thesis

As aforementioned, this thesis aims at developing numerical methods suitable for the direct numerical simulation and of multiphase flows in order to be used in basic research and situations encountered in industrial application. At the same time, the study of such multiphase flows can be an opportunity for gaining insight into the complex physics associated with them.

To accomplish these goals, the second Chapter is devoted to present the mathematical formulation of two-phase flows with interfaces. The conservative level-set method for capturing the interface between two fluids is combined with a variable density projection scheme to simulate incompressible two-phase flows on unstructured meshes. All equations are discretized by using a conservative finite-volume approximation on a collocated grid arrangement. A high order scheme based on a flux limiter formulation, is adopted for approximating the convective terms, while the diffusive fluxes are centrally differenced. Gradients are computed by the least-squares approach. Physical properties are assumed to vary smoothly in a narrow band around the interface to avoid numerical instabilities. Finally, the numerical method is validated against classical advection test and two-phase flow examples including topology changes.

The following Chapter (Chapter 3) is devoted to a numerical study of gravity-driven bubbly flow using a mass conservative level-set method. First, the shape and terminal velocity of a single bubble which rises in a quiescent liquid are calculated and validated against experimental results reported in the literature. Then, different initial arrangements of bubble pairs were considered to study its hydrodynamic interaction. Finally, the gravity-driven bubbly flow is explored in a periodic vertical pipe including the coalescence and breakup of multiple bubbles. The results show that the conservative level-set approach is able to accurately capture the deformation of the interface on simulations of bubbly flows, and can remain numerically stable for a wide range of Morton and Reynolds numbers. Moreover, conservation properties are shown to be excellent, while accuracy remains satisfactory even for the most complex flows.

In Chapter 4, a methodology is presented for interface capturing in two-phase flows by combining volume-of-fluid with level-set methods. While the volume-of-fluid transport relies on a robust and accurate polyhedral library for interface captur-

ing, geometrical properties of interface (curvature) are calculated by using a level-set function, which is reconstructed through an iterative geometrical procedure. The method is validated on 2D and 3D test cases well known in the scientific literature. Conservation properties are shown to be excellent, while geometrical accuracy remains high even for the most challenging cases involving topology changes.

In Chapter 5, a novel multiple marker level-set method is introduced for Direct Numerical Simulation of deformable fluid particles (bubbles and droplets), which is integrated in a finite-volume framework on collocated unstructured grids. Each fluid particle is described by a separate level-set function, thus, different interfaces can be solved in the same control volume, avoiding artificial and potentially unphysical coalescence of fluid particles. Therefore, bubbles or droplets are able to approach each other closely, within the size of one grid cell, and can even collide. The proposed algorithm is developed in the context of the conservative level-set method, whereas, surface tension is modeled by the continuous surface force approach. The pressure-velocity coupling is solved by the fractional-step projection method. For validation of the proposed numerical method, the gravity-driven impact of a droplet on a liquid-liquid interface is studied; then, the binary droplet collision with bouncing outcome is examined, and finally, it is applied on simulation of gravity-driven bubbly flow in a vertical column.

Finally, in Chapter 6, closing of this thesis, conclusions and further research work are highlighted.

References

[1] Balcázar, N., Jofre, L., Lehmkhul, O., Castro, J., Rigola, J., 2014. A finite-volume/level-set method for simulating two-phase flows on unstructured grids. International Journal of Multiphase Flow 64, 55-72

[2] Banerjee, S., Numerical Methods. Short courses: Modelling and Computation of Multiphase Flows. Zurich, Switzerland, 2012.

[3] Banerjee, S., Nultifield Models. Short courses: Modelling and Computation of Multiphase Flows. Zurich, Switzerland, 2012.

[4] Brennen, C.E., Fundamentals of Multiphase Flow. Cambridge University Press, 2005.

[5] Clift, R., Grace, J.R., Weber, M.E., Bubbles, Drops and Particles. Academin Press, New York, 1978.

References

[6] Deen, N.G., Van Sint Annaland, M., Kuipers, J.A.M. , 2009. Direct numerical simulation of complex multi-fluid flows using a combined front tracking and immersed boundary method, Chemical Engineering Science 64, 2186-2201.

[7] Deen, N.G., Van Sint Annaland, M., Kuipers, J.A.M. , 2004. Multi-scale modeling of dispersed gasâliquid two-phase flow. Chemical Engineering Science 64, 1853-1861.

[8] Hetsroni, G., The nature of multiphase flows. Short courses: Modelling and Computation of Multiphase Flows. Zurich, Switzerland, 2012.

[9] Morales-Ruiz, S., Rigola, J., Rodriguez, I., Oliva, A., 2012. Numerical resolution of the liquid-vapour two-phase flow by means of the two-fluid model and a pressure based method. International Journal of Multiphase FLow 43, 118-130.

[10] Osher, S., Sethian, J.A., 1988. Fronts propagating with curvature-dependent speed: Algorithms based on Hamilton-Jacobi formulations. J. Comput. Phys. 79. 175-210.

[11] Prosperetti, A., Tryggvason, G., Computational Methods for Multiphase Flow. Cambridge University Press, 2007.

[12] Scardovelli, R., Zaleski, S., 1999. Direct numerical simulation of free surface and interfacial flow, Annu. Rev. Fluid Mech. 31, 567-603.

[13] Sussman, M., Smereka, P., Osher, S., 1994. A Level Set Approach for Computing Solutions to Incompressible Two-Phase Flow. J. Comput. Phys. 144. 146-159.

[14] Tryggvason, G., 2010. Virtual motion of real particles. Journal of fluid mechanis 650. 1-4.

[15] Tryggvason, G., Introduction to computational multiphase flows. Short courses: Modelling and Computation of Multiphase Flows. Zurich, Switzerland, 2012.

[16] Tryggvason, G., Scardovelli, R., Zaleski, S., Direct Numerical Simulation of Gas-Liquid Multiphase Flows. Cambridge University Press, 2011.

[17] Unverdi, S., Tryggvason, G., 1992. A front-tracking method for viscous, incompressible, multifluid flows. J. Comput. Phys. 100. 25-37.

[18] Van Wachem, B.G.M, Almstedt, A.E., 2003. Methods for multiphase computational fluid dynamics. Chemical Engineering Journal 96. 81-98.

[19] Yang, G., Liang-Shih,F., 2006. 3-D Direct numerical simulation of gas-liquid and gas-liquid-solid flow systems using the level-set and immersed-boundary methods. Advances in Chemical Engineering 31 2-61.

[20] http://www.cttc.upc.edu/

[21] Lehmkhul, O., Numerical resolution of turbulent flows on complex geometries. Ph.D. Thesis, Universitat Politècnica de Catalunya, 2012.

[22] Castro, J., Simulation of heat and mass transfer phenomena in the critical elements of H2O-LiBr absorption cooling machines. Experimental validation and application to design. Ph.D. Thesis, Universitat Politècnica de Catalunya, 2005.

[23] Morales, S., Numerical Simulation of the Thermal and Fluid Dynamics Behaviour of Liquid-Vapour Two-Phase Flow in Evaporators and Condensers. Ph.D. Thesis, Universitat Politècnica de Catalunya, 2009.

[24] Trias, F., Direct numerical simulation and regularization modelling of turbulent flows on loosely coupled parallel computers using symmetry-preserving discretizations. Ph.D. Thesis, Universitat Politècnica de Catalunya, 2006.

Chapter 2

A finite-volume/level-set method for simulating two-phase flows on unstructured grids

Most of the contents of this chapter have been published as:

Abstract. The conservative level-set method for capturing the interface between two fluids is combined with a variable density projection scheme to simulate incompressible two-phase flows on unstructured meshes. All equations are discretized by using a conservative finite-volume approximation on a collocated grid arrangement. A high order scheme based on a flux limiter formulation, is adopted for approximating the convective terms, while the diffusive fluxes are centrally differenced. Gradients are computed by the least-squares approach. Physical properties are assumed to vary smoothly in a narrow band around the interface to avoid numerical instabilities. The numerical method is validated against classical advection test and two-phase flow examples including topology changes.

2.1 Introduction

The numerical simulation of two-phase flows is a vast topic, with applications in a wide variety of environmental, geophysical and engineering situations ([39]). Due to inherent complexity from a physical as well numerical point view, a large choice of techniques has been developed for modeling of two-phase flows with moving inter-phase boundaries, for instance: the front-tracking (FT) method, the volume-of-fluid (VOF) method, and the level set (LS) method. In these methods, two-phase flow is treated as a single flow with the density and viscosity varying smoothly across the moving interface which is captured in an Eulerian framework (VOF and LS) or in a Lagrangian framework (FT). Although the idea behind these methods is similar, their numerical implementation may differ greatly. Each method has its own advantages and disadvantages, and for this reason it is not possible to assert which method is generally superior.

Direct numerical simulations of multiphase flows using a front tracking method are studied by [51] and [49]. In this approach, a stationary Eulerian grid is used for the fluid flow and the interface is tracked explicitly by a separate Lagrangian grid. This method is extremely accurate but also rather complex to implement due to the fact that dynamic re-meshing of the Lagrangian interface mesh is required ([12]). Contrary to LS and VOF method, automatic merging of interfaces does not occur, and difficulties arise when multiple interfaces interact with each other as in coalescence and break-up. A review of the VOF method can be found in [39]. In this approach, the interface is given implicitly by a color function, defined to be the fraction of volume within each cell of one of the fluids. In order to advect the VOF function, the interface needs to be reconstructed using a geometric technique. The VOF method has an excellent mass conservation property but it lacks accuracy for the direct calculations of interface geometric properties (normal and curvature) from the VOF function, whose spatial derivatives are not continuous near the interface.

Successful implementations of the level-set method have been demonstrated, for instance, by [36, 44, 43, 42, 46, 41, 34, 35, 13, 29, 30, 10]. In standard level-set (SLS) methods the interface is defined implicitly by the zero contour of a signed distance function ([36, 42]). The evolution of this function in space and time is governed by an advection equation, combined with a special re-distancing algorithm. An advantage of the level-set algorithm is its simplicity to compute geometric properties of the interface, required for instance to calculate the curvature of the surface. A disadvantage of SLS method, is that the discrete solution of transport equations is prone to numerical error and leads to loss or gain of mass. Recently [34] and [35] have proposed a conservative level-set (CLS) method, where mass conservation problem that is known to affect SLS method is greatly reduced. Additionally this approach benefits of automatic handling of topology changes and efficient parallelization with no additional cost.

2.1. Introduction

Most of numerical algorithms mentioned above have been developed for regular cartesian grids, so that their easiness of implementation, capability and accuracy on unstructured grids is still to be proven, though there are exceptions. For instance in the context of finite-element discretizations [30] have extended SLS method to unstructured meshes. [54] propose a three-dimensional hybrid SLS and VOF method based on finite-volume discretization, on tetrahedral grids, for free surface flow without surface tension, which conserve volume of fluid exactly. [6] propose a two-dimensional finite element method for incompressible two-phase flows with surface tension on a second order projection scheme, where fluid phases are advected by SLS approach and curvature is estimated by the least-squares method combined with a piecewise linear approximation to the interface. [25] present a SLS method based on variable-order finite element approximations on unstructured meshes, suitable for free surface flow without surface tension. [15] have introduced a pure finite-volume method for the problem of incompressible two-phase flow with surface tension using SLS formulation to track the interfaces on two-dimensional unstructured meshes.

Despite those efforts, the literature that involve applying finite-volume approach to a CLS based interface capturing method on three-dimensional unstructured meshes is limited. In this context, the present work is aimed at making progress in the direction of developing a numerical method to solve incompressible two-phase flows on unstructured meshes (2D and 3D), based on the CLS method for interface capturing. Thus, the mass conservation error that is known to affect SLS methods is circumvented; whereas unstructured meshes can be adapted to complex domains, enabling us an efficient mesh distribution in regions where interface resolution has to be maximized, which is in general hard to achieve on structured grids. In addition, the finite-volume method is attractive due to its simplicity and to the fact that it ensures satisfaction of the integral forms of the conservation laws over the entire domain. In this regard, we also propose a finite-volume discretization of the conservation equations on a collocated grid arrangement. Moreover, in order to avoid spurious oscillations around steep gradient regions, a novel Total Variation Diminishing (TVD) scheme based on flux limiters, has been developed in the framework of unstructured meshes, which is applied to discretize the convective term of the interface advection equation. Furthermore, a classical fractional step method ([7]) is used to solve incompressible Navier-Stokes equations that are coupled to a transport equation for the conservative level-set function; whereas the effect of surface tension is modeled by using the continuum surface force approach (CSF) according to [3].

The outline of the chapter is as follows: A mathematical review of fluid mechanics with interfaces is given in section 2.2. Here, the coupling of the Navier-Stokes equations for two-phase flow is introduced through the inter-phase jump conditions, which incorporate surface tension. The conservative level-set method is presented in section 2.3. Section 2.4 discusses the numerical method. The code validation and

numerical results are presented in section 2.5. Finally, the conclusions are presented in section 2.7.

2.2 Fluid mechanics with interfaces: One fluid formulation

The conservation of momentum and mass of two immiscible incompressible fluids is described by the Navier-Stokes equations defined on a spatial-time domain $\Omega \times [0, T]$ with boundary $\partial \Omega$:

$$\frac{\partial}{\partial t}(\rho_k \mathbf{v}_k) + \nabla \cdot (\rho_k \mathbf{v}_k \mathbf{v}_k) = \nabla \cdot \mathbf{S}_k + \rho_k \mathbf{g} \qquad \text{in } \Omega_k \times [0, T] \tag{2.1}$$

$$\mathbf{S}_k = -p_k \mathbf{I} + \mu_k \left(\nabla \mathbf{v}_k + (\nabla \mathbf{v}_k)^T \right) \tag{2.2}$$

$$\nabla \cdot \mathbf{v}_k = 0 \qquad \text{in } \Omega_k \times [0, T] \tag{2.3}$$

Here, $\Omega = \Omega_1 \cup \Omega_2 \cup \Gamma$, $k = \{1, 2\}$ denote the subdomains associated with the two different fluid phases, $\Gamma = \partial \Omega_1 \cap \partial \Omega_2$ is the fluid interface, ρ and μ denote the density and dynamic viscosity of the fluids, $\mathbf{v}$ is the velocity field, $\mathbf{g}$ is the gravity acceleration, p is the pressure, $\mathbf{S}$ is the stress tensor and $\mathbf{I}$ is the identity tensor.

Assuming no mass transfer between the fluids yields a continuous velocity condition at the interface:

$$\mathbf{v}_1 = \mathbf{v}_2 \qquad \text{in } \Gamma \times [0, T] \tag{2.4}$$

The jump in normal stresses along the fluid interface is balanced by the surface tension. Neglecting the variations of the surface tension coefficient σ gives the following boundary condition for momentum conservation at the interface:

$$(\mathbf{S}_1 - \mathbf{S}_2) \cdot \mathbf{n} = \sigma \kappa \mathbf{n} \qquad \text{in } \Gamma \times [0, T] \tag{2.5}$$

where $\mathbf{n}$ is the unit normal vector outward to $\partial \Omega_1$ and κ is the interface curvature. The system given by equations 2.1 to 2.3 and the interface boundary conditions given by equations 2.4 and 2.5, can be combined into the following:

$$\frac{\partial}{\partial t}(\rho \mathbf{v}) + \nabla \cdot (\rho \mathbf{v} \mathbf{v}) = -\nabla p + \nabla \cdot \mu \nabla \mathbf{v} + \nabla \cdot \mu (\nabla \mathbf{v})^T + \rho \mathbf{g}$$
$$+ \sigma \kappa \mathbf{n} \delta_\Gamma \qquad \text{in } \Omega \times [0, T] \tag{2.6}$$

$$\nabla \cdot \mathbf{v} = 0 \qquad \text{in } \Omega \times [0, T] \tag{2.7}$$

$$\beta = \beta_1 H_1 + \beta_2 (1 - H_1) \qquad \text{with } \beta \in \{\rho, \mu\} \tag{2.8}$$

where, δ_Γ is the Dirac delta function localized at the interface, and H_1 is the Heaviside step function, defined as:

$$H_1 = \begin{cases} 1 & \text{if } \mathbf{x} \in \Omega_1, \\ 0 & \text{if } \mathbf{x} \notin \Omega_1. \end{cases} \tag{2.9}$$

2.3 Conservative Level-set method

The level-set method, wich was first derived by [36], is a versatile method for capturing the motion of free surfaces. Instead of the signed distance function $d(\mathbf{x}, t)$ used to represent the interface in the classical LS method [36, 44], [34] employed a regularized indicator function ϕ in the context of their CLS method:

$$\phi(\mathbf{x}, t) = \frac{1}{2} \left(tanh \left(\frac{d(\mathbf{x}, t)}{2\varepsilon} \right) + 1 \right) \tag{2.10}$$

where ε is a parameter that sets the thickness of the profile, ϕ takes the value 0 in one fluid and the value 1 in the other fluid. The interface Γ is defined by the location of the $\phi = 0.5$ iso-surface:

$$\Gamma = \{\mathbf{x} \mid \phi(\mathbf{x}, t) = 0.5\} \tag{2.11}$$

The level set function ϕ is advected by a vector field $\mathbf{v}$ that is, in case of two-phase flows, the solution of the Navier-Stokes equations. The interface transport equation can be written in conservative form provided the velocity field is solenoidal, $\nabla \cdot \mathbf{v} = 0$, namely,

$$\frac{\partial \phi}{\partial t} + \nabla \cdot \phi \mathbf{v} = 0 \tag{2.12}$$

In order to avoid unphysical oscillations in the level set function, a TVD flux limiter scheme is used to discretize the convective term. Furthermore, an additional re-initialization equation [34, 20] is introduced to keep the profile and thickness of the interface constant,

$$\frac{\partial \phi}{\partial \tau} + \nabla \cdot \phi(1 - \phi)\mathbf{n}_{\tau=0} = \nabla \cdot \varepsilon \nabla \phi \tag{2.13}$$

This equation is advanced in pseudo-time τ, it consists of a compressive flux $\phi(1 - \phi)\mathbf{n}_{\tau=0}$ that aims at sharpening the profile, and of a diffusion term $\nabla \cdot \varepsilon \nabla \phi$ that ensure the profile remains of characteristic thickness ε. Geometrical information on the interface, such as normal vector $\mathbf{n}$ or curvature κ, is obtained through:

$$\mathbf{n} = \frac{\nabla \phi}{\|\nabla \phi\|} \tag{2.14}$$

31

$$\kappa(\phi) = -\nabla \cdot \mathbf{n} \tag{2.15}$$

Implementing surface tension in a numerical scheme involves two issues: the curvature κ needs to be determined, and the resulting pressure jump must be applied appropriately to the fluids. Since our discretization will be based on the finite-volume integration of the Navier-Stokes Eq. (5.1), the aforementioned problems can be conveniently addressed through the CSF method [3]. Thus, the singular term, $\sigma\kappa\mathbf{n}\delta_\Gamma$, is converted to a volume force as follows,

$$\sigma\kappa\mathbf{n}\delta_\Gamma = \sigma\kappa(\phi)\nabla\phi \tag{2.16}$$

where $\kappa(\phi)$ is given by Eq. (5.8). The most significant computational advantage of this method is that explicit tracking of the interface is unnecessary. In addition, the fluid properties, $\beta \in \{\mu, \rho\}$, are regularized by employing the level-set function in Eq. (2.8),

$$\beta(\phi) = \beta_1\phi + \beta_2(1 - \phi) \tag{2.17}$$

In this way the level-set method has been coupled to the incompressible Navier-Stokes equations. In the conservative level-set method, the interface thickness is controled by the parameter ε in the re-initialization Eq. (5.6). A smaller ε will reduce the smearing of density, viscosity and surface tension force; however, there is a numerical restriction on how small we can choose ε, because the calculation of interface normals and curvature will be more accurate if the transition in the level-set function ϕ is smooth. Moreover, a too small ε compared to the grid size produces numerical oscillations in the steady state solution of the re-initialization Eq. (5.6). An expression for the calculation of ε will be introduced in Section 2.4.1.

2.4   Numerical method

In this work, the finite-volume (FV) method is used to discretize the governing equations. In a FV method, the computational domain is covered by a set of time-invariant, non-overlapping control volumes. On each of these control volumes, the integral form of the fluid flow equations is discretized. A collocated grid arrangement is adopted, hence, all computed variables are stored at centroids of the cells.

The presented numerical methods are implemented in an in-house solver called TermoFluids. TermoFluids is an unstructured FV flow solver, designed for direct numerical simulation and large-eddy simulation of turbulent flows [47]. The reader is referred to [27] for details on the TermoFluids framework that are beyond the scope of this paper.

Equation	ψ	ξ	$G^{\mathbf{c}}(\psi)$	$\mathbf{c}$	λ	S_ψ
Momentum Eq.(5.1)	v_i	ρ	v_i	$\mathbf{v}$	μ	$-\partial_{x_i}p + \partial_{x_j}\mu\partial_{x_i}v_j + \rho g_i$
						$+\sigma\kappa\partial_{x_i}\phi$
Advection Eq.(5.5)	ϕ	1	ϕ	$\mathbf{v}$	0	0
Re-initialization Eq.(5.6)	ϕ	1	$\phi(1-\phi)$	$\mathbf{n}$	ε	0

Table 2.1: Summary of terms used in Eq. (2.18). S_{v_i} is expressed in cartesian tensor notation, where $x_i \in \{x, y, z\}$, $v_i \in \{v_x, v_y, v_z\}$, $\partial_{x_i} \equiv \partial/\partial x_i$ and $g_i \in \{g_x, g_y, g_z\}$.

2.4.1 Spatial discretization

The spatial discretization is performed by using the integral form of the transport equations:

$$\int_{V_P} \frac{\partial \xi\psi}{\partial t}dV = \oint_{A_P} (-\xi G^{\mathbf{c}}(\psi)\mathbf{c} + \lambda\nabla\psi) \cdot d\mathbf{A} + \int_{V_P} S_\psi dV \qquad (2.18)$$

The volume of the cell P is designed as V_P and A_P is its surface with the local area vector $d\mathbf{A}$. A summary of terms used in Eq. (2.18) is given in Table 2.1. A_P can be decomposed in n_f single faces, $f \in \{f_1, f_2, ..., f_{n_f}\}$, as sketched in Fig. 2.2. Each face has its area vector $\mathbf{A}_f$, and is lying between two cells P and F; where P is the main cell, and $F \in \{F_1, F_2, ..., F_{n_f}\}$ is its neighbor cell, In what follows, next definitions will be used:

- $\psi_P \equiv \bar{\psi}(\mathbf{x}_P) = \frac{1}{V_P}\int_{V_P} \psi dV$, is an approximation of a scalar function ψ localized at the cell centroid $\mathbf{x}_P$.

- $\psi_f \equiv \bar{\psi}(\mathbf{x}_f) = \frac{1}{A_f}\int_{A_f} \psi dA$, is an approximation of a scalar function ψ localized at the face centroid $\mathbf{x}_f$.

Interpolation

All variables are defined at cell centroids in a collocated grid arrangement. However, the face values of physical properties ξ_f and λ_f, gradient $(\nabla\psi)_f$ and interface normal $\mathbf{n}_f$, are needed in many calculations. Hence, a distance-weighted linear interpolation is used to calculate these values:

$$\xi_f = \sum_{q \in \{P,F\}} w_q\xi_q \text{ , with } w_q = 1 - \frac{||\Delta\mathbf{x}_{f \to q}||}{\sum_{q \in \{P,F\}} ||\Delta\mathbf{x}_{f \to q}||} \qquad (2.19)$$
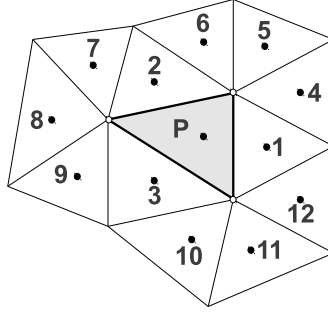
Figure 2.1: Node stencil used for the gradient reconstruction by using the least-squares method.

Gradient reconstruction

A stencil which identifies neighboring points of the cell P (see Fig. 2.1) is used on approximating the variation of a dependent variable ψ by a truncated Taylor series, e.g., for a linear approximation,

$$\psi_i = \psi_P + (\mathbf{x}_i - \mathbf{x}_P) \cdot (\nabla \psi)_P \qquad \text{i=1, 2, ..., } n \tag{2.20}$$

The application of Eq. (2.20) to all points included in the cell stencil, $\mathbf{x}_i \in \{\mathbf{x}_1, \mathbf{x}_2, ..., \mathbf{x}_n\}$, gives a system of linear equations for the derivatives at centroid $\mathbf{x}_P$, which is written in matrix notation:

$$\underbrace{\begin{pmatrix} x_1 - x_P & y_1 - y_P & z_1 - z_P \\ x_2 - x_P & y_2 - y_P & z_2 - z_P \\ \vdots & \vdots & \vdots \\ x_n - x_P & y_n - y_P & z_n - z_P \end{pmatrix}}_{\mathbf{M}} \underbrace{\begin{pmatrix} (\partial_x \psi)_P \\ (\partial_y \psi)_P \\ (\partial_z \psi)_P \end{pmatrix}}_{(\nabla \psi)_P} = \underbrace{\begin{pmatrix} \psi_1 - \psi_P \\ \psi_2 - \psi_P \\ \vdots \\ \psi_n - \psi_P \end{pmatrix}}_{\mathbf{Y}} \tag{2.21}$$

The resulting over-determined system of linear equations $\mathbf{M}(\nabla \psi)_P = \mathbf{Y}$ is solved by the least-squares method [21]:

$$(\nabla \psi)_P = (\mathbf{M}^T \mathbf{M})^{-1} \mathbf{M}^T \mathbf{Y} \tag{2.22}$$
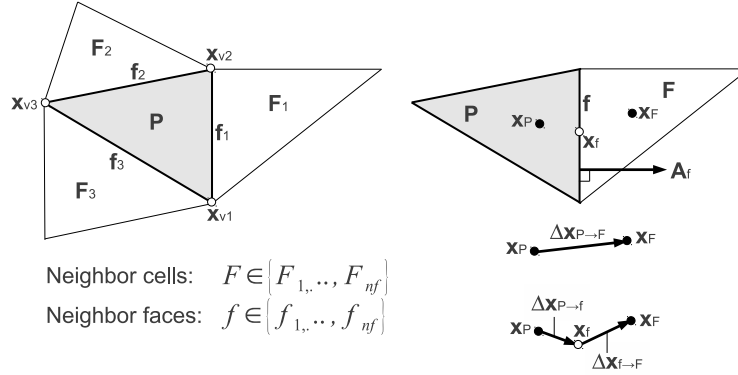
Figure 2.2: Control volume used for discretization of Eq. (2.18).

Diffusive term

The diffusion flux through cell faces is discretized by using a central difference scheme:

$$\oint_{A_P} \lambda \nabla \psi \cdot d\mathbf{A} \approx \sum_f \lambda_f (\nabla \psi)_f \cdot \mathbf{A}_f$$

$$= \sum_f \lambda_f ||\mathbf{A}_f|| \left(\frac{\psi_F - \psi_P}{||\Delta \mathbf{x}_{P \to F}||} + (\nabla \psi)_f \cdot \left(\frac{\mathbf{A}_f}{||\mathbf{A}_f||} - \frac{\Delta \mathbf{x}_{P \to F}}{||\Delta \mathbf{x}_{P \to F}||} \right) \right) \tag{2.23}$$

The first term on the right-hand side of Eq. (2.23) is the normal diffusion, and the second term is the cross diffusion; λ_f and $(\nabla \psi)_f$ are calculated by using linear interpolation, Eq. (2.19).

Convective and compressive terms

A proper interpolation of ψ_f, in the convective and compressive terms, of Eq. (2.18), is essential to the accuracy as well as the stability of the numerical solution. From Fig. 2.3, ψ_f is written as the sum of a diffusive first-order upwind part and an anti-diffusive term [45, 11, 28]:

$$\psi_f = \psi_{C'} + \frac{1}{2} L(\theta_f)(\psi_{D'} - \psi_{C'}) \tag{2.24}$$

where $\psi_{C'} \equiv \psi(\mathbf{x}_{C'})$, $\psi_{D'} \equiv \psi(\mathbf{x}_{D'})$, $\mathbf{x}_{C'}$ and $\mathbf{x}_{D'}$ refer to the points in Fig. 2.3. The anti-diffusive part is multiplied by the flux limiter, $L(\theta)$, which is a function of θ, the

upwind ratio of consecutive gradients of the solution, defined as:

$$\theta_f = \frac{\psi_{C'} - \psi_{U'}}{\psi_{D'} - \psi_{C'}} \tag{2.25}$$

where,

$$\begin{cases} \psi_{C'} = \psi_C + (\mathbf{x}_{C'} - \mathbf{x}_C) \cdot (\nabla \psi)_C, \\ \psi_{D'} = \psi_D + (\mathbf{x}_{D'} - \mathbf{x}_D) \cdot (\nabla \psi)_D, \\ \psi_{U'} = \psi_U + (\mathbf{x}_{U'} - \mathbf{x}_U) \cdot (\nabla \psi)_U. \end{cases} \tag{2.26}$$

From Fig. 5.5, $\mathbf{x}_C$ and $\mathbf{x}_D$ refer to the upwind cell centroid and downwind cell centroid respect to the face f, $\mathbf{x}_U$ is the far upwind cell centroid, and $\mathbf{x}_f$ is the face centroid. The points $\mathbf{x}_{C'}$, $\mathbf{x}_{D'}$, $\mathbf{x}_{U'} = \mathbf{x}_{C'} - \Delta\mathbf{x}_{C' \to D'}$, and $\mathbf{x}_f$ are along the line l_f, which is perpendicular to the face f. The point $\mathbf{x}_U$ is the closest centroid to the point $\mathbf{x}_{U'}$, which is selected from the centroids of all cells adjacent to the cell C, in upwind direction with respect to the face f (see Fig. 2.3).

Furthermore, the flux limiters used in this paper have the forms:

$$L(\theta) \equiv \begin{cases} max\{0, min\{2\theta, 1\}, min\{2, \theta\}\} & \text{TVD Superbee limiter,} \\ 1 & \text{Central difference limiter,} \\ 0 & \text{First-order upwind limiter.} \end{cases} \tag{2.27}$$

Thus, both convection and compression terms, are discretized as follows:

$$\oint_{A_P} \xi G^{\mathbf{c}}(\psi)\mathbf{c} \cdot d\mathbf{A}_P \approx \sum_f G^{\mathbf{c}}(\psi_f)\xi_f U_f^{\mathbf{c}}$$

$$= \sum_f [[\xi_f U_f^{\mathbf{c}}, 0]] G^{\mathbf{c}}(\psi_{C'}) - [[-\xi_f U_f^{\mathbf{c}}, 0]] G^{\mathbf{c}}(\psi_{D'})$$

$$+ \frac{1}{2}\xi_f U_f^{\mathbf{c}} L(\theta_f) \left(G^{\mathbf{c}}(\psi_{D'}) - G^{\mathbf{c}}(\psi_{C'}) \right) \tag{2.28}$$

Here, $\mathbf{c} \in \{\mathbf{v}, \mathbf{n}\}$, $U_f^{\mathbf{v}} \equiv \mathbf{v}_f \cdot \mathbf{A}_f$ is the volume flux, $U_f^{\mathbf{n}} \equiv \mathbf{n}_f \cdot \mathbf{A}_f$ is the compression flux, and $[[a, b]]$ denotes the maximum of the two arguments a and b. $U_f^{\mathbf{n}}$ and ξ_f are calculated by using linear interpolation, Eq. (2.19), and $U_f^{\mathbf{v}}$ is obtained by a mass conservative interpolation scheme (see section 2.4.2).
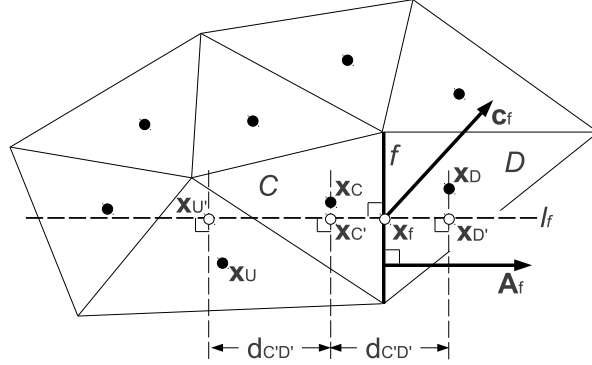
Figure 2.3: Convective and compressive node stencil. Here, $\mathbf{c}_f \in \{\mathbf{v}_f, \mathbf{n}_f\}$, $\mathbf{v}$ is the velocity field, $\mathbf{n}$ is the interface normal defined in Eq. (5.7), and $d_{C'D'} = ||\mathbf{x}_{D'} - \mathbf{x}_{C'}||$.

Source term

The source term in the momentum equations (see Table 2.1) is discretized as follows:

$$\int_{V_{cv}} S_{\mathbf{v}} dV_{cv} = -\sum_f p_f \mathbf{A}_f + \sum_f \mu_f (\nabla \mathbf{v})_f^T \cdot \mathbf{A}_f + \rho_P \mathbf{g} V_P$$
$$+ \sigma \kappa_P (\nabla \phi)_P V_P \tag{2.29}$$

where p_f, μ_f, $(\nabla \mathbf{v})_f^T$ are calculated by linear interpolation, Eq. (2.19). The gradients ∇v_i are computed by using the least-squares method, Eq. (2.22). The source term in advection Eq. (5.5) and re-initialization Eq. (5.6) is zero.

Interface normal and curvature

One of the most important aspects for the computation of surface tension model, Eq. 5.9, is the approximation used for the interface normal, $\mathbf{n}$. In this context, different methods for estimation of interface normals have been studied by [26], where it concludes that a wide and symmetric stencil is neccesary for a reasonable estimation of $\mathbf{n}$. In addition, least-squares method has been successfully used for estimation of interface normals, for instance in [26] and [53]. Thus, in this work, the least-squares method (see Section 2.4.1) has been selected for aproximation of $\mathbf{n}$ at cell centroids,

$$\mathbf{n}_P = \frac{(\nabla \phi)_P}{||(\nabla \phi)_P||} \tag{2.30}$$

37

where $(\nabla \phi)_P$ is evaluated by using Eq. (2.22). Furthermore, it is expected that the numerical oscillations will be smeared out due the size of the statistical sample used to build the gradient stencil (see Fig. 2.1).

Once interface normals have been determined with the least-squares approach, the curvature is directly computed from **n**:

$$\kappa_P = \frac{1}{V_P} \int_{V_P} \nabla \cdot \mathbf{n} dV = \frac{1}{V_P} \oint_{A_P} \mathbf{n} \cdot d\mathbf{A} = \frac{1}{V_P} \sum_f \mathbf{n}_f \cdot \mathbf{A}_f \tag{2.31}$$

where, $\mathbf{n}_f$ is calculated by using linear interpolation, Eq. (2.19).

Interface thickness

Interface profile needs to be sufficiently resolved so that the transport step can be accurate and stable. Solving Eq. (5.6) to steady-state results in a smooth transition of ϕ at the interface. The width of the transition region depends on the diffusion coefficient ε, which is defined based on the mesh resolution by:

$$\varepsilon_P = C_\varepsilon (\Delta_P)^\alpha \tag{2.32}$$

where $\Delta_P = (V_P)^{1/3}$ is defined as the characteristic size of the control volume P. From Fig. 2.4, as ε_P decreases the level set function becomes sharper. However, when ε_P becomes too small, numerical stability can be affected. In numerical experiments we have found that the value $C_\varepsilon = 0.5$ and $0.9 \leq \alpha \leq 1$, are satisfactory (see Fig. 2.4). This is in agreement with the values used by [34].

Boundary conditions

In addition to cell centers, scalar fields (v_i, p, ϕ) are also stored at boundary faces of the cells. Thus, the boundary conditions are directly updated at the boundary face itself. For the boundary face b, the Dirichlet boundary condition is given, $\psi_b = \psi_{given}$.

For a Neumann boundary condition, the gradient is specified at the boundary face, $(\nabla \psi)_b \cdot (\mathbf{A}_b / \|\mathbf{A}_b\|) = 0$, where $\mathbf{A}_b$ is the area vector of b, pointing outside the boundary cell. Hence, ψ_b is approximated as:

$$\psi_b = \psi_P + (\mathbf{x}_{P'} - \mathbf{x}_P) \cdot (\nabla \psi)_P \tag{2.33}$$

where, $\mathbf{x}_{P'} = \mathbf{x}_b + (\mathbf{A}_b / \|\mathbf{A}_b\|) \cdot (\mathbf{x}_P - \mathbf{x}_b)$.
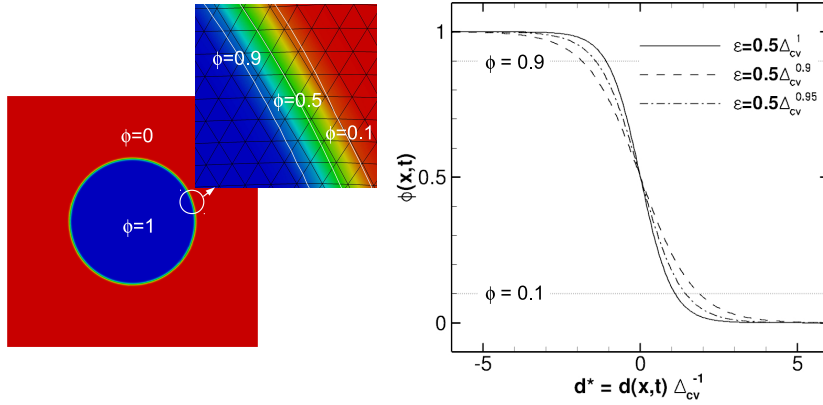
Figure 2.4: Interface thickness is controlled by the parameter ε. Here, d^* is a dimensionless distance function.

2.4.2 Time discretization

Time integration of Eq. (2.18) is outlined as:

$$V_P(\psi_P^{n+1} - \psi_P^n) = \int_t^{t+\Delta t} (R_\psi^c)_P dt \qquad (2.34)$$

Here, $(R_\psi^v)_P$ corresponds to the discrete space operator, applied to the right-hand side term of Eq. (2.18). Eq. (2.34) is a system of ordinary differential equations in time. The integration in time can be performed in implicit or explicit manner, for the present study an explicit Adams-Bashforth or third order TVD Runge-Kutta multi-stepping scheme is used throughout.

CLS Advection

The advection Eq. (5.5) is integrated in time with a 3-step third-order accurate TVD Runge-Kutta scheme [16] denoted by RK3,

$$\begin{cases} (\phi_P^{**} - \phi_P^n)V_P = (R_\phi^v)_P^n \Delta t, \\ (\phi_P^* - \frac{3}{4}\phi_P^n - \frac{1}{4}\phi_P^{**})V_P = \frac{1}{4}(R_\phi^v)_P^{**}\Delta t, \\ (\phi_P^{n+1} - \frac{1}{3}\phi_P^n - \frac{2}{3}\phi_P^*)V_P = \frac{2}{3}(R_\phi^v)_P^*\Delta t. \end{cases} \qquad (2.35)$$

39

where,

$$\left(R_\phi^{\mathbf{v}}\right)_P = -\sum_f \phi_f U_f^{\mathbf{v}} \tag{2.36}$$

Here, $(R_\phi^{\mathbf{v}})_P$ is discretized by using a TVD Superbee scheme, Eqs. (2.24,2.28). A mass conservative interpolation scheme is used for the evaluation of the volume flux $U_f^{\mathbf{v}} = \mathbf{v}_f \cdot \mathbf{A}_f$ (see section 2.4.2).

CLS Reinitialization

The re-initialization Eq. (5.6) is integrated in pseudo-time (τ) by using the RK3 method:

$$\begin{cases} (\phi_P^{**} - \phi_P^n)V_P = (R_\phi^{\mathbf{n}})_P^n \Delta\tau, \\ (\phi_P^* - \frac{3}{4}\phi_P^n - \frac{1}{4}\phi_P^{**})V_P = \frac{1}{4}(R_\phi^{\mathbf{n}})_P^{**} \Delta\tau, \\ (\phi_P^{n+1} - \frac{1}{3}\phi_P^n - \frac{2}{3}\phi_P^*)V_P = \frac{2}{3}(R_\phi^{\mathbf{n}})_P^* \Delta\tau. \end{cases} \tag{2.37}$$

where,

$$\left(R_\phi^{\mathbf{n}}\right)_P = -\sum_f \phi_f(1 - \phi_f)U_f^{\mathbf{n}} + \sum_f \varepsilon_f(\nabla\phi)_f \cdot \mathbf{A}_f \tag{2.38}$$

Here, the compression term $\sum_f \phi_f(1 - \phi_f)U_f^{\mathbf{n}}$ is discretized by using a central difference (CD) limiter, Eqs. (2.24, 2.28). $U_f^{\mathbf{n}} = (\mathbf{n}_{\tau=0})_f \cdot \mathbf{A}_f$ is calculated by linear interpolation, Eq. (2.19). The diffusive term $\sum_f \varepsilon_f \nabla\phi \cdot \mathbf{A}_f$ is discretized by applying Eq. (2.23).

The time τ is fictitious in the re-initialization Eq. (5.6), and it plays a role to lead the solution into a stationary state. Since an explicit scheme is used, the time step is restricted by the viscous term of Eq. (5.6):

$$\Delta\tau = C_\tau min\left(\frac{(\Delta_P)^2}{\varepsilon_P}\right) \tag{2.39}$$

where, C_τ is taken to be ~ 0.01. Only a few time steps are needed to reach the steady state of Eq. (2.37).

Pressure correction scheme on collocated meshes

Given solution values at t_n, the Navier-Stokes equations are integrated to t_{n+1} by using a sequence of fractional steps. The fractional step method, is in general a method of approximation of the evolution equations based on decomposition of the operators they contain [7, 18]. In the first step an explicit Adams-Bashforth scheme is used to evaluate a predictor velocity $\mathbf{v}^*$:

$$\mathbf{v}_P^* = \mathbf{v}_P^n + \frac{\Delta t}{\rho(\phi_P^n)V_P}\left(\frac{3}{2}(\mathbf{R_v^v})_P^n - \frac{1}{2}(\mathbf{R_v^v})_P^{n-1}\right) \tag{2.40}$$

where,

$$(\mathbf{R_v^v})_P = -\sum_f \rho_f \mathbf{v}_f U_f^{\mathbf{v}} + \sum_f \mu_f(\nabla \mathbf{v})_f \cdot \mathbf{A}_f$$
$$+ \sum_f \mu_f(\nabla \mathbf{v})_f^T \cdot \mathbf{A}_f + \rho(\phi_P)\mathbf{g}V_P + \sigma\kappa(\phi_P)(\nabla\phi)_P V_P \qquad (2.41)$$

Here, the convective term, $\sum_f \rho_f \mathbf{v}_f U_f^{\mathbf{v}}$, is discretized by using a CD limiter (see Eqs. (2.24,2.28)). Moreover, following the work of [48] and [32], the conservative nature of the Navier-Stokes equations is intimately tied up with the symmetries of the differential operators. Thus, in order to retain a skew-symmetric discretization of the collocated convective operator, ρ_f is approximated by linear interpolation with weight factor $w_q = 0.5$ (see Eq. (2.19)). The volume flux $U_f^{\mathbf{v}}$ is computed by using a mass conservative scheme, which will be introduced in Eq. (5.15). The diffusion term, $\sum_f \mu_f(\nabla \mathbf{v})_f \cdot \mathbf{A}_f$, is discretized by Eq. (2.23); whereas the source term is discretized by Eq. (2.29), excluding the pressure term.

In step two, the velocities at the new time instant t_{n+1} are computed by:

$$\mathbf{v}_P^{n+1} = \mathbf{v}_P^* - \frac{\Delta t}{\rho(\phi_P^n)}(\nabla p^{n+1})_P \qquad (2.42)$$

A Poisson equation for the pressure is generated by requiring that the volume fluxes in Eq. (2.42) sum to zero over each cell. Hence, under the incompressibility constraint given by Eq. (5.2), divergence of Eq. (2.42) leads to:

$$\sum_f \mathbf{v}_f^* \cdot \mathbf{A}_f = \sum_f (p_F^{n+1} - p_P^{n+1})\frac{\Delta t ||\mathbf{A}_f||}{\rho_f ||\Delta\mathbf{x}_{P\to F}||} \qquad (2.43)$$

This is a variable coefficient Poisson equation for the pressure, endowed with the Neumann boundary condition, which is solved by using a preconditioned conjugate gradient (PCG) method. Face values in Eq. (2.43), $\mathbf{v}_f^*$ and ρ_f, are calculated by using linear interpolation of the adjacent cell values, Eq. (2.19).

To avoid pressure-velocity decoupling when the pressure projection is made on collocated meshes [14, 37], a cell face volume flux, $U_f^{\mathbf{v}}$, is defined so that fluxes conserve mass exactly:

$$(U_f^{\mathbf{v}})^{n+1} = \mathbf{v}_f^* \cdot \mathbf{A}_f - \left(\frac{\Delta t}{\rho(\phi^n)}\nabla p^{n+1}\right)_f \cdot \mathbf{A}_f$$
$$= \sum_{q \in \{P,F\}} w_q \left(\mathbf{v}_q^{n+1} + \frac{\Delta t}{\rho(\phi_q^n)}(\nabla p^{n+1})_q\right) \cdot \mathbf{A}_f - \frac{\Delta t}{\rho_f}(\nabla p^{n+1})_f \cdot \mathbf{A}_f \qquad (2.44)$$

where,

$$\begin{cases} (\nabla p^{n+1})_f \cdot \mathbf{A}_f = (p_F^{n+1} - p_P^{n+1}) \frac{||\mathbf{A}_f||}{||\Delta \mathbf{x}_{P \to F}||}, \\ (\nabla p^{n+1})_P = \frac{1}{V_P} \sum_f \mathbf{A}_f \sum_{q \in \{P,F\}} w_q p_q^{n+1} \end{cases}$$ (2.45)

Here, $\mathbf{v}_f^* = \sum_{q \in \{P,F\}} w_q \mathbf{v}_q^*$, where $\mathbf{v}_q^*$ was replaced by Eq. (2.42). Following the work of [14] there are two sources of kinetic energy error when the Navier-Stokes equations are discretized on collocated curvilinear grids: interpolation error and pressure error. The interpolation error will be present if second-order, mesh dependent weighting factors are used. It can be eliminated by choosing first-order fixed weights of $w_q = 0.5$. Pressure error can not be eliminated and it scales like $O(\Delta_P^2)$ and $O(\Delta t)$. Thus, mesh refinement and small time steps or high order temporal schemes are necessary to decrease the kinetic energy error on collocated meshes. In the present work, mesh-independent weights ($w_q = 0.5$) are used for interpolation in Eqs. (2.43-2.45), with the aim of reduce kinetic energy error linked to interpolation.

Time step restrictions

The magnitude of the allowable time step for stable calculations is determined from the gravity, surface tension, convective and viscous terms. The convection time step is limited by the CFL constraint:

$$(\Delta t)_{conv} \leqslant min \left(\frac{\Delta_P}{||\mathbf{v}_P||} \right)$$ (2.46)

The viscous time step restriction is given by:

$$(\Delta t)_{visc} \leqslant min \left(\frac{(\Delta_P)^2 \rho(\phi_P)}{\mu(\phi_P)} \right)$$ (2.47)

The stability restriction due to the gravity can be expressed in the form of a CFL-like condition $\mathbf{v}_g (\Delta t)_g (\Delta_P)^{-1} < 1$; where $\mathbf{v}_g = (\Delta t)_g \mathbf{g}$ is the gravity induced velocity. Thus, the maximal allowed gravity time step size is given by:

$$(\Delta t)_g \leqslant \left(min \left(\frac{\Delta_P}{||\mathbf{g}||} \right) \right)^{1/2}$$ (2.48)

According to the study by [3], the time step restriction because of the explicit treatment of surface tension is given as follows:

$$(\Delta t)_{cap} \leqslant min \left(\left(\frac{\rho_1 + \rho_2}{4\pi\sigma} \right)^{1/2} (\Delta_P)^{3/2} \right)$$ (2.49)

Finally, the global stability constraint is given by:

$$\Delta t \leqslant min\left((\Delta t)_{conv}, (\Delta t)_{visc}, (\Delta t)_{cap}, (\Delta t)_{g}\right) \qquad (2.50)$$

Thus, Eq. (50) enforces that the discrete information can evolve no more than one grid cell since the discrete equations consider only fluxes between adjacent cells.

2.4.3   Solution algorithm

It is assumed that when the solution is initialized not only are the physical states $(\mathbf{v}, p, \rho, \mu, \varepsilon)$ known for all cells, but also the level-set field $(\phi(\mathbf{x}, 0))$. For each time update from t_n to t_{n+1} the numerical scheme can then be summarized as follows:

1. Choose an appropriate time step Δt satisfying Eq. (2.50).

2. Advance the conservative level set function ϕ, by solving Eq. (2.35).

3. Solve re-initialization Eq. (2.37), for steady state.

4. Curvature, density and viscosity fields are updated from the level set field.

5. The Navier-Stokes equations are solved by using the fractional step method:
    Calculate the predictor velocity by solving Eq. (5.12).
    Solve pressure Eq. (2.43) by using a PCG method.
    Calculate the corrected velocity by solving Eq. (2.42).

6. Update the mass conservative volume flux, U_f^v, by solving Eq. (5.15).

7. Repeat step 1 to step 9 until the desired time-level is reached.

2.5   Numerical experiments

2.5.1   Single vortex deformation of a circle

In order to validate the CLS solver, a variant of the problem of [38] is investigated in a square domain $\Omega = [0, 1] \times [0, 1]$ (see Fig. 2.5). A circle of radius $r = 0.15$, initially centered at $(0.5, 0.75)$ is deformed under a solenoidal velocity field:

$$\begin{cases} u(x, y) = -\sin^2(\pi x)\sin(2\pi y), \\ v(x, y) = \sin^2(\pi y)\sin(2\pi x). \end{cases} \qquad (2.51)$$

At $t = 0.5T$ the flow field is reversed so that the exact solution at $t = T$ should theoretically coincide with the initial condition. This problem will be solved on three

meshes (see Fig. 2.5) at $\Delta t = 10^{-4}$, with an interface thickness parameter of $\varepsilon_P = 0.5\Delta_P$.

Figure 2.7 shows the initial and final shapes of the circles advected to periods $T = 2$ and $T = 8$. It is noted that for the period $T = 2$ the circle returns to its original shape with greater accuracy than for a period $T = 8$. For the case with $T = 8$, the predicted results are plotted in Fig. 2.6. The resulting vortex field stretching the circular interface into a very long filament that spirals around the center of the domain, which compares very well with those results obtained using other state-of-the-art methods for structured meshes, for example [34, 13, 40]. Clearly at $t = 4$, the width of the ligament should fall bellow the resolution of the mesh M_3. However, because the conservative re-initialization step, the CLS method attempts to maintain the area on the mesh, which leads to the formation of drops of the size of one or two grid cells. This behavior can be delayed by refining the grid. But, because the filament asymptotes to infinitesimal thickness, any grid will provide inadequate resolution.

For the sake of comparison, the relative global mass errors are defined as:

$$E_0(t) = \frac{\int_V \phi(\mathbf{x}, t)dV - \int_V \phi(\mathbf{x}, 0)dV}{\int_V \phi(\mathbf{x}, 0)dV} \tag{2.52}$$

$$E_1(t) = \frac{\int_V \phi(\mathbf{x}, t)dV - \int_V \phi(\mathbf{x}, 0)dV}{\int_V \phi(\mathbf{x}, 0)dV} \text{ , for } 0.5 \leq \phi \leq 1 \tag{2.53}$$

where V is the volume of the whole domain Ω. Since $\Delta t \ll min\{\Delta_P/\mathbf{v}_P\}$, the predicted errors ($E_0$ and E_1) come mainly from the approximation of the spatial derivatives. The computed mass losses are plotted in Fig. 2.8 and Fig. 2.9, which indicates that CLS method is mass conservative and remarkably resilient for interface capturing, even when large complex topological changes have occurred.

2.5.2 Two-dimensional rising bubble

This complex benchmark test case has been thoroughly studied by three independent research groups who managed to determine accurate and quantitative reference solutions for the circularity, rise velocity, and center of mass of a bubble rising in another fluid [23, 22]. The computational domain and initial configuration are shown in Fig. 2.10a, where a circular bubble of diameter $d = 0.5$ is positioned in a rectangular domain $\Omega = [0, 2d] \times [0, 4d]$. The bubble and the surrounding fluid are initially at rest. Non-slip boundary condition is applied at the top and bottom boundaries, and free slip boundary condition on the vertical walls.

The physical parameters of the two fluids defining the test case are given in Table 2.2. The subscript 1 refers to the heavier fluid in Ω_1, and the subscript 2 refers to the bubble in Ω_2. Computations were performed on three meshes, which divide
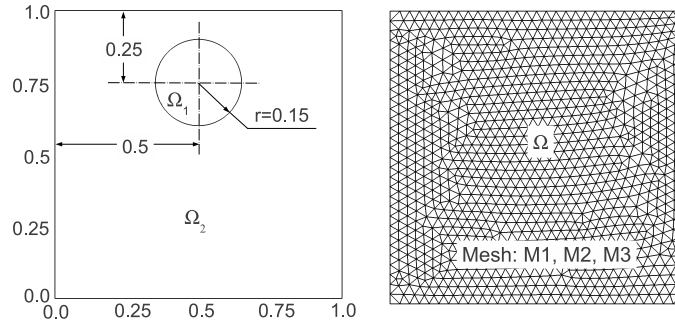
Figure 2.5: Single vortex deformation of a circle: Initial condition and mesh configuration ($M1 = 2.3 \times 10^4 cv$, $M2 = 9.1 \times 10^4 cv$, $M3 = 2.1 \times 10^5 cv$).
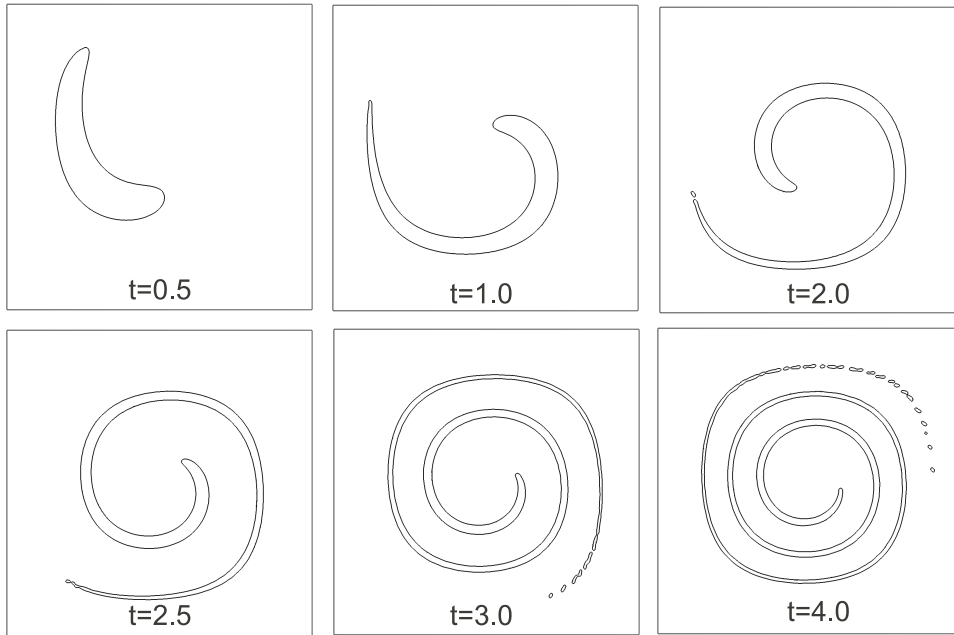
Figure 2.6: Single vortex deformation of a circle: period $T = 8.0$, mesh M3.
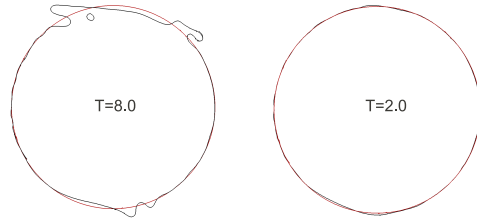
Figure 2.7: Single vortex deformation of a circle: interface location for the circle at $t = T = \{2.0, 8.0\}$ for the mesh M_3 ($2.1 \times 10^5 cv$). Computed interface (black line) and exact solution (red line).
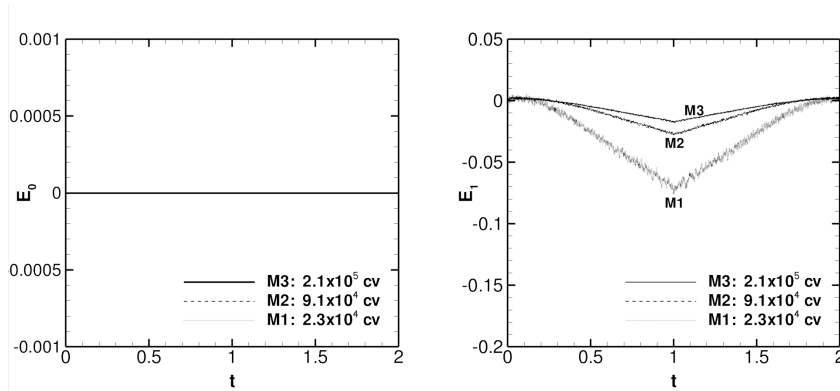
Figure 2.8: Temporal evolution of the normalized mass errors E_0 and E_1 for the circle in a deformation field test for different meshes, and period $T = 2$.
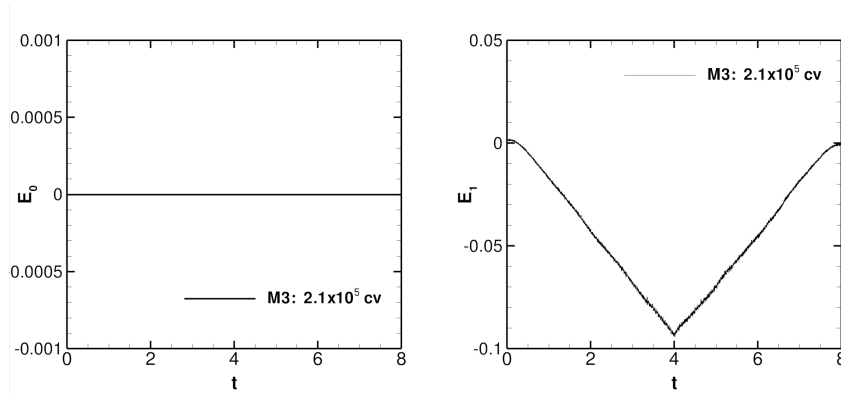
Figure 2.9: Temporal evolution of the normalized mass errors E_0 and E_1 for the circle in a deformation field test for the mesh M_3, and period $T = 8$.
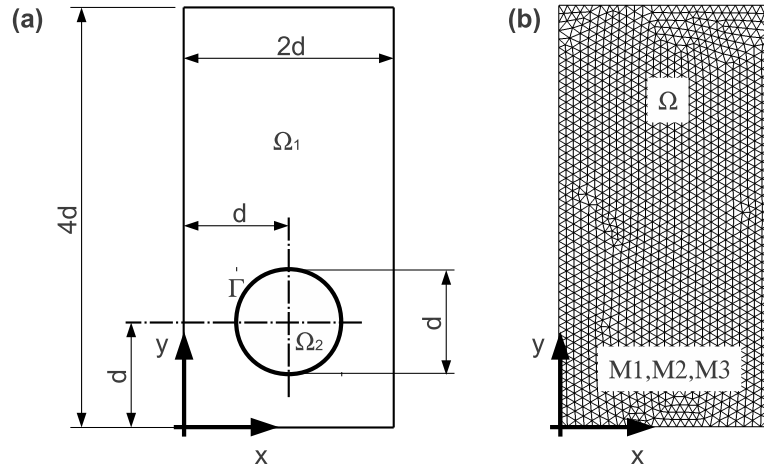
Figure 2.10: Two dimensional rising bubble. (**a**) Computational domain and (**b**) mesh configuration ($M1 = 1.6 \times 10^4$ cv, $M2 = 4.6 \times 10^4$ cv, $M3 = 4.2 \times 10^5$ cv).
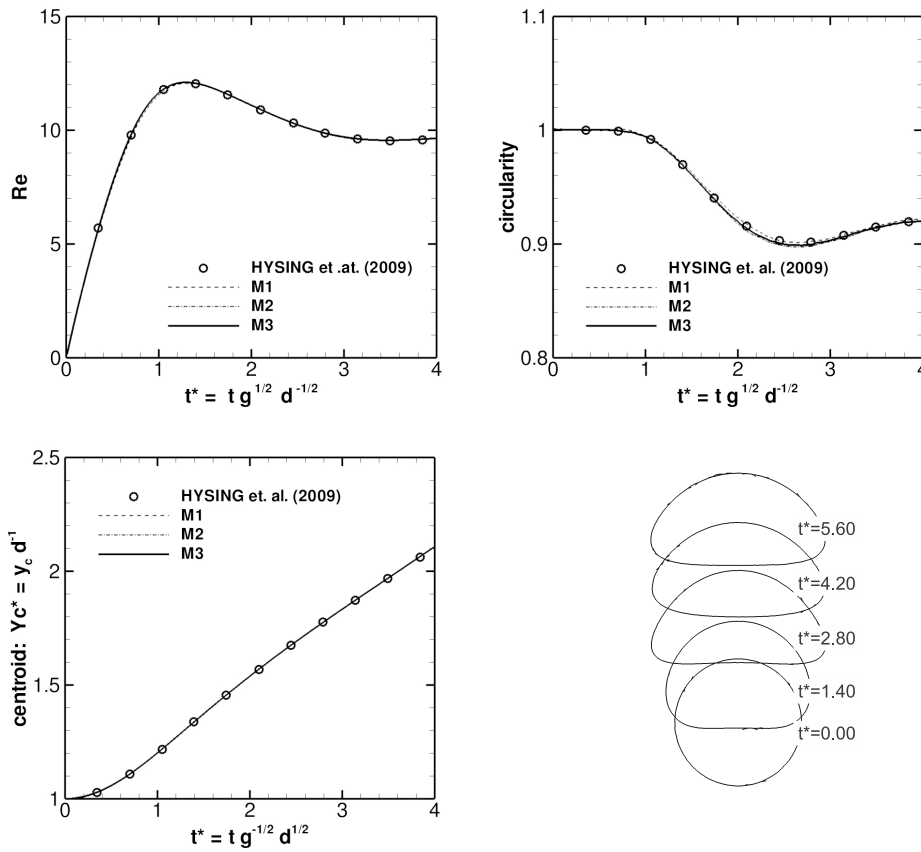
Figure 2.11: Two dimensional rising bubble. Comparison between numerical predictions and reference data [23]. Mesh configuration is specified in Table 2.3 and Fig. 2.10.

ρ_1	ρ_2	μ_1	μ_2	g	σ	ρ_1/ρ_2	μ_1/μ_2
1000	100	10	1	0.98	24.5	10	10

Table 2.2: Physical parameters defining the two dimensional rising bubble test case.

the domain in control volumes (cv) of triangular element type (see Fig. 2.10b). A summary of numerical parameters used in time and spatial discretization is given in Table 2.3.

For code validation, rise velocity, centroid and circularity of the bubble are taken as benchmark quantities. Rise velocity is defined as the vertical component (v_c) of the mean velocity $\mathbf{v}_c$:

$$\mathbf{v}_c = (u_c, v_c) = \frac{\int_{\Omega_2} \mathbf{v} dV}{\int_{\Omega_2} dV} \tag{2.54}$$

The center of mass of the bubble is defined by

$$\mathbf{x}_c = (x_c, y_c) = \frac{\int_{\Omega_2} \mathbf{x} dV}{\int_{\Omega_2} dV} \tag{2.55}$$

The bubble circularity ζ_{2D} is defined as

$$\zeta_{2D} = \frac{\text{perimeter of area-equivalent circle}}{\text{perimeter of bubble}} = \frac{\pi d}{\int_{\Omega} ||\nabla \phi|| dV} \tag{2.56}$$

where $\Omega = \Omega_1 \cup \Omega_2$. For a perfect circular bubble the circularity will be equal to unity and decrease as the bubble is deformed.

Fig. 2.11 depicts the time evolution of the benchmark quantities: center of mass ($Y_c^* = y_c/d$), terminal Reynolds number ($Re = \rho_1 v_c d/\mu_1$) and circularity. All quantities are in excellent agreement with the data published by [23].

Snapshots of the predicted bubble shapes, using the mesh M_3, are shown in Fig. 2.11. The bubble, being initially circular, first stretches horizontally and develops a slight dimple at the bottom. This bubble deformation causes a change in the interface curvature and surface tension force, which tends to keep bubble to a circular form. Finally, the bubble reaches a more stable ellipsoidal shape.

2.5.3   Three-dimensional buoyant bubbles

Dynamic behavior of a rising bubble has been a subject of experimental and numerical studies for many years. Experimental studies and correlations were reviewed by [8], and by [2]. For bubbles rising freely in infinite domains, a generalized graphical
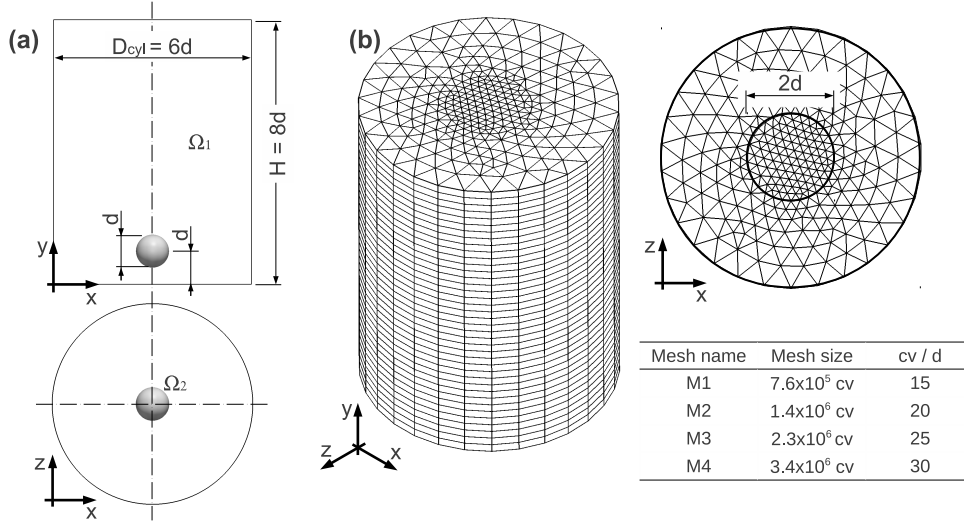
Figure 2.12: Three-dimensional buoyant bubble: (**a**) schematic diagram of the solution domain and initial condition. (**b**) The mesh configuration is adapted to densify the grid at the center of the domain, covering a cylindrical zone of diameter 2d around the symmetry axis with an approximately constant grid size (cv/d). In external zone, the grid size grows linearly until it reaches the boundary wall.

correlation is given by [17]. This diagram shows the shape regimes and terminal velocities in terms of Eötvös number (Eo), Morton number (M), and Reynolds number (Re), which are defined as follows:

$$Eo = \frac{gd^2\Delta\rho}{\sigma} \qquad M = \frac{g\mu_1^4\Delta\rho}{\rho_1^2\sigma^3} \qquad Re = \frac{\rho_1 U_T d}{\mu_1} \qquad (2.57)$$

where $U_T = \int_{\Omega_2} v_y \phi dV / \int_{\Omega_2} dV$ is the terminal velocity of the bubble, defined as the steady velocity that the bubble reaches when there is a balance between buoyancy and drag forces, $\Delta\rho = \rho_1 - \rho_2$ specifies the density difference between the fluid phases, the subscript 1 refers to the heavier fluid and the subscript 2 to the lighter fluid.

Computational domain and mesh configuration are described in Fig. 2.12a. According to numerical simulations of [33], when $D_{cyl} \geq 6d$ the effect of sidewalls on the shape and terminal velocity of the bubble is minimal. In addition, following the empirical studies of [19] the terminal rise velocity can be estimated through the
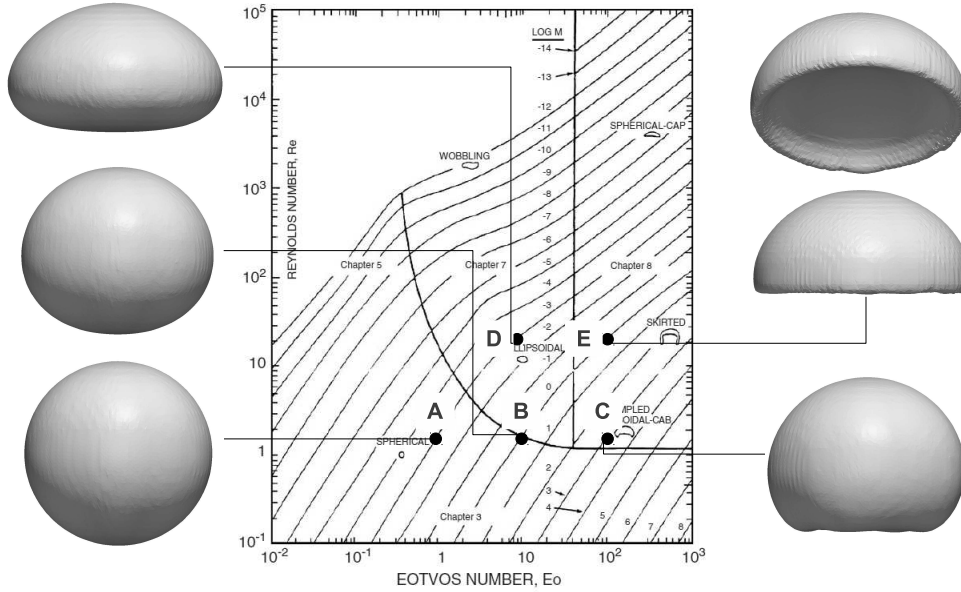
Figure 2.13: Bubble diagram of Grace for the shape and terminal velocities of gas bubbles in quiescent viscous liquids, reproduced from [8]. The simulated cases are indicated with capitals.

Mesh name	Mesh size	cv/d	Δt	ε_P
$M1$	$1.6 \times 10^4 cv$	50	1.0×10^{-5}	$0.5(\Delta_P)^{0.9}$
$M2$	$4.6 \times 10^4 cv$	100	1.0×10^{-5}	$0.5(\Delta_P)^{0.9}$
$M3$	$4.2 \times 10^5 cv$	200	1.0×10^{-5}	$0.5(\Delta_P)^{0.9}$

Table 2.3: Simulation parameters for the meshes used in two dimensional rising bubble test case, cv/d denotes the number of control volumes (cv) used per bubble diameter (d).

51

Figure 2.14: Three-dimensional buoyant bubble (case **E**): $Eo = 97.1$, $M = 0.971$, $\rho_1/\rho_2 = 100$, $\mu_1/\mu_2 = 100$. Mesh configuration is specified in Fig. 2.12, where $M1 \equiv 15cv/d$, $M2 \equiv 20cv/d$, $M3 \equiv 25cv/d$, $M4 \equiv 30cv/d$.

Figure 2.15: Three-dimensional buoyant bubble (case **D**): $Eo = 10.0$, $M = 9.71 \times 10^{-4}$, $\rho_1/\rho_2 = 100$, $\mu_1/\mu_2 = 100$. Mesh configuration is specified in Fig. 2.12, where $M1 \equiv 15cv/d$, $M2 \equiv 20cv/d$, $M3 \equiv 25cv/d$.
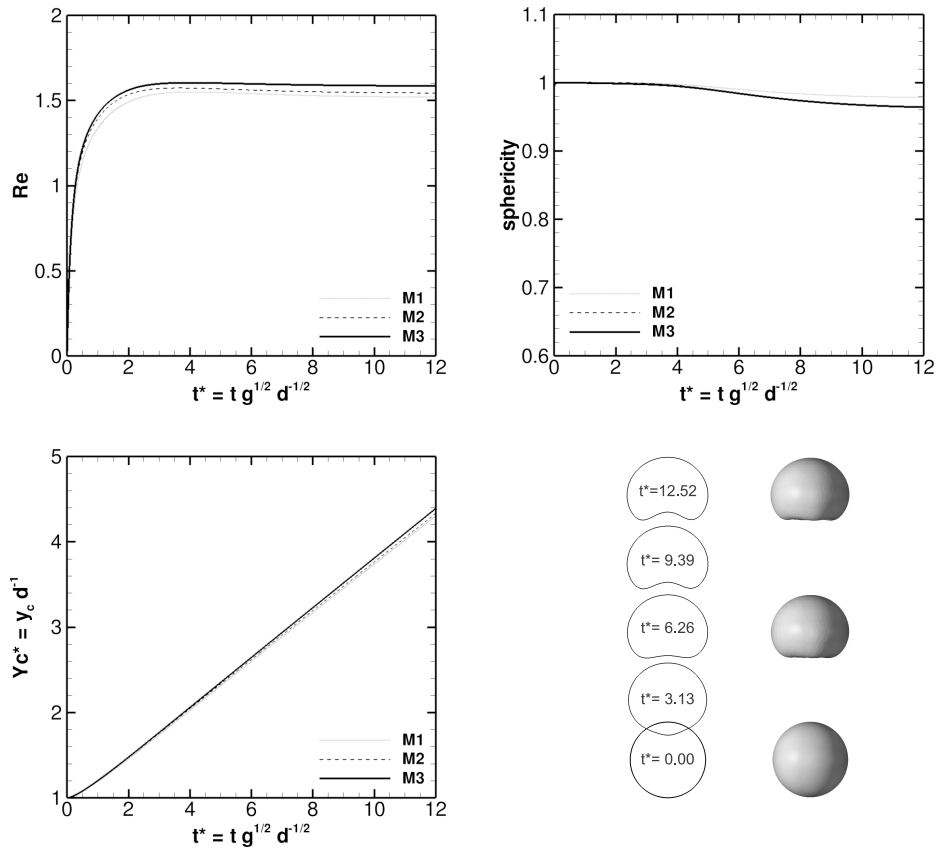
Figure 2.16: Three-dimensional buoyant bubble (case **C**): $Eo = 97.1$, $M = 1.0 \times 10^3$, $\rho_1/\rho_2 = 100$, $\mu_1/\mu_2 = 100$. Mesh configuration is specified in Fig. 2.12, where $M1 \equiv 15cv/d$, $M2 \equiv 20cv/d$, $M3 \equiv 25cv/d$.

Figure 2.17: Three-dimensional buoyant bubble (case **B**): $Eo = 10.0$, $M = 1.0$, $\rho_1/\rho_2 = 100$, $\mu_1/\mu_2 = 100$. Mesh configuration is specified in Fig. 2.12, where $M1 \equiv 15cv/d$, $M2 \equiv 20cv/d$, $M3 \equiv 25cv/d$.

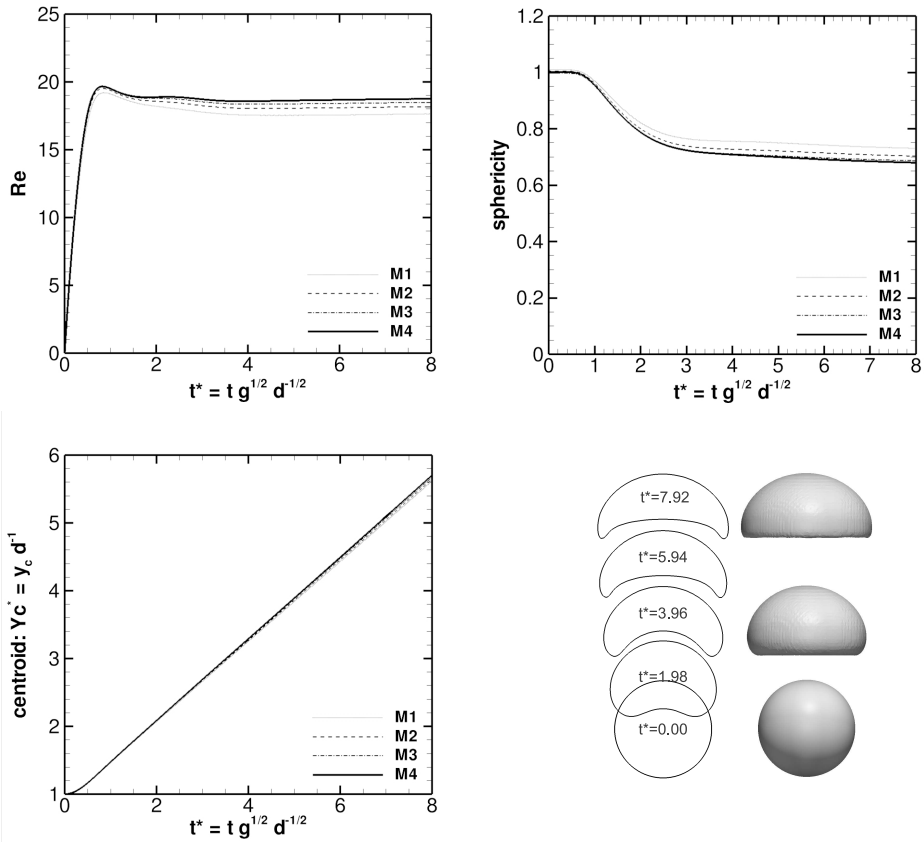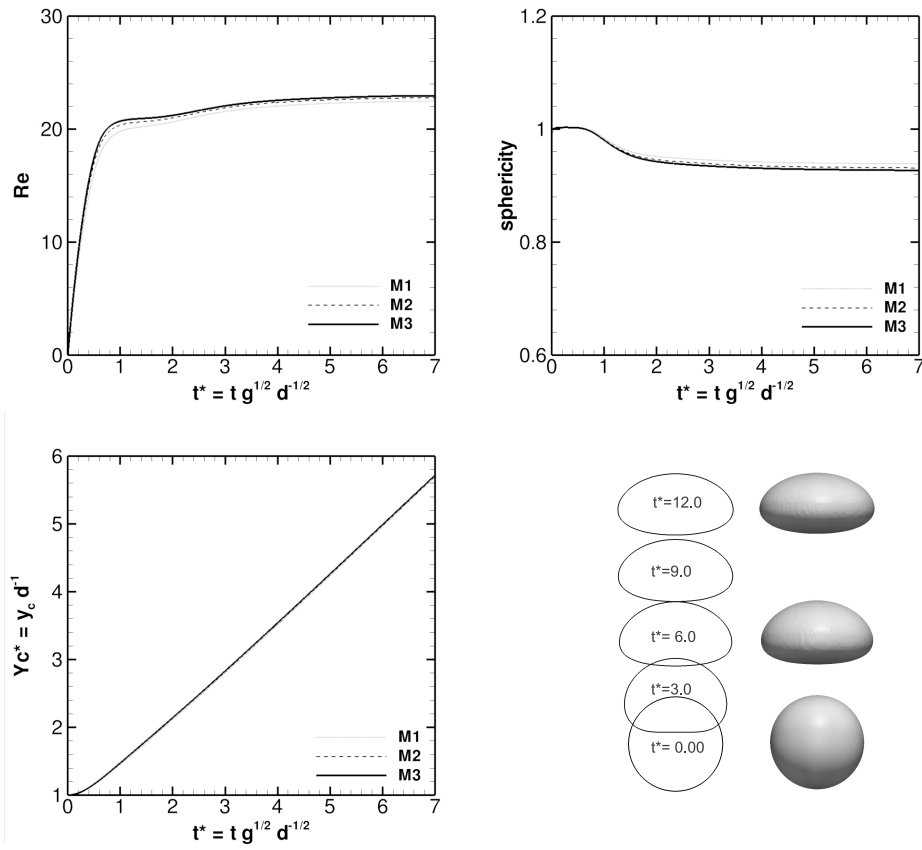**Figure 2.18:** Three-dimensional buoyant bubble (case **A**): $Eo = 1.0$, $M = 1.26 \times 10^{-3}$, $\rho_1/\rho_2 = 100$, $\mu_1/\mu_2 = 100$. Mesh configuration is specified in Fig. 2.12, where $M1 \equiv 15cv/d$, $M2 \equiv 20cv/d$, $M3 \equiv 25cv/d$.
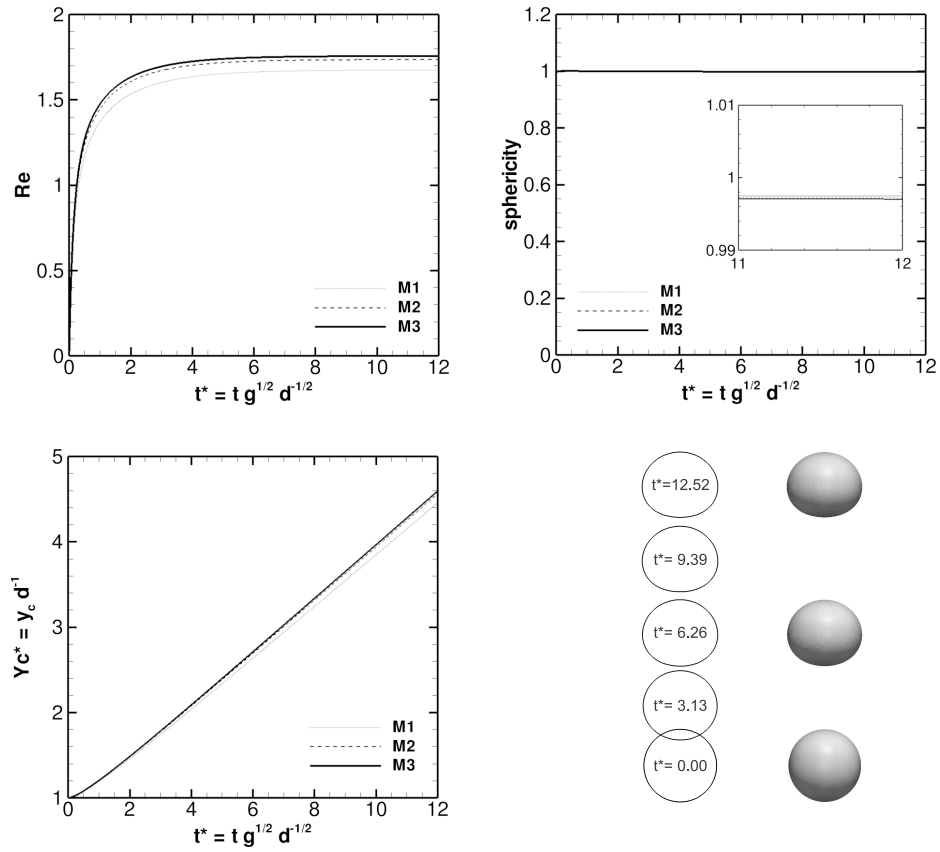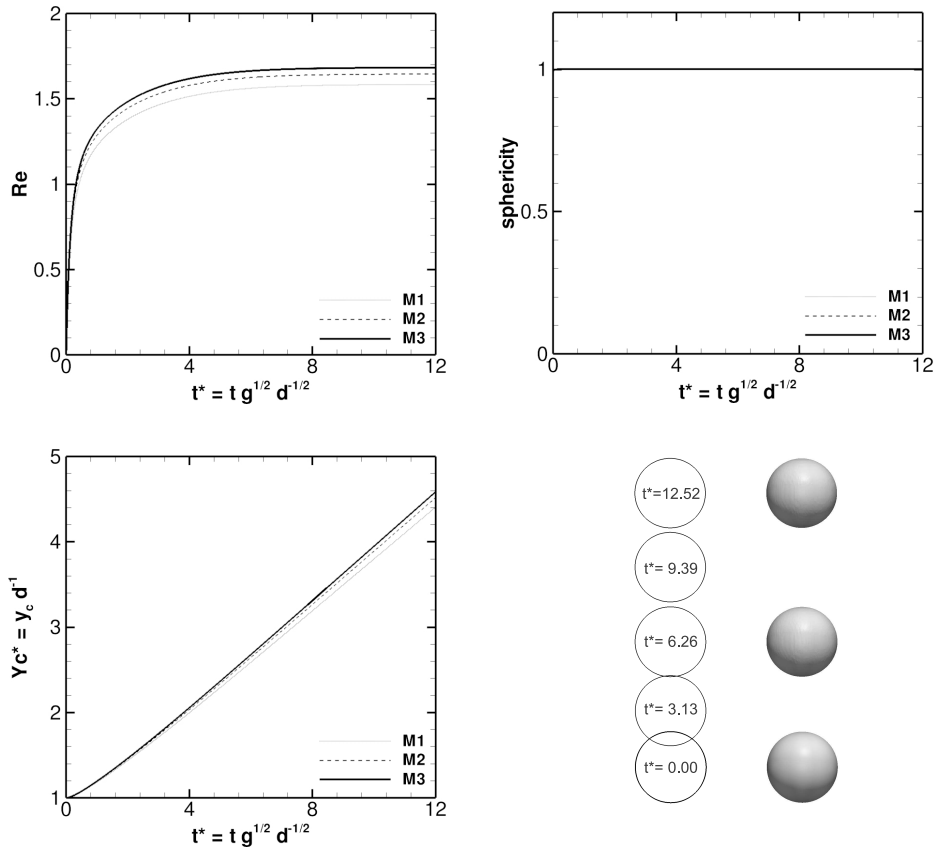
semi-empirical relation:

$$\frac{U_T}{U_T^\infty} \approx 1 - \left(\frac{d}{D_{cyl}}\right)^2 \tag{2.58}$$

where D_{cyl} denotes the domain extend in a plane perpendicular to the gravity direction, and U_T^∞ represents the terminal rise velocity in a domain of infinite extension. Studies of [24] and [52] reported numerical results that confirm the empirical findings of [19]. From previously mentioned studies and with the intend of saving computational resources such as computational time and occupation memory, our simulations were computed by selecting a diameter $D_{cyl} = 6d$ for the computational domain (see Fig. 2.12a). Thus, it is expected that the effect of confinement on the terminal velocity of the bubble will be given by $U_T/U_T^\infty \approx 0.9722$. Height of the cylindrical domain is taken as $H = 8d$, so that the top wall is sufficiently far from point of release of bubble to allow the bubble to reach terminal velocity. From Fig. 2.12b, control volumes are distributed in such way that the grid is densified around the symmetry axis of the cylinder by using an approximately constant grid size (Δ_P). This zone corresponds to the region crossed by the bubble. In the outer region, the grid size increases in radial direction following a linear distribution (See Figure 2.12b for more details).

Initially the spherical bubble of diameter d is located on the symmetry axis at the distance d from the bottom wall. No-slip boundary condition is imposed on top, bottom and lateral walls. Both liquid and bubble are assumed initially quiescent and computations are stopped before the bubble comes close to the upper boundary, to avoid contamination of the results by confinement effects.

The density and viscosity ratios are specified respectively as $\rho_1/\rho_2 = 100$ and $\mu_1/\mu_2 = 100$. Numerical studies have been performed in the past using these parameters by [52] and [5]. The time step size is fixed to $\Delta t^* = 1.98 \times 10^{-4}$ ($t^* = tg^{1/2}d^{-1/2}$) except for cases A, B and C (See Table 2.13) where the time step is reduced to $\Delta t^* = 4.95 \times 10^{-5}$. All computations were made using an interface thickness parameter of $\varepsilon_P = 0.5(\Delta_P)^{0.9}$.

Numerical simulations were performed by varying the physical properties of the dispersed phase and the continuous phase, in order to capture the various shapes of the moving bubble. Numerical results for various values of Eo number and M number are shown in Fig. 2.13. The dimensionless numbers reported here are evaluated at the initial stage using the droplet diameter d. In the regimes of low Reynolds and Eötvös numbers characterized by the high surface tension (Fig. 2.13, point A), the bubbles maintain spherical shape while they are rising in the continuous phase (see Fig. 2.18). For intermediate Eötvös number (Fig. 2.13, points B,D), bubble shape and motion are also a function of the Morton number. Bubbles with large M become ellipsoidal before a spherical cap shape is adopted (Fig. 2.13, point B) but continue to have a well defined steady state motion. As the Eötvös number increases, the bub-

Bubble regime	Case	M	Eo	Re_G	Re_C	Mesh
Spherical	**A**	1.26×10^{-3}	1.0	1.7	1.68	$M3$
Ellipsoidal	**B**	1.00×10^{0}	10.0	1.7	1.76	$M3$
Ellipsoidal Cap.	**C**	1.00×10^{3}	97.1	1.5	1.58	$M3$
Ellipsoidal	**D**	9.71×10^{-4}	10.0	22.0	22.95	$M3$
Skirted	**E**	9.71×10^{-1}	97.1	20.0	18.74	$M4$

Table 2.4: Simulation of three-dimensional buoyant bubbles for different regimes according to the bubble diagram of [17]. Re_G represents the experimental Reynolds number in a domain of infinite extension obtained from the Grace diagram, and Re_C represents the numerical prediction of the Reynolds number in a finite domain $D_{cyl} \times H = 6d \times 8d$.

ble bottom becomes flat or slightly dimpled (Fig. 2.13, point C), and skirt bubble is formed at higher Reynolds numbers (Fig. 2.13, point E). From the simulations presented here, it can be concluded the current numerical method is robust enough to predict the various bubble shapes under a wide range of flow regimes.

The center of mass ($\mathbf{x}_c$), sphericity (ζ_{3D}) and the rise velocity ($\mathbf{v}_c$) are measured and plotted for different meshes in Figs. 2.14, 2.15, 2.16, 2.17, 2.18. These quantities are defined as:

$$
\begin{cases}
\mathbf{v}_c = (u_c, v_c, w_c) = \frac{\int_{\Omega_2} \mathbf{v} dV}{\int_{\Omega_2} dV}, \\
\mathbf{x}_c = (x_c, y_c, z_c) = \frac{\int_{\Omega_2} \mathbf{x} dV}{\int_{\Omega_2} dV}, \\
\zeta_{3D} = \frac{\text{area of volume-equivalent sphere}}{\text{area of bubble}} = \frac{\pi d^2}{\int_{\Omega} ||\nabla \phi|| dV}.
\end{cases}
\tag{2.59}
$$

In Figs. 2.14-2.18 the center of mass (y_c) is scaled with the bubble diameter d and the time with $t_{ref} = d^{1/2} g^{-1/2}$. Furthermore, a comparison of the Reynolds numbers for the experiment and simulation cases is listed in Table 2.4. Results from simulations agree with those of experiments fairly well.

2.5.4 Bubble merging

With the confidence from validating the CLS method for a single bubble rising in a viscous liquid, the model is used to explore the complex interaction between two bubbles rising in a liquid. The bubble coalescence process is simplified and based purely on geometric criteria rather than criteria related to the complex interface physics. This means that coalescence happens automatically whenever two interfaces come within one grid cell of one other.

This test case consists in co-axial and oblique coalescence of two bubbles rising in a liquid. The simulation domain and initial bubble arrangement are shown in Fig.
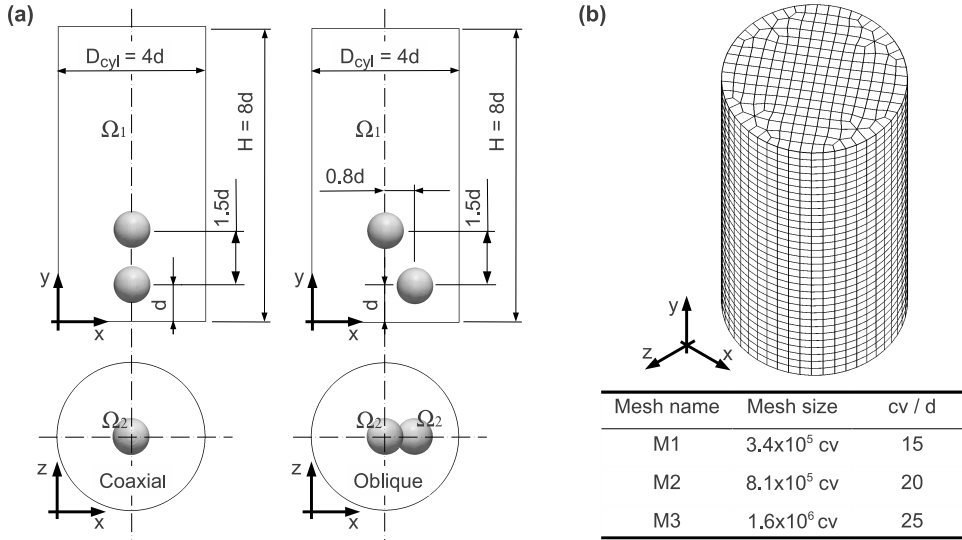
Figure 2.19: Bubble merging. (**a**) schematic diagram of the solution domain and initial arrangement of bubbles (**b**) The domain is covered by hexahedral elements.

2.19a. As can be seen from Fig. 2.19b, the domain is divided in hexahedral control volumes uniformly distributed in the whole space. Three mesh resolutions have been selected to carry out the numerical simulations, which are denoted as $M_1 \equiv 15cv/d$, $M_2 \equiv 20cv/d$ and $M_3 \equiv 25cv/d$ (see Figure 2.19b). The fluid properties and initial arrangement of bubbles are the same as in the volume-of-fluid computations of [52]. The Morton and Eötvös numbers are set to $M = 2 \times 10^{-4}$ and $Eo = 16$ falling between the skirted and spherical cap regimes in Fig. 2.13. The density and viscosity ratios are specified as $\rho_1/\rho_2 = 100$ and $\mu_1/\mu_2 = 100$, where subscripts 1 and 2 refer to the outer-liquid phase and bubble phase respectively. Free-slip boundary condition is used at lateral side of the domain and no-slip boundary condition at the top and bottom boundaries. Numerical simulations are performed using $\varepsilon_P = 0.5(\Delta_P)^{0.9}$ and $\Delta t^* = 1.98 \times 10^{-4}$ ($t^* = tg^{1/2}d^{-1/2}$). The temporal evolution of the Reynolds number, defined as $Re = \rho_1 v_c d/\mu_1$, is shown in Figure (2.26) for both co-axial and oblique coalescence. We can notice how the Reynolds number converges as the mesh resolution increases.

Snapshots of topological changes in the coalescence process of two coaxial bubbles are shown in Figs. 2.20-2.21. When they start to rise, bubbles become ellipsoids due to a pressure difference between the top and bottom surfaces of the bubbles. As the bubbles rise, a liquid jet is formed behind the leading bubble, which induces

Figure 2.20: Coaxial bubble coalescence of two initially spherical bubbles: $M = 0.0002$, $Eo = 16$, $\rho_1/\rho_2 = 100$, $\mu_1/\mu_2 = 100$.

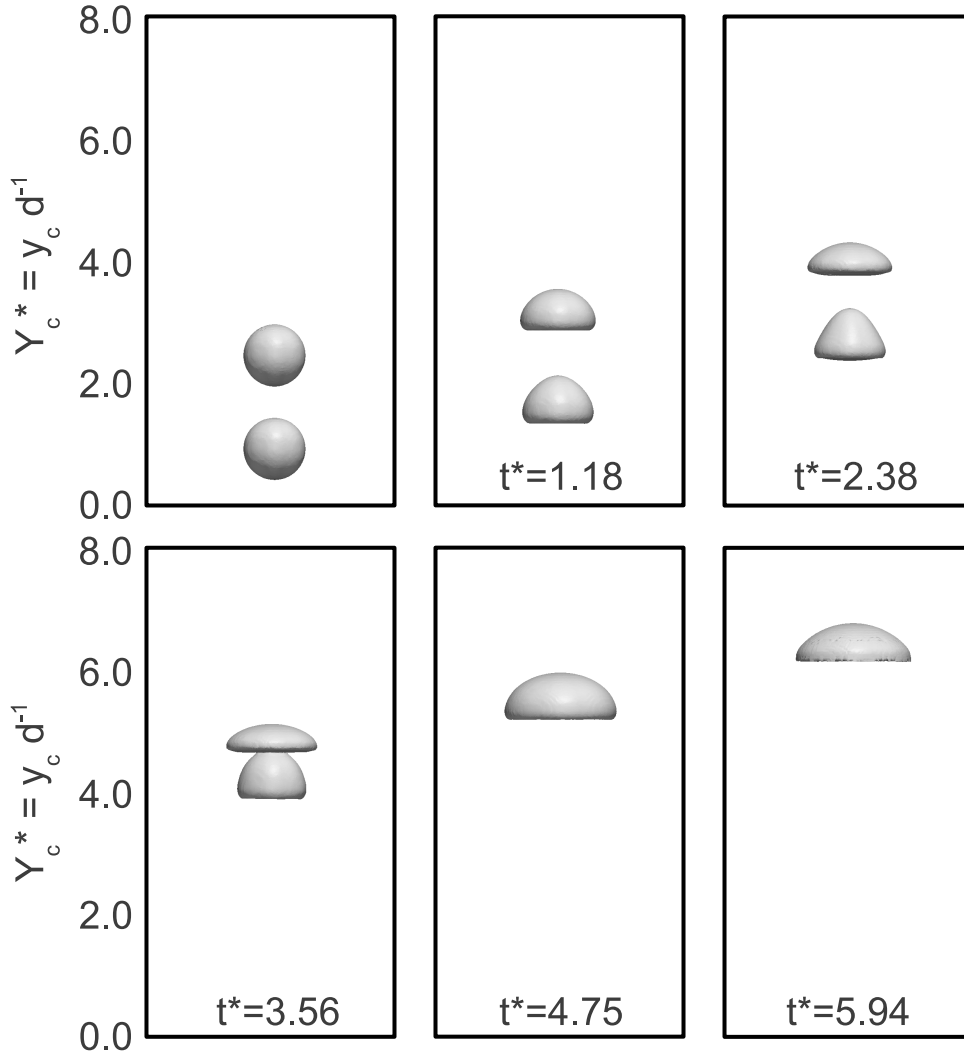t*=2.97   t*=3.56   t*=4.16   t*=4.75

Figure 2.21: Coaxial coalescence of two initially spherical bubbles: velocity field.

a severe deformation in vertical direction of the following bubble. Once two bubbles are approaching, the trailing bubble accelerates because the suction by the top bubble. As time progresses, the two bubbles start to touch, leaving a mushroom-like structure. Finally, the thin liquid film between bubbles is squeezed out and ruptured, completing the coalescence process.

Snapshots of topological changes for oblique coalescence of two bubbles are presented in Fig. 2.22. Although this coalescence process is in general similar to previous case, the pattern of bubbles evolution is different. The most significant feature is that the trailing bubble experiences a considerable asymmetrical deformation in the wake region of the leading bubble. This is because a horizontal component of velocity is generated, which produces an alignment effect of bubbles. Additionally, it is observed a deformation of the trailing bubble into a prolate shape inclined with respect to the vertical direction. On the other hand, the shape evolution in the leading bubble is similar to the case of a single bubble rising although its major axis tilts a small angle with the $y - axis$ when the trailing bubble enters its wake region.

In both cases, numerical predictions match fairly well in terms of bubble shapes with experimental results reported by [4] (see Fig. 2.24). Similar observations have been found by [52] using volume-of-fluid method (VOF).

2.5.5   Collapse of a liquid column.

The collapse of a liquid column is a classical experiment used in the validation of numerical methods for simulating two-phase flows. Experimental data about the reduction of the column height and position of the wave front have been provided by [31]. A fluid column, initially at rest on a horizontal plane collapses under the effect of the gravity. The fluid spreads out and the height of the column falls. The computational domain and the initial configuration are shown in Fig. 2.27. Water
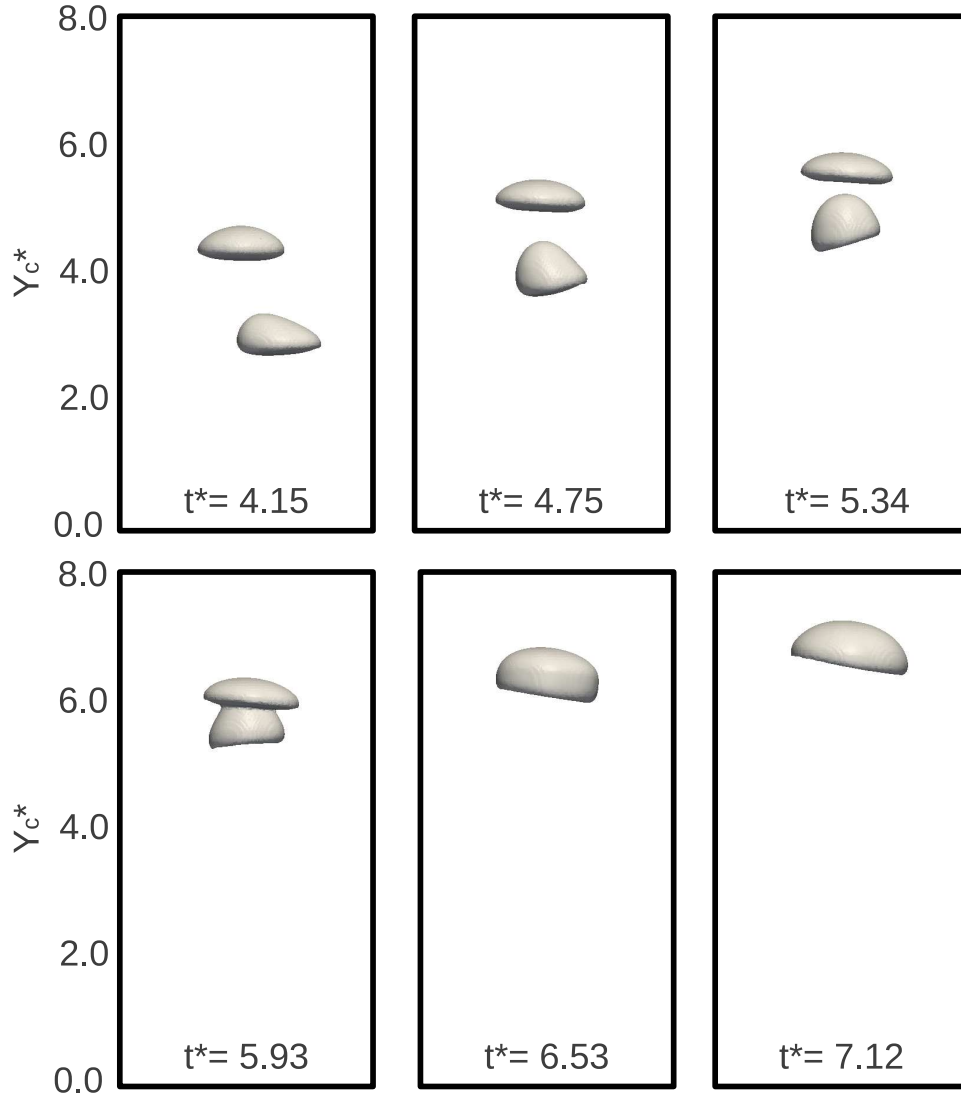
Figure 2.22: Oblique bubble coalescence of two initially spherical bubbles. Here $M = 0.0002$, $Eo = 16$, $\rho_1/\rho_2 = 100$, $\mu_1/\mu_2 = 100$.

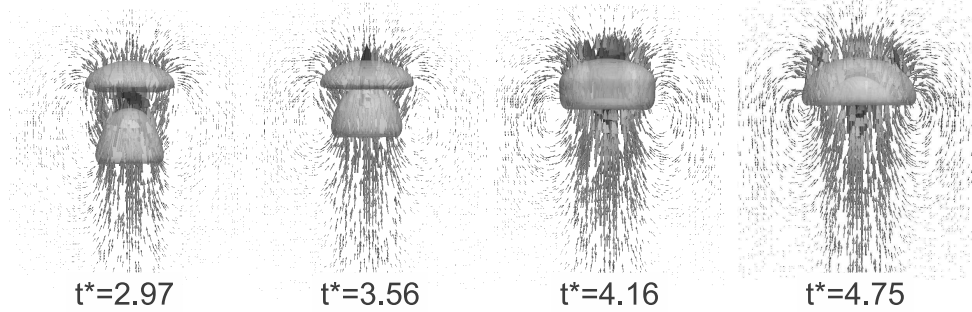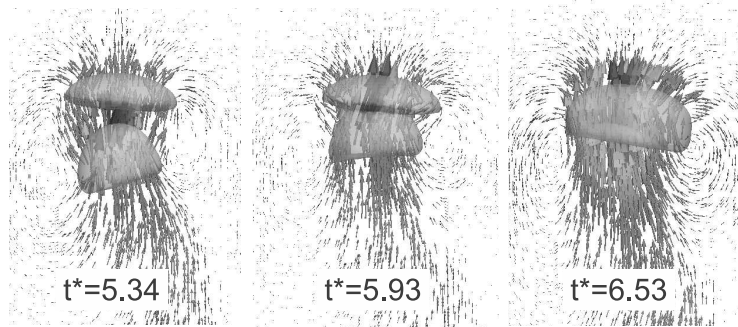**Figure 2.23:** Oblique coalescence of two initially spherical bubbles: velocity field.
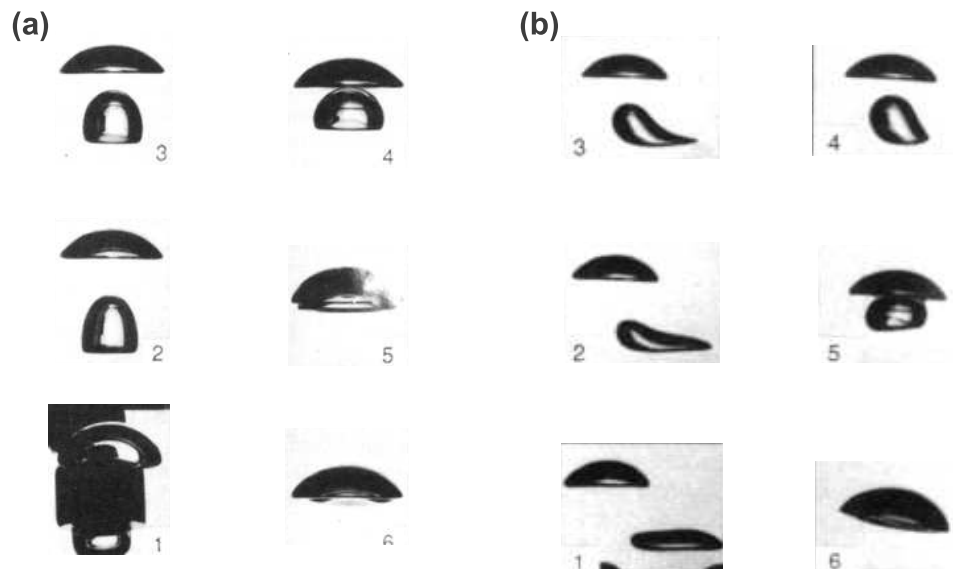
Figure 2.24: Experiments reported by [4] for the coalescence of two bubbles. (a) Coaxial coalescence (b) Oblique coalescence
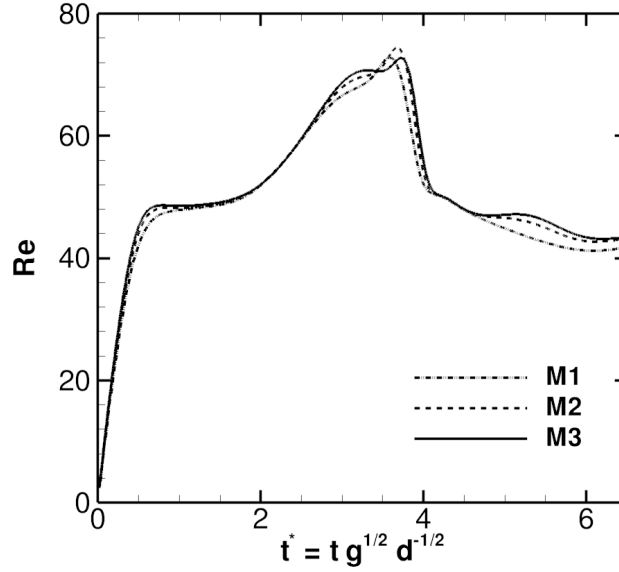
Figure 2.25: Time-history of the Reynolds number for coaxial coalescence of two bubbles, $M = 2 \times 10^{-4}$ and $Eo = 16$. The mesh resolution is given by $M_1 \equiv 15cv/d$, $M_2 \equiv 20cv/d$ and $M_3 \equiv 25cv/d$.

is used as liquid in Ω_1 and air is present as outer medium in Ω_2. This problem is initialized with a water column of width a and height a in a rectangular domain $\Omega = [0, 5a] \times [0, 1.25a]$ where $a = 0.05715m$.

The properties of the water are set to $\rho_1 = 1000kg/m^3$ and $\mu_1 = 1 \times 10^{-3}kg/ms$, the water-air density ratio and viscosity ratio are 1000 and 100 respectively. The surface tension coefficient is set to $\sigma = 0.0755N/m$, and the acceleration of gravity is taken to be $\mathbf{g} = (0, -9.81, 0)m/s^2$. Free-slip boundary condition is applied at all boundaries except at the top, where Neumann boundary condition is used. This test case is computed on two different mesh configurations (see Fig. (2.27)) at $\Delta t = 1.0 \times 10^{-5}s$, with an interface thickness parameter of $\varepsilon_P = 0.5(\Delta_P)^{0.9}$. Because a conservative form of the Navier-Stokes equations is discretized, momentum conservation is guaranteed, however, the momentum ($\rho\mathbf{v}$) in the convective term of Eq. 5.1 presents a jump discontinuity at the interface. This may lead to numerical issues when high density ratio and high Reynolds number are simultaneously present, as in the current test case. In this context, when a central difference limiter was used to solve the present test case, unphysical large velocities around the interface were
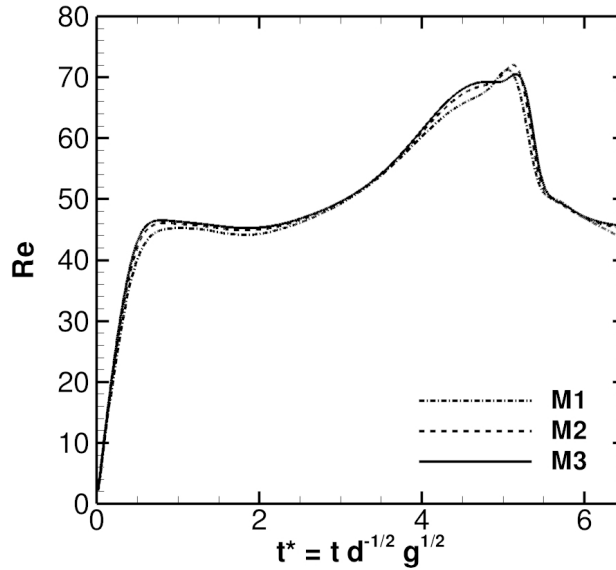
Figure 2.26: Time-history of the Reynolds number for oblique coalescence of two bubbles, $M = 2 \times 10^{-4}$ and $Eo = 16$. The mesh resolution is given by $M_1 \equiv 15cv/d$, $M_2 \equiv 20cv/d$ and $M_3 \equiv 25cv/d$.

observed. Thus, to overcome the aforementioned issue, an upwind limiter was used on the discretization of the convective term in Eq. 5.1, for this particular test case.

Snapshots of the predicted free surfaces at different times are given in Fig. 2.27. Gravity causes the liquid in the left to seek the lowest level of potential energy. Thus, the water front advances to occupy the bottom of the domain Ω. At time $t = 0.2s$ about 80% of the base is covered with water. At time $t = 0.25s$ the wave front touches the right wall. At time $t = 0.4s$ the horizontal water-air interface is almost parallel to the base of the container, and the liquid in the right starts to fall back due to the effect of the gravity. At time $t = 0.5s$ a backward moving wave advances to the left wall, whereas a large air bubble is trapped.

The non-dimensional height of the water column $H^* = y/(2a)$ at the left wall versus the non-dimensional time $t^* = t\,(g/a)^{1/2}$ is shown in Fig. 2.28a. Results calculated correspond very well with the experimental data presented by [31]. In addition, the non-dimensional position of the leading edge $Z^* = x/a$ is plotted against non-dimensional time $t^* = t(2g/a)^{1/2}$ in Fig. 2.28b. The numerical results present

(a)

Mesh name	Mesh size	Element type
M1	2.3×10^4 cv	triangular
M2	1.0×10^4 cv	quadrangular

(b)
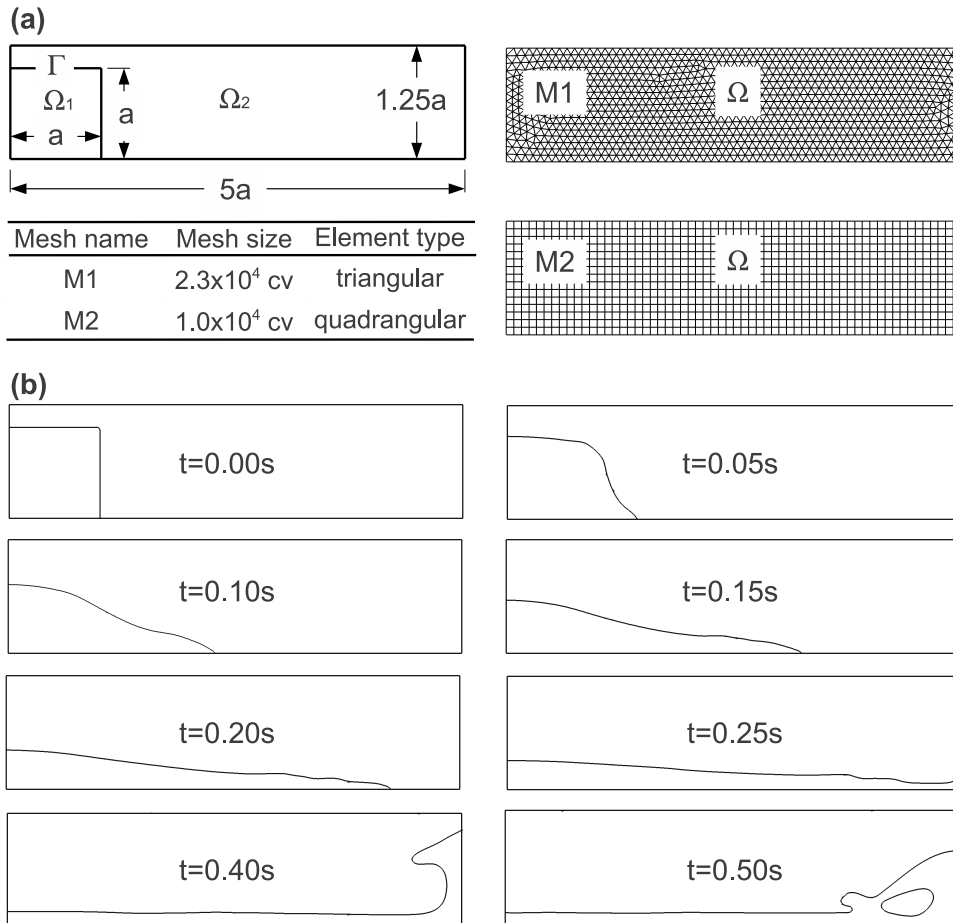
Figure 2.27: (**a**) Initial condition and mesh configuration ($M1$,$M2$). (**b**) Snapshots of the numerical solution using mesh $M1$ for collapse of a liquid column.
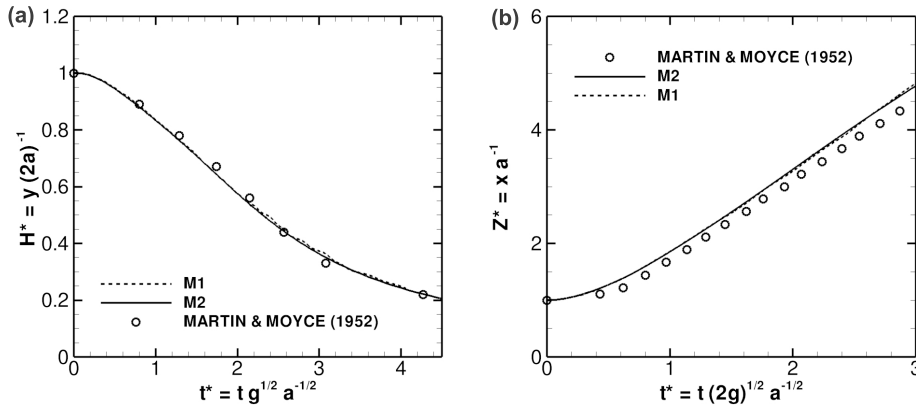
Figure 2.28: (**a**) Remaining water column H^* and (**b**) predicted surge front position Z^* for collapse of a liquid column.

a slight difference respect to experimental data of [31] which predict slower front propagation speed. This difference may be because in experiment is used a gate to retain the water column, which produces a dead time before propagation of the liquid. Results presented by other researchers [9, 40, 50] show the same tendency.

2.6 Parallel scalability

The parallelization performance of the presented numerical methods and computer code was investigated using a three-dimensional buoyant bubble test case (section 2.5.3) with a mesh resolution of 3.6×10^6 elements. The numerical methods used in this chapter were implemented in a C++ computer code called TermoFluids [27], wich utilises the Message Passing Interface (MPI) for parallel communications. A standard domain decomposition method is used for the parallelization of the multiphase solver, where each subdomain is assigned to a separate process of the parallelization and has approximately the same number of grid cells to optimize load balancing, while minimizing the amount of communication between partitions. The parallel performance tests were carried out on the IBM MareNostrum-III supercomputer at the Barcelona Supercomputing Center (BSC).

The time required for one time-iteration of the multiphase solver scheme on 128 processors was used as a reference time to normalize the CPU results of the numerical simulations. To investigate the parallel scalability of the computer code, tests were performed for a number of processors varying from 128 (or 28125CV/CPUs)

to 512 (or 7031CV/CPUs), as shown in Fig. 2.29. The parallel performance of the overall algorithm with 256 CPUs and 512 CPUs is around 90% and 76% respectively.
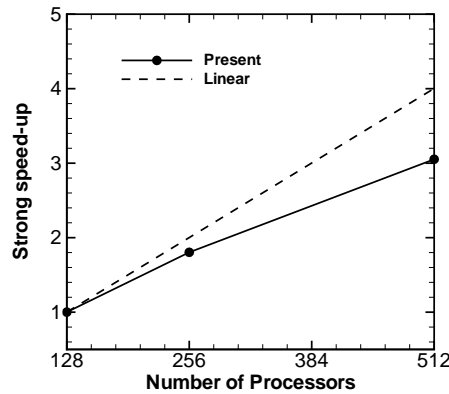
Figure 2.29: Parallel scalability of the multiphase solver for the case of a three dimensional buoyant bubble (section 2.5.3) using a mesh of 3.6×10^6 elements (See Fig. 2.12).

2.7   Concluding remarks

A conservative level set method is presented which is integrated in a finite-volume method for solving incompressible two-phase flows on collocated unstructured grids of arbitrary element type. Special care is taken to develop an accurate TVD flux limiter formulation to discretize the convective term on unstructured meshes, avoiding unphysical oscillations in the level set function. In order to improve accuracy and robustness, gradients and normals are computed by the least-squares method. Surface tension is introduced through the CSF model. Such combination of numerical techniques, results in a robust algorithm that allows to simulate virtually all kinds of two-phase flows with inter-phase boundaries (bubbles, waves, films etc.).

The proposed approach is mass conservative and demonstrates a good accuracy, which has been studied in 2D and 3D computations. Predicted results have been shown to compare fairly well with the experimental and numerical results in the literature. It is found that the present method is a viable tool for accurate modeling of two-phase flows on unstructured grids.

Acknowledgments

References

[1] Balcázar, N., Jofre, L., Lehmkhul, O., Castro, J., Rigola, J., 2014. A finite-volume/level-set method for simulating two-phase flows on unstructured grids. International Journal of Multiphase Flow 64, 55-72

[2] Bhaga, D., Weber, M.E., 1981. Bubbles in viscous liquids: shapes, wakes and velocities, J Fluid Mech 105, 61-85

[3] Brackbill, J.U., Kothe, D.B., Zemach, C., 1992. A Continuum Method for Modeling Surface Tension, J. Comput. Phys. 100, 335-354.

[4] Brereton, G., Korotney, D., Coaxial and Oblique Coalescence of Two Rising Bubbles, in Dynamics of bubbles and Vortices Near a Free Surface, vol. 119, ASME, New York, 1991

[5] Chakraborty, I., Biswas, G., Ghoshdastidar, P.S., A coupled level-set and volume-of-fluid method for the buoyant rise of gas bubbles in liquids, 2013. International Journal of Heat and Mass Transfer 58, 240-259.

[6] Chen, T., Minev P., Nandakumar, K., A projection scheme for incompressible multiphase flow using adaptive Eulerian grid, 2004. Int. J. Numer. Meth. Fluids 45, 1-19.

[7] Chorin, A.J., Numerical solution of the Navier-Stokes equations. 1968. Math. Comput. 22, 745-762.

[8] Clift, R., Grace, J.R., Weber, M.E., Bubbles, Drops and Particles. Academin Press, New York, 1978.

[9] Colagrossi, A., Landrini, M., Numerical simulation of interfacial flows by smoothed particle hydrodynamics. 2003. J. Comput. Phys. 191, 448-475

[10] Croce, R., Griebel M., Schweitzer, A., Numerical simulation of bubble and droplet deformation by a level set approach with surface tension in three dimensions, 2010. Int. J. Numer. Meth. Fluids 62, 963-993.

[11] Darwish, M.S., Moukalled, F., 2003. TVD schemes for unstructured grids. International Journal of Heat and Mass Transfer 46, 599-611

[12] Deen, N.G., Van Sint Annaland, M., Kuipers, J.A.M. , 2009. Direct numerical simulation of complex multi-fluid flows using a combined front tracking and immersed boundary method, Chemical Engineering Science 64, 2186-2201.

[13] Desjardins, O., Moureau, V., Pitsch, H., 2008. An accurate conservative level set/ghost fluid method for simulating turbulent atomization, J. Comput. Phys. 227, 8395â8416

[14] Felten, F.N., Lund, T.S., 2006. Kinetic energy conservation issues associated with the collocated mesh scheme for incompressible flow, J. Comput. Phys. 215, 465-484

[15] Frolkovic, P., Logashenko, D., Wittum G., 2008. Flux-based level set method for two-phase flows, In R. Eymard and J.-M. Herard (editors), Finite Volumes for Complex Applications, ISTE and Wiley 415-422

[16] Gottlieb, S., Shu, C., 1998. Total Variation Dimishing Runge-Kutta Schemes, Mathematics of Computations 67, 73-85.

[17] Grace, J.R., 1973. Shapes and velocities of bubbles rising in infinite liquids, Trans IChemE 51, 116-120.

[18] Guermond, J.L., Minev, P., Jie, S., 2006. An overview of projection methods for incompressible flows, Comput. Methods Appl. Mech. Engrg. 195, 6011-6045.

[19] Harmathy, T.Z., 1960. Velocity of large drops and bubbles in media of infinite or restricted extend, AIChE J. 6, 281-288.

[20] Harten, A., 1977. The Artificial Compression Method for Computation of Shocks and Dontact Discontinuities: I. Single conservation laws, Comm. Pure Appl. Math., 611-638.

[21] Haselbacher, A., Vasilyev, O., 2003. Commutative discrete filtering on unstructured grids based on least-squares techniques, J. Comput. Phys. 187, 197-211.

[22] Hysing, S., 2012. Mixed element FEM level set method for numerical simulation of immiscible fluids, J. Comput. Phys. 231, 2449-2465.

References

[23] Hysing, S., Turet, S., Kuzmin, D., Parolini, N., Burman, E., Ganesan, S., Tobiska, L., 2009. Quantitative benchmark computations of two-dimensional bubble dynamics, International Journal for Numerical Methods in Fluids 60, 1259-1288.

[24] Hua, J., Stene, J., Lin, P., 2008. Numerical simulation of 3D bubbles rising in viscous liquids using a front tracking method, J. Comput. Phys. 227, 3358-3382.

[25] Kees, C.E., Akkerman, I., Farthing, M.W., Bazilevs Y., 2011. A conservative level set method suitable for variable-order approximations and unstructured meshes, J. Comput. Phys. 230, 4536-4558.

[26] Kothe, D.B., Rider, W.J., Mosso, S.J., Brock, J.S., 1996. Volume Tracking of Interfaces Having Surface Tension in Two and Three Dimensions, AIAA 96-0859. 25.

[27] Lehmkuhl, O., Perez-Segarra, C.D., Soria, M., Oliva, A., 2007, A new Parallel unstructured CFD code for the simulation of turbulent industrial problems on low cost PC cluster, Proceedings of the Parallel CFD 2007 Conference, pp.1-8.

[28] Lian-xia, L., Hua-sheng, L., Li-jian, Q., 2008. An improved r-factor algorithm for TVD schemes. International Journal of Heat and Mass Transfer 51, 610-617

[29] Marchandise, E., Geuzaine, P., Chevaugeon, N., 2006. A Quadrature free discontinuous Galerkin method for the level set equation, J. Comput. Phys. 212, 338-357.

[30] Marchandise, E., Geuzaine, P., Chevaugeon, N., Remacle, J., 2007. A stabilized finite element method using a discontinuous level set approach for the computation of bubble dynamics, J. Comput. Phys. 225, 949-974.

[31] Martin, J.C., Moyce, J., 1952. An experimental study of the collapse of liquid columns on a rigid horizontal plane, Philosophical Transactions of the Royal Society of London. Series A. Mathematical and Physical Sciences 244, 312-324.

[32] Morinishi, Y., 2010. Skew-symmetric form of convective terms and fully conservative finite difference schemes for variable density low-Mach number flows, J. Comput. Phys. 229, 276-300.

[33] Mukundakrishnan, K., Quan, S., Eckmann, D.M., Ayyaswamy, P.S., 2007. Numerical study of wall effects on buoyant gas-bubble rise in a liquid-filled finite cylinder, Phys. Rev. E. 76, 036308-01â036308-15.

[34] Olsson, E., Kreiss, G., 2005. A conservative level set method for two phase flow, J. Comput. Phys. 210, 225-246.

[35] Olsson, E., Kreiss, G., Zahedi, S., 2007. A conservative level set method for two phase flow II, J. Comput. Phys. 225, 785-807.

[36] Osher, S., Sethian, J.A., 1988. Fronts propagating with curvature-dependent speed: Algorithms based on Hamilton-Jacobi formulations, J. Comput. Phys. 79, 175-210.

[37] Rhie, C.M., Chow, W.L., 1983. Numerical Study of the Turbulent Flow past an Airfoil with Trailing Edge Separation, AIAA J. 21, 1525-1532.

[38] Rider, W., Kothe, D., 1995. Stretching and tearing interface tracking methods. In: 12th AIAA CFD Conference, 95-1717, AIAA.

[39] Scardovelli, R., Zaleski, S., 1999. Direct numerical simulation of free surface and interfacial flow, Annu. Rev. Fluid Mech. 31, 567-603.

[40] Sheu, W.H. , Yu, C.H., Chiu, P.H., 2009. Development of a dispersively accurate conservative level set scheme for capturing interface in two phase flows. J. Comput. Phys. 228, 661-686.

[41] Sussman, M., Puckett, E.G., 2000. A Coupled Level Set and Volume-of-Fluid Method for Computing 3D and Axisymmetric Incompressible Two-Phase Flows, J. Comput. Phys. 162, 301-337.

[42] Sussman, M., Fatemi, E., 1999. An efficient interface-preserving level set redistancing algorithm and its application to interfacial incompressible fluid flow, SIAM J. Sci. Comput. 20, 1165-1191.

[43] Sussman, M., Fatemi, E., Smereka, P., 1998. An Improved Level Set Method for Incompressible Two-Phase Flows, Journal of Computers and Fluids 27, 663-680.

[44] Sussman, M., Smereka, P., Osher, S., 1994. A Level Set Approach for Computing Solutions to Incompressible Two-Phase Flow, J. Comput. Phys. 144, 146-159.

[45] Sweby, P.K., 1984. High Resolution Using Flux Limiters for Hyperbolic Conservation Laws, SIAM Journal on Numerical Analysis 21, 995-1011.

[46] Tornberg, A., Engquist, B., 2000. A Finite element based level set method for multiphase flow applications, Computing and Visualization in Science 3, 93-101.

[47] Trias, F.X., Lehmkuhl, O., 2011. A Self-Adaptive Strategy for the Time Integration of Navier-Stokes Equations. Numerical Heat Transfer, Part B 60, 116-134.

References

[48] Trias F.X., Lehmkuhl O., Oliva A., Pérez-Segarra C., Verstappen R., 2014. Symmetry-preserving discretization of Navier-Stokes equations on collocated unstructured grids. J. Comput. Phys. 144, 246-267.

[49] Tryggvason, G., Bunner, B., Esmaeeli, A., Juric, D., Al-Rawahi, N., Tauber, W., Han, J., Nas, S., Jan, Y-J., 2001. A Front-Tracking Method for the Computations of Multiphase Flow, J. Comput. Phys. 169, 708-759.

[50] Ubbink, O., Numerical prediction of two fuid systems with sharp interfaces. Ph.D. Thesis, Imperial College of Science, Technology and Medicine, London, 1997.

[51] Unverdi, S., Tryggvason, G., 1992. A front-tracking method for viscous, incompressible, multifluid flows, J. Comput. Phys. 100, 25-37.

[52] Van Sint Annaland, M., Deen, N.G., Kuipers, J.A.M., 2005. Numerical Simulation of gas bubbles behaviour using a three-dimensional volume-of-fluid method, Chemical Engineering Science 60, 2999-3011.

[53] Van Wachem, B., Schouten, J., 2002. Experimental Validation of 3-D Lagrangian VOF Model: Bubble Shape and Rise Velocity, AIChE Journal 48, 2744-2753.

[54] Lv, X., Zou, Q., Zhao, Y., Reeve, D., 2010. A novel coupled level set and volume of fluid method for sharp interface capturing on 3D tetrahedral grids, J. Comput. Phys. 229, 2573-2604.

References

Chapter 3

Numerical investigation of gravity-driven bubbly flow using a conservative level-set method

Part of the contents of this chapter have been published as:

Balcázar, N., Jofre, L., Lehmkuhl, O., Rigola, J., Castro, J., Oliva, A., A multiple marker level-set method for simulation of bubbly flows. In proceedings of 6th European Conference on Computational Fluid Dynamics (ECFD VI) (July, 2014).

Balcázar, N., Jofre, L., Lehmkuhl, O., Rigola, J., Castro, J., Oliva, A., A finite-volume/level-set interface capturing method for unstructured grids: simulations of bubbles rising through viscous liquids. Advances in Fluid Mechanics X 82 (2014), pp. 239.

Abstract.   This chapter presents a numerical study of gravity-driven bubbly flow using a conservative level-set method. First, the shape and terminal velocity of a single bubble which rises in a quiescent liquid are calculated and contrasted against experimental and numerical results reported in the literature. Then, different initial arrangements of bubble pairs were considered to study its hydrodynamic interaction. Finally, the gravity-driven bubbly flow is explored in a vertical duct with periodic boundary conditions. The results show that the conservative level-set approach is able to accurately capture the deformation of the interface on simulations of bubbly flows, and can remain numerically stable for a wide range of Morton and Reynolds numbers. Moreover, conservation properties are shown to be excellent, while accuracy remains satisfactory even for the most complex flows.

3.1 Introduction

Bubbles play an important role in many natural and industrial processes. Steam generators in nuclear plants, rocket engines, unit operations in chemical engineering such as distillation, absorption, extraction, heterogeneous catalysis and bioreactors are only a few among a multitude of applications that involve the motion of dispersed bubbles or drops in liquids. In industrial applications, such as bubble columns and the gas lift reactor [37], the flow usually involves swarms of bubbles created by a large number of nozzles or by a perforated plate, with moderate to large bubble concentration, which offer large interfacial areas enhancing efficiency of heat and mass transfer. The current understanding of such flows and their predictive models are far from satisfactory because of the difficulty in describing hydrodynamic interactions of bubbles. Therefore, understanding fundamental behaviour of bubble dynamics appears mandatory before a complete knowledge of bubble swarms can be achieved. Bubble interactions have significant consequences on bubble-size distribution, their breakup and coalescence behaviour, and their understanding can help us to improve Euler-Lagrange or Euler-Euler modelling of bubbly flows. Recognition of this has motivated a large number of numerical and experimental investigations of bubble dynamics. Despite those efforts many challenging problems still remain as pointed out in recent reviews (see [37], [58]).

The experiments of [4], [15], [27] and others provide a fairly detailed picture of the motion of bubbles rising through a quiescent viscous liquid for a wide range of Morton and Reynolds numbers. However, experimental studies of the interaction of two fluid particles are very limited. For instance, coalescence and bouncing of bubble pairs of $O(1mm)$ in both pure water and aqueous surfactant solutions was studied experimentally by [17]. He showed that there is a critical Weber number for the criteria of coalescence. [51] experimentally studied the motion and wake of a pair of slightly deformed bubbles rising side by side in silicone oil and water. They showed that the patterns of the trajectories of rising bubbles are strongly dependent on the Reynolds number, furthermore, bubbles can collide each other above a critical Reynolds number. [56] studied the transverse migration of both clean and fully contaminated spherical bubbles rising near a plane vertical wall in a quiescent viscous liquid for Reynolds number less than 100 using an optical technique. They found that the lift force of clean spherical bubbles is directed away from the wall for $Re < 35$ and toward it for higher $Re > 35$. In the context of bubbly flow, experiments were performed by [35] in order to measure the velocities of both phases in a monodispersed bubbly flow in a vertical column, using water and water-glycerin mixtures, for a range of Reynolds numbers from 10 to 500. [64] presented experimental results concerning the averaged behaviour of bubble suspensions for large Reynolds number and moderately small Weber. [54] investigated how freely rising ellipsoidal bubbles approach each other, make contact, coalesce or break, using

swarms of 10-20 bubbles of low Morton number.

On the other hand, due the rapid development in computational power, the Computational Multi-Fluid Dynamics (CMFD) has emerged as a powerful tool to study the bubble interaction mechanisms. Thus, some numerical studies have been performed about bubble dynamics in recent years. For instance, [61] studied terminal Reynolds numbers and shapes of isolated gas bubbles rising in quiescent liquids by using a Volume-of-Fluid method. Both [28] and [44] presented extensive simulations on a single bubble rising in a quiescent liquid by using the front-tracking method. [42] studied the effect of the density and viscosity ratio on the motion of single drops rising in immiscible liquids using a coupled level-set and volume-of-fluid method together with a sharp interface treatment for the interfacial jump conditions. The same methodology was employed by [43] to investigate the buoyancy-driven motion of a single skirted bubble rising through a viscous liquid. [3] tested different surface tension models for the Volume-of-Fluid method in order to study single bubbles rising in a quiescent liquid. [49] used a boundary-fitted method on orthogonal coordinates to perform a numerical study of buoyancy-driven motion of single gas bubbles. [11] performed a two-dimensional numerical simulation of the motion and coalescence of bubble pairs rising in a stationary liquid, using the moving particle semi-implicit method. [52] carried out two-dimensional simulations of the dynamics of single bubbles and a small group of bubbles using the level-set method. The Lattice-Boltzmann method was used by [33], [21] and [13] to investigate the bubble motion and bubble coalescence in liquids. [62] presented a numerical study of bubble interactions using an adaptive Lattice-Boltzmann method. [12] and [25] employed the Volume-of-fluid method to study the effects of liquid viscosity and surface tension on coalescence of two co-axial bubbles. [45] studied the effect of Reynolds number and viscosity on liquid film drainage mechanism formed during the interaction of two drops driven by buoyancy. A body fitted mesh has been applied by [32] to investigate the interaction of two bubbles rising side by side. [26] extend previous work to study the interaction between two bubbles as a function of Reynolds number, distance between the bubble centroids and the configuration angle between them. Drag and transverse forces were described using some simple models based on a physical description of the interaction. [8, 9] and [18] characterized the rise velocity, microstructure and velocity fluctuations on swarms of spherical and ellipsoidal bubbles using the Front-Tracking method.

These are some relevant studies on the hydrodynamics of single and multiple bubbles. To the best of the author's knowledge, there are not detailed computations of bubbly flow using the conservative level-set method [39, 40, 1], which is a promising technique for simulating two-phase flows with interfaces. Moreover, the experimental and numerical studies cited above demonstrate that numerical investigations of bubble interactions and bubbly flows considering their coalescence are

very limited in the scientific literature. Therefore, in the present paper we survey our results from 3D direct numerical simulations of buoyant bubbles by using the conservative level-set (CLS) method. Thus, the objectives of this research are as follows: first to demonstrate the accuracy of the CLS method to predict bubble shapes and drag coefficients of single bubbles for various flow regimes; second, to investigate hydrodynamic interaction mechanisms for bubble pairs with different relative initial positions; and, the third objective is to apply the CLS method to simulate the dynamic evolution of a suspension of many bubbles rising in a cylindrical wall confined domain, considering coalescence of bubbles when they collide.

The present paper is organized as follows: The governing equations employed in this study are given in section 3.2. Section 3.3 is devoted to the description of the numerical method, while the simulation results for bubble interactions are presented in section 3.4. Finally, concluding remarks are given in section 5.5.

3.2 Governing equations

For incompressible two-phase flows with uniform surface tension and no phase change, the Navier-Stokes equations, valid for the whole domain Ω and incorporating the jump conditions at the interface Γ, are:

$$\frac{\partial}{\partial t}(\rho \mathbf{v}) + \nabla \cdot (\rho \mathbf{v}\mathbf{v}) = -\nabla p + \nabla \cdot \mu \left(\nabla \mathbf{v} + (\nabla \mathbf{v})^T\right) + (\rho - \rho_0)\mathbf{g} + \sigma \kappa \mathbf{n} \delta_\Gamma \qquad (3.1)$$

$$\nabla \cdot \mathbf{v} = 0 \qquad (3.2)$$

where $\mathbf{v}$ is the velocity vector, p is the pressure, $\mathbf{g}$ is the gravity acceleration, δ_Γ is the Dirac delta function concentrated at the interface, σ is the constant surface tension coefficient, κ is the curvature of the interface, and $\mathbf{n}$ denotes the unit normal vector on the interface. Since ρ and μ are constant in each fluid with a jump at the interface, they can be defined as:

$$\rho = \rho_1 H_1 + \rho_2(1 - H_1) \qquad \mu = \mu_1 H_1 + \mu_2(1 - H_1) \qquad (3.3)$$

Here the subscripts 1 and 2 denote fluid 1 and fluid 2, respectively, and H_1 is the Heaviside step function that is one at fluid 1 and zero elsewhere. For gravity-driven bubbly flows in periodic domains, it is necessary to ensure that the net resultant force in the direction of gravity is zero. Hence, a force equal to the space-averaged density times the gravitational acceleration, $\rho_0 \mathbf{g}$ where $\rho_0 = \int_\Omega (H_1 \rho_1 + (1 - H_1)\rho_2)\, dV$, is subtracted from the right hand side of the Navier-Stokes equations.

In the CLS method [39, 40, 1] a regularized indicator function, ϕ, is introduced for interface capturing:

$$\phi(\mathbf{x}, t) = \frac{1}{2}\left(tanh\left(\frac{d(\mathbf{x}, t)}{2\varepsilon}\right) + 1\right) \qquad (3.4)$$

where ε is a tunable parameter that sets the thickness of the profile. With this profile the interface Γ is defined by the location of the $\phi = 0.5$ iso-surface, $\Gamma = \{\mathbf{x} \mid \phi(\mathbf{x}, t) = 0.5\}$.

The conservative level-set function ϕ is advected by a vector field $\mathbf{v}$ that is the fluid velocity given by the solution of the Navier-Stokes equations. The interface transport equation can be written in conservative form provided the velocity field is solenoidal, $\nabla \cdot \mathbf{v} = 0$, namely,

$$\frac{\partial \phi}{\partial t} + \nabla \cdot \phi \mathbf{v} = 0 \tag{3.5}$$

Furthermore, an additional re-initialization equation is introduced to keep the profile and thickness of the interface constant,

$$\frac{\partial \phi}{\partial \tau} + \nabla \cdot \phi(1 - \phi)\mathbf{n} = \nabla \cdot \varepsilon \nabla \phi \tag{3.6}$$

This equation is advanced in pseudo-time τ, it consists of a compressive term, $\phi(1 - \phi)\mathbf{n}|_{\tau=0}$, which forces the level-set function to be compressed onto the interface along the normal vector $\mathbf{n}$, and of a diffusion term $\nabla \cdot \varepsilon \nabla \phi$ that ensure the profile remains of characteristic thickness ε. Geometrical information on the interface, such as normal vector $\mathbf{n}$ or curvature κ, is obtained through:

$$\mathbf{n} = \frac{\nabla \phi}{\|\nabla \phi\|} \tag{3.7}$$

$$\kappa(\phi) = -\nabla \cdot \mathbf{n} \tag{3.8}$$

Implementing surface tension in a numerical scheme involves two issues: the curvature κ needs to be determined and the resulting pressure jump must be applied appropriately to the fluids. The aforementioned problems can be conveniently addressed through the CSF method [6]. Thus, the singular term, $\sigma\kappa\mathbf{n}\delta_\Gamma$, is converted to a volume force as follows,

$$\sigma\kappa\mathbf{n}\delta_\Gamma = \sigma\kappa(\phi)\nabla\phi \tag{3.9}$$

where $\kappa(\phi)$ is given by Eq. (5.8). In addition, the fluid properties are regularized by employing the level-set function,

$$\rho = \rho_1\phi + \rho_2(1 - \phi) \qquad \mu = \mu_1\phi + \mu_2(1 - \phi) \tag{3.10}$$

3.3 Numerical method

Following the work of [1], the Navier-Stokes/level-set equations have been discretized on a collocated unstructured grid arrangement by means of the finite-volume

method. In order to avoid unphysical oscillations in the level-set function, a TVD Superbee limiter, is used to discretize the convective term in advection Eq. (3.5). Central difference scheme, is used to discretize both the convective and compressive terms of momentum Eq. (3.1) and re-initialization Eq. (3.6), respectively. A distance-weighted linear interpolation is used to find the face values of physical properties and interface normals, while gradients are computed at cell centroids by using the least-squares method.

The velocity-pressure coupling has been solved by means of a classical fractional step projection method. Momentum Eq. (3.1) is decomposed into two steps:

$$\frac{\rho\mathbf{v}^* - \rho\mathbf{v}^n}{\Delta t} = -\frac{3}{2}\mathbf{A}_h(\rho\mathbf{v}^n) + \frac{1}{2}\mathbf{A}_h(\rho\mathbf{v}^{n-1}) + \mathbf{D}_h(\mathbf{v}^n) + \rho\mathbf{g} + \sigma\kappa\nabla_h(\phi) \qquad (3.11)$$

and

$$\mathbf{v}^{n+1} = \mathbf{v}^* - \frac{\Delta t}{\rho}\nabla_h(p^{n+1}) \qquad (3.12)$$

where ∇_h represents the gradient operator, $D_h(\mathbf{v}) = \nabla_h \cdot \mu\left(\nabla_h\mathbf{v} + \nabla_h^T\mathbf{v}\right)$ represents the diffusion operator, and $\mathbf{A}_h(\rho\mathbf{v}) = \nabla_h \cdot (\rho\mathbf{v}\mathbf{v})$ is the advection operator. The resulting velocity $\mathbf{v}^*$ from Eq. (5.12), which does not satisfy the continuity Eq. (5.2), is corrected by Eq. (5.13). Substituting Eq. (5.12) into the continuity Eq. (5.2) yields a Poisson equation for pressure,

$$\nabla_h \cdot \left(\frac{1}{\rho}\nabla_h(p^{n+1})\right) = \frac{1}{\Delta t}\nabla_h \cdot (\mathbf{v}^*) \qquad (3.13)$$

Poisson Eq. (3.13) discretization, leads to a linear system, which is solved by using a preconditioned conjugate gradient method. In order to avoid pressure-velocity decoupling when the pressure projection is made on collocated meshes [46, 19], a cell face velocity $\mathbf{v}_f$ is defined so that $\nabla_h \cdot \mathbf{v} = 0$ (see Eq. 3.2) in each control volume. Namely in discretized form:

$$\mathbf{v}_f = \sum_{q\in\{P,F\}} \frac{1}{2}\left(\mathbf{v}_q^{n+1} + \frac{\Delta t}{\rho(\phi_q^n)}(\nabla_h p^{n+1})_q\right) - \frac{\Delta t}{\rho_f}(\nabla_h p^{n+1})_f \qquad (3.14)$$

where P and F are denoting the adjacent cell nodes to the face f. Please, the reader is referred to [1] for technical detail of Eq. 3.14. This velocity is used to advect the level-set function and momentum in Eq. 3.5 and Eq. 3.11 respectively.

For the temporal discretization, explicit Adams-Bashforth scheme is used for the momentum Eq. (3.11), while for the corrector Eq. (3.12) an explicit first-order scheme has been used. Advection Eq. (3.5) and Re-initialization Eq. (3.6) are integrated in time with a 3-step third-order accurate TVD Runge-Kutta method. Solving Eq. (3.6) to steady-state results in a smooth transition of ϕ at the interface that depends of

the diffusion coefficient ε. In this paper, all numerical simulations were performed by setting $\varepsilon = 0.5h$ where $h = (V_{cell})^{1/3}$ is the characteristic size of the grid cell. Therefore, ε is chosen to be as small as possible in order to limit mass conservation errors, while maintaining reasonable resolution of the conservative level-set function to avoid numerical issues. In our simulations one iteration per physical time step of re-initialization Eq. (3.6) was sufficient to keep the profile of the level-set function. In the level-set method, coalescence happens automatically whenever two interfaces come within one grid cell of one other. Hence, in the present simulations we allowed for possible coalescence and breakup of the bubbles.

The time increment Δt, which is limited by the CFL conditions and the stability condition for the capillary force, is given by:

$$\Delta t = 0.1 min \left(\frac{h}{|\mathbf{v}|}, \frac{\rho h^2}{\mu}, \left(\frac{h}{|\mathbf{g}|} \right)^{1/2}, h^{3/2} \left(\frac{\rho_1 + \rho_2}{4\pi\sigma} \right)^{1/2} \right) \tag{3.15}$$

The global algorithm for solving the equations can be summarized as follows:

1. Calculate Δt by Eq. 3.15.

2. Solve level-set advection Eq. 3.5.

3. Solve re-initialization Eq. 3.6 for steady state.

4. Calculate $\mathbf{v}$ and p by the fractional-step method, Eq. 3.11, Eq. 3.13 and Eq. 3.12.

5. Calculate $\mathbf{v}_f$ by Eq. 3.14.

6. Repeat step 2 to 7 until the desired time-level.

The described two-phase flow solver was implemented in an in-house code called TermoFluids [31], which is a C++ code designed for direct numerical simulation and large eddy simulation of turbulent flows [57, 48]. The reader is referred to [1] for technical details of the spatial and temporal discretizations of the Navier-Stokes and level-set equations on collocated unstructured grids.

3.4 Results and discussion

3.4.1 Single bubble rise

In order to test the ability of the CLS method for simulating different bubble regimes, this section is devoted to investigate the dynamics of buoyancy bubbles. The bubble shape and its rise velocity, which is correlated to the drag coefficient, is a complex function of the hydrodynamics, viscous and interfacial forces. The experiments of

[15, 4], and others provide a fairly detailed picture of the motion of bubbles and drops through a quiescent viscous liquid. The relevant physical quantities in their experiments are: $\rho_g, \rho_l, \mu_g, \mu_l, \sigma, d, g, U_T$, where $d = (6V/\pi)^{1/3}$ is the spherical volume equivalent diameter of the bubble, and U_T is the rise velocity. Nondimensionalization results in the next parameters:

$$M \equiv \frac{g\mu_l^4 \Delta\rho}{\rho_l^2 \sigma^3} \qquad Eo \equiv \frac{gd^2\Delta\rho}{\sigma} \qquad Re \equiv \frac{\rho_l U_T d}{\mu_l} \qquad \eta_\rho \equiv \frac{\rho_l}{\rho_g} \qquad \eta_\mu \equiv \frac{\mu_l}{\mu_g} \qquad (3.16)$$

where, η_ρ and η_μ are respectively the density and viscosity ratio; M is the Morton number, $\Delta\rho = \rho_l - \rho_g$, specifies the density difference between the fluid phases; Eo is the Eötvös number, and Re is the Reynolds number. For given fluids, the Eötvös number is a characteristic of the bubble size and the Morton number is a parameter representing the viscosity of the liquid. For the sake of simplicity, we also introduce the following non-dimensional time, $t^* = t\sqrt{g/d}$.

The computational setup is schematically indicated in Fig. 3.1. In the initial state, the spherical bubble is located on the symmetry axis of the cylinder. The numerical simulations were performed on a cylindrical domain of $(D_\Omega, H_\Omega) = (8d, 12d)$ where D_Ω is the cylinder diameter and H_Ω is the cylinder height (see Fig. 3.1), under periodic boundary conditions between the top and bottom boundaries, and Neumann boundary condition at the side wall. Moreover, with the intend of saving computational resources such as computational time and occupation of memory, our simulations were computed on a non uniform hexahedral mesh, as show in Fig. 3.1b. The mesh was generated by a constant step extrusion of a two-dimensional unstructured grid along the symmetry axis of the cylinder, being the step size H_Ω/N_{planes}, where N_{planes} is the number of planes in which the vertical axis is divided (see Fig. 3.1b-c). The mesh was concentrated around the symmetry axis of the domain, where a uniform grid size (h_{min}) was fixed, to maximize resolution of the bubble. The mesh size grows exponentially to the border, where it reaches a maximum size of $h_{max} \approx 10 h_{min}$ (see Fig. 3.1b). Grid refinement and domain size studies were performed, for the condition $Eo = 116$, $M = 41.1$, $\eta_\rho = 100$ and $\eta_\mu = 100$. Fig. 3.2a shows the variation in Re as a function of dimensionless time t^* and Table 3.1 shows the value of the computed terminal Reynolds number and the relative error. As the grid size is reduced, the relative difference of Re between successive meshes becomes small.

Fig. 3.2b and Table 3.2 display results obtained on different domain sizes. A decrease in cylinder diameter reduces the bubble rise velocity (Re), while the shape of the bubble remains almost unchanged. These observations are confirmed by empirical and numerical findings reported by [24, 38, 28, 61]. Therefore, a domain size $(D_\Omega, H_\Omega) = (8d, 12d)$ and cell size $h = d/30$ were chosen as the standard conditions for numerical tests in this section (see Fig. 3.1 for a detailed description). Another
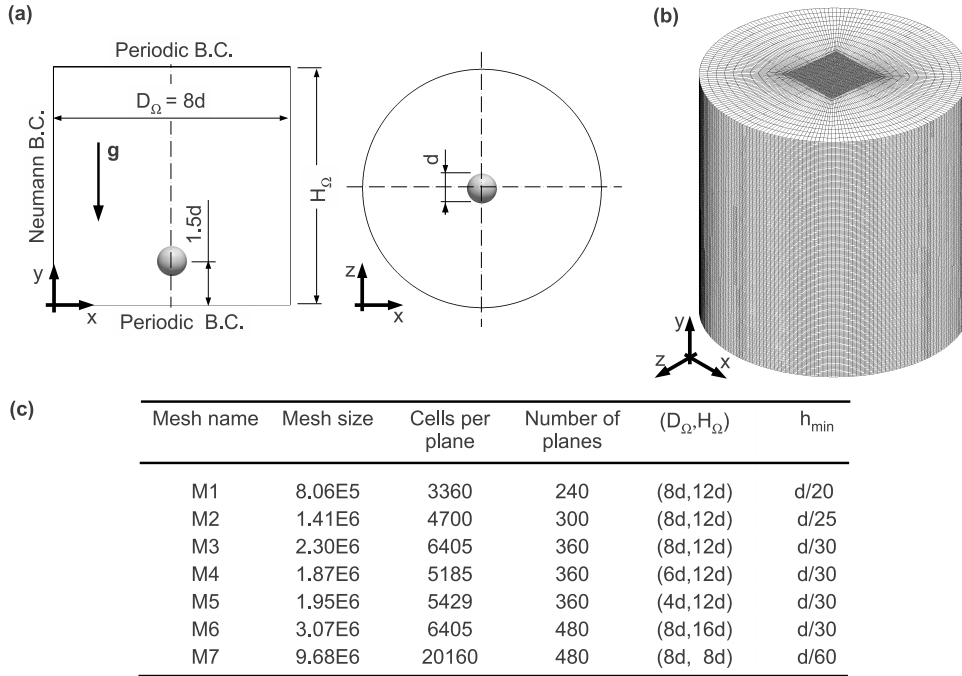
Figure 3.1: Computational system for single bubble simulations. (a) Sketch of initial condition and boundary conditions. (b) Mesh structure. (c) Mesh configuration.

Mesh	Cell size	(D_Ω, H_Ω)	Re	Relative error (ε_r)
M_1	$h = d/20$	$(8d, 12d)$	6.75	5.71%
M_2	$h = d/25$	$(8d, 12d)$	6.84	4.47%
M_3	$h = d/30$	$(8d, 12d)$	6.94	3.03%

Table 3.1: Influence of the grid size (h) on the Reynolds number, $Eo = 116$, $M = 41.1$, $\eta_\rho = 100$ and $\eta_\mu = 100$. Experimental reference $Re = 7.16$ ([4]). Mesh configuration and domain are shown in Fig. 3.1.
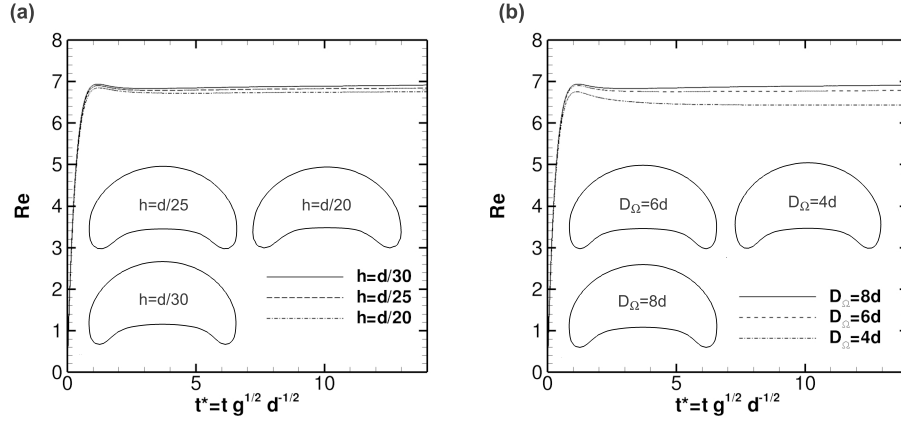
Figure 3.2: Grid and domain convergence for condition $Eo = 116$, $M = 41.1$, $\eta_\rho = 100$ and $\eta_\mu = 100$. (a) Grid refinement convergence, $D_\Omega = 8d$ and $H_\Omega = 12d$. (b) Domain size convergence, $h = d/30$ and $H_\Omega = 8d$.

Mesh	Cell size	(D_Ω, H_Ω)	Re	Relative error (ε_r)
M_4	$h = d/30$	$(4d, 12d)$	6.44	10.01%
M_5	$h = d/30$	$(6d, 12d)$	6.78	5.30%
M_3	$h = d/30$	$(8d, 12d)$	6.94	3.03%

Table 3.2: Influence of the domain size (D_Ω) on the Reynolds number, $Eo = 116$, $M = 41.1$, $\eta_\rho = 100$ and $\eta_\mu = 100$. Experimental reference $Re = 7.16$ ([4]). Mesh configuration and domain are shown in Fig. 3.1.

important aspect to get accurate simulations is the mass conservation of the bubble phase. The mass gain or loss may affect the shape of the interface and also the dynamics of the problem. Fig. 3.4b shows the satisfaction of this requirement by an illustrative simulation for $Eo = 116$, $M = 266$, $\eta_\rho = 100$, $\eta_\mu = 100$ and $h = d/30$. As the bubble is rising in the liquid, the instantaneous mass is calculated and compared with the initial mass. The mass error is then calculated by the expression $\Delta m = (m(t) - m(0))/m(0)$ where $m(t) = \int \phi dV$. From Fig. 3.4b, the instantaneous mass of the bubble is conserved fairly well. This is one of the most interesting advantages of the CLS method.

Fig. 3.3 shows some representative examples of bubble regimes, in which we compare numerical results against previous experiments reported by [4]. Generally, small bubbles, which have low Eötvös number ($Eo < 1$) tend to maintain the spherical shape, no matter how large the Reynolds number. Similarly, for low Reynolds number ($Re < 1$), the bubbles will also tend to be spherical, no matter how large the Eötvös number [4]. On the other hand, beyond the previously described regimes, the final bubble shape is given by the relative strength of the flow forces and the surface tension force, which are given by Re and Eo, respectively. Thus, for intermediate Reynolds and Eötvös numbers ($1 < Re < 100$ and $1 < Eo < 100$), various bubble shapes have been found in experimental investigations: oblate ellipsoid, disk-like, oblate ellipsoidal cap, skirt bubble, and spherical-cap [15, 4]. In spite of the difference in shapes, the bubbles rise steadily in a viscous liquid (high M) along a rectilinear path. Indeed, the present numerical predictions compare fairly well with the experimental findings of [4], as shown in Fig. 3.3. Regarding the terminal Reynolds number (see Table 3.3 and Fig. 3.3), the maximum error occurred at creeping flow regime with the lowest terminal Reynolds. Similar observations were reported by [28] using the front-tracking method (see Table 3.3). Fig. 3.4a demonstrates the influence of Morton number on the bubble motion at a fixed $Eo = 116$. The Morton number varies from 5.51 to 848. It is observed that the instantaneous Reynolds number evolves to steady state for all Morton numbers, however, the Morton number has different effects on the time evolution of the bubble velocity. At large M the Reynolds number quickly increases to a constant value, whereas at low M the Reynolds number first increases to a maximum value and then decreases until steady state value. Moreover, as the Morton number increases the overshoot on Re is more pronounced, indicating that the bubble motion has a tendency to reduce their stability.

Now, the accuracy of the CLS method is examined by comparison of the drag coefficient with experimental correlations and theoretical predictions. The drag coefficient (C_D) can be obtained from a simulation where a bubble is released in an initially quiescent liquid. Thus, from a steady state balance in the vertical direction,
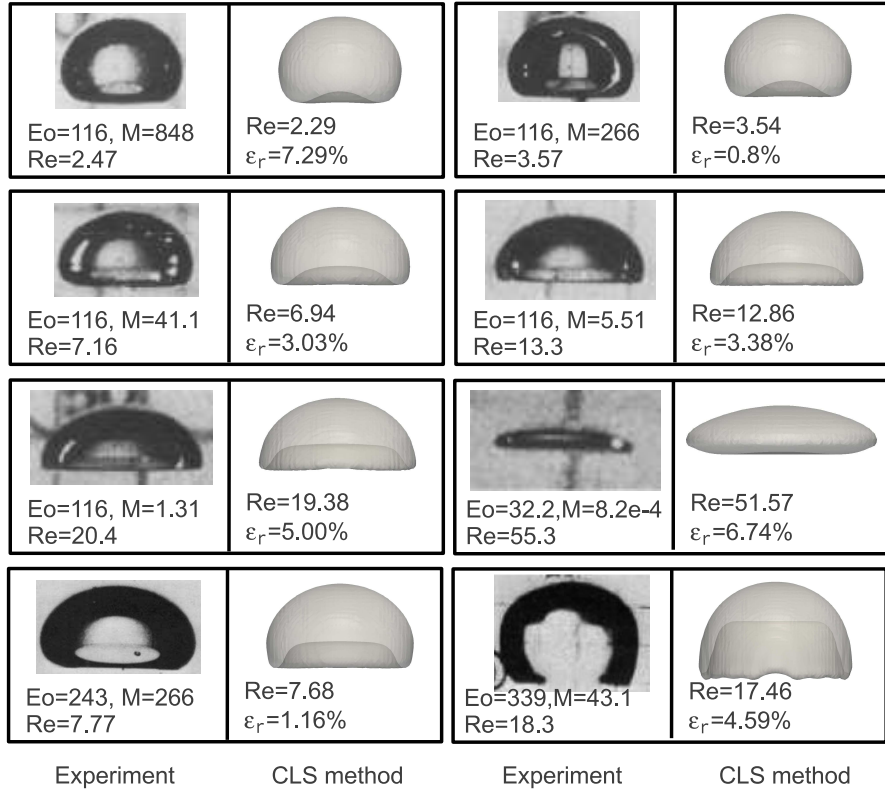
Experiment	CLS method	Experiment	CLS method
Eo=116, M=848 Re=2.47	Re=2.29 ε_r=7.29%	Eo=116, M=266 Re=3.57	Re=3.54 ε_r=0.8%
Eo=116, M=41.1 Re=7.16	Re=6.94 ε_r=3.03%	Eo=116, M=5.51 Re=13.3	Re=12.86 ε_r=3.38%
Eo=116, M=1.31 Re=20.4	Re=19.38 ε_r=5.00%	Eo=32.2,M=8.2e-4 Re=55.3	Re=51.57 ε_r=6.74%
Eo=243, M=266 Re=7.77	Re=7.68 ε_r=1.16%	Eo=339,M=43.1 Re=18.3	Re=17.46 ε_r=4.59%

Figure 3.3: Comparison of terminal bubble shape and Reynolds number observed in experiments reported by [4], and the CLS method with mesh resolution $h = d/30$. The error in the Reynolds number is calculated by $\varepsilon_r = |Re_{exp} - Re_{num}|Re_{exp}^{-1}$. All numerical experiments were carried out using $\eta_\rho = 100$, $\eta_\mu = 100$.

		Re			
Eo	M	[4]	[28]	Present	Mesh
116	848	2.47	2.317	2.29	M_3
116	266	3.57	3.621	3.54	M_3
116	41.1	7.16	7.0	6.94	M_3
116	5.51	13.3	13.17	12.86	M_3
116	131	20.4	19.88	19.38	M_3
32.3	8.2×10^{-4}	55.3	52.96	51.57	M_3
243	266	7.77	8.397	7.68	M_3
339	43.1	18.3	17.91	17.46	M_7

Table 3.3: A comparison of our computational results against experimental results of [4] and numerical results reported by [28] using the front-tracking method. Mesh configuration is shown in Fig. 3.1.
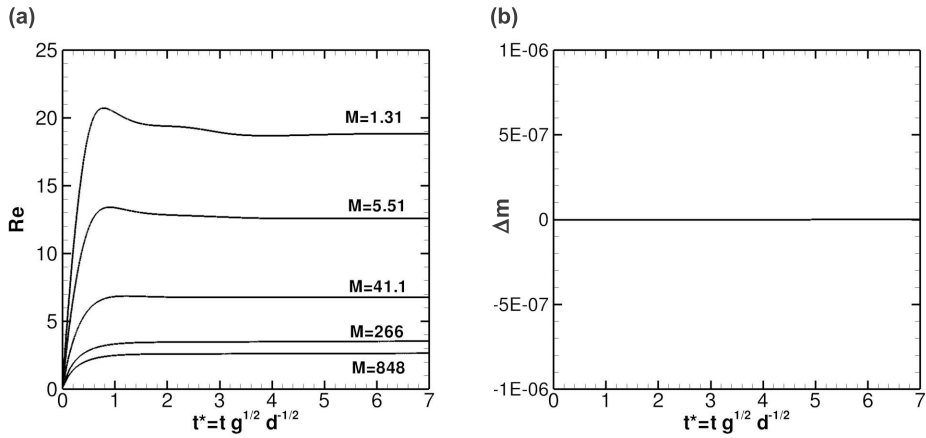

Figure 3.4: (**a**) Influence of Morton number (M) on terminal Reynolds number (Re). Re is plotted against non-dimensional time (t^*), $h = d/30$, $Eo = 116$, $\eta_\rho = 100$, $\eta_\mu = 100$. (**b**) Mass conservation of bubble phase, $Eo = 116$, $M = 266$, $\Delta m = \frac{m(t) - m(0)}{m(0)}$ where $m(t) = \int_\Omega \phi(\mathbf{x}, t) dV$.
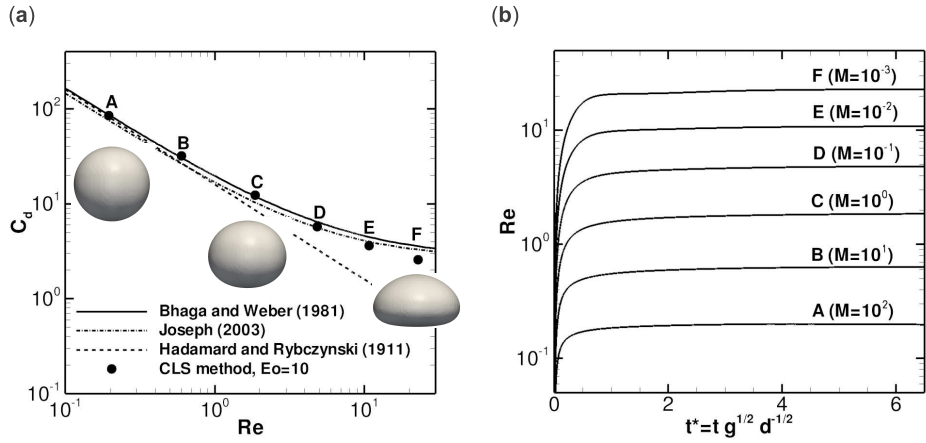
(a)

(b)

Figure 3.5: (*a*) Comparison of numerical prediction of drag coefficient C_D as a function of the Reynolds number Re, against Eq. (3.18) and Eq. (3.20) (*b*) Instantaneous Reynolds number as a function of the dimensionless time t^*. Physical conditions are given by $Eo = 10$, $\eta_\rho = 100$, $\eta_\mu = 100$, $10^{-3} \leq M \leq 10^3$ (low viscosity values).
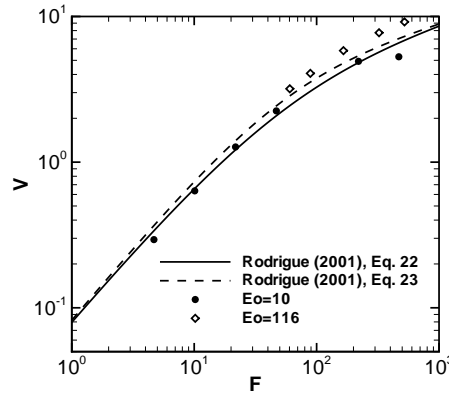

Figure 3.6: Velocity number (V) as a function of the flow number (F). Correlations are taken from [47].

3.4. Results and discussion

C_D can be computed from the terminal rise velocity U_T:

$$C_D = \frac{4(\rho_l - \rho_g)||\mathbf{g}||d}{3\rho_l U_T^2} \tag{3.17}$$

[4] proposed an experimental correlation between C_D and Re for fluids with Morton number $M > 4 \times 10^{-3}$:

$$C_D = \left((2.67)^{0.9} + (16/Re)^{0.9}\right)^{1/0.9} \qquad M > 4 \times 10^{-3} \tag{3.18}$$

The numerical results are also compared against theoretical predictions of [29], which was derived based on the theory of viscous potential flow. The drag coefficient is given as:

$$C_D = 0.445 \left(6 + \frac{32}{Re}\right) \tag{3.19}$$

[23] and [50] generalize the Stokes result for the viscous drag force on a solid sphere, to fluid particles of arbitrary and finite internal viscosity. From integration of pressure and shear stress on the fluid particle surface, they infer the drag coefficient at very low Re:

$$C_D = \frac{8}{Re} \frac{2 + 3\eta_\mu^{-1}}{1 + \eta_\mu^{-1}} \qquad Re \ll 1 \tag{3.20}$$

For the sake of comparison, a set of numerical simulations were carried out to calculate C_D from Eq. (3.17). Figure 3.5b shows the terminal Reynolds number as a function of dimensionless time, with $Eo = 10$, $10^{-3} \leq M \leq 10^2$, $\eta_\rho = 100$ and $\eta_\mu = 100$; whereas, Fig. 3.5a shows the drag coefficient as a function of the Reynolds number. As M decreases, the bubble deformation increases and the spherical bubble approximation (see Eq. 3.20) is valid for only high M, as one would indeed expect; moreover, numerical predictions of C_D are in good agreement with Eq. 3.18 and Eq. 3.19. In addition, the flow number (F) and the velocity number (V) defined as:

$$F = g \left(\frac{d^8 \rho_l^5}{\sigma \mu_l^4}\right)^{1/3} \tag{3.21}$$

$$V = U_t \left(\frac{d^2 \rho_l^2}{\sigma \mu_l}\right)^{1/3} \tag{3.22}$$

are evaluated from the numerical results given in Fig. 3.5 and Table 3.3 for $Eo = 10$ and $Eo = 116$ respectively. These results are compared to the following correlations reported by [47]:
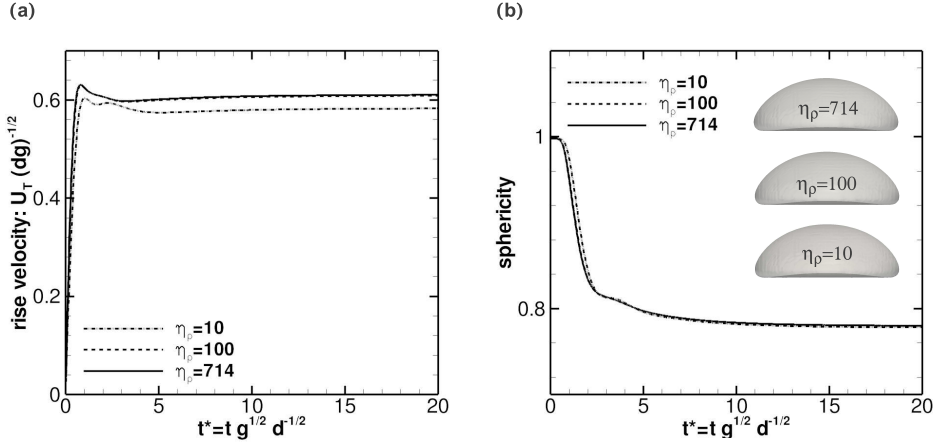
$$V = \frac{F}{12 \left(1 + 0.049 F^{3/4}\right)} \tag{3.23}$$

89

(a)

(b)

Figure 3.7: The effect of density ratio (η_ρ) on bubble dynamics at $Eo = 39.4$, $M = 0.065$, $\eta_\mu = 6.67 \times 10^3$ and $\eta_\rho = \{10, 100, 714\}$. (a) Terminal shapes and dimensionless rise velocity ($\mathbf{v} \cdot \mathbf{e}_y g^{-1/2} d^{1/2}$) versus dimensionless time. (b) Sphericity ($\pi d^2 / \int_\Omega |\nabla \phi| dV$) versus dimensionless time.

$$V = \frac{F}{12 \left(1 + 0.0185F\right)^{3/4}} \tag{3.24}$$

From Fig. 3.6 it is observed that numerical predictions are in good agreement with the correlations given by Eq. 3.23 and Eq. 3.24.

To further investigate the effect of density ratio on the terminal velocity (U_t) and bubble shape, we simulate a bubble rising under buoyancy for $Eo = 39.4$, $M = 0.065$, $\eta_\mu = 6.37 \times 10^3$ and $\eta_\rho = \{10, 100, 714\}$. Physical properties were chosen so that experimental data reported by [27] are equivalent to dimensionless parameters used in this section. Since the experiment was done in a large container with negligible wall effects, we use a very large computational domain with $(D_\Omega, H_\Omega) = (8d, 16d)$, which corresponds to the mesh M_6 in Fig. 3.1c. Fig. 3.7a shows the rise velocity and terminal bubble shapes as a function of the density ratio, whereas Fig. 3.7b shows the time evolution of bubble sphericity. It can be seen that the bubble shapes are not affected by density ratio, as shown in Fig. 3.7a and Fig. 3.7b. The rise velocity is sensitive to η_ρ, indeed, a lower density ratio provides a lower value of terminal velocity U_T, such that the bubble will reach smaller distances in the same period of time. In addition, the sensitivity of rise velocity to density ratio is drastically reduced if $\eta_\rho \geq 100$ (see Fig. 3.7a). Table 3.4 shows the relative error on the terminal rise velocity. It can be observed that as the density ratio increases, the relative error

3.4. Results and discussion

η_ρ	η_μ	Eo	M	U_T^* (CLS method)	ε_r	Mesh
10	6.67×10^3	39.4	0.065	0.5833	6.31%	M_6
100	6.67×10^3	39.4	0.065	0.6098	2.06%	M_6
714	6.67×10^3	39.4	0.065	0.6118	1.73%	M_6

Table 3.4: Effect of density ratio on terminal velocity. Here, $U_T^* = U_T d^{-1/2} g^{-1/2}$ and $\varepsilon_r = |U_T - U_{T,exp}| U_{T,exp}^{-1}$. The reference solution $U_{T,exp} = 0.215 m/s$ ($U_{T,exp}^* = 0.6226$) was obtained experimentally by [27] at $Eo = 39.4$, $M = 0.065$, $\eta_\rho = 714$ and $\eta_\mu = 6.67 \times 10^3$.

η_ρ	η_μ	Eo	M	U_T^* (CLS method)	ε_r	Mesh
100	10	39.4	0.065	0.5699	8.46%	M_6
100	100	39.4	0.065	0.6038	3.02%	M_6
100	6.67×10^3	39.4	0.065	0.6118	2.06%	M_6

Table 3.5: Effect of viscosity ratio on terminal velocity. Here, $U_T^* = U_T d^{-1/2} g^{-1/2}$ and $\varepsilon_r = |U_T - U_{T,exp}| U_{T,exp}^{-1}$. The reference solution $U_{T,exp} = 0.215 m/s$ ($U_{T,exp}^* = 0.6226$) was obtained experimentally by [27] at $Eo = 39.4$, $M = 0.065$, $\eta_\rho = 714$ and $\eta_\mu = 6.67 \times 10^3$.

is reduced.

The effect of viscosity ratio is evaluated by comparing the terminal velocity and shape for $Eo = 39.4$, $M = 0.065$, $\eta_\mu = \{10, 100, 6.37 \times 10^3\}$ and $\eta_\rho = 100$. As in the above test cases, the mesh M_6 is used to perform the present simulations (see Fig. 3.1c). From Fig. 3.8a, it is noted that as the value of viscosity ratio is increased, terminal velocity tends to collapse into a single curve. Effect of η_μ on terminal shape is presented in Fig. 3.8b. In addition, it is found that the the effect of viscosity ratio on bubble shape is stronger than on bubble velocity, however, the variation of bubble rising velocity is less than 1% when the viscosity ratio changes from 100 to 6.67×10^3. The aforementioned results are in agreement with numerical findings of [28].

Regarding the flow pattern we have investigated the influence of bubble shape on the wake behind the bubble. In the experiment of [4] hydrogen bubble tracers were used to get the flow visualization, whereas shadowgraph and Schlieren techniques were employed by [27] to study the wake structure of spherical cap bubbles. Fig. 3.9a shows the terminal bubble wake for the case $Eo = 39.4$, $M = 0.065$, $\eta_\rho = 714$, $\eta_\mu = 6670$. The closed toroidal wake and bubble shape predicted by the CLS method are in close agreement with the experimental findings of [27], furthermore, a comparison of the present results with numerical simulations reported by [49, 63, 22] are presented in Fig. 3.9a, which confirm the accuracy of the present simulations. Figs. 3.9b-c show results obtained in the present work and also numerical and ex-
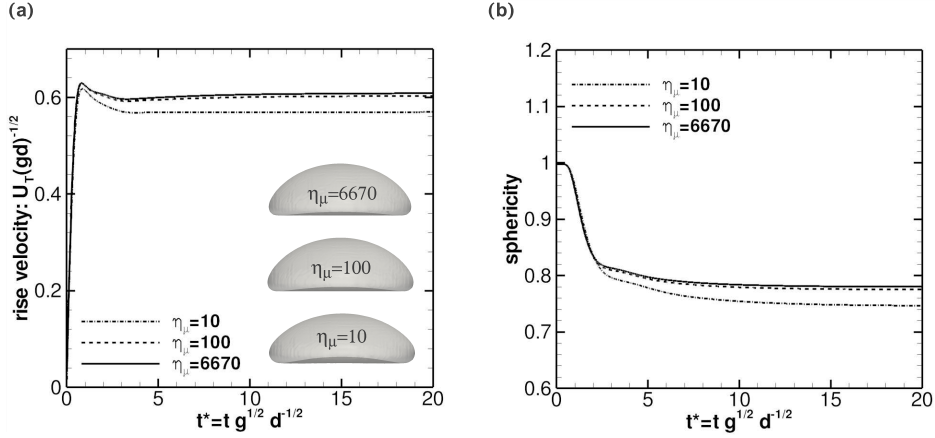
Figure 3.8: The effect of viscosity ratio (η_ρ) on bubble dynamics at $Eo = 39.4$, $M = 0.065$, $\eta_\mu = \{10, 100, 6.67 \times 10^3\}$ and $\eta_\rho = 100$. (a) Terminal shapes and dimensionless rise velocity ($\mathbf{v} \cdot \mathbf{e}_y g^{-1/2} d^{1/2}$) versus dimensionless time. (b) Sphericity ($\pi d^2 / \int_\Omega |\nabla \phi| dV$) versus dimensionless time.

perimental wakes reported on [28] and [4] respectively. These cases correspond to dimensionless parameters $Eo = 116$, $M = 0.065$, $\eta_\rho = 100$, $\eta_\mu = 100$ (Fig. 3.9b), and $Eo = 292$, $M = 26.7$, $\eta_\rho = 100$, $\eta_\mu = 100$ (Fig. 3.9b-c). Secondary wake recirculations were observed for the aforementioned cases (see Fig. 3.9b-c) , which could explain the bright zones (caused by refraction effects [4]) just behind the bubble rim at the experimental images reported by [4]; moreover, the present results performed by the CLS method are confirmed by numerical predictions reported by [28, 44] using the front-tracking method.

Fig. 3.10 shows the effect of the convective scheme used to discretize the momentum equation (Eq. 3.1) on the rising velocity and bubble shape, for $Eo = 39.4$, $M = 0.065$, $\eta_\rho = 714$, $\eta_\mu = 6.67 \times 10^3$. This case has been solved using the mesh M_6 (see Fig. 3.1c) which corresponds to 30 control volumes per bubble diameter ($h = d/30$ around the symmetry axis). Following the work of [1], the finite-volume discretization of the convective term on momentum equation is based on the use of
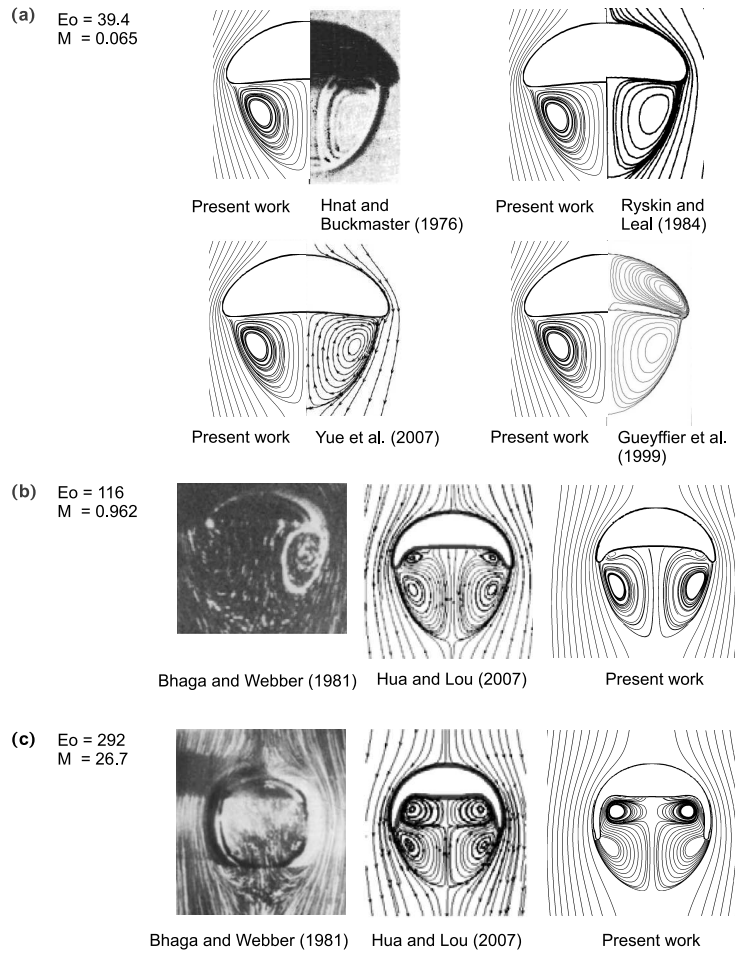
(a) Eo = 39.4
M = 0.065

Present work   Hnat and
               Buckmaster (1976)

Present work   Ryskin and
               Leal (1984)

Present work   Yue et al. (2007)

Present work   Gueyffier et al.
               (1999)

(b) Eo = 116
M = 0.962

Bhaga and Webber (1981)   Hua and Lou (2007)   Present work

(c) Eo = 292
M = 26.7

Bhaga and Webber (1981)   Hua and Lou (2007)   Present work

Figure 3.9: Comparisons of experimental and numerical results previously published against present results (CLS method) for the wake pattern. (a) $Eo = 39.4$, $M = 0.065$, $\eta_\rho = 714$, $\eta_\mu = 6.67 \times 10^3$. Reference results are reported in [27, 49, 63, 22]. (b) $Eo = 116$, $M = 0.962$, $\eta_\rho = 100$, $\eta_\mu = 100$. Reference results are reported in [4, 28]. (c) $Eo = 292$, $M = 26.7$, $\eta_\rho = 100$, $\eta_\mu = 100$. Reference results are reported in [4, 28]. The meshes used in present simulations are M_6 (a), M_3 (b) and M_7 (c). See Fig. 3.1c for mesh description.

(a)

(b)
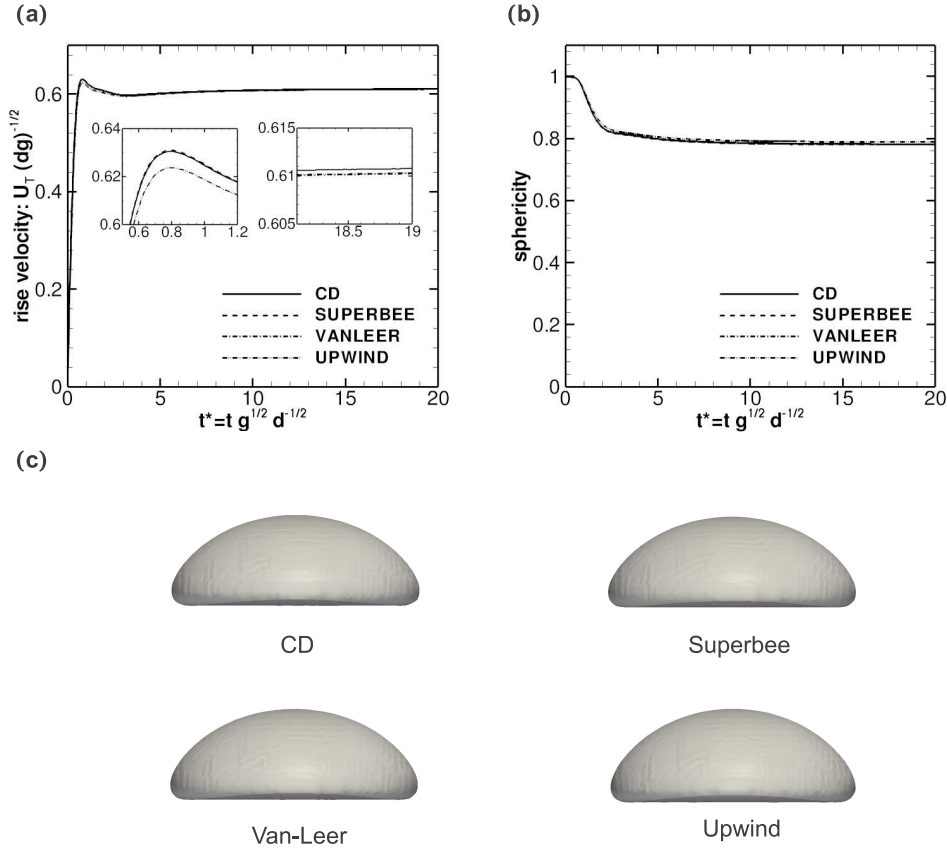

(c)

CD

Superbee

Van-Leer

Upwind

Figure 3.10: Effect of the convective scheme used to discretize the momentum equation (see Eq. 3.1). Here, $Eo = 39.4$, $M = 0.065$, $\eta_\rho = 714$, $\eta_\mu = 6.67 \times 10^3$. (a) Effect on the rise velocity. (b) Effect on the sphericity (bubble shape). (c) Qualitative comparison of terminal bubble shape.

flux limiters, $L(\theta)$, which are defined as follow

$$L(\theta) \equiv \begin{cases} 1 & \text{Central difference limiter (CD)}, \\ max\{0, min\{2\theta, 1\}, min\{2, \theta\}\} & \text{TVD Superbee limiter}, \\ \frac{\theta + |\theta|}{1 + |\theta|} & \text{TVD Van-Leer limiter}, \\ 0 & \text{First-order upwind limiter}. \end{cases} \quad (3.25)$$

Flux limiter	$U_T(gd)^{-1/2}$	ε_r	sphericity	Mesh
CD	0.6109	1.88%	0.7818	M_6
Superbee	0.6105	1.94%	0.7802	M_6
Van-Leer	0.6104	1.96%	0.7805	M_6
Upwind	0.6105	1.94%	0.7890	M_6

Table 3.6: Effect of flux limiters used to discretize the momentum equation on terminal rising velocity. Here, U_T is the terminal rise velocity ($\mathbf{v}_c \cdot \mathbf{e}_y$ at $t^* = 20$) and $\varepsilon_r = |U_T - U_{T,exp}|U_{T,exp}^{-1}$ is the error in the computed velovity. The reference solution $U_{T,exp} = 0.215m/s$ ($U_{T,exp}(gd)^{-1/2} = 0.6226$) was obtained experimentally by [27] for $Eo = 39.4$, $M = 0.065$, $\eta_\rho = 714$ and $\eta_\mu = 6.67 \times 10^3$.

where θ is a monitor variable defined as the upwind ratio of consecutive gradients of the velocity components. Please, the reader is referred to [1] or Chapter 2 for technical details on the application of flux limiters to discretize the convective term of momentum equation on unstructured grids. Regarding the numerical results, Fig. 3.10a illustrates the effect of flux limiters on the rising velocity. A close-up on the time $t \approx 0.8$ shows that the upwind limiter underestimates the overshoot on the rising velocity, while the other flux limiters lead to similar results. Figs. 1 y 2 show that the sphericity and shape of the bubbles are in close agreement, independently of the flux limiter used, however it is noted a slight deviation of the sphericity when an upwind limiter is used in comparison with the other ones (see Table 3.6). In addition, regarding the rising velocity, the deviation of numerical results from experimental results, ε_r, was found to be minor by using a CD limiter, as shown in Table 3.6.

Thus, the calculated drag coefficients, bubble shapes, Reynolds number and wake structure are consistent with the existing correlations and experimental data reported in the literature. These various comparisons serve to validate the accuracy and versatility of the CLS method.

3.4.2 Hydrodynamic interaction of bubble pairs

Following the previous validation cases, the CLS method is used to explore the complex interaction between two spherical or ellipsoidal bubbles.

Fig. 3.11 shows the computational system and mesh configuration used for simulating the interaction of a pair of bubbles. The bubble simulations in the current section are performed in a cuboid domain with periodic boundary conditions in the vertical direction and Neumann boundary conditions at the lateral boundaries. The distance between the bubble centroids and the lateral walls was set to be larger than 4 bubble diameters to minimize the confinement effect (see Table 3.2). From Fig. 3.11b the domain is divided in 2.9×10^6 hexahedral volumes, which is equivalent to 30
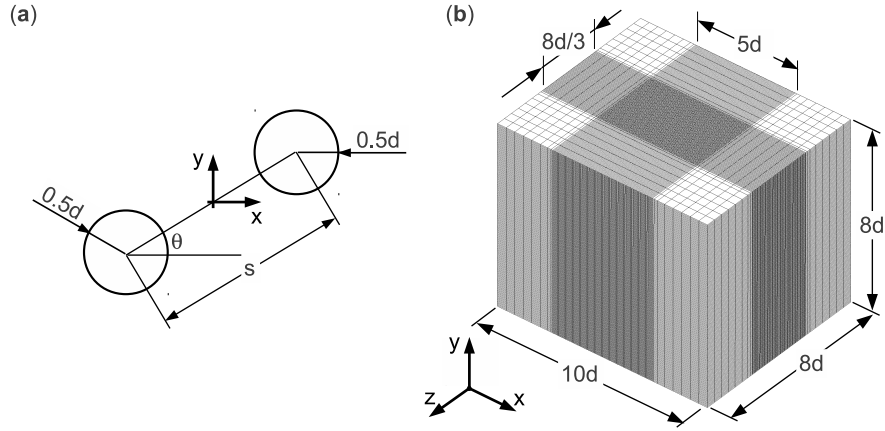
Figure 3.11: Computational framework for simulating the interaction of a pair of bubbles. (a) Sketch of the initial configuration. (b) Mesh configuration. The domain is divided in 2.9×10^6 hexahedral volumes, which is equivalent to 30 cv/d.

control volumes per bubble diameter (cv/d). Numerical experiments were carried out under conditions of different Eo and M numbers. In addition, the interaction between a pair of bubbles is influenced by their center-to-center separation distance, s, and their configuration angle, θ, as shown in Fig. 3.11a. Moreover, as initial condition, the bubbles are at rest and a spherical shape is assumed.

Spherical bubbles

A first experiment is carried out to capture the coalescence of two spherical bubbles. According to the experiment results of [17], two bubbles in pure water coalesce if their Weber number based on the approach velocity is less than a critical value. [51] experimentally studied the motion and coalescence of a pair of bubbles rising side by side in a quiescent silicone oil and water. His results demonstrated that the bubbles bounce or coalesce after collision, which is strongly dependent on the critical Reynolds and Weber number. Fig. 3.12 shows the coalescence of two identical bubbles predicted from numerical simulation (CLS method) and that observed in experiment by [17]. The geometrical parameters were fixed to $s = 1.11d$ and $\theta = 0$, and physical properties correspond to dimensionless parameters $Eo = 1.53$, $M = 1.107 \times 10^{-9}$, $\eta_\rho = 1149$ and $\eta_\mu = 1000$ (see Eq. 5.17). It can be seen from Fig. 3.12 that the bubbles approach each other until the film between the bubbles was about one cell size , and then finally coalesced to form a single bubble. After coales-
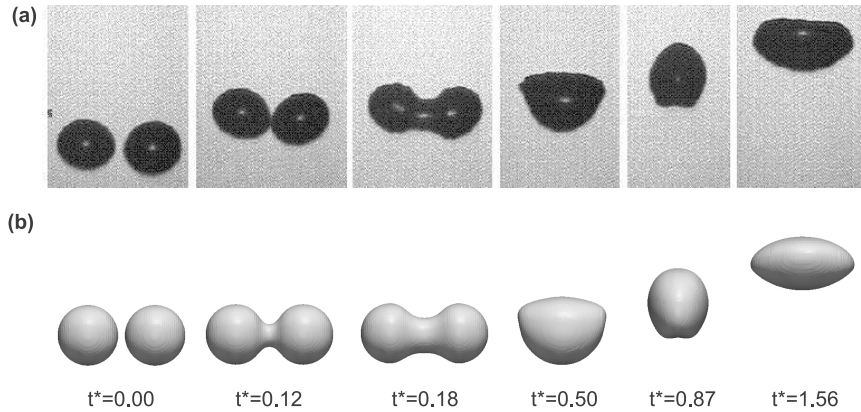
Figure 3.12: Bubble coalescence of two identical bubbles $\theta = 0$, $s = 1.11d$, $Eo = 1.53$, $M = 1.107 \times 10^{-9}$, $\rho_1/\rho_2 = 1149$, $\mu_1/\mu_2 = 1000$ (a) Experimental observations reported by [17]. (b) Numerical results by using the conservative level-set method ($t^* \equiv t\sqrt{g/d}$).

cence the shape of the bubble is not stable. Surface oscillations are observed, due to the difference in pressure and surface energy, between the single larger bubble and the two small bubbles [17]. It can be seen from Fig. 3.12 that the bubble shapes of both before and after coalescence predicted by CLS method are in qualitative agreement with the experiment findings reported by [17]. Similar results were reported by [11] using a moving particle semi-implicit method.

According to empirical findings of [56] and [51], and numerical studies of [32], when two spherical bubbles rise side by side, a horizontal force is induced and it causes either repellence or attraction between the bubbles, as result of the competition between vortical and irrotational interaction mechanisms. Thus, the lateral force changes sign for a certain critical Reynolds number (Re_c). For instance, [32] numerically studied the motion of a pair of spherical rising bubbles aligned horizontally by using DNS and predicted that $Re_c \approx 30$ if the horizontal distance between the bubbles is $s = 1.5d$ and $\theta = 0$, a value confirmed by the experimental results of [56]. Following previous results, a set of numerical experiments were performed for $Eo = 0.34$, $4.8 \times 10^{-6} \leqslant M \leqslant 1 \times 10^{-8}$, $\eta_\rho = 100$, $\eta_\mu = 100$, $s = 1.5d$ and $\theta = 0$. From Fig. 3.13a, in simulations where $Re \lesssim 32$ the bubbles separate from each other. On the other hand, for cases with $Re \gtrsim 32$ the bubbles approach each other. Such behaviour has been explained by [32] in terms of the vorticity: when Re is large enough for the vorticity to remain confined in a boundary layer whose thick-
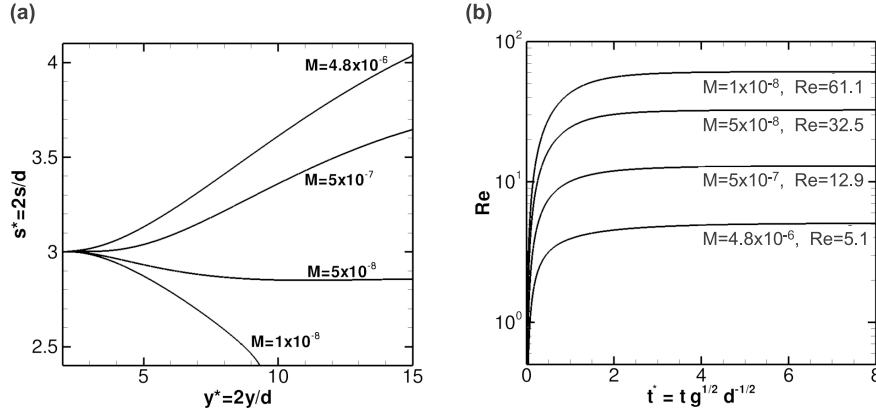
Figure 3.13: Interaction of a pair of bubbles rising side-by-side, $Eo = 0.36$, $\eta_\rho = 100$, $\eta_\mu = 100$, $4.8 \times 10^{-6} < M < 1 \times 10^{-8}$, $s|_{t=0} = 1.5d$, $\theta = 0$. (a) Evolution of the nondimensional distance $s^* = 2s/d$ between the centers of the bubbles at different vertical positions. (b) Terminal Reynolds number of a single spherical bubble for the corresponding cases in (a).

ness is small compared to the distance between the two bubbles, the interaction is dominated by the irrotational mechanism, consequently, the transverse force is then attractive. However, when viscous effects are dominant, the vorticity spreads out about each bubble until it is canceled in the gap by the vorticity existing around the other bubble, resulting in a repulsive transverse force for small values of Re. Indeed, the numerical prediction of the transitional Reynolds number ($Re_c \approx 32$) given by the CLS method, is consistent with numerical and experimental results previously published [32, 62, 5, 51, 56].

The effect of the initial configuration angle on the hydrodynamic interaction between two spherical bubbles is studied for $s = 1.5d$, $0° \leqslant \theta \leqslant 90°$, $Eo = 0.34$, $M = 1 \times 10^{-8}$ (or $Re = 61.1$ for the corresponding single bubble). The evolution of $s^* = 2s/d$ and θ are reported in Fig. 3.14 versus dimensionless time t^* for different initial orientation angles θ_0. Fig. 3.14b shows a decrease of the configuration angle as it evolves in time, which indicates a torque action on the bubbles that tends to align them side-by-side. The plot of the dimensionless distance (see Fig. 3.14a) indicates that the two bubbles being attracted for $0° \leqslant \theta \leqslant \theta_c$ but repelled for $\theta_c \leqslant \theta \leqslant 90°$, where θ_c is the angle of transition. From Fig. 3.14a, θ_c is between $30°$ and $45°$, which is in good agreement with the value $\theta_c \approx 37°$ reported by [26].
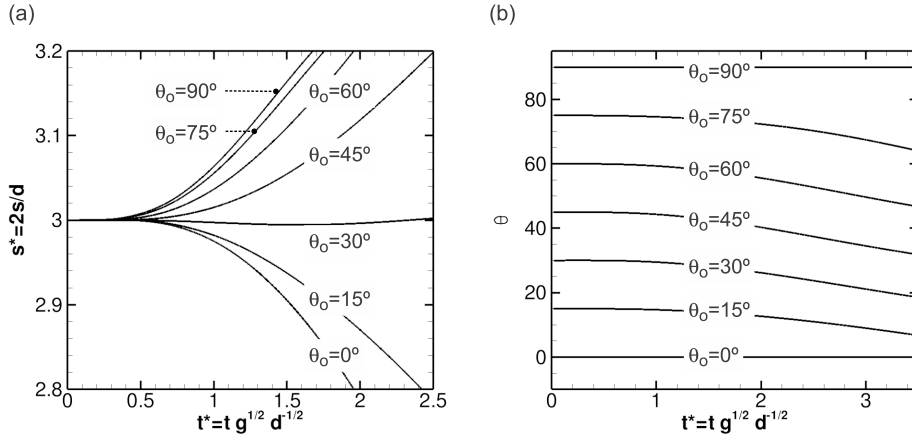
(a)

(b)

Figure 3.14: Evolution of the dimensionless distance between the centroids of the bubbles versus dimensionless vertical position. Bubbles rise in spherical shape regime, $Eo = 0.34$, $M = 1 \times 10^{-8}$, $\eta_\rho = 100$, $\eta_\mu = 100$.
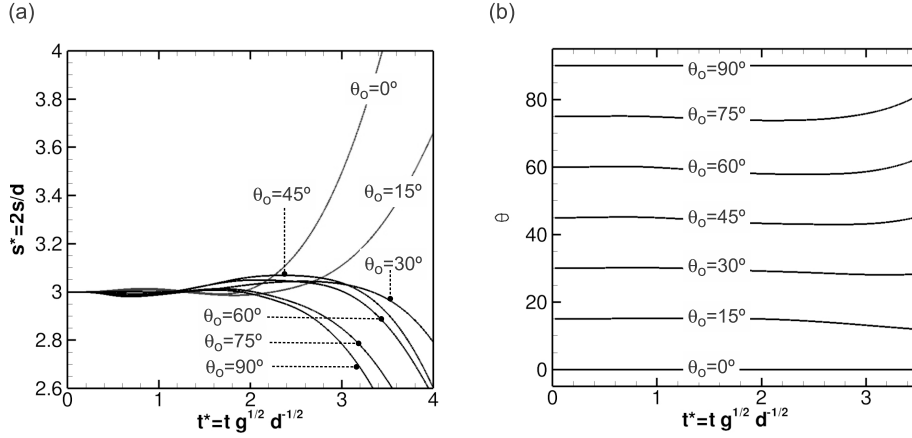
(a)

(b)

Figure 3.15: Evolution of the dimensionless distance between the centroids of the bubbles versus dimensionless vertical position. Bubbles rise in ellipsoidal shape regime, $Eo = 4.0$, $M = 1 \times 10^{-9}$, $\eta_\rho = 100$, $\eta_\mu = 100$.
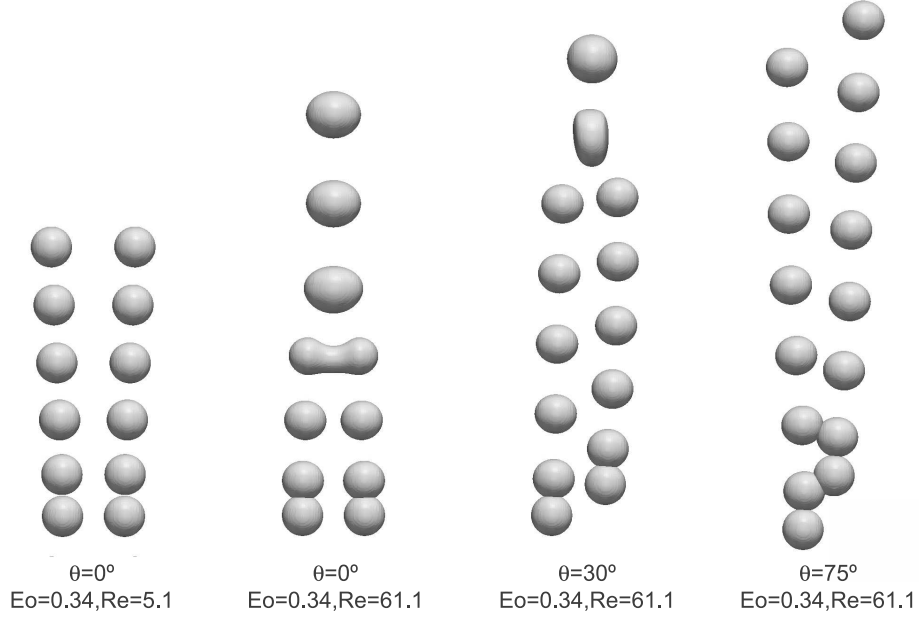
θ=0°
Eo=0.34,Re=5.1

θ=0°
Eo=0.34,Re=61.1

θ=30°
Eo=0.34,Re=61.1

θ=75°
Eo=0.34,Re=61.1

Figure 3.16: Snapshots of the bubble position released in staggered configuration with $Eo = 0.34$ (spherical regime), $\eta_\rho = 100$, $\eta_\mu = 100$. The Δt^* between shots is 1.25. The indicated Re number is defined based on the rise velocity of an isolated bubble under the same conditions.

Ellipsoidal bubbles

In this section we study the interaction of two bubbles on ellipsoidal regime with $Eo = 4$, $M = 1 \times 10^{-9}$, $\eta_\rho = 100$, $\eta_\mu = 100$, $s = 1.5d$, $0° < \theta|_{t=0} < 90°$. Fig. 3.17 shows the variation of shape and position for different initial configuration angles. For $\theta|_{t=0} = 0°$, the trajectory and shape of bubbles are symmetric about $y - z$ plane. For cases with $\theta|_{t=0} = 0°$ and $\theta|_{t=0} = 15°$, the bubbles separate each other until $t^* \approx 0.8$, where s starts to decrease up to $t^* \approx 1.7$. From this time a repulsion force acts between the bubbles and s continues to increase faster, as shown in Fig. 3.15a. For $\theta|_{t=0} \gtrsim 30°$, the dynamic evolution of s is the opposite than previous cases (see Fig. 3.15a), it was observed an attractive force between bubbles, which concludes with coalescence of small bubbles to form a larger one (see Fig. 3.17c). The shape of the larger bubble is different compared with spherical regime (see Fig. 3.16), thereby indicating that the coalescence dynamics is a function of the Eötvös number.
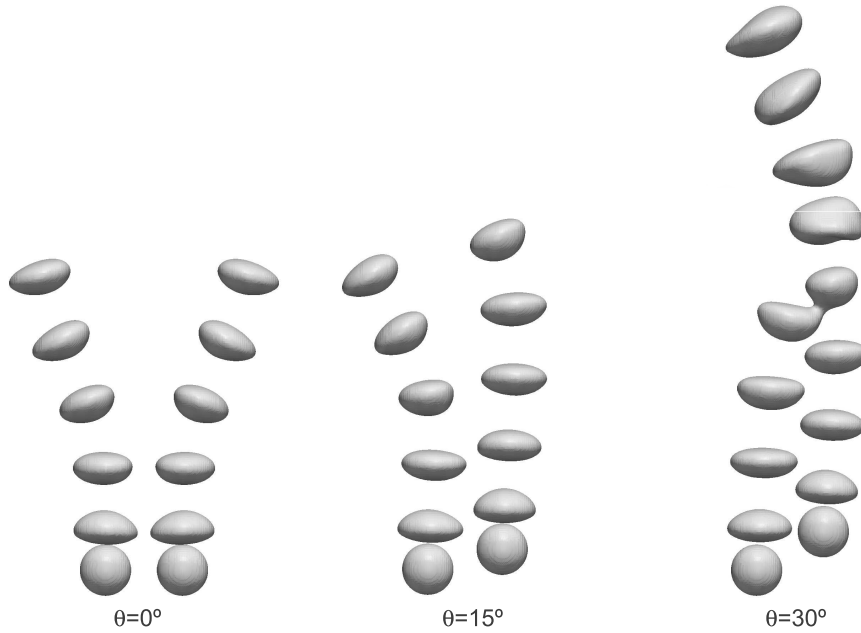
100

Figure 3.17: Snapshots of the bubble position released in a staggered configuration with $Eo = 4$ (ellipsoidal regime), $M = 1 \times 10^{-9}$, $\eta_\rho = 100$, $\eta_\mu = 100$. The Δt^* between shots is 1.25. According to the Grace diagram [15], the Reynolds number corresponds to $Re \approx 700$, based on the rise velocity of an isolated bubble under the conditions mentioned above.

In this regime, the wake behind the upper bubble creates an artificial lift force for the downstream bubble, which gradually moves in the wake of the leading bubble. When the two bubbles are close to collide, a considerable asymmetrical deformation was observed. Then, the larger bubble continues rising in wobbling regime. Fig. 3.15b shows the time evolution of θ for different initial orientation angles, for $\theta|_{t=0} \gtrsim 30°$ bubbles tend to align with vertical axis before to start the coalescence process. Indeed, the impact angle increases as $\theta|_{t=0}$ is larger. For $\theta|_{t=0} = 15°$, the orientation angle tends to align with the side-by-side configuration (see Fig. 3.15b). From previous findings, it is argued that deformation of bubbles has a strong effect on its interaction. In fact, the vorticity is larger for ellipsoidal bubbles than for spherical bubbles, since the vorticity generated at the interface is proportional to the curvature [2, 9].

3.4.3 Multiple bubble interaction

The bubbly flow is not a fully developed flow regime because given enough time, the bubbles may collide each other, and their agglomeration could lead to form large bubbles or the so-called slug flow. Moreover, in most industrial applications, the bubble flow rate is high and the flow is often referred to as churn flow, where the coalescence and break-up is strong. In general, the hydrodynamic of bubbly flow is still far to be understood. One major problem is the lack of proper experimental techniques to probe the bubbles [37]. However, for relatively simple systems, DNS can help us to understand the complex bubble interactions on bubbly flows. For instance, [58] have employed a front-tracking/finite-volume method to conduct DNS of bubbly flows with nearly spherical and ellipsoidal bubbles rising in a vertical channel with upward and downward flows and characterized the void fraction distribution and the velocity profile. Following previous motivation, this section is devoted to test the capabilities of the CLS method to simulate the hydrodynamic interaction of multiple bubbles rising freely in an initially quiescent liquid. In experimental studies, the coalescence is prevented by the addition of salt to the liquid [35, 64]. On the other hand, numerical methods such as Front-Tracking [59] avoids the merging and break-up of interfaces by using a separate mesh for each bubble. In present simulations there is no such restriction and the bubble coalescence will be permitted.

The computational domain is specified as a circular channel bounded by rigid wall, as shown Fig. 3.18a. The size of the domain is $D_\Omega \times H_\Omega = 6.6d \times 13.3d$, and it is discretized by 13×10^6 hexahedral volumes (see Fig. 3.18b). Thus, the equivalent bubble diameter, d, is resolved by 30 mesh cells. Imposed boundary conditions are non-slip at the rigid wall and periodic on the streamwise (y-direction). In this way bubbles go out of the domain on the top side, and they come back in the domain again from the opposite side. A free bubble array of thirty bubbles is initially placed in the periodic column following a random pattern. This corresponds to a dilute bubbly flow, with an overall volumetric fraction of $\alpha = 3.45\%$.

Fig. 3.19 shows the evolution of bubbly flow for $Eo = 2.5$, $M = 5.9 \times 10^{-4}$, $\eta_\rho = 10$, $\eta_\mu = 10$ (nearly spherical shape regime). At the early stage, bubbles move upward through a basically stagnant liquid, and the rise trajectory of the bubbles hardly deviates from a straight line. Bubbles rise due the buoyancy force and each bubble forms its own wake, which affects the motion of the nearby bubbles. As the time advances, trailing bubbles are attracted by the wake of the leading bubbles and coalescence processes are observed. This in turn, influences the bubble size distribution, interfacial area and bubble induced liquid flow, as shown in Fig. 3.21 and Fig. 3.20. The strong wake interaction promotes bubble agglomeration and the collision between them increases the coalescence of small bubbles to form larger ones. From Fig. 3.19, it can be seen a major bubble concentration around the symmetry axis of
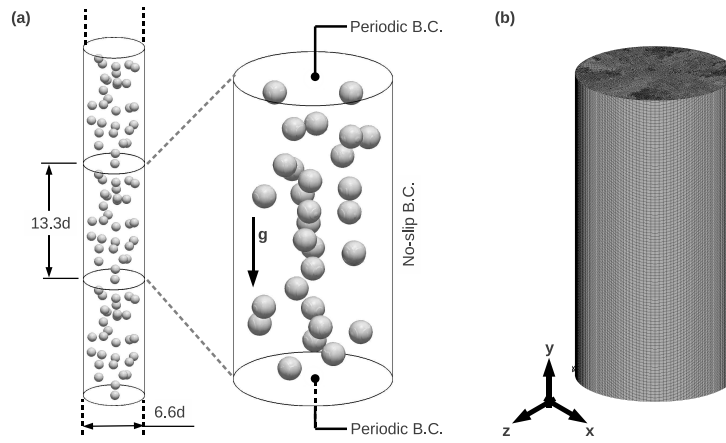
Figure 3.18: Computational setup for simulation of multiple bubbles rising in a periodic vertical duct. (a) Initial condition and Boundary conditions. (b) Mesh configuration.
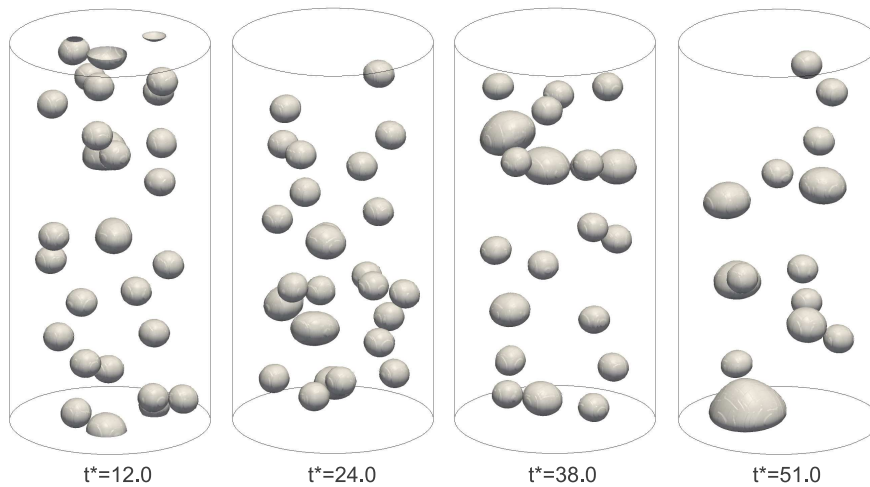

Figure 3.19: Bubble swarm in nearly spherical shape regime; $Eo = 2.25$, $M = 5.9 \times 10^{-4}$, $\eta_\rho = 10$, $\eta_\mu = 10$.
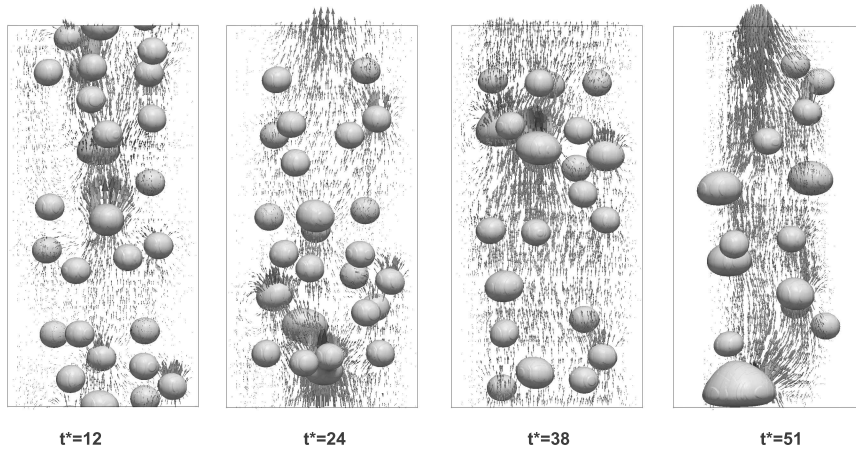
Figure 3.20: Bubble swarm in nearly spherical shape regime; $Eo = 2.25$, $M = 5.9 \times 10^{-4}$, $\eta_\rho = 10$, $\eta_\mu = 10$. Velocity field.
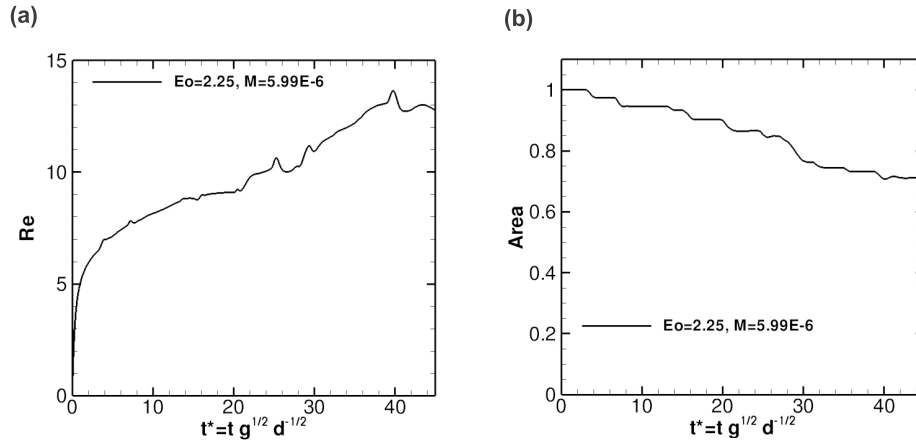

Figure 3.21: Figure (**a**) shows results of Reynolds number (Re) plotted versus time, with $Re(t) = \rho_1 d \mu_1^{-1} \int_\Omega \phi(\mathbf{x}, t) \mathbf{v} \cdot \mathbf{e}_y dV$. The effect of different bubble shape regime on the interfacial area was plotted in Figure (**b**), with $Area(t) = \int_\Omega ||\nabla \phi(\mathbf{x}, t)|| dV / \int_\Omega ||\nabla \phi(\mathbf{x}, 0)|| dV$

the circular duct, moreover the bubbles do not collide with the wall. Hydrodynamics and gravity start to interact on global scales, and specific patterns are identified in the liquid circulation: the liquid flows up in the center of the circular duct and down close to the wall, as shown in Fig. 3.20. In present simulations, the cluster of bubbles form a chimney, which can be clearly seen in Fig. 3.20. This type of cluster formation is known to be the basic foundation for the transition from bubbly to slug flow. The trend for the bubbles to move to the center of the domain is consistent with simulation results reported by [13] and [62].

3.5 Conclusions

In the present chapter, a conservative level-set method has been used to study the dynamics of single and multiple bubbles on a one-directional periodic domain. The numerical method offers a high degree of accuracy in prediction of terminal Reynolds numbers, drag coefficient and the bubble shape for a wide range of Eo and M numbers. The methodology described is also capable of predicting the hydrodynamic interaction of bubble pairs and bubble swarms. The numerical results showed that bubble shapes, Reynolds numbers and wake patterns predicted by the CLS method agree well with experimental and numerical findings reported in the literature. In addition, numerical results of bubble pair interactions are in good agreement with numerical results previously published by using other methodologies. For the conditions selected in this paper ($s = 1.5d$, $0° \leqslant \theta \leqslant 90°$), both repulsive and attractive interactions were observed for spherical and ellipsoidal bubbles, which are a function of the Reynolds number and the initial configuration angle. The performed simulation with multiple bubbles demonstrates that CLS method can be employed to deliver useful information on the dynamics of bubbly flow. To the best of the author's knowledge, the aforementioned 3D simulations of single and multiple bubbles using the CLS method are presented for the first time.

Acknowledgments

References

[1] Balcázar, N., Jofre, L., Lehmkhul, O., Castro, J., Rigola, J., 2014. A finite-volume/level-set method for simulating two-phase flows on unstructured grids. International Journal of Multiphase Flow 64, 55-72

[2] Batchelor, G.K., 1967. An introduction to Fluid Dynamics, Cambridge University Press.

[3] Baltussen, M.W.,Kuipers, J.A.M.,Deen, N.G., 2014. A critical comparison of surface tension models for the volume of fluid method, Chem. Eng. Sci., 109, 65-74.

[4] Bhaga, D., Weber, M.E., 1981. J. Fluid Mech. 105, 61-85.

[5] Bonometti, T., Magnaudet, J., 2007. An interface-capturing method for incompressible two-phase flows. Validation and application to bubble dynamics, J Fluid Mech 105, 61-85

[6] Brackbill, J.U., Kothe, D.B., Zemach, C., 1992. A Continuum Method for Modeling Surface Tension, J. Comput. Phys. 100, 335-354.

[7] Brereton, G., Korotney, D., Coaxial and Oblique Coalescence of Two Rising Bubbles, in Dynamics of bubbles and Vortices Near a Free Surface, vol. 119, ASME, New York, 1991

[8] Bunner, B., Tryggvason, G., 2002. Dynamics of homogeneous bubbly flows Part 1. Rise velocity and microstructure of the bubbles, J. Fluid Mech. 466, 17-52.

[9] Bunner, B., Tryggvason, G., 2003. Effect of bubble deformation on the properties of bubbly flows, J. Fluid Mech. 495, 77-118.

[10] Chakraborty, I., Biswas, G., Ghoshdastidar, P.S., A coupled level-set and volume-of-fluid method for the buoyant rise of gas bubbles in liquids, 2013. International Journal of Heat and Mass Transfer 58, 240-259.

[11] Chen, R.H., Tian, W.X., Su, G.H., Qiu, S.Z., Ishiwatari, Y., Oka, Y., 2011. Numerical investigation on a coalescence of bubble pairs, Chem. Eng. Sci. 66, 5055-5063.

[12] Chen, L., Li, Y., Manesh, R., 1998. The coalescence of bubbles - A numerical study, In: Third International Conference on Multiphase Flow, ICMF́98, Lyon, France.

[13] Cheng, M., Hua, J., Lou, J., Simulation of bubble-bubble interaction using a lattice Boltzmann method, 2010. Computers & Fluids. 39, 260-270.

References

[14] Chorin, A.J., Numerical solution of the Navier-Stokes equations. 1968. Math. Comput. 22, 745-762.

[15] Clift, R., Grace, J.R., Weber, M.E., Bubbles, Drops and Particles. Academin Press, New York, 1978.

[16] Deen, N.G., Van Sint Annaland, M., Kuipers, J.A.M. , 2009. Direct numerical simulation of complex multi-fluid flows using a combined front tracking and immersed boundary method, Chemical Engineering Science 64, 2186-2201.

[17] Duineveld, P.C., 1998. Bouncing and coalescence of bubble pairs rising at high Reynolds number in pure water or aqueous surfactant solutions, Appl. Sci. Res. 58, 409-439

[18] Esmaeeli, A., Tryggvason, G., 2005. A DNS study of the buoyant rise of bubbles at O(100) Reynolds number, Physics of Fluids 17, 093303.

[19] Felten, F.N., Lund, T.S., 2006. Kinetic energy conservation issues associated with the collocated mesh scheme for incompressible flow, J. Comput. Phys. 215, 465-484

[20] Gottlieb, S., Chi-Wang, S., 1998. Total Variation Dimishing Runge-Kutta Schemes, Mathematics of Computations 67, 73-85.

[21] Gupta, A., Kumar, R., 2008. Lattice Boltzmann simulation to study multiple bubble dynamics, International Journal of Heat and Mass Transfer 51, 5192-5203.

[22] Gueyffier, D., Li, J., Nadim, A., Scardovelli, R., Zaleski, S., 1999. Volume-of-fluid interface tracking with smoothed surface stress methods for three-dimensional flows, J. Comput. Phys. 152, 423-456.

[23] Hadamard, J.S., 1911. Mouvement permanent lent dâune sphere liquide et visqueuse dans un liquide visqueux, C. R. Acad. Sci. 152, 1735.

[24] Harmathy, T.Z., 1960. Velocity of large drops and bubbles in media of infinite or restricted extend, AIChE J. 6, 281-288.

[25] Hasan, N., Zakaria, Z. B., 2011. Computational approach for a pair of bubble coalescence process, International Journal of Heat and Fluid Flow 32, 755-761.

[26] Hallez, Y., Legendre, D., 2011. Interaction between two spherical bubbles rising in a viscous liquid, Journal of Fluid Mechanics 673, 406-431.

[27] Hnat, J.G., Buckmaster, J.D., 1976. Spherical cap bubbles and skirt formation, Phys. Fluids 19, 182-194

107

[28] Hua, J., Stene, J., Lin, P., 2008. Numerical simulation of 3D bubbles rising in viscous liquids using a front tracking method, J. Comput. Phys. 227, 3358-3382

[29] Joseph, D., 2003. Rise velocity of a spherical cap bubble, J. Fluid Mech. 488, 213-223

[30] Katz, J., Meneveau C., 1996. Wake induced relative motion of bubbles rising in line, Int. J. Multiphase Flow, 22 (2), 239-258.

[31] Lehmkuhl, O., Perez-Segarra, C.D., Soria, M., Oliva, A., 2007, A new Parallel unstructured CFD code for the simulation of turbulent industrial problems on low cost PC cluster, Proceedings of the Parallel CFD 2007 Conference, pp.1-8

[32] Legendre, D., Magnaudet, J., 2003. Hydrodynamic interactions between two spherical bubbles rising side by side in a viscous liquid, J. Fluid Mech. 497, 133-166

[33] Liu, H., Valocchi, A., 2012. Three-dimensional lattice Boltzmann model for immiscible two-phase flow simulations, Phys. Rev. E 85, 046309.

[34] Lu, J., Biswas, S., Tryggvason, G., 2006. A DNS study of laminar bubbly flows in a vertical channel, Int. J.Multiphase Flow 32, 643-660

[35] Martínez-Mercado, J., Palacios-Morales, C.A., Zenit, R., 2007. Measurement of pseudoturbulence intensity in monodispersed bubbly liquids for $10 < Re < 500$, Physics of fluids 19, 103302.

[36] Ming, C., Jingong, H., Jing, L., 2010. Simulation of bubble-bubble interaction using a lattice Boltzmann method, Computers & Fluids 19, 260-270.

[37] Mudde, R., 2005. Gravity-Driven bubbly flows, Annu. Rev. Fluid Mech. 37, 393-423.

[38] Mukundakrishnan, K., Quan, S., Eckmann, D.M., Ayyaswamy, P.S., 2007. Numerical study of wall effects on buoyant gas-bubble rise in a liquid-filled finite cylinder, Phys. Rev. E. 76, 036308-01â036308-15.

[39] Olsson, E., Kreiss, G., 2005. A conservative level set method for two phase flow, J. Comput. Phys. 210, 225-246.

[40] Olsson, E., Kreiss, G., 2007. A conservative level set method for two phase flow II, J. Comput. Phys. 225, 785-807.

[41] Osher, S., Sethian, J.A., 1988. Fronts propagating with curvature-dependent speed: Algorithms based on Hamilton-Jacobi formulations, J. Comput. Phys. 79, 175-210.

References

[42] Ohta, M., Yamaguchi, S., Yoshida, Y., Sussman, M., 2010. The sensitivity of drop motion due to the density and viscosity ratio, Physics of fluids 22, 072102.

[43] Ohta, M., Sussman, M., 2012. The buoyancy-driven motion of a single skirted bubble or drop rising through a viscous liquid, Physics of fluids 24, 112101.

[44] Pivello, M.R., Villar, M.M., Serfaty, R., Roma, A.M., Silveira-Neto, A., 2014. A fully adaptive front tracking method for the simulation of two phase flows, Int. J. Multiph. Flow 58, 72-82.

[45] Pournader, O., Mortazavi, S., 2013. Three dimensional interaction of two drops driven by buoyancy, Computers & Fluids 88, 543-556.

[46] Rhie, C.M., Chow, W.L., 1983. Numerical Study of the Turbulent Flow past an Airfoil with Trailing Edge Separation, AIAA J. 21, 1525-1532.

[47] Rodrigue, D., 2001. Generalized correlation for bubble motion, AIChE Journal. 47, 39-44.

[48] Rodríguez, I., Borrell, R., Lehmkuhl, O., Pérez-Segarra, C.D., Oliva, A., 2011. Direct numerical simulation of the flow over a sphere at Re = 3700, J. Fluids Mech. 679, 263â287.

[49] Ryskin, G., Leal, L.G., 1984. Numerical solution of free-boundary problems in fluid mechanics. Part 2. Buoyancy-driven motion of a gas bubble through a quiescent liquid, J. Fluids Mech. 148, 19-35.

[50] Rybczynski, W., 1911. Uber die fortschreitende bewegung einer flssigen kugel in einem zhen medium. Bull. Acad. Sci. Cracovi, Ser. A 40

[51] Sanada, T., Sato, A., Shirota, M., Watanabe, M., 2009. Motion and coalescence of a pair of bubbles rising side by side, Chem. Eng. Sci. 64, 2659-2671.

[52] Smolianski, A., Haario, H., Luukka, P., 2008. Numerical study of dynamics of single bubbles and bubble swarms, Appl. Math. Model. 32, 641-659.

[53] Sussman, M., Smereka, P., Osher, S., 1994. A Level Set Approach for Computing Solutions to Incompressible Two-Phase Flow, J. Comput. Phys. 144, 146-159.

[54] Stewart, C.W., 1995. Bubble Interaction in Low-Viscosity Liquids, Int. J. Multiphase Flow 21, 1037-1046.

[55] Sweby, P.K., 1984. High Resolution Using Flux Limiters for Hyperbolic Conservation Laws, SIAM Journal on Numerical Analysis 21, 995-1011.

[56] Takemura, F., Magnaudet, J., 2003. The transverse force on clean and contaminated bubbles rising near a vertical wall at moderate Reynolds number, Journal of Fluid Mechanics 495, 235-253.

[57] Trias, F.X., Lehmkuhl, O., 2011. A Self-Adaptive Strategy for the Time Integration of Navier-Stokes Equations. Numerical Heat Transfer, Part B 60, 116-134.

[58] Tryggvason, G., Dabiri, S., Abouhasanzadeh, B., Jaicai, L., 2013. Multiscale considerations in direct numerical simulations of multiphase flows, Phys. Fluids 25, 031302.

[59] Tryggvason, G., Bunner, B., Esmaeeli, A., Juric, D., Al-Rawahi, N., Tauber, W., Han, J., Nas, S., Jan, Y-J., 2001. A Front-Tracking Method for the Computations of Multiphase Flow, J. Comput. Phys. 169, 708-759.

[60] Unverdi, S., Tryggvason, G., 1992. A front-tracking method for viscous, incompressible, multifluid flows, J. Comput. Phys. 100, 25-37.

[61] Van Sint Annaland, M., Deen, N.G., Kuipers, J.A.M., 2005. Numerical Simulation of gas bubbles behaviour using a three-dimensional volume-of-fluid method, Chemical Engineering Science 60, 2999-3011.

[62] Yu, Z., Yang, H., Fan, L., 2011. Numerical simulation of bubble interactions using adaptive lattice Boltzmann method, Chem. Eng. Sci. 66, 3441-3451.

[63] Yue, P., Feng, J.J., Bertelo, C.A., Hu, H.H., 2007. An arbitrary Lagrangian-Eulerian method for simulating bubble growth in polymer foaming, J. Comput. Phys. 226, 2229-2249.

[64] Zenit, R., Koch D.L., Sangani, A.S., 2001. Measurements of the average properties of a suspension of bubbles rising in a vertical channel, J. Fluid Mech. 429, 307-342

Chapter 4

A coupled volume-of-fluid/level-set method for simulation of surface-tension driven interfacial flows

Abstract.   This chapter presents a methodology for interface capturing in two-phase flows by combining volume-of-fluid with level-set methods. While the volume-of-fluid transport relies on a robust and accurate polyhedral library for interface capturing, geometrical properties of interface (curvature) are calculated by using a level-set function, which is reconstructed through an iterative geometrical procedure. The method is validated on 2D and 3D test cases. Conservation properties are shown to be excellent, while geometrical accuracy remains satisfactory even for the most complex flows.

4.1   Introduction

The accurate modelling of two-phase flows is vital for many engineering and scientific applications, such as combustion process, boilers, bubbly flow, fuel cells, unit operations in chemical engineering, cooling of nuclear reactors among others. Accurately modeling of interfacial flows is challenging because of the discontinuity in material properties such as density and viscosity, and because of the interface boundary conditions. For this kind of flows it is vital to accurately compute interfacial quantities such as curvature and normal vectors because they are used to evaluate the surface tension. Errors in the calculated surface tension force will induce nonphysical velocities, commonly known as spurious or parasitic currents [26]. These velocities can grow with time and so significantly degrade simulation results. In particular, it is important that the predicted interface topologies are not numerical artifacts arising from errors in modelling interface evolution [26].

Due the complexity of two-phase flows from a numerical and physical point view, a lot of numerical methods have been developed for interface capturing in the past decades. For instance: the front tracking (FT) method [43, 42], level set (LS) methods [24, 39, 23, 1], volume-of-fluid (VOF) methods [12, 17, 18], and hybrid methods such as CLSVOF [40] and VOSET [38]. In these methods, two-phase flow is treated as a single flow with the density and viscosity varying smoothly across the moving interface which is captured in an Eulerian framework (VOF, LS, CLSVOF, VOSET) or in a Lagrangian framework (FT). Although the idea behind these methods is similar, their numerical implementation may differ greatly. A review of advantage and disadvantages of the aforementioned techniques, in the context of simulation of multiphase flows with sharp interfaces is given in [17]. In the front-tracking method [43, 42], a stationary Eulerian grid is used for the fluid flow and the interface is tracked explicitly by a separate Lagrangian grid. his method is extremely accurate but also rather complex to implement due to the fact that dynamic re-meshing of the Lagrangian interface mesh is required [8]. Contrary to LS and VOF method, automatic merging of interfaces does not occur, and difficulties arise when multiple interfaces interact with each other as in coalescence and break-up. In the VOF method [12, 17, 18], the interface is given implicitly by a color function, defined to be the fraction of volume within each cell of one of the fluids. In order to advect the VOF function, the interface needs to be reconstructed using a geometric technique. An advantage of VOF method is the fact that accurate algorithms [18] can be used to advect the interface, so that the mass is conserving while still maintaining a sharp representation of the interfaces [40]. However a disadvantage of the VOF method is the fact that it is difficult to compute accurate curvatures from the volume fraction function used to represent the interface, which presents a step discontinuity. In level-set methods [24, 39] the interface is represented by the zero-contour of a signed distance function. The evolution of this function in space and time is governed by

an advection equation, combined with a special re-distancing algorithm. One of the advantage of the level-set approach is the fact that the interface curvature can be computed accurately. A disadvantage of this method, is that the discrete solution of transport equations is prone to numerical error and leads to loss or gain of mass.

On the basis of the aforementioned analysis of VOF and LS methods, it can be found that they have complementary advantages and disadvantages, so it is an inevitable trend to develop new methods combining VOF and LS approaches [40, 38]. In the present coupled VOF/LS method an accurate VOF method introduced by [18] is used to advect the interface, while the interface curvature used to evaluate the surface tension force is computed from a reconstructed level-set function. A signed distance function is reconstructed from the geometrical information (planes) provided by the VOF method, using an iterative geometrical procedure. A classical fractional step method [5] is used to solve incompressible Navier-Stokes equations that are coupled to a transport equation for the marker function (e.g. level-set or color function); whereas the effect of surface tension is modeled according to the continuum surface force approach (CSF) introduced by [3]. The Navier-Stokes equations have been discretized using a finite-volume approach on a collocated unstructured grid, according to the work of [1].

The outline of this chapter is as follows: A summary of the governing equations and numerical methods is given in Section 4.2. In Section 4.3 numerical experiments are presented in order to validate the surface tension methods here proposed. The experiments are simulation of two-dimensional drop test case introduced by [13, 14], three-dimensional buoyant bubble, deformation of a drop under shear flow and coalescence of two bubbles. The conclusions are given in Section 5.5.

4.2 Governing equations and discretization

4.2.1 Incompressible two-phase flow

The Navier-Stokes equations for incompressible, Newtonian and two-phase flows can be combined into a set of equations in a spatial domain Ω [1], with a singular source term for the surface tension force at the interface Γ [25, 3, 6]:

$$\frac{\partial}{\partial t}(\rho \mathbf{v}) + \nabla \cdot (\rho \mathbf{v} \mathbf{v}) = -\nabla p + \nabla \cdot \mu \left(\nabla \mathbf{v} + (\nabla \mathbf{v})^T \right) + \rho \mathbf{g} + \sigma \kappa \mathbf{n} \delta_\Gamma \qquad (4.1)$$

where $\mathbf{v}$ and p denote the fluid velocity field and pressure, ρ is the fluid density, μ is the dynamic viscosity, $\mathbf{g}$ is the gravitational acceleration and the super-index T represents the transpose operator. δ_Γ is a Dirac delta function concentrated at the interface Γ, σ is the surface tension coefficient, κ is the curvature of the interface and $\mathbf{n}$ denotes the unit normal vector on the interface. Because of incompressibility, the

velocity field is divergence-free:

$$\nabla \cdot \mathbf{v} = 0 \tag{4.2}$$

Physical properties change discontinuously across the interface:

$$\rho = \rho_1 H_1 + \rho_2 (1 - H_1) \tag{4.3}$$
$$\mu = \mu_1 H_1 + \mu_2 (1 - H_1)$$

with ρ_1, ρ_2 and μ_1, μ_2 the densities and viscosities of the first and second fluids, respectively. H_1 is the Heaviside step function that is one at fluid 1 and zero elsewhere.

4.2.2 Volume-of-fluid method

In the volume-of-fluid method an indicator function f is used to track the interface,

$$f(\mathbf{x}, t) = \begin{cases} 0 & \text{if } \mathbf{x} \in \Omega_1 \\ 1 & \text{if } \mathbf{x} \in \Omega_2 \end{cases} \tag{4.4}$$

with Ω_1 and Ω_2 the sub-domains occupied by the fluid 1 and 2 respectively. Discretely, the information effectively stored at the cell Ω_P is the volume-averaged indicator function, namely the volume fraction:

$$f_P = \frac{\int_{\Omega_P} f(\mathbf{x}, t) dV}{\int_{\Omega_P} dV} \tag{4.5}$$

where V is the volume of the cell Ω_P. The advection equation for f is given by:

$$\frac{\partial f}{\partial t} + \mathbf{v} \cdot \nabla f = 0 \tag{4.6}$$

where $\mathbf{v}$ is the fluid velocity.

Following the work of [18], Eq. (4.6) is solved in two steps: first a geometric interface reconstruction is used to calculate the volumetric fluxes of one of the fluids across mesh cell faces, and second an advection step based on the reconstructed interface is performed by means of a first order Euler explicit scheme. The method here used reconstructs interfaces using piecewise planar approximations (PLIC). Therefore, a plane Π is defined for each cell

$$\mathbf{e}_\Pi \cdot \mathbf{x}_\Pi - d_\Pi = 0 \tag{4.7}$$

Here $\mathbf{x}_\Pi$ is any position vector on the plane Π, d_Π is determined such that the truncation between cell and plane satisfies a restriction for volume conservation [18], and $\mathbf{e}_\Pi$ is the plane normal computed according to the Youngs interface reconstruction

method [36, 18], hence, $\mathbf{e}_\Pi = -\nabla f/||\nabla f||$ for each cell, with the gradient ∇f evaluated by means of the least-squares approach [11, 18, 1]. Volumes are advected in a single unsplit Lagrangian-Eulerian (LE) geometrical algorithm based on constructing flux polyhedrons by tracing back the Lagrangian trajectories of the cell-vertex velocities [18]. The reader is referred to [18] for technical details of the above mentioned technique. The volume-of-fluid method used in this work has been implemented by [18] in the framework of a parallel C++ code called TermoFluids [21], which is used for programming the new algorithms deployed in the present VOF/LS method.

4.2.3   Combined VOF-LS method

The main idea is to benefit from the advantage of each strategy, which is to minimize mass loss through the accurate VOF method introduced in [18] and to keep a fine description of the interface curvature using a level-set function. With the geometrical information of the interface given by the VOF method, a signed distance function is reconstructed following an iterative geometric algorithm presented in Section 4.2.4.

4.2.4   Signed distance function construction

The algorithm to compute the signed distance function can be summarized as follows:

1. The signed distance function, $d(\mathbf{x}_P, t)$, is initialized at each mesh cell P as follows:

$$d(\mathbf{x}_P, t) = \begin{cases} d_{max} \text{ if } f(\mathbf{x}_P, t) \geq 0.5 \\ -d_{max} \text{ otherwise} \end{cases} \tag{4.8}$$

   where $f(\mathbf{x}_P, t)$ is the VOF function defined in Eq. 4.5, and d_{max} is the maximum geometrical size of the space domain.

2. In order to save computational time, only a set of cells near the interface are flagged to compute the distance function. This flagged zone is formed by the cells in a region of $\Delta_\Gamma = 3h$ width from the interface, as shown in Fig. 4.1. Here $h = V_{cell}^{1/3}$ represents the cell size and V_{cell} is the cell volume.

3. The shortest distance $|d(\mathbf{x}, t)|$ is computed in the flagged region created in step 4, following the algorithm explained in section 4.2.5. For the sake of clarity, a two-dimensional example is illustrated in Fig. 4.2.

4. The signed distance function is computed as follows:

$$d(\mathbf{x}_P, 0) = \begin{cases} |d(\mathbf{x}_P, t)| \text{ if } f(\mathbf{x}_P, t) \leqslant 0.5 \\ -|d(\mathbf{x}_P, t)| \text{ otherwise} \end{cases} \tag{4.9}$$

115

4.2.5   Minimum distance from a cell-centroid to an interface-plane Π

This procedure is applicable to compute the minimum distance from a cell-centroid $\mathbf{x}_P$ to an interface-plane Π limited by a convex polygon which contains the coplanar points $\mathbf{x}_1, ..., \mathbf{x}_i, \mathbf{x}_{i+1}, ..., \mathbf{x}_n$, as shown in Fig. 4.4 where $n = 5$. Following the example illustrated in Fig. 4.4, the algorithm is summarized as follows:

1. A set of planes Π_{i-j} is defined, such that Π_{i-j} is perpendicular to the interface-plane Π. In addition, $\Pi_{i,j}$ contains a pair of coplanar points $(\mathbf{x}_i, \mathbf{x}_j)$ for $(i,j) = (1,2), ..., (n-1,n), (n,1)$, as shown in Fig. 4.4a, where $n = 5$. If the next inequality is true for all the subindex (i,j)

$$((\mathbf{x}_n - \mathbf{x}_P) \times (\mathbf{x}_1 - \mathbf{x}_P)) \cdot ((\mathbf{x}_i - \mathbf{x}_P) \times (\mathbf{x}_j - \mathbf{x}_P)) \geqslant 0 \qquad (4.10)$$

   then $\mathbf{x}_P$ is contained inside the region enclosed by the planes $\Pi_{1-2}, .., \Pi_{n-1}$ (see Fig. 4.4a). Thus, the shortest distance from $\mathbf{x}_P$ to the interface-plane Π is calculated as follows:

$$|d(\mathbf{x}_P, t)| = |(\mathbf{x}_P - \mathbf{x}_\Pi) \cdot \mathbf{e}_\Pi| \qquad (4.11)$$

   and the algorithm finished, otherwise it continues to the step 3. Here, $\mathbf{e}_\Pi$ is a unit vector perpendicular to the plane Π, while $\mathbf{x}_\Pi = (1/n) \sum_{i=1}^n \mathbf{x}_i$ is a point contained in the plane Π.

2. A new set of planes $\Lambda_{i-j,k}$ is defined, such that $\Lambda_{i-j,k}$ is perpendicular to the interface-plane Π, $\Lambda_{i-j,k}$ is perpendicular to the vector $\Delta\mathbf{x}_{i,j} = \mathbf{x}_i - \mathbf{x}_j$ with $(i,j) = \{(1,2), (2,3), ..., (n,1)\}$, and $\Lambda_{i-j,k}$ contains a point $\mathbf{x}_k$ for $k = \{i, j\}$, as shown in Fig. 4.4b. If the next constraint is true

$$0 \leq \frac{(\mathbf{x}_P - \mathbf{x}_i) \cdot (\mathbf{x}_j - \mathbf{x}_i)}{||\mathbf{x}_j - \mathbf{x}_i||} \leq 1 \qquad (4.12)$$

   then $\mathbf{x}_P$ is contained in the region enclosed by the planes $\Pi_{i,j}$, $\Lambda_{i-j,i}$ and $\Lambda_{i-j,j}$, as shown in Fig. 4.4b. In this case the minimum distance is given by

$$|d(\mathbf{x}_P, t)| = \left|\left|(\mathbf{x}_P - \mathbf{x}_i) - \frac{\mathbf{x}_j - \mathbf{x}_i}{||\mathbf{x}_j - \mathbf{x}_i||}\left((\mathbf{x}_P - \mathbf{x}_i) \cdot \left(\frac{\mathbf{x}_j - \mathbf{x}_i}{||\mathbf{x}_j - \mathbf{x}_i||}\right)\right)\right|\right| \qquad (4.13)$$

   and the algorithm finished, otherwise it continues to the step 4.

3. In this case the minimum distance is given by

$$|d(\mathbf{x}_P, t)| = min\{||\mathbf{x}_P - \mathbf{x}_1||, ..., ||\mathbf{x}_P - \mathbf{x}_n||\} \qquad (4.14)$$
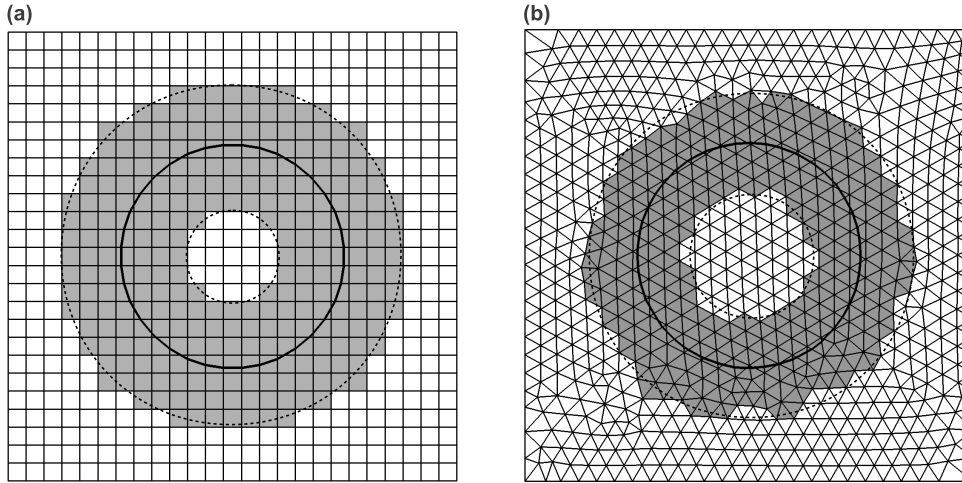
   as shown in Fig. 4.4c, where $n = 5$.

(a)

(b)

Figure 4.1: Examples of two-dimensional flagged region near the interface. (a) Cartesian mesh (b) Triangular mesh

Π_6

Π_5

Π_4

Π_3
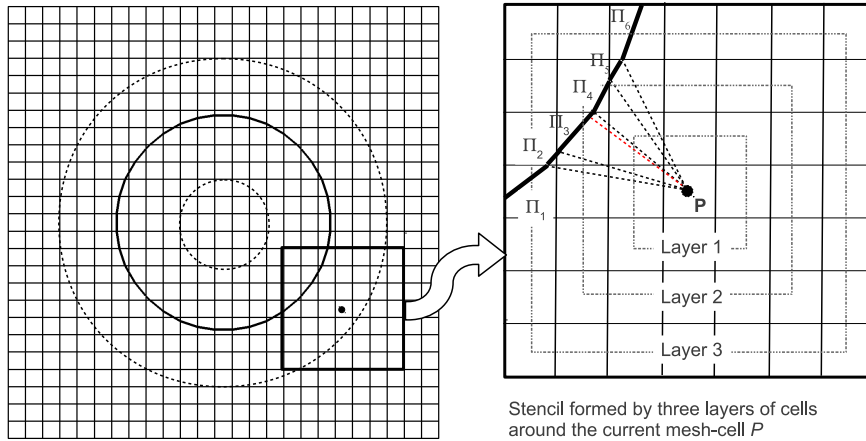
Π_2

Π_1

P

Layer 1

Layer 2

Layer 3

Stencil formed by three layers of cells around the current mesh-cell *P*

Figure 4.2: In this figure, $d(\mathbf{x}_P, t) = min\{d^{min}_{P \to \Pi_1}, ..., d^{min}_{P \to \Pi_i}, ..., d^{min}_{P \to \Pi_n}\}$, where $d^{min}_{P \to \Pi_i}$ is the minimum distance from $\mathbf{x}_P$ to the plane Π_i and $\mathbf{x}_P$ is the centroid of the cell P. The red line indicates the shortest line segment from $\mathbf{x}_P$ to $\{\Pi_1, ..., \Pi_n\}$ contained in the stencil of three layers around the cell P.
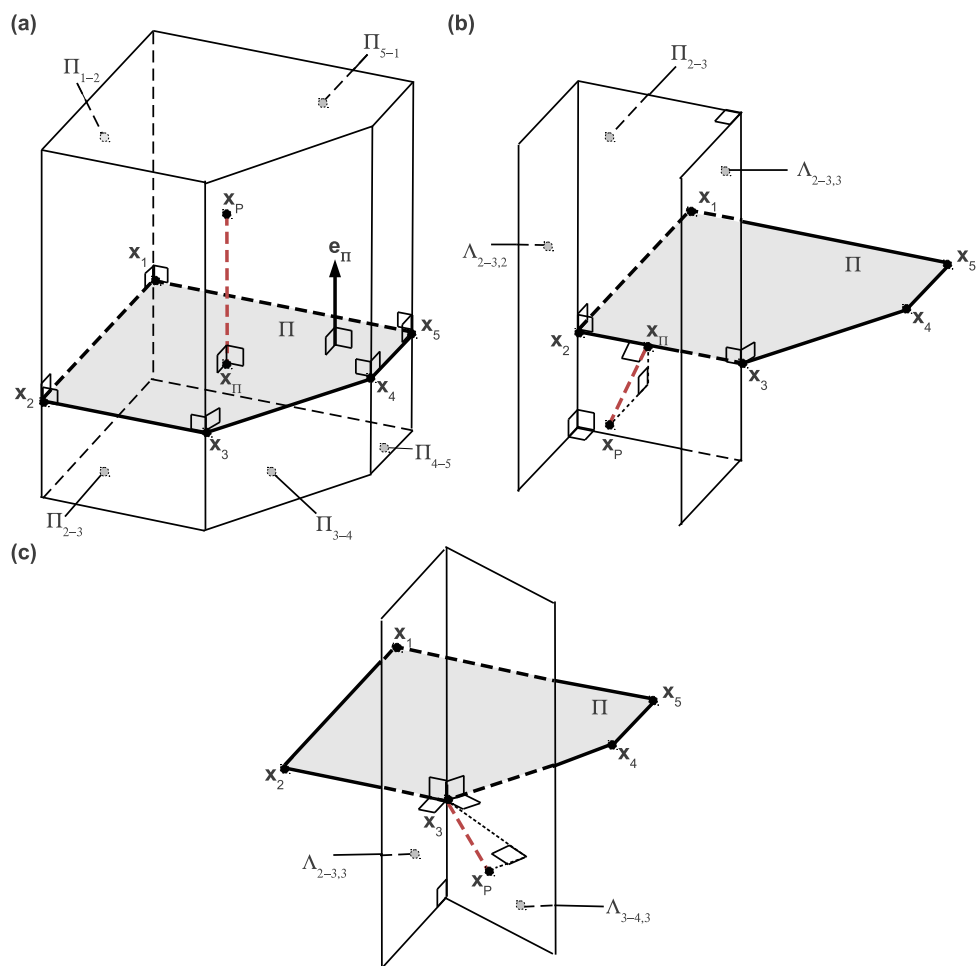
Figure 4.3: Minimum distance from $\mathbf{x}_P$ to the plane Π_i, in a three-dimensional framework.

4.2.6 Assessment of the distance function construction

In this section the accuracy of the distance function constructed by the algorithm introduced in Section 4.2.4 is measured. The distance function error E_2 is defined as

$$E_2 = \left(\frac{1}{n_{cells}} \sum_{P=1}^{n_{cells}} \left(d_P - d_P^{exact} \right)^2 \right)^{1/2} \tag{4.15}$$

where n_{cells} is the number of cells contained in a flagged zone of $3h$ width around the interface. Two test cases have been carried out to perform the construction of the signed distance function around a cylindrical bubble and a spherical bubble of diameters $d_b = 0.5$. The bubbles are centered in a square domain $2d_b \times 2d_b$ and a cubic domain $2d_b \times 2d_b \times 2d_b$, respectively. Fig. 4.4 shows a convergence of first order for the algorithm given in section 4.2.4, in both cases. Fig. 4.5 illustrates the signed distance function for a single cylindrical bubble and multiple bubbles, which is calculated by the aforementioned geometrical algorithm. In Fig. 4.5 the black lines denotes the interfaces and the colour lines the signed distance function. Thus, from Fig. 4.5 it is demonstrated that the presented algorithm is robust enough to compute $d(\mathbf{x}, t)$ even in presence of multiple interfaces.

4.2.7 Evaluation of the surface tension force

Surface tension force is computed through the level-set function given by the geometric algorithm presented in Section 4.2.4. Implementing surface tension in a numerical scheme leads to two problems: first the curvature κ has to be accurately computed, and second the pressure jump has to be appropriately applied on the interface through the delta function δ_Γ. Because a finite-volume discretization of the governing equations will be employed [1], the surface tension force in Eq. 4.1 can be conveniently calculated according to the continuum surface force model (CSF) introduced by [3]. In the CSF algorithm, surface tension forces are computed as a body force,

$$\sigma \kappa \mathbf{n} \delta_\Gamma = \sigma \kappa \nabla \phi \tag{4.16}$$

where $\mathbf{n}\delta_\Gamma$ has been approximated by the gradient of the Fermi-Dirac function ϕ

$$\phi = \frac{1}{1 + e^{d(\mathbf{x},t)/\varepsilon}} \tag{4.17}$$

with $\varepsilon = Ch$ a parameter that controls the number of cells over which the delta function is regularized. The aforementioned function ϕ has been employed in conservative level-set formulations [23, 44, 1]. In standard level-set methods [39] as the presented in Section A.1, the CSF model takes the form

$$\sigma \kappa \mathbf{n} \delta_\Gamma = \sigma \kappa \delta_\varepsilon \nabla d \tag{4.18}$$
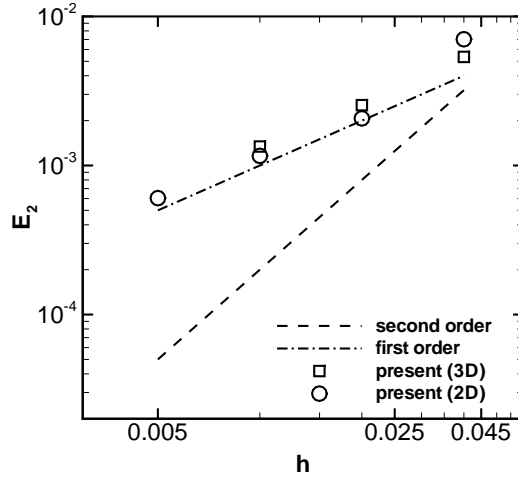
119

Figure 4.4: Error in distance function computation. (a) Circle of diameter $d_b = 0.5$ centered in a unit square domain (isometric cartesian mesh). (b) Sphere of diameter $d_b = 0.5$ centered in a unit cubic domain (isometric cartesian mesh).
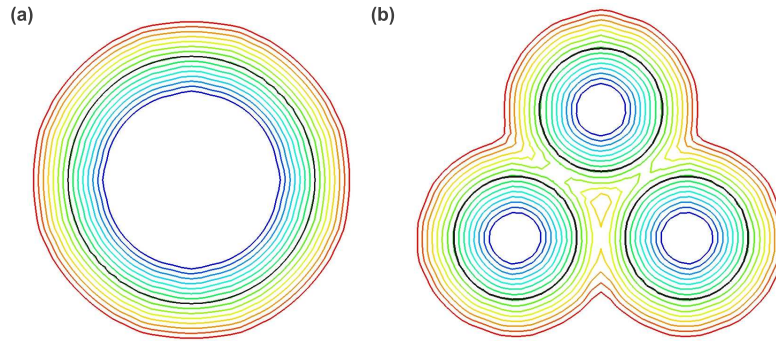

Figure 4.5: Examples of signed distance function construction. The black line indicates the interface position while the colour lines represents the contours of the signed distance function. (a) Cylindrical bubble of diameter $d_b = 0.5$ centered in a unit square domain, with $h = d_b/25$ (isometric cartesian mesh). (b) Multiple cylindrical bubbles of diameter $d_b = 0.25$ in a unit square domain, with $h = d_b/25$ (isometric cartesian mesh).

where the delta function δ_ε is given by

$$\delta_\varepsilon^{cos}(d(\mathbf{x},t)) = \begin{cases} \frac{1}{2\varepsilon}\left(1 + cos\left(\frac{\pi d(\mathbf{x},t)}{\varepsilon}\right)\right) & \text{if } |d(\mathbf{x}_P,t)| \leqslant \varepsilon \\ 0 \text{ otherwise} \end{cases} \tag{4.19}$$

with $\varepsilon = 1.5h$ [39]. In this work, surface tension force will be computed by using Eq. 4.16 with $\varepsilon = 0.5h$, unless otherwise stated. From the level-set function, $d(\mathbf{x},t)$, the curvature κ is obtained by the following equation

$$\kappa = \nabla \cdot \mathbf{n} \tag{4.20}$$

with the interface normal vectors, $\mathbf{n}$, given by

$$\mathbf{n} = \left(\frac{\nabla d}{||\nabla d||}\right) \tag{4.21}$$

Here ∇d is calculated by using the least-squares method [19, 1]. The reader is referred to [1] (or Chapter 2) for details on the finite-volume discretization of Eq. 4.20, and the application of the least squares method for gradient evaluation.

4.2.8   Regularization of the physical properties

Physical properties in Eqs. 4.3 can be regularized by taking $H_1 = \psi$,

$$\rho = \rho_1\psi + \rho_2(1 - \psi) \tag{4.22}$$
$$\mu = \mu_1\psi + \mu_2(1 - \psi)$$

where $\psi = \{f, \phi, H_\varepsilon\}$, f is the VOF function presented in Eq. 4.5, ϕ is the Fermi-Dirac function defined in Eq. 4.17 [23, 44, 1], and H_ε is a smoothed Heaviside function introduced in standard level-set formulations [39]

$$H_\varepsilon(d(\mathbf{x},t)) = \begin{cases} 0 \text{ if } d(\mathbf{x},t) < -\varepsilon \\ \frac{1}{2}\left(1 + \frac{d(\mathbf{x},t)}{\varepsilon} - \frac{1}{\pi}sin\left(\frac{\pi d(\mathbf{x},t)}{\varepsilon}\right)\right) & \text{if } |d(\mathbf{x}_P,t)| \leqslant \varepsilon \\ 1 \text{ if } d(\mathbf{x},t) > \varepsilon \end{cases} \tag{4.23}$$

For the present VOF/LS formulation, physical properties will be regularized by using $\psi = f$, unless otherwise stated.

4.2.9   Solution procedure for the coupled VOF/LS method

The Navier-Stokes equations (Eqs. 4.1) have been discretized by using the finite-volume approach on a collocated unstructured grid, according to [1] (or Chapter 2).

In the aforementioned work the velocity-pressure coupling is solved by means of a classical fractional step projection method [5, 35]. The reader is referred to [1] (or Chapter 2) for technical details on the spatial discretization and temporal discretization of the Navier-Stokes equations on collocated unstructured grids. The solution procedure used in this work is summarized as follows:

1. Initialize $\mathbf{v}(\mathbf{x}_P, 0)$, $f(\mathbf{x}_P, 0)$, $d(\mathbf{x}_P, 0)$, physical properties and interface geometric properties.

2. The time increment Δt, which is limited by the CFL conditions and the stability condition for the capillary force [3], is calculated by

$$\Delta t = C_{\Delta t} min \left(\frac{h}{||\mathbf{v}||}, \frac{\rho h^2}{\mu}, \left(\frac{h}{||\mathbf{g}||} \right)^{1/2}, h^{3/2} \left(\frac{\rho_1 + \rho_2}{4\pi\sigma} \right)^{1/2} \right) \quad (4.24)$$

   where $C_{\Delta t} = 0.005$ for the current VOF/LS method.

3. The interface is advected by using the volume-of fluid method introduced by [18] (see Section 4.2.2).

4. The signed distance function $d(\mathbf{x}, t)$ is calculated by the geometric algorithm given in Section 4.2.4.

5. The curvature is computed by using the Eq. 4.20.

6. Physical properties (ρ, μ) are updated by using the Eq. 4.22.

7. An intermediate velocity $\mathbf{v}^*$ is evaluated by

$$\frac{\rho\mathbf{v}^* - \rho\mathbf{v}^n}{\Delta t} = -\frac{3}{2}\mathbf{A}_h(\rho\mathbf{v}^n) + \frac{1}{2}\mathbf{A}_h(\rho\mathbf{v}^{n-1}) + \mathbf{D}_h(\mathbf{v}^n) + \rho\mathbf{g} + \sigma\kappa\nabla_h(\phi) \quad (4.25)$$

   where ∇_h represents the gradient operator, $D_h(\mathbf{v}) = \nabla_h \cdot \mu \left(\nabla_h \mathbf{v} + \nabla_h^T \mathbf{v} \right)$ represents the diffusion operator, and $\mathbf{A}_h(\rho\mathbf{v}) = \nabla_h \cdot (\rho\mathbf{v}\mathbf{v})$ is the convective operator.

8. The pressure field p is computed by the Poisson equation

$$\nabla_h \cdot \left(\frac{1}{\rho}\nabla_h(p^{n+1}) \right) = \frac{1}{\Delta t}\nabla_h \cdot (\mathbf{v}^*) \quad (4.26)$$

   Discretization of Eq. 4.26 leads to a linear system, which is solved by using a preconditioned conjugate gradient method.

9. The resulting velocity $\mathbf{v}^*$ from Eq. (4.25), does not satisfy the continuity Eq. (4.2). Therefore it is corrected by

$$\mathbf{v}^{n+1} = \mathbf{v}^* - \frac{\Delta t}{\rho} \nabla_h(p^{n+1}) \tag{4.27}$$

10. In order to avoid pressure-velocity decoupling when the pressure projection is made on collocated meshes [37, 33], a cell face velocity $\mathbf{v}_f$ is calculated so that $\nabla_h \cdot \mathbf{v} = 0$ (see Eq. 4.2) at each control volume. Namely in discretized form:

$$\mathbf{v}_f = \sum_{q \in \{P,F\}} \frac{1}{2} \left(\mathbf{v}_q^{n+1} + \frac{\Delta t}{\rho(\phi_q^n)} (\nabla_h p^{n+1})_q \right) - \frac{\Delta t}{\rho_f} (\nabla_h p^{n+1})_f \tag{4.28}$$

where P and F are denoting the adjacent cell nodes to the face f.

11. Repeat steps 2-10 until time step required.

As in previous chapters, the described numerical methods were implemented in the in-house C++ code TermoFluids [21].

4.3 Results and discussion

4.3.1 Static drop

The first test case is the verification of the stationary Laplace solution for a circular droplet with diameter d_{drop}. In the absence of viscous, gravitational or external forces, the circular interface with surface tension should remain at rest with the pressure jump at the interface exactly balancing the surface tension force (Laplace's law):

$$\Delta P_{exact} = \sigma \kappa_{exact} \tag{4.29}$$

where, the exact curvature is given by $\kappa_{exact} = 2/d_{drop}$ for a circular drop. The correct solution is a zero velocity field and a pressure field that rises from a constant value of $p_{out} = p_0$ outside the drop to a value $p_{in} = p_0 + 2\sigma/d_{drop}$ inside the droplet. However, at a discretized level, the accurate calculation of the curvature and the balance between the surface tension and pressure jump are not trivial problems, and, as a result spurious currents arise.

The computational domain considered is a square having side lengths of $2d_{drop}$ units, where $d_{drop} = 0.5$ is the diameter of a bubble positioned at the center of the domain. The coefficient of surface tension, and the viscosity inside and also outside
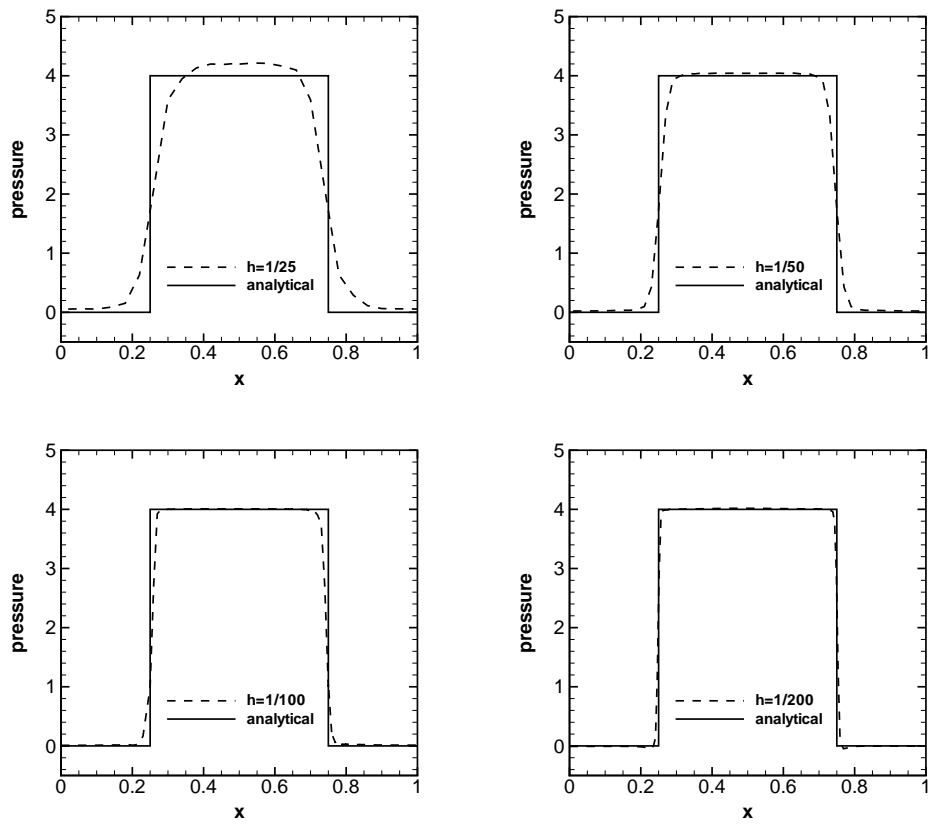
123

Figure 4.6: Pressure profiles at the cross section of $y = 0.5$ for $t = 50$. The solid line indicates the exact Young-Laplace pressure $\Delta p = 2\sigma/d$.
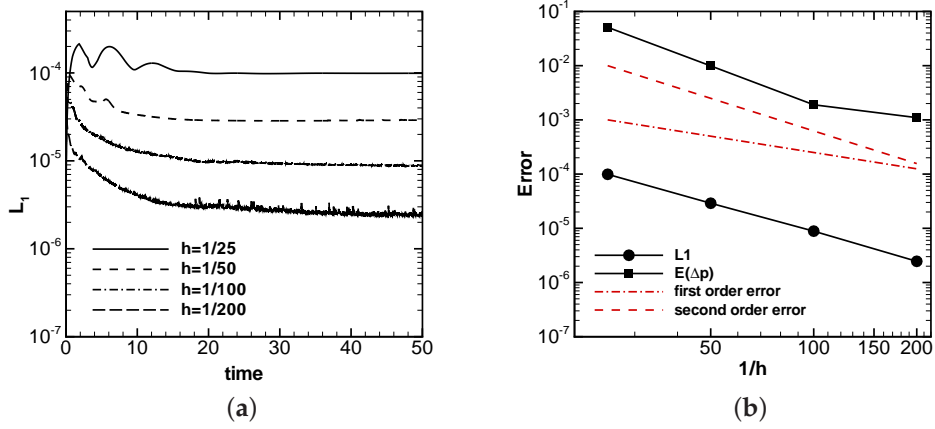
Figure 4.7: (**a**) The convergence of errors with time in velocity (L_2) for the flows in a circular drop by using VOF/LS method. (**b**) The convergence rate for the velocity and pressure jump in terms of mesh refinement by using VOF/LS method at $t = 50$.

the bubble were all set unity while the densities were given a magnitude of 10^4. This corresponds to a Laplace number $La = d_{drop}\sigma\rho\mu^{-2} = 5000$.

In the computational results that follow, the error in the pressure jump and in the velocity is investigated. The numerical jump in pressure is evaluated as follows:

$$E(\Delta p) = \frac{|p_{in} - p_{out} - 2\sigma/d_{drop}|}{2\sigma/d_{drop}} \tag{4.30}$$

where $p_i n$ is the pressure inside the drop measured as the average of the pressure on a circle of diameter $0.2d_{drop}$ centered at the symmetric axis of the drop, while p_{out} is the outside pressure measured as the average of the pressure from a disc of diameter $2d_{drop}$ centered at the symmetry axis of the drop to the boundary of the domain, $\partial\Omega$. To measure the error in velocity, the following L_1 error norm is used:

$$L_1(\mathbf{v}) = \frac{1}{N_{cells}} \sum_{k}^{N_{cells}} (\mathbf{v}_k \cdot \mathbf{v}_k)^{1/2} \frac{\mu}{\sigma} \tag{4.31}$$

which is computed on the whole of the space domain Ω.

In Table 4.1 the aforementioned errors $E(\Delta p)$ and $L_1(\mathbf{v})$ are given for different cell sizes (h). As with all Eulerian interface tracking methods there are spurious currents present, however, $L_1(\mathbf{v})$ quickly decreased and converged with second order
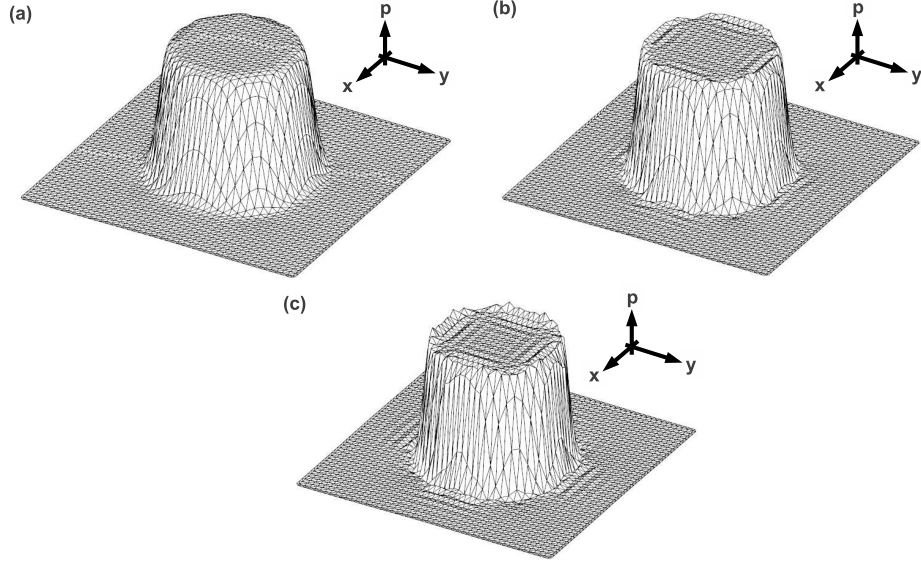
125

Figure 4.8: Static drop solved with a cell size $h = 1/50$. Effect of the parameter ε defined in Eq. 4.17, $\phi = \frac{1}{1+e^{d(\mathbf{x},t)/\varepsilon}}$, on the pressure jump computed by Eq. 4.16, $\sigma\kappa\mathbf{n}\delta_\Gamma = \sigma\kappa\nabla\phi$. (a) $\varepsilon = 0.50h$ (b) $\varepsilon = 0.25h$ (c) $\varepsilon = 0.10h$

Cell size ($1/h$)	$L_1 = \sum_k^{all\ cells} \left(\mathbf{v}_k \cdot \mathbf{v}_k\right)^{1/2} \mu/\sigma$	$E(\Delta p) = \frac{|p_{in}-p_{out}-2\sigma/d_{drop}|}{2\sigma/d_{drop}}$
25	9.91×10^{-5}	0.0510
50	2.90×10^{-5}	0.0099
100	8.86×10^{-6}	0.0019
200	2.46×10^{-6}	0.0011

Table 4.1: Errors for the non-dimensional velocity and pressure by using the present coupled VOF/LS method.
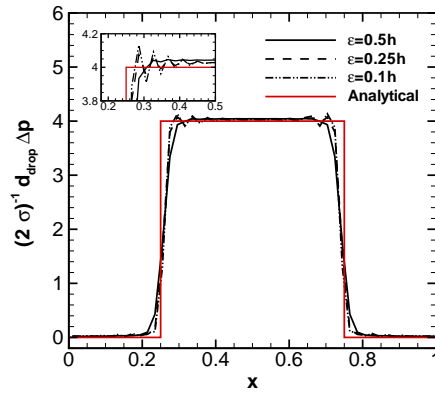
Figure 4.9: Static drop solved with a cell size $h = 1/50$. Effect of the ε parameter of Eq. 4.17, $\phi = \frac{1}{1+e^{d(\mathbf{x},t)/\varepsilon}}$, on the pressure jump.
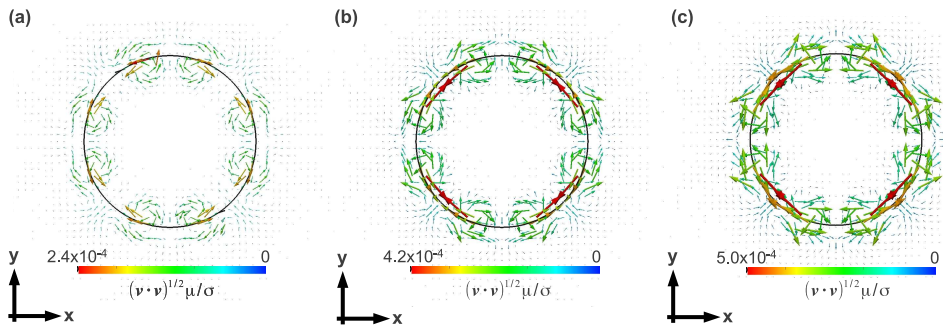
Figure 4.10: Static drop solved with a cell size $h = 1/50$. Effect of the ε parameter of Eq. 4.17, $\phi = \frac{1}{1+e^{d(\mathbf{x},t)/\varepsilon}}$, on the normalized magnitude of the spurious velocities $(\mathbf{v} \cdot \mathbf{v}\mu/\sigma)^{1/2}$. (a) $\varepsilon = 0.50h$ (b) $\varepsilon = 0.25h$ (c) $\varepsilon = 0.10h$

127
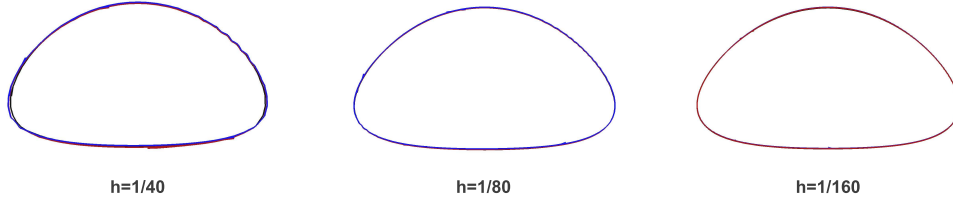
Figure 4.11: An assessment of the bubble shape for different interface capturing techniques at $time = 3$. CLS (black line), VOF/LS with $\psi = \phi$ (red line), VOF/LS with $\psi = f$ (blue line). Here, ψ is a smoothed Heaviside function used in regularization of physical properties (see Eq. 4.22).

accuracy (see Fig. 4.7). Regarding the pressure jump, Fig. 4.6 illustrates how well the computed pressure fulfilled the Young-Laplace law (see Eq. 4.29) with the mesh refinement. In addition, $E(\Delta p)$ decreased very rapidly with the mesh refinement as is illustrated in Fig. 4.7b. Figs. 4.8 and 4.9 illustrate the effect of ε (see Eqs. 4.16 and 4.17) on the pressure jump, keeping the mesh size to $h = 1/50$. It can be seen that oscillations appear in the pressure profile near the interface when $\varepsilon < 0.5h$, however, for $\varepsilon = 0.5h$ pressure approximation is sharp and non oscillating. In addition, Fig. 4.10 shows that the magnitude of the spurious velocities increases as the regularization parameter ε decreases. Thus, parasitic currents generated by VOF/LS method are quite small in magnitude compared with other methods reported in the literature [44, 14]. The above mentioned results confirms that surface tension model was implemented correctly and it produces accurate results.

4.3.2 Two-dimensional rising bubble

This complex test case has been used to determine quantitative reference solutions for the circularity (ζ), rise velocity (v_c), and center of mass (y_c) of a bubble rising in an initially quiescent liquid by [13, 14]. In addition, the aforementioned problem was selected for code validation in the conservative level-set method introduced by [1]. Therefore, the reader is referred to [1] or Chapter 2 of this thesis for a detailed description of the computational setup, initial conditions and boundary conditions. The test case begins with a cylindrical bubble with diameter $d_{bubble} = 0.5$ centered in the lower half of a $\Omega = 1 \times 2$ rectangular domain. The bubble rises due to buoyancy force while its shape is deformed. In order to have quantitative references, the
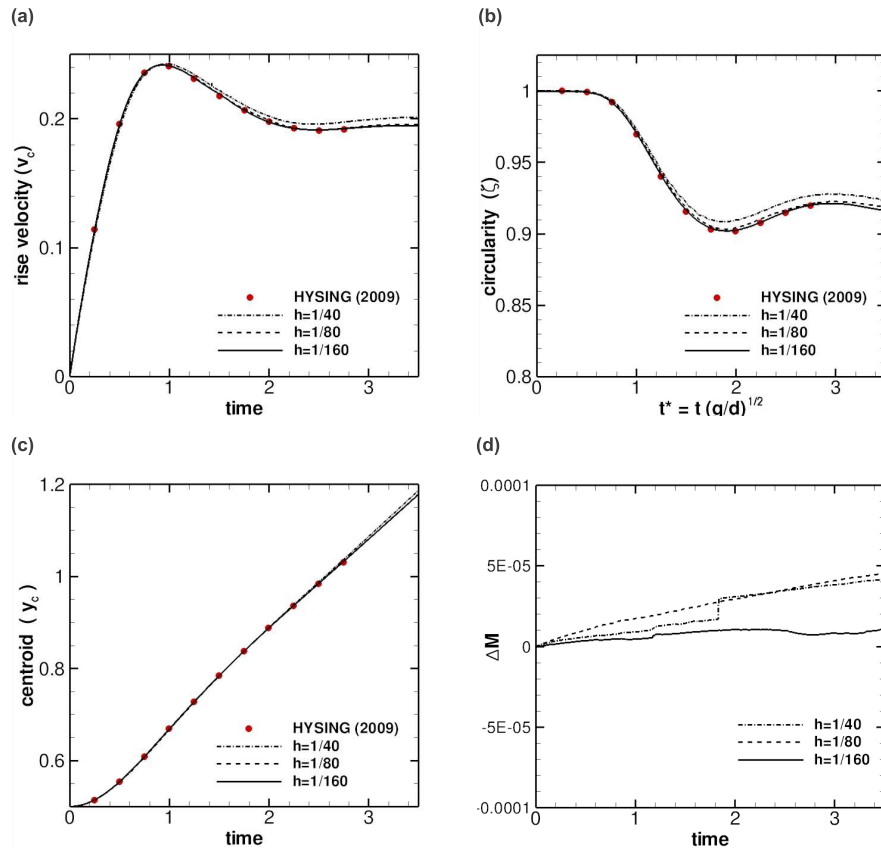
Figure 4.12: Two-dimensional rising bubble. Physical properties in Eq. 4.22 are regularized by $\psi = \phi$, where ϕ is defined by Eq. 4.17. (a) rise velocity (b) circularity (c) bubble centroid (d) error in mass conservation $\Delta M = \frac{M(t) - M(0)}{M(0)}$ where $M(t) = \int_{\Omega} f(\mathbf{x}, t) dV$.
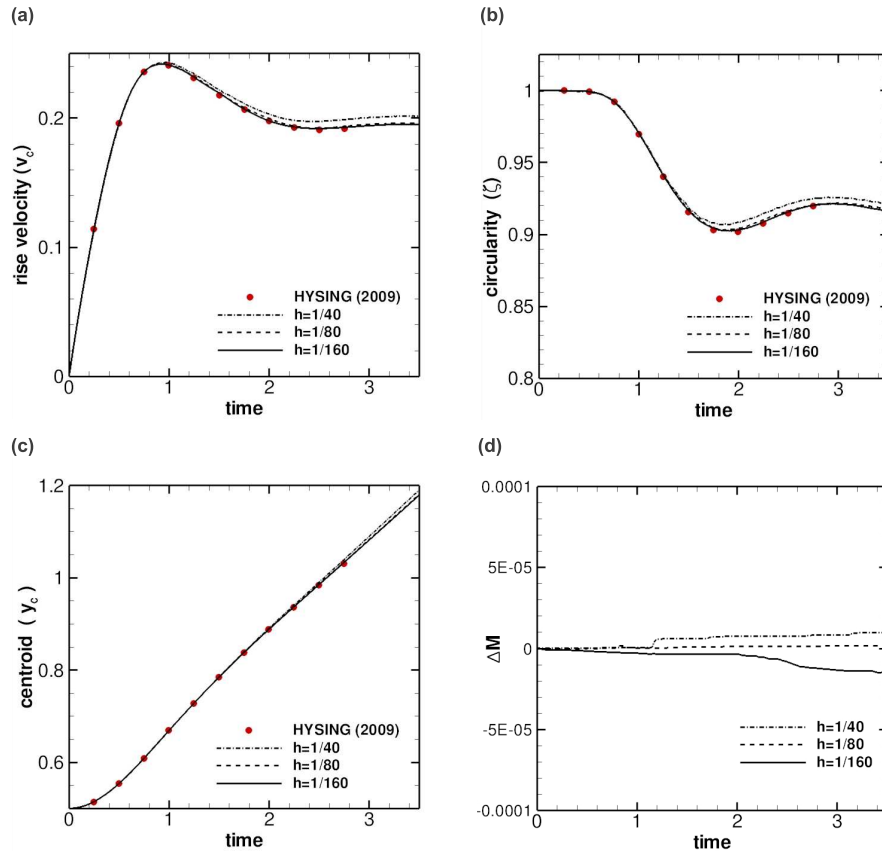
Figure 4.13: Two-dimensional rising bubble. Physical properties in Eq. 4.22 are regularized by $\psi = f$, where f is the VOF function defined in Eq. 4.5. (a) rise velocity (b) circularity (c) bubble centroid (d) error in mass conservation $\Delta M = \frac{M(t) - M(0)}{M(0)}$ where $M(t) = \int_\Omega f(\mathbf{x}, t) dV$.
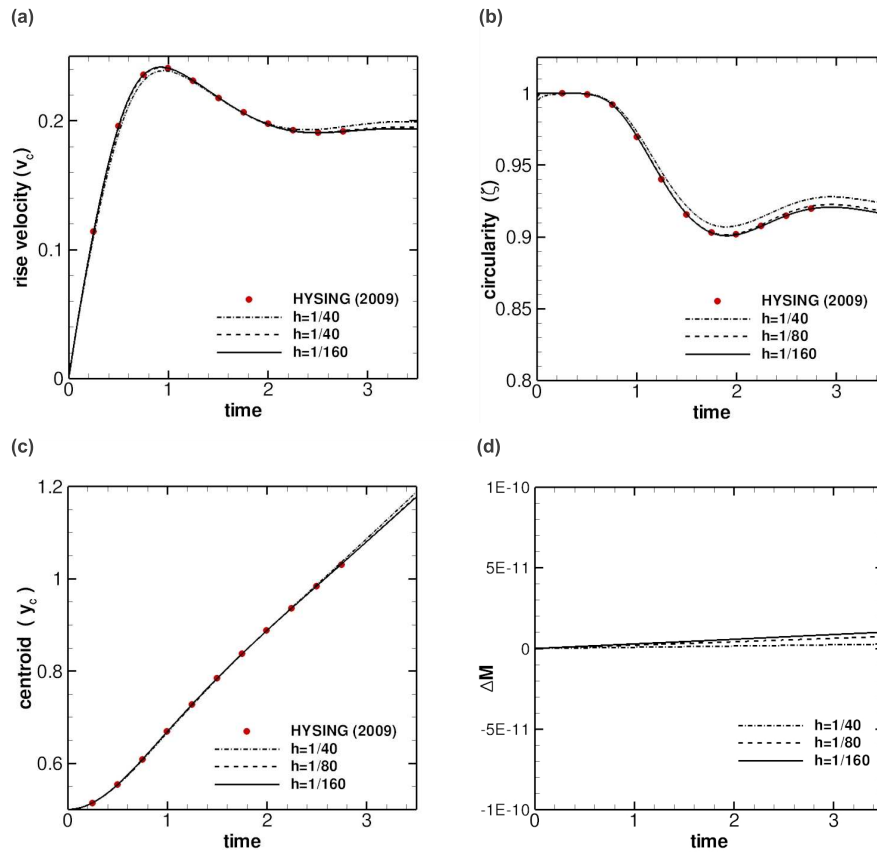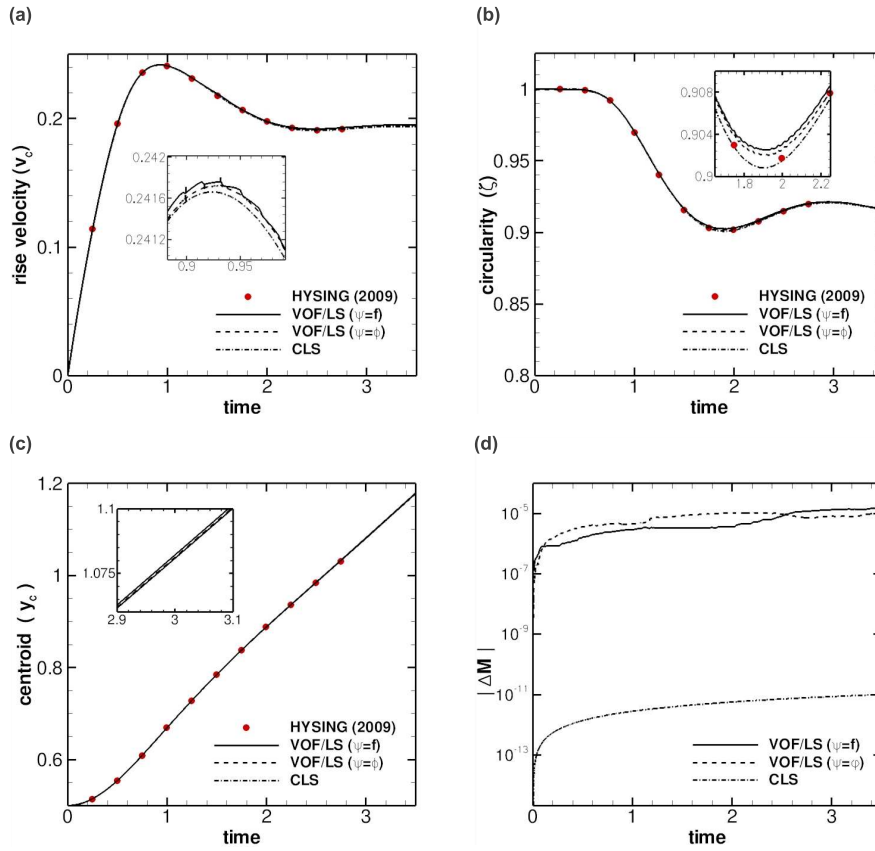
Figure 4.14: Two-dimensional rising bubble solved with a conservative level-set method (CLS) introduced by [1] (Chapter 2). (a) rise velocity (b) circularity (c) bubble centroid (d) error in mass conservation $\Delta M = \frac{M(t) - M(0)}{M(0)}$ where $M(t) = \int_\Omega f(\mathbf{x}, t) dV$.

Figure 4.15: An assessment of interface capturing techniques, $h = 1/160$. Here, ψ is a smoothed Heaviside function used in regularization of physical properties (see Eq. 4.22). (a) rise velocity (b) circularity (c) bubble centroid (d) error in mass conservation $\Delta M = \frac{M(t) - M(0)}{M(0)}$ where $M(t) = \int_\Omega f(\mathbf{x}, t) dV$.

aforementioned benchmark quantities are defined as follow

$$
\begin{cases}
v_c = \dfrac{\int_{\Omega_2} \mathbf{v} \cdot \mathbf{e}_y \, dV}{\int_{\Omega_2} dV}, \\[2mm]
y_c = \dfrac{\int_{\Omega_2} \mathbf{x} \cdot \mathbf{e}_y \, dV}{\int_{\Omega_2} dV}, \\[2mm]
\zeta = \dfrac{\text{perimeter of area-equivalent circle}}{\text{perimeter of bubble}} = \dfrac{\pi d_{bubble}^2}{\int_{\Omega} ||\nabla f(\mathbf{x},t)|| dV}.
\end{cases}
\tag{4.32}
$$

where Ω_2 denotes the region inside the bubble and $\mathbf{e}_y$ is a unit vector parallel to the $y-axis$.

The physical parameters of the two fluid phases defining the test case are given in Table 4.2. The subscript 1 is used for the continuous fluid phase and the subscript 2 is assigned to the lighter fluid of the bubble. Numerical simulations were carried

ρ_1	ρ_2	μ_1	μ_2	g	σ	ρ_1/ρ_2	μ_1/μ_2
1000	100	10	1	0.98	24.5	10	10

Table 4.2: Physical parameters defining the two dimensional rising bubble test case.

out on uniform cartesian meshes with cell size $h = 1/40, 1/80, 1/160$. In Fig. 4.11 the bubbles shapes on various grids at the time $t = 3$ are compared for different interface capturing methods. There is an excellent qualitative agreement between the bubble shapes computed by the present VOF/LS method with $\psi = \{f, \phi\}$ and the conservative level-set method (CLS) introduced by [1] (see Chapter 2), moreover, the bubble shapes are indistinguishable when they are visualized on the cartesian grids with $h = 1/80$ and $h = 1/160$.

Figs. 4.13, 4.12 and 4.14 show the time evolution of the benchmark quantities defined in Eq. 4.32 for different grids. It can be observed that the bubble rise velocity, circularity, and bubble centroid, tracked by the present VOF/LS method ($\psi = \{f, \phi\}$) and CLS method introduced by [1], converge with mesh refinement to the reference data reported by [13]. Fig 4.13c, 4.12c and 4.14c show that all numerical methods present a very low error in mass conservation property. Fig. 4.15 shows a comparison of the numerical results obtained by using the above mentioned methods for $h = 1/160$. Fig. 4.11a and 4.15b illustrate that the time evolution of the rise velocity and circularity present slight oscillations for the VOF/LS method with $\psi = f$, however, this oscillations are smoothed when a VOF/LS method with $\psi = \phi$ is used. On the other hand, the time evolutions of the benchmark quantities obtained by the CLS method are free of oscillations. Regarding the mass conservation property, Fig. 4.15d demonstrates a better performance of the CLS method where the error is of order $O(10^{-11})$, in comparison with the present VOF/LS methods which present an error of order $O(10^{-5})$.

Table 4.3 shows that the inflection point of minimum circularity and center of mass $y_c(t = 3)$ and maximum rise velocity (v_c^{max}) are in very close agreement with numerical data reported by [14]. Thus, through the performed simulations and by comparing present results against those given by [14, 13] and numerical results given by the CLS method introduced by [1], it is demonstrated that the present VOF/LS method can perform two-phase flow simulations with high accuracy.

4.3.3   Three-dimensional buoyant bubbles

As a validation of the implemented VOF/LS method in three dimensions, the buoyant motion of a bubble in an initially quiescent fluid is simulated. The dimensions of the domain are $[D_\Omega, H_\Omega] = [8d, 8d]$, where d is the initial bubble diameter, H_Ω is the cylinder height and D_Ω is the cylinder diameter, as shown in Fig. 4.16a. Thus, wall effect is minimized, while the bubble has enough approach distance to reach terminal velocity before impact. No-slip boundary conditions are imposed at the top $(y = H_\Omega)$ and bottom $(y = 0)$ walls, and Neumann boundary condition is used at the lateral boundary, $r = 0.5D_\Omega$ (see Fig. 4.16a). The 3D bubble motion is computed on an non-uniform hexahedral mesh. as shown in Fig. 4.16b and 4.16c. The mesh was generated by a constant step extrusion of a two-dimensional unstructured grid along the symmetry axis of the cylindrical domain, being the step size H_Ω/N_{planes}, where N_{planes} is the number of planes in which the vertical axis is divided (see Fig. 4.16b and 4.16c). The mesh was concentrated around the symmetry axis of the domain, where a uniform grid size (h) was fixed, to maximize resolution of the bubble. The mesh size grows exponentially to the border, where it reaches a maximum size (see Fig. 4.16b and 4.16c). Following the work of [7], the relevant physical quantities for the present test case are determined by the Eötvös number (Eo), Morton number (M), and Reynolds number (Re), which are defined as in previous chapters:

$$Eo = \frac{gd^2\Delta\rho}{\sigma} \qquad M = \frac{g\mu_1^4\Delta\rho}{\rho_1^2\sigma^3} \qquad Re = \frac{\rho_1 U_T d}{\mu_1} \qquad (4.33)$$

where $U_T = \int_{\Omega_2} v_y\phi dV / \int_{\Omega_2} dV$ is the terminal velocity of the bubble, $\Delta\rho = \rho_1 - \rho_2$ specifies the density difference between the fluid phases, the subscript 1 refers to the heavier fluid and the subscript 2 to the lighter fluid.

For the sake of comparison, the experimental results found in [2, 15] and numerical results presented in Chapter 2 using the CLS method are used. Fig. 4.17 shows a study of the grid convergence for the case $Eo = 116$, $M = 41.1$, $\eta_\rho = 100$ and $\eta_\mu = 100$. It can be observed that the dynamics of the bubble can be accurately captured by using the mesh M_3, which is equivalent to $h = d/25$. Regarding the terminal Reynolds number, there is not a big difference using the grid resolutions $20cv/d$ and $15cv/d$, as shown in Fig. 4.17a. However, the bubble shape is better represented if a

$1/h = 40$			Method	
	[14]	CLS [1]	VOF/LS ($\psi = f$)	VOF/LS ($\psi = \phi$)
ζ_{min}	0.9016	0.9070	0.9068	0.9084
$t\vert_{\zeta=\zeta_{min}}$	1.9234	1.8917	1.8210	1.9182
v_c^{max}	0.2418	0.2389	0.2433	0.2473
$t\vert_{v_c=v_c^{max}}$	0.9141	0.9521	0.9870	0.9960
$y_c(t = 3)$	1.0818	1.0873	1.0902	1.0902

$1/h = 80$			Method	
	[14]	CLS [1]	VOF/LS ($\psi = f$)	VOF/LS ($\psi = \phi$)
ζ_{min}	0.9014	0.9013	0.9030	0.9032
$t\vert_{\zeta=\zeta_{min}}$	1.8734	1.8956	1.8947	1.8989
v_c^{max}	0.2418	0.2413	0.2419	0.2416
$t\vert_{v_c=v_c^{max}}$	0.9375	0.9286	0.9448	0.9340
$y_c(t = 3)$	1.0810	1.0817	1.0834	1.0818

$1/h = 160$			Method	
	[14]	CLS [1]	VOF/LS ($\psi = f$)	VOF/LS ($\psi = \phi$)
ζ_{min}	0.9014	0.9008	0.9025	0.9020
$t\vert_{\zeta=\zeta_{min}}$	1.9070	0.9027	1.9255	1.9281
v_c^{max}	0.2419	0.2417	0.2418	0.2417
$t\vert_{v_c=v_c^{max}}$	0.9281	0.9241	0.9285	0.9287
$y_c(t = 3)$	1.0812	1.0808	1.0821	1.0812

Table 4.3: Minimum circularity (ζ_{min}) and maximum rise velocity (v_c^{max}), with corresponding incident times, and the final position of the center of mass. Present computations (VOF/LS method) are compared against numerical results reported by Hysing et al. [14] and computations performed by the conservative level-set method introduced in [1] (Chapter 2).
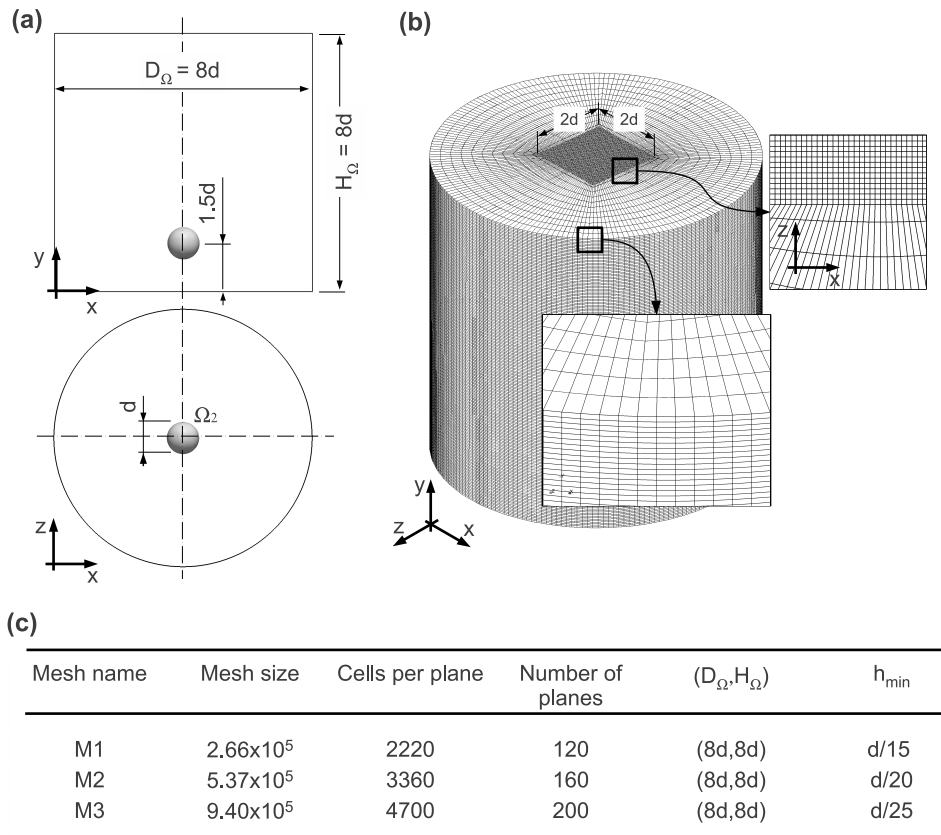
(c)

Mesh name	Mesh size	Cells per plane	Number of planes	(D_Ω, H_Ω)	h_{min}
M1	2.66×10^5	2220	120	(8d,8d)	d/15
M2	5.37×10^5	3360	160	(8d,8d)	d/20
M3	9.40×10^5	4700	200	(8d,8d)	d/25

Figure 4.16: Full 3D rising bubble. (a) Computational setup and initial conditions. (b) Mesh configuration. (c) Mesh parameters and domain size
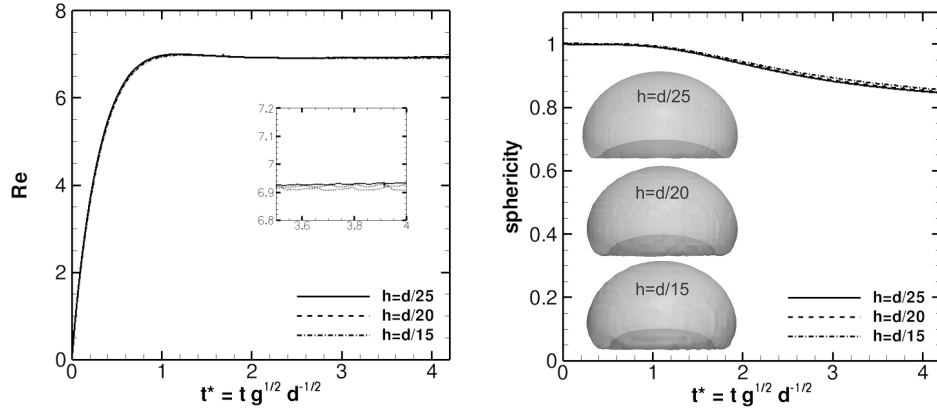
Figure 4.17: Mesh convergence for $Eo = 116$, $M = 41.1$, $\eta_\mu = 100$ and $\eta_\rho = 100$. Computations were performed by using the VOF/LS method.
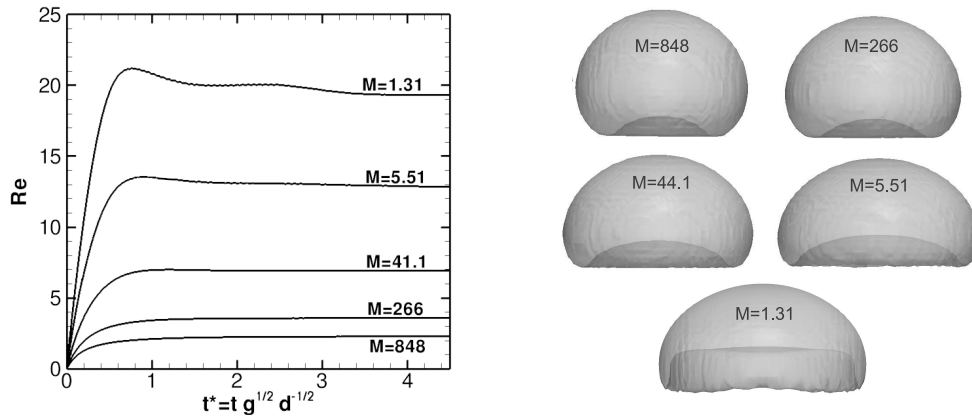
Figure 4.18: Time evolution of the Reynolds number for $Eo = 116$, $\eta_\mu = 100$ and $\eta_\rho = 100$, and bubble shapes computed by using the VOF/LS method.

137
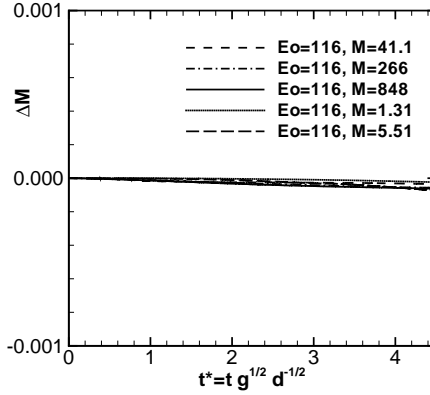
Figure 4.19: Time evolution of the mass error $(\Delta M = (M(t) - M(0))/M(0))$ using the VOF/LS method. Here $M(t) = \int_{\Omega} f(\mathbf{x}, t)dV$. As reference the maximun mass conservation error is $O(10^{-5})$.

mesh resolution $h = d/25$ is used, hence, to discuss the numerical results this mesh resolution is selected in all simulations, unless otherwise stated.

A set of numerical experiments has been performed for $Eo = 100$, $1 < M < 10^3$, $\eta_\rho = 100$ and $\eta_\mu = 100$. Fig. 4.18 shows the time evolution of the Reynolds number and bubble shapes calculated by using the VOF/LS method implemented in this work. Particularly, the characteristic overshoot of the instantaneous Reynolds number after the bubbles start to ascend is well represented in the cases with $M > 5.51$. A comparison of the computed terminal Reynolds number against experiments of [2] and numerical simulations of [16] is given in Table 4.4. There is a close agreement between present results and reference data of the literature. Fig. 4.20 shows a comparison of the droplet shape between experiments of [2] and numerical results using the CLS method introduced in [1] against present results using the implemented VOF/LS method. The relative error in the computed Reynolds number, $e_r = \frac{Re_{num} - Re_{exp}}{Re_{exp}}$, is also illustrated in the above mentioned figure.

As further validation, Fig. 4.21 and Fig. 4.22 show numerical results for a single bubble rising in a viscous fluid, using dimensionless parameters that correspond to experimental conditions given in one of the cases reported by [15], namely $Eo = 39.4$ and $M = 0.065$, while density and viscosity ratios are fixed to $\eta_\rho = 100$ and $\eta_\mu = 100$, respectively. The bubble deforms and it rises with time, and the shape is deformed into a spherical cap shape in the steady state, as shown in Fig. 4.21. Regarding to

Figure 4.20: Comparison of bubbles shapes and terminal Reynolds numbers reported in experiments of [2] and numerical results obtained by the CLS method introduced in [1], against computations using the present VOF/LS method.
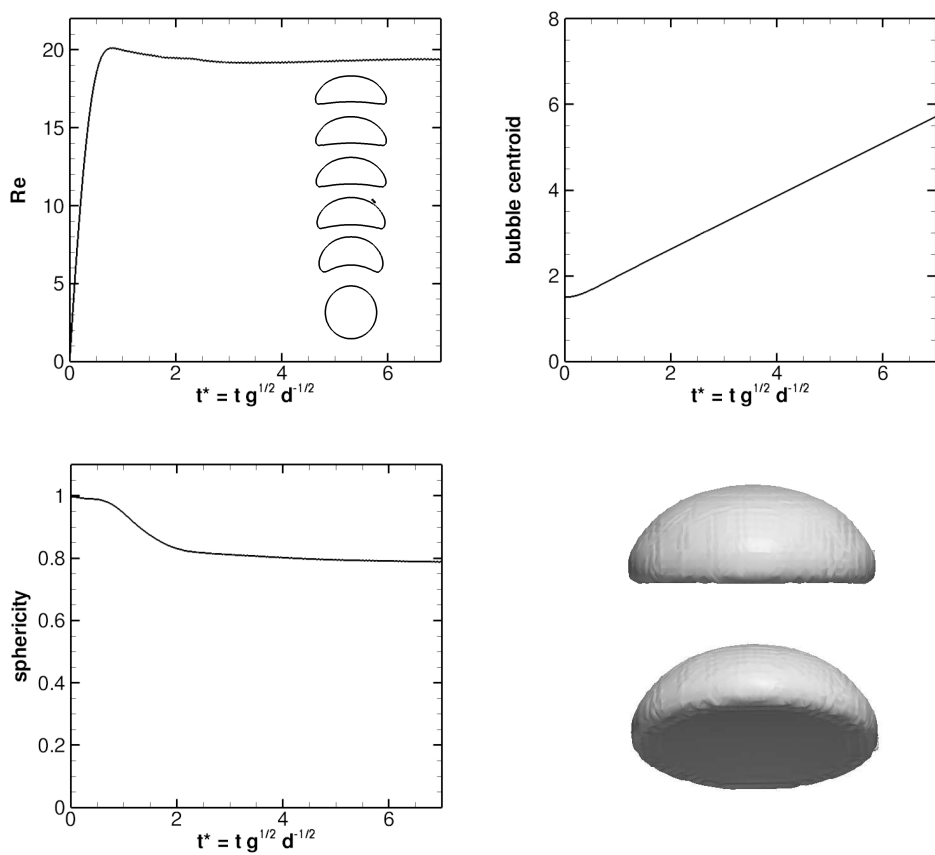
Figure 4.21: Buoyant bubble for $Eo = 39.4$, $M = 0.065$, $\eta_\rho = 100$ and $\eta_\mu = 100$.

Figure 4.22: Comparison of wake structure reported in experiment of [15] and numerical results of the literature [31, 32, 34], against computations using the present VOF/LS method. $Eo = 39.4$, $M = 0.065$, $\eta_\rho = 100$ and $\eta_\mu = 100$.

| | | Re | | | |
Eo	M	[2]	[16]	Present VOF/LS	Mesh
116	848	2.47	2.317	2.33	M_3
116	266	3.57	3.621	3.64	M_3
116	41.1	7.16	7.0	6.95	M_3
116	5.51	13.3	13.17	12.83	M_3
116	131	20.4	19.88	19.30	M_3

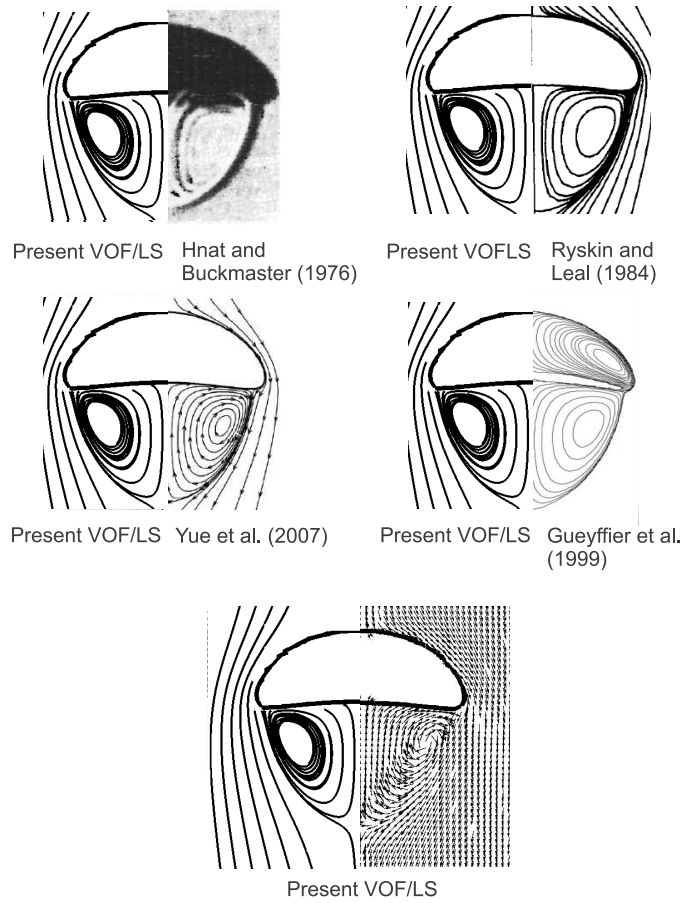**Table 4.4:** A comparison of present computational results using the VOF/LS method against experimental data of [2] and numerical data reported by [16] using the front-tracking method. Mesh configuration is shown in Fig. 4.16c. For present computations, $\eta_\rho = 100$ and $\eta_\mu = 100$.

the Reynols number, [15] reported a terminal velocity of $U_T = 0.215 m/s$ which corresponds to $Re = 19.6$. As is illustrated in Fig. 4.21, the terminal Reynols number calculated using the present VOF/LS method is $Re = 19.37$, hence, there is a close agreement with the value reported in [2]. In Fig. 4.22, the bubble shape and wake structure based on the present VOF/LS method is compared with the experiment of [2], and other well validated simulation results including the body-fitted method [31], ALE approach [32] and VOF approach [34]. Present results reproduce the experiments of [2], however, there are slight differences with other numerical results due to the variation in numerical methodology. Despite the above mentioned differences, the present results are also in good agreement with other numerical studies reported in the literature.

4.3.4 Bubble merging

This test case consists in co-axial coalescence of two bubbles rising in a liquid. The simulation domain is the same that the previous test case, whereas the initial bubble arrangement is in agreement with the computational set-up reported in [1]. The fluid properties and initial arrangement of bubbles are the same as in the volume-of-fluid computations of [17] and level-set calculations of [1]. Namely, the Morton and Eötvös numbers are set to $M = 2 \times 10^{-4}$ and $Eo = 16$ falling between the skirted and spherical cap regimes in Fig. 2.13. The density and viscosity ratios are specified as $\eta_\rho = \rho_c/\rho_d = 100$ and $\eta_\mu = \mu_d/\mu_d = 100$, where subscripts c and d refer to the outer-liquid phase and bubble fluid respectively. Free-slip boundary condition is used at lateral side of the domain and no-slip boundary condition at the top and bottom boundaries.

Snapshots of topological changes in the coalescence process of are shown in Figs. 4.3.4 and 4.3.4. As the bubbles rise, a liquid jet is formed behind the leading bubble,
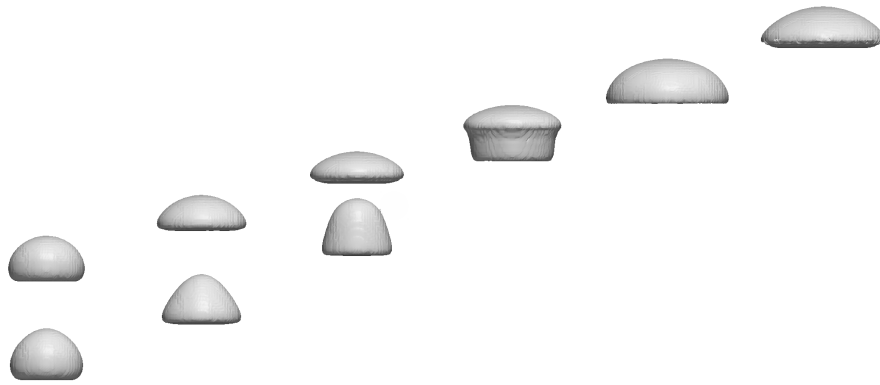
Figure 4.23: Coaxial coalescence of two bubbles using the coupled VOF/LS method
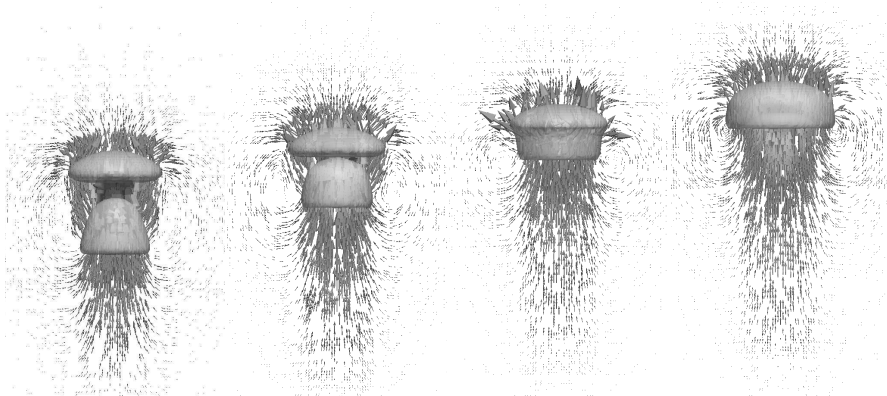
Figure 4.24: Velocity field in coaxial coalescence of two bubbles using the coupled VOF/LS method
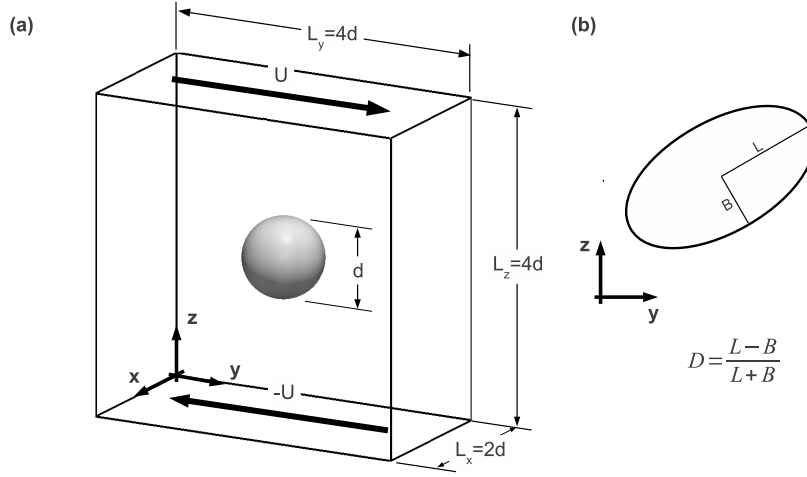
Figure 4.25: Deformation os a droplet in a shear flow. (a) Computational setup and initial condition. (b) Definition of the droplet deformation parameter D.

which induces a severe deformation in vertical direction of the following bubble. Once two bubbles are approaching, the trailing bubble accelerates because the suction by the top bubble. As time progresses, the two bubbles start to touch, leaving a mushroom-like structure. Finally, the thin liquid film between bubbles is squeezed out and ruptured, completing the coalescence process. Numerical predictions match fairly well in terms of bubble shapes with experimental results reported by [4]. Similar results have been found by [17] using a volume-of-fluid method and by [1] using a conservative level-set method.

4.3.5   Deformation of a droplet in a shear flow

The computational setup is given in Fig. 4.25a. A spherical drop of diameter d is located at the center of a computational domain $x \in [0, 8]$, $y \in [0, 4]$, $z = \in [0, 8]$, without effect of gravity force. The opposite velocities $\pm U$ are imposed on the top and bottom walls, periodic boundary condition is applied in x direction and Neumann boundary condition in y direction. The initial condition at time $t = 0$ is a drop with spherical form and the initial velocity field is null inside the computational domain. All the computations have been done using a uniform cartesian mesh of $120 \times 60 \times 120$ (or 8.64×10^5 control volumes), hence, the cell size is $h = d/30$.

The deformation behaviour of the droplet is determined by the Reynolds number

Figure 4.26: Stationary results of the deformed surfaces subjected to a linear shear flow of different capillary numbers Ca. The velocity vectors are also shown in a $z - y$ cross section passing through $x = 0$.

Figure 4.27: Stationary results of the droplet shapes. The velocity vectors are shown in a $z - y$ cross section passing through $x = 0$.

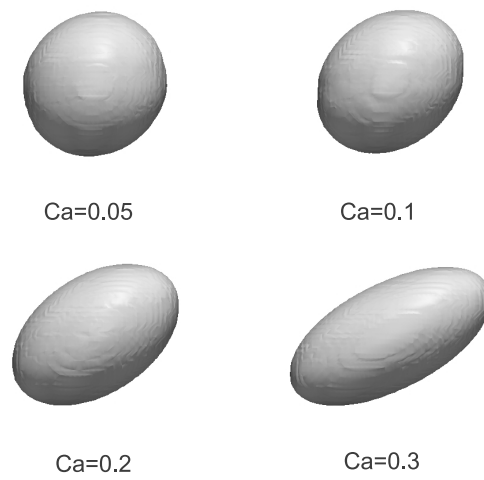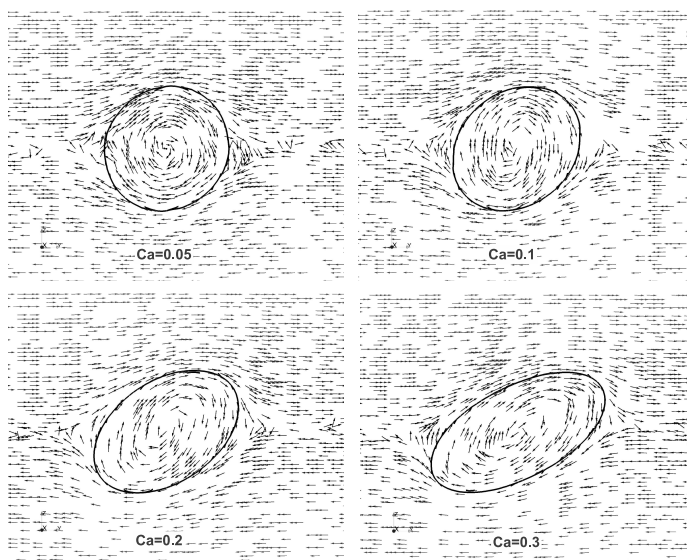| Case	η_ρ	η_μ	Re	Ca
A	1.0	1.0	0.1	0.05
B	1.0	1.0	0.1	0.1
C	1.0	1.0	0.1	0.2
D	1.0	1.0	0.1	0.3

Table 4.5: Dimensionless parameters for the droplet deformation.

(Re) and the capillary number (Ca). The viscosity is given by the Reynolds number

$$Re \equiv \frac{\rho_c \dot{\gamma} d^2}{4\mu_c} \tag{4.34}$$

where the shear rate is defined by $\dot{\gamma} = 2U/L_z$. The capillary number is given by

$$Ca \equiv \frac{\dot{\gamma} \mu_d d}{2\sigma} \tag{4.35}$$

This dimensionless parameter is a measure of the relative effect of the shear stress versus the surface tension across the fluid-fluid interface. The same viscosity and density are specified for both drop fluid and continuous fluid, thus $\eta_\rho = \rho_c/\rho_d = 1$ and $\eta_\mu = \mu_c/\mu_d = 1$, where the sub-index c is used for the continuous fluid and d the droplet fluid. The dimensionless numbers used in these test cases are summarized in Table 4.5.

The droplet shapes at steady state are shown in Fig. 4.26, whereas the velocity fields are illustrated in Fig. 4.27. The interface becomes ellipsoidal and its deformation and rotation are larger as the capillary number increases. A theoretical solution was derived by [41] to predict small distortions of the droplets from the spherical form at slow speeds, on the hypothesis of Stokes flow. This result show that the droplet is distorted into an ellipse where the deformation parameter given by $D = \frac{L-B}{L+B}$ (see Fig. 4.25b) is linearly changed with the capillary number (Eq. 4.35). Here L and B denote the semi-major and semi-minor axes of the ellipse, as shown in Fig. 4.25b. The correlation between the capillary number Ca versus the steady droplet deformation parameter D is plotted in Fig. 4.28. There is a close agreement between present results using the VOF/LS method and the numerical findings of [29]. Moreover, for small capillary numbers, the shape in steady state is close to the theoretical predictions of [41], while the theory underestimates the droplet deformation parameter for large capillary numbers (see Fig. 4.28).
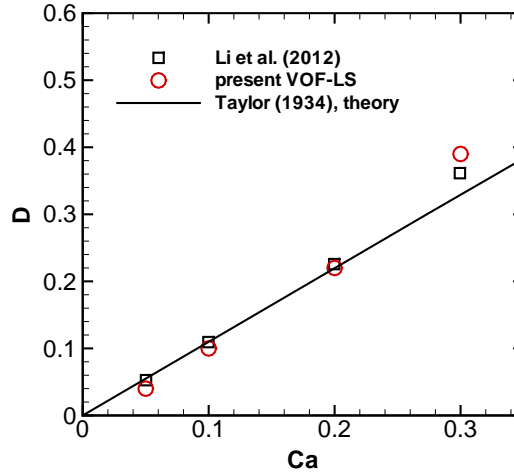
Figure 4.28: Correlation between capillary number Ca and Taylor deformation parameter D.

4.4 Conclusions

A coupled VOF and LS method, which combines the advantages and overcomes the disadvantages of both techniques, has been proposed for computing incompressible two-phase flows with surface tension effects. From the comparison of the numerical tests performed, it is possible to conclude that this method can be used to perform numerical simulations of surface-tension flows with high accuracy. The advantages of the proposed technique can be summarized as follows:

- The mass can be conserved because VOF method is used to advect the interface.

- The signed distance function, obtained by the iterative geometric operation, is used to calculate the curvature. By using this level-set function the surface tension force can be accurately computed.

The parasitic currents caused by the numerical errors have been effectively reduced using a reconstructed distance function to evaluate the curvature, while the surface tension force is approximated by using the gradient of a regularized indicator function. Further simulations of buoyant bubbles and droplet deformation have proven

that the present VOF/LS method is enough robust and accurate for practical applications.

References

[1] Balcázar, N., Jofre, L., Lehmkhul, O., Castro, J., Rigola, J., 2014. A finite-volume/level-set method for simulating two-phase flows on unstructured grids. International Journal of Multiphase Flow 64, 55-72

[2] Bhaga, D., Weber, M.E., 1981. Bubbles in viscous liquids: shapes, wakes and velocities, J Fluid Mech 105, 61-85

[3] Brackbill, J.U., Kothe, D.B., Zemach, C., 1992. A Continuum Method for Modeling Surface Tension, J. Comput. Phys. 100, 335-354.

[4] Brereton, G., Korotney, D., Coaxial and Oblique Coalescence of Two Rising Bubbles, in Dynamics of bubbles and Vortices Near a Free Surface, vol. 119, ASME, New York, 1991

[5] Chorin, A.J., Numerical solution of the Navier-Stokes equations. 1968. Math. Comput. 22, 745-762.

[6] Chang, Y.C., Hou, T.Y., Merriman, B., Osher, S., A level-set formulation of Eulerian interface capturing methods for incompressible two-phase flows. 1996. Journal of Computational Physics 124, 462-488.

[7] Clift, R., Grace, J.R., Weber, M.E., Bubbles, Drops and Particles. Academin Press, New York, 1978.

[8] Deen, N.G., Van Sint Annaland, M., Kuipers, J.A.M. , 2009. Direct numerical simulation of complex multi-fluid flows using a combined front tracking and immersed boundary method, Chemical Engineering Science 64, 2186-2201.

[9] Engquist, B., Tornberg, A.K., Tsai, R., 2005. Discretization of Dirac delta functions in level set methods, Journal of Computational Physics 207, 28-51.

[10] Gottlieb, S., Shu, C., 1998. Total Variation Dimishing Runge-Kutta Schemes, Mathematics of Computations 67, 73-85.

[11] Haselbacher, A., Vasilyev, O., 2003. Commutative discrete filtering on unstructured grids based on least-squares techniques, J. Comput. Phys. 187, 197-211.

[12] Hirt, C., Nichols, B., 1981. Colume of fluid (VOF) method for the dynamics of free boundary, J. Comput. Phys. 39, 201-225

[13] Hysing, S., Turet, S., Kuzmin, D., Parolini, N., Burman, E., Ganesan, S., Tobiska, L., 2009. Quantitative benchmark computations of two-dimensional bubble dynamics, International Journal for Numerical Methods in Fluids 60, 1259-1288.

[14] Hysing, S., 2012. Mixed element FEM level set method for numerical simulation of immiscible fluids, J. Comput. Phys. 231, 2449-2465.

[15] Hnat, J.G., Buckmaster, J.D., 1976. Spherical cap bubbles and skirt formation, Phys. Fluids 19, 182-194

[16] Hua, J., Stene, J., Lin, P., 2008. Numerical simulation of 3D bubbles rising in viscous liquids using a front tracking method, J. Comput. Phys. 227, 3358-3382

[17] Van Sint Annaland, M., Deen, N.G., Kuipers, J.A.M., 2005. Numerical Simulation of gas bubbles behaviour using a three-dimensional volume-of-fluid method, Chemical Engineering Science 60, 2999-3011.

[18] Jofre, L., Lehmkuhl, O., Castro, J., Oliva, A., 2014. A 3-D Volume-of-Fluid advection method based on cell-vertex velocities, Computers & Fluids 94, 14-29

[19] Kothe, D.B., Rider, W.J., Mosso, S.J., Brock, J.S., 1996. Volume Tracking of Interfaces Having Surface Tension in Two and Three Dimensions, AIAA 96-0859. 25.

[20] Kim, J., 2005. A continuous surface tension force formulation for diffuse-interface models, Journal of Computational Physics 204, 784-804

[21] Lehmkuhl, O., Perez-Segarra, C.D., Soria, M., Oliva, A., 2007, A new Parallel unstructured CFD code for the simulation of turbulent industrial problems on low cost PC cluster, Proceedings of the Parallel CFD 2007 Conference, pp.1-8.

[22] López, J., Gómez, P., Hernández, J., Faura, F., 2013. A two-grid adaptive volume of fluid approach for dendritic solidification, Computers & Fluids. 86, 326-342.

[23] Olsson, E., Kreiss, G., 2005. A conservative level set method for two phase flow, J. Comput. Phys. 210, 225-246.

[24] Osher, S., Sethian, J.A., 1988. Fronts propagating with curvature-dependent speed: Algorithms based on Hamilton-Jacobi formulations, J. Comput. Phys. 79, 175-210.

[25] Peskin, C.S., 1977. Numerical analysis of blood flow in the heart, J. Comput. Phys. 25, 220-252.

[26] Raesi, M., Mostaghimi, J., Bussmann, M., 2010. A volume-of-fluid interfacial flow solver with advected normals, Computers & Fluids 39, 1401-1410.

References

[27] Li, J., Renardy, Y.Y., Renardy, M., 2000. Numerical simulation of breakup of a viscous drop in simple shear flow through a volume-of-fluid method, Physics of fluids 12, 269-282.

[28] Taylor, G.J., 1934. The Formation of Emulsions in Definable Fields of Flow, Proc. R. Soc. Lond 146, 501-523.

[29] Satoshi, L., Kazuyasu, S., Shintaro, T., Shu, T., Yoichiro, M., Feng, X., 2012. An interface capturing method with a continuous function: The THINC method with multi-dimensional reconstruction, Journal of Computational Physics 231, 2328-2358.

[30] Renardy, Y., Renardy, M., 2002. PROST: A Parabolic Reconstruction of Surface Tension for the Volume-of-Fluid Method, Journal of Computational Physics 183, 400â421.

[31] Ryskin, G., Leal, L.G., 1984. Numerical solution of free-boundary problems in fluid mechanics. Part 2. Buoyancy-driven motion of a gas bubble through a quiescent liquid, J. Fluids Mech. 148, 19-35.

[32] Yue, P., Feng, J.J., Bertelo, C.A., Hu, H.H., 2007. An arbitrary Lagrangian-Eulerian method for simulating bubble growth in polymer foaming, J. Comput. Phys. 226, 2229-2249.

[33] Felten, F.N., Lund, T.S., 2006. Kinetic energy conservation issues associated with the collocated mesh scheme for incompressible flow, J. Comput. Phys. 215, 465-484

[34] Gueyffier, D., Li, J., Nadim, A., Scardovelli, R., Zaleski, S., 1999. Volume-of-fluid interface tracking with smoothed surface stress methods for three-dimensional flows, J. Comput. Phys. 152, 423-456.

[35] Guermond, J.L., Minev, P., Jie, S., 2006. An overview of projection methods for incompressible flows, Comput. Methods Appl. Mech. Engrg. 195, 6011-6045.

[36] Parker, B., Youngs, D., 1992. Two and three dimensional Eulerian simulation of fluid flow with material interfaces. Technical report 01/92, UK Atomic Weapons Establishment

[37] Rhie, C.M., Chow, W.L., 1983. Numerical Study of the Turbulent Flow past an Airfoil with Trailing Edge Separation, AIAA J. 21, 1525-1532.

[38] Sun, D.L., Tao, J., W.Q., 2010. A coupled volume-of-fluid and level-set (VOSET) method for computing incompressible two-phase flows, International Journal of Heat and Mass Transfer 53, 645-655.

[39] Sussman, M., Smereka, P., Osher, S., 1994. A Level Set Approach for Computing Solutions to Incompressible Two-Phase Flow, J. Comput. Phys. 144, 146-159.

[40] Sussman, M., Puckett, E.G., 2000. A Coupled Level Set and Volume-of-Fluid Method for Computing 3D and Axisymmetric Incompressible Two-Phase Flows, J. Comput. Phys. 162, 301-337.

[41] Taylor, G.I., 1934. The deformation of emulsions in definable fields of flows, Proc. R. Soc. Lond. A 146, 501-523

[42] Tryggvason, G., Bunner, B., Esmaeeli, A., Juric, D., Al-Rawahi, N., Tauber, W., Han, J., Nas, S., Jan, Y-J., 2001. A Front-Tracking Method for the Computations of Multiphase Flow, J. Comput. Phys. 169, 708-759.

[43] Unverdi, S., Tryggvason, G., 1992. A front-tracking method for viscous, incompressible, multifluid flows, J. Comput. Phys. 100, 25-37.

[44] Zahedi, S., Kronbichler, M., Kreiss, G., 2011. Spurious currents in finite element based level set methods, Int. J. Numer. Meth. Fluids, 25-37.

[45] Zahedi, S., Tornberg, A.K., 2010. Delta function approximations in level set methods by distance function extension, Journal of Computational Physics 229, 2199-2219.

Chapter 5

A multiple marker level-set method for simulation of deformable fluid particles

Most of the contents of this chapter have been published as:

Abstract.   A novel multiple marker level-set method is introduced for Direct Numerical Simulation of deformable fluid particles (bubbles and droplets), which is integrated in a finite-volume framework on collocated unstructured grids. Each fluid particle is described by a separate level-set function, thus, different interfaces can be solved in the same control volume, avoiding artificial and potentially unphysical coalescence of fluid particles. Therefore, bubbles or droplets are able to approach each other closely, within the size of one grid cell, and can even collide. The proposed algorithm is developed in the context of the conservative level-set method, whereas, surface tension is modeled by the continuous surface force approach. The pressure-velocity coupling is solved by the fractional-step projection method. For validation of the proposed numerical method, the gravity-driven impact of a droplet on a liquid-liquid interface is studied; then, the binary droplet collision with bouncing outcome is examined, and finally, it is applied on simulation of gravity-driven bubbly flow in a vertical column.

5.1 Introduction

Bubbles and droplets are ubiquitous and they play an important role in many natural and industrial processes. Among them one can mention steam generators in nuclear plants, rocket engines, boiling heat transfer, microfluidic applications, unit operations in chemical engineering such as distillation, absorption, liquid-liquid extraction, heterogeneous catalysis and bio-reactors [32]. Thus, the practical implications of a better understanding and predictive capabilities of droplet and bubble flows is enormous. Furthermore, all these applications have stimulated basic research on bubble and droplet dynamics, however, although numerous experimental and numerical investigations have provided considerable insight into the mechanisms governing droplet and bubble flows, many challenging problems still remain as pointed out in recent publications [32, 20, 56, 54].

The development of computers has promoted Direct Numerical Simulation (DNS) of the Navier-Stokes equations as another means of performing controlled experiments [56, 54], providing a good way to non-invasive measure of droplet and bubble flows, although computationally demanding. Thus, DNS allows us to control the size distribution of bubbles or droplets, their deformability, whether they coalesce or not, and modify the flow conditions [54]. For DNS of multiphase flow problems with two immiscible fluid phases, standard Eulerian descriptions are often adopted together with interface-tracking methods such as volume-of-fluid [45] and level-set [37, 47] methods, or front-tracking methods [57, 55]. A review of advantage and disadvantages of the aforementioned techniques, in the context of simulation of multiphase flows with sharp interfaces is given in [59]. The main advantage of using a front-tracking method is that bubbles or droplets do not coalesce unless a specific merge condition is implemented. Especially for bubble swarm simulations this is an important aspect. On the other hand, in conventional level-set and volume-of-fluid methods, two fluid particles will automatically coalesce when their interfaces are enough close from each other. Indeed, up to now, most research on systems with multiple droplets or bubbles have been performed using the front-tracking method [42, 54].

In spite of the rapid progress in DNS of complex multiphase flows, capturing the dynamics of deformable fluid-fluid interfaces in close hydrodynamic interaction is extremely difficult challenge for any numerical method because of the critical role played by the very thin near contact lubrication zone between the interfaces, where large pressures develop and resist coalescence sometimes preventing it altogether. In this regard, the front tracking method introduced by [57] and [55] has been used to perform simulations where the aforementioned issues have an important impact on the numerical results. For instance, [34] and [33] have employed the front tracking method to perform numerical simulations of binary drop collisions. [52] examine the collision of a fluid drop with a wall and develop a multiscale approach to compute

the flow in the film between the drop and the wall. In addition, the front tracking method has been extensively used in simulation of homogeneous bubbly flows, for instance in [54] and [42]. [38] carried out numerical simulations and experiments of the dynamics of head-on collision between two identical droplets. Using this empirical information as an input, the simulated collision images obtained by using a front tracking method were found to agree well with the experimental observations.

Regarding interface capturing methods (e.g. level-set and volume-of-fluid), [11] have extended the level-set/volume-of-fluid method of [46] to a multiple marker approach in order to avoid the numerical merging of interfaces. This method was extended by [23] to include a coalescence criterion based on a film drainage model to predict if and when two colliding droplets will coalesce. In the same line, [17] adapted a multiple marker approach to a volume-of-fluid method in order to deploy an algorithm for the temporal suppression of the coalescence in binary droplet collisions, where one droplet is composed of a high viscous liquid and the other one is of lower viscosity. In some special cases, such as the head-on collision between two equal sized droplets, the numerical coalescence which is inherent to interface-tracking methods can be controlled by manipulating the boundary conditions at the symmetry plane in between the two droplets [21, 26]. [63] and [9] have explore adaptive mesh refinement algorithms in order to capture thin films formed when two masses collide. However, this films can become very thin and it get down to just about few nanometers before it ruptures, as consequence this approach would lead to huge computational effort due to a large number of grid cells or levels of adaptive grid refinement which is currently not feasible in a Direct Numerical Simulation even with high performance computing techniques.

The method here proposed overcome the previous stated issues in a computationally efficient and robust manner. The concept of multiple marker is coupled with a conservative level-set method introduced in [2] to deploy a numerical algorithm capable to simulate the dynamics of multiple bubbles and droplets on complex spatial domains without numerical merging of fluid particles. Thus, using the conservative level-set method [35], mass conservation problem that is known to affect standard level-set formulations [46] is circumvented. Moreover, the unstructured formulation of the multiphase solver allow us an efficient distribution of the mesh on complex domains [2]. The extended algorithm is based on the idea of describing separate interfaces with different level-set functions to prevent numerical and potentially unphysical coalescence of bubbles and droplets, without excessive mesh refinement. Therefore, bubbles or drops are able to approach each other closely, within the size of one grid cell, and can even collide. Another important aspect is that the volume of the fluid particles remain constant throughout the simulation, this is an important aspect on numerical simulation of homogeneous bubble swarms. The surface tension force and the interfacial geometrical properties are computed from the tracked

interface, by using the continuum surface force model (CSF) introduced by [5], furthermore, the aforementioned approach has been adapted to be applicable in the context of the multiple marker level-set method.

This paper is organized in the following order: The governing equations employed in this study are given in section 5.2. Section 5.3 is devoted to a description of the numerical method, while the simulation results are presented in section 5.4. Finally, concluding remarks are presented in section 5.5.

5.2 Governing equations

5.2.1 Incompressible two-phase flow

The Navier-Stokes equations for the dispersed fluid in Ω_d and continuous fluid in Ω_c can be combined into a set of equations in an entire domain $\Omega = \Omega_d \cup \Omega_c$, with a singular source term for the surface tension force at the interface Γ:

$$\frac{\partial}{\partial t}(\rho\mathbf{v}) + \nabla \cdot (\rho\mathbf{v}\mathbf{v}) = -\nabla p + \nabla \cdot \mu \left(\nabla\mathbf{v} + (\nabla\mathbf{v})^T\right) + \rho\mathbf{g} + \mathbf{f}_\sigma \tag{5.1}$$

where $\mathbf{v}$ and p denote the fluid velocity and pressure field respectively, ρ is the fluid density, μ is the dynamic viscosity, $\mathbf{g}$ is the gravitational acceleration, and $\mathbf{f}_\sigma$ is the surface tension force. Because of incompressibility, the velocity field is divergence-free:

$$\nabla \cdot \mathbf{v} = 0 \tag{5.2}$$

Moreover, physical properties change discontinuously across the interface:

$$\rho = \rho_d H_d + \rho_c(1 - H_d) \tag{5.3}$$
$$\mu = \mu_d H_d + \mu_c(1 - H_d)$$

with ρ_d, ρ_c and μ_d, μ_c the densities and viscosities of the disperse and continuous fluids, respectively, while H_d is the Heaviside step function that is one in Ω_d and zero elsewhere.

5.2.2 Multiple marker level-set method

In level-set methods [37, 47], merging of interfaces happens automatically whenever two interfaces come within one grid cell of each other. To circumvent this issue, multiple markers, ϕ_i, are introduced to represent each subdomain, Ω_i, in the dispersed phase $\Omega_d = \{\Omega_1, ..., \Omega_{n_d}\}$, where n_d is the number of separate regions included in Ω_d (see Fig. 5.1). Thus, the inclusion of separate markers will permit to solve two or more interfaces, Γ_i, at the same grid cell. In the present work, a multiple tracking

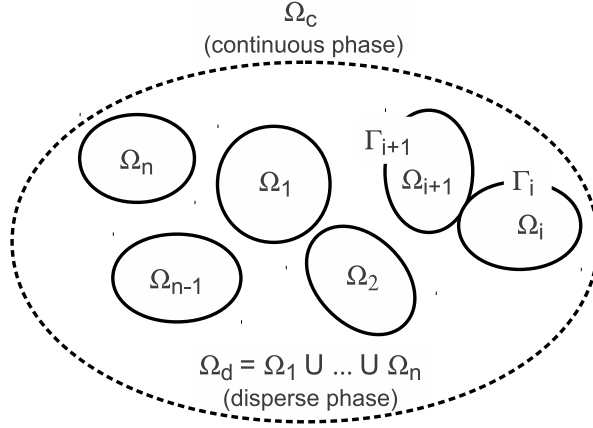**Figure 5.1:** Schematic representation of the continuous fluid phase Ω_c and dispersed fluid phase Ω_d. Interfaces are represented by Γ_i.

methodology is introduced in the context of the conservative level-set method [35, 2], hence, mass conservation issue that is known to affect classical level-set formulations is circumvented. Following the work of [35], a regularized indicator function, ϕ_i, is used for interface capturing:

$$\phi_i(\mathbf{x}, t) = \frac{1}{2} \left(tanh \left(\frac{d_i(\mathbf{x}, t)}{2\varepsilon} \right) + 1 \right) \qquad \text{with } i = 1, .., n_d \qquad (5.4)$$

where $d_i(\mathbf{x}, t)$ is a signed distance function [37, 47] and ε is a tunable parameter that sets the thickness of the level-set profile. With this profile the interface, Γ_i, is defined by the location of the $\phi_i = 0.5$ iso-surface, $\Gamma_i = \{\mathbf{x} \mid \phi_i(\mathbf{x}, t) = 0.5\}$.

The conservative level-set function ϕ_i is advected by a vector field $\mathbf{v}$ that is, in case of two-phase flows, the solution of the Navier-Stokes equations (Eqs. 5.1 and 5.2). The interface transport equation can be written in conservative form provided the velocity field is solenoidal, $\nabla \cdot \mathbf{v} = 0$, namely,

$$\frac{\partial \phi_i}{\partial t} + \nabla \cdot \phi_i \mathbf{v} = 0 \qquad (5.5)$$

Furthermore, an additional re-initialization equation is introduced to keep the profile and thickness of the interface constant,

$$\frac{\partial \phi_i}{\partial \tau} + \nabla \cdot \phi_i (1 - \phi_i) \mathbf{n}_i = \nabla \cdot \varepsilon \nabla \phi_i \qquad (5.6)$$

This equation is advanced in pseudo-time τ, it consists of a compressive term, $\phi_i(1 - \phi_i)\mathbf{n}_i|_{\tau=0}$, wich forces the level-set function to be compressed onto the interface along the normal vector $\mathbf{n}_i$, and of a diffusion term $\nabla \cdot \varepsilon \nabla \phi_i$ that ensure the profile remains of characteristic thickness ε. Geometrical information on the interface Γ_i, such as normal vector $\mathbf{n}_i$ or curvature κ_i, is obtained through:

$$\mathbf{n}_i(\phi_i) = \frac{\nabla \phi_i}{\|\nabla \phi_i\|} \tag{5.7}$$

$$\kappa_i(\phi_i) = -\nabla \cdot \mathbf{n}_i \tag{5.8}$$

The accurate computation of the surface tension ($\mathbf{f}_\sigma$ in Eq. 5.1) is one of the most critical elements of any method designed to follow the motion of the interface between immiscible fluids. In this regard, implementing surface tension in a numerical scheme involves two issues: the curvature κ_i needs to be determined, and the resulting pressure jump must be applied appropriately to the fluids. Because finite-volume method is used for discretization of governing equations, the aforementioned problems can be conveniently addressed through the continuous surface force (CSF) method proposed by [5]; which has been adapted to include multiple markers in the same grid cell. Thus, the surface tension term, $\mathbf{f}_\sigma$ in Eq. 5.1, is converted to a volume force as follows:

$$\mathbf{f}_\sigma = \sigma \sum_i \kappa_i(\phi_i) \nabla \phi_i \tag{5.9}$$

where κ_i is given by Eq. (5.8) and σ is the surface tension coefficient. In addition, the fluid properties are regularized by employing a global level-set function, ϕ_d, for the disperse phase:

$$\rho = \rho_d \phi_d + \rho_c(1 - \phi_d) \qquad \mu = \mu_d \phi_d + \mu_c(1 - \phi_d) \tag{5.10}$$

where

$$\phi_d(\mathbf{x}, t) = max\{\phi_1(\mathbf{x}, t), ..., \phi_{n_d-1}(\mathbf{x}, t), \phi_{n_d}(\mathbf{x}, t)\} \tag{5.11}$$

5.3   Numerical method

In this section, the numerical method is presented for the sake of completeness.The governing equations have been discretized on a collocated unstructured grid arrangement by means of the finite-volume method, according to [2]. In order to avoid unphysical oscillations in the level-set function, a TVD Superbee limiter [50, 2], is used to discretize the convective term in advection Eq. (5.5). is used to discretize the convective term in advection Eq. (5.5), while the compressive term of the re-initialization Eq. (5.6) is discretized by using a central difference (CD) scheme. A

CD scheme is used to discretize the convective term of momentum Eq. (5.1) unless otherwise stated. A distance-weighted linear interpolation is used to find the cell-face values, while gradients are computed at cell centroids by using the least-squares method (see [2]).

The velocity-pressure coupling has been solved by means of a classical fractional step projection method [8, 19]. Thus, momentum Eq. (5.1) is decomposed into two steps:

$$\frac{\rho \mathbf{v}^* - \rho \mathbf{v}^n}{\Delta t} = -\frac{3}{2}\mathbf{A}_h(\rho \mathbf{v}^n) + \frac{1}{2}\mathbf{A}_h(\rho \mathbf{v}^{n-1}) + \mathbf{D}_h(\mathbf{v}^n) + \rho \mathbf{g} + \sigma \sum_i \kappa_i \nabla_h(\phi_i) \quad (5.12)$$

and

$$\mathbf{v}^{n+1} = \mathbf{v}^* - \frac{\Delta t}{\rho}\nabla_h(p^{n+1}) \quad (5.13)$$

where ∇_h represents the gradient operator, $D_h(\mathbf{v}) = \nabla_h \cdot \mu \left(\nabla_h \mathbf{v} + \nabla_h^T \mathbf{v}\right)$ represents the diffusion operator, and $\mathbf{A}_h(\rho \mathbf{v}) = \nabla_h \cdot (\rho \mathbf{v}\mathbf{v})$ is the advection operator.

The resulting velocity $\mathbf{v}^*$ from Eq. (5.12), which does not satisfy the continuity Eq. (5.2), is corrected by Eq. (5.13). Substituting Eq. (5.12) into the continuity Eq. (5.2) yields a Poisson equation for pressure,

$$\nabla_h \cdot \left(\frac{1}{\rho}\nabla_h(p^{n+1})\right) = \frac{1}{\Delta t}\nabla_h \cdot (\mathbf{v}^*) \quad (5.14)$$

Poisson Eq. (5.14) discretization, leads to a linear system, which is solved by using a preconditioned conjugate gradient method. In order to avoid pressure-velocity decoupling when the pressure projection is made on collocated meshes [40, 16], a cell face velocity $\mathbf{v}_f$ is defined so that $\nabla_h \cdot \mathbf{v} = 0$ (see Eq. 5.2) at each control volume. Namely in discretized form:

$$\mathbf{v}_f = \sum_{q \in \{P,F\}} \frac{1}{2}\left(\mathbf{v}_q^{n+1} + \frac{\Delta t}{\rho(\phi_q^n)}(\nabla_h p^{n+1})_q\right) - \frac{\Delta t}{\rho_f}(\nabla_h p^{n+1})_f \quad (5.15)$$

where P and F are denoting the adjacent cell nodes to the face f. This velocity is used to advect the markers and momentum in Eq. 5.5 and Eq. 5.12 respectively. For the temporal discretization, explicit Adams-Bashforth scheme is used to solve the momentum Eq. (5.12), while for the corrector Eq. (5.13) an explicit first-order scheme has been used. Advection Eq. (5.5) and re-initialization Eq. (5.6) are integrated in time with a 3-step third-order accurate TVD Runge-Kutta method [18]. Solving Eq. (5.6) to steady-state results in a smooth transition of ϕ at the interface that depends of the diffusion coefficient ε. In this paper, all numerical simulations were performed by setting $\varepsilon = 0.5h$ where $h = (V_{cell})^{1/3}$ is the characteristic size of the grid cell

and V_{cell} is the cell volume. Therefore ε is chosen to be as small as possible in order to reduce the smearing of: density, viscosity and surface tension force, while the transition in the CLS function, ϕ, is enough smooth to avoid numerical issues. In present simulations two iterations per physical time-step of re-initialization Eq. (5.6) are sufficient to keep the profile of the level-set function.

The time increment Δt, which is limited by the CFL conditions and the stability condition for the capillary force, is given by:

$$\Delta t = 0.1 min \left(\frac{h}{||\mathbf{v}||}, \frac{\rho h^2}{\mu}, \left(\frac{h}{||\mathbf{g}||} \right)^{1/2}, h^{3/2} \left(\frac{\rho_1 + \rho_2}{4\pi\sigma} \right)^{1/2} \right) \tag{5.16}$$

Thus, the computational approach for simulating bubbles and drops without numerical coalescence can be summarized as follows:

1. Initialize $\mathbf{v}_P$ ($P \equiv$ cell centroid), $\mathbf{v}_f$ ($f \equiv$ face centroid), and ϕ_i for $i = 1, .., n_d$.

2. Calculate the time step (Δt) according to Eq. A.15.

3. Advection (using $\mathbf{v}_f$) and re-initialization of ϕ_i for $i = 1, .., n_d$

4. Computation of $\mathbf{n}_i$, κ_i for $i = 1, .., n_d$, and ϕ_d, ρ_d, μ_d

5. Computation of $\mathbf{v}_P$ and p by solving Eq. 5.12, Eq. 5.14 and Eq. 5.13.

6. Computation of $\mathbf{v}_f$ by Eq. 5.15.

7. Repeat steps 2-6 until time step required.

The described numerical methods were implemented in an in-house solver called TermoFluids [24], which is a C++ code designed for Direct Numerical Simulation and Large Eddy Simulation of turbulent flows [53, 41]. The reader is referred to [2] for technical details on the discretization of the Navier-Stokes/level-set equations on collocated unstructured grids, that are beyond the scope of this paper.

5.4 Numerical experiments

5.4.1 Drop impact on a liquid-liquid interface

The gravity-driven impact of a single drop onto a liquid-liquid interface is studied in order to validate the accuracy of the implemented multi-marker/level-set method

Case	$\rho_c[kg/m^3]$	$\rho_d[kg/m^3]$	$\mu_c[mPas]$	$\mu_d[mPas]$	$\sigma[mN/m]$
A	949	1128	19.0	6.3	29.1
B	960	1131	48.0	6.7	29.5

Table 5.1: Material properties in experiments of [30]. The subscript c is used for silicon oil. The subscript c is used for water/glycerin.

against experimental and numerical data reported by [30] and [11], respectively. Following the work of [10], bubbles and droplets rising or falling freely in infinite media can be characterized by four dimensionless numbers:

$$M \equiv \frac{g\mu_c^4\Delta\rho}{\rho_c^2\sigma^3} \qquad Eo \equiv \frac{gd^2\Delta\rho_c}{\sigma} \qquad \eta_\rho \equiv \frac{\rho_c}{\rho_d} \qquad \eta_\mu \equiv \frac{\mu_c}{\mu_d} \tag{5.17}$$

where, η_ρ and η_μ are respectively the density and viscosity ratio; M is the Morton number; Eo is the Eötvös number; $\Delta\rho = |\rho_c - \rho_d|$, specifies the density difference between the continuous and dispersed fluid phases, and d is the spherical volume equivalent diameter of the droplet. Here, the subscript d denotes the dispersed fluid phase and c the continuous fluid phase. For given fluids, the Eötvös number is a characteristic of the droplet size and M is a parameter representing the viscosity of the continuous fluid phase.

In this section, numerical simulations were performed for a set of dimensionless parameters corresponding to conditions of experiments in [30] which are listed in Table 5.2. Material properties used in experiments of [30] are listed in Table 5.1, namely, water as dispersed phase (d) and silicon oil as continuous phase (c). For the sake of comparison, we also introduce the following dimensionless time, $t^* = t/t_i$, where $t_i = d/U_i$ and U_i is equivalent to the drop terminal velocity. The dimensional values of d, U_i, t_i and the corresponding dimensionless parameters used in experiments of [30] are listed in Table 5.3.

$$Re \equiv \frac{\rho_c U_i d}{\mu_c} \qquad We \equiv \frac{\rho_c d U_i^2}{\sigma} \qquad Fr \equiv \frac{\rho_c U_i^2}{\Delta\rho g d} \tag{5.18}$$

where Re is the Reynolds number defined based on the impact velocity U_i, We is the Weber number and Fr is the Froude number. The key difference between the two cases is the value of the continuous fluid viscosity, μ_c, in Table 5.1.

The computational set-up is schematically indicated in Fig. 5.2a. The size of the cylindrical domain is fixed to $(D_\Omega, H_\Omega) = (8d, 10d)$, where d is the initial diameter of the spherical drop, D_Ω is the cylinder diameter and H_Ω is the cylinder height. Thus, confinement effect is minimized, while the drop has enough approach distance to reach terminal velocity before impact. No-slip boundary conditions are imposed at

Case	Eo	M	η_ρ	η_μ
A	6.4	8.82×10^{-8}	1.19	0.33
B	6.0	1.03×10^{-7}	1.18	0.14

Table 5.2: Dimensionless parameters used in present numerical simulations and experiments of [30].

	Units	Case A	Case B
Diameter, d	cm	1.03	1.03
Drop impact velocity, U_i	cm/s	13.2	9.8
Drop impact time scale, t_i	ms	78.0	105.0
Reynold number, Re_i		68.0	20.0
Reynold number, We_i		7.0	3.8
Froude number, Fr_i		1.0	0.6

Table 5.3: Experimental parameters in experiments of [30].

the top ($y = H_\Omega$) and bottom ($y = 0$) walls, and free-slip boundary condition is used at the lateral boundary, $r = 0.5D_\Omega$ (see Fig. 5.2a). Moreover, with the intend of saving computational resources such as computational time and occupation of memory, our simulations were performed on a non uniform hexahedral mesh, as shown in Fig. 5.2b. The mesh was generated by a constant step extrusion of a two-dimensional unstructured grid along the symmetry axis of the cylindrical domain, being the step size H_Ω/N_{planes}, where N_{planes} is the number of planes in which the vertical axis is divided (see Fig. 5.2b). The mesh was concentrated around the symmetry axis of the domain, where a uniform grid size (h_{min}) was fixed, to maximize resolution of the drop. The mesh size grows exponentially to the border, where it reaches a maximum size (see Fig. 5.2b).

In Figs. 5.3 and 5.4, the time history of the Reynolds number is displayed for different mesh resolutions. The results show regular convergence and essentially the same behavior during the impact event for all resolutions. In what follows, the mesh resolution $h = d/30$ is selected for discussion of the results. The computed impact Reynolds number are $Re = 65.8$ for the case A with $\eta_\mu = 0.33$, and $Re = 22.2$ for the case B with $\eta_\mu = 0.14$, which are in close agreement with the experimental values given in Table 5.3. In Figs. 5.5a and 5.5b, the time history of the instantaneous Reynolds number is displayed for different initial approach distances between the droplet centroid and the liquid-liquid interface, ΔH (see Fig. 5.2a). These simulations were carried out using a mesh resolution $h = d/30$ (mesh M_3). It is found that the choice $\Delta H = 6.5d$ is enough to reach convergence of the drop velocity, as shown Fig 5.5a and 5.5b. Thus $\Delta H = 6.5d$ is selected for discussion of the numerical
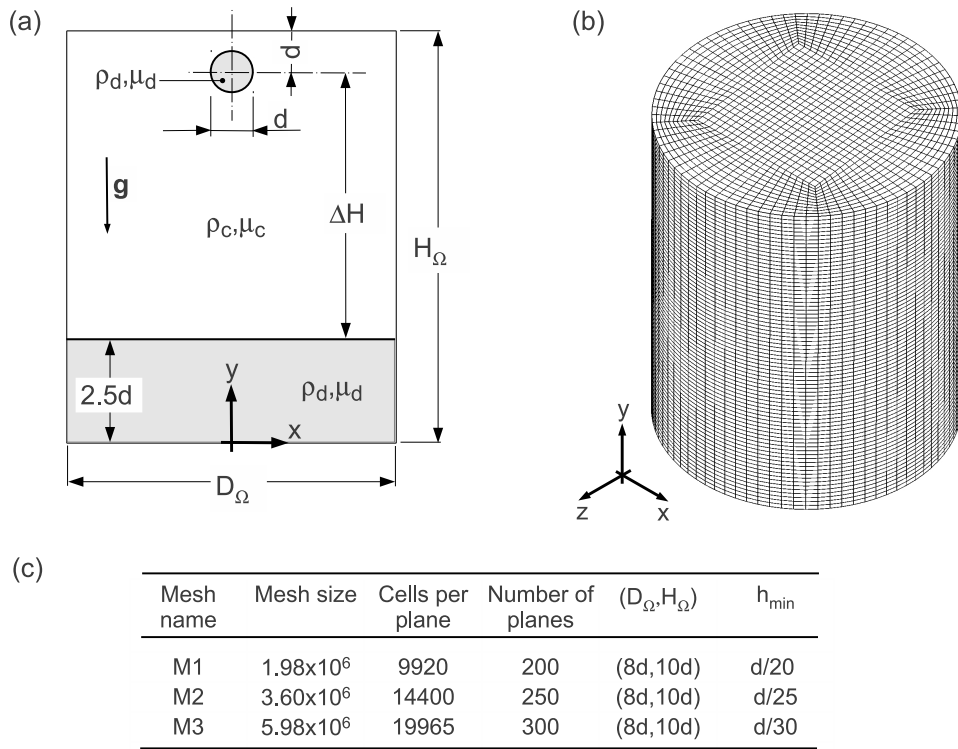
Figure 5.2: (a) Computational setup with initial configuration of the droplet and liquid-liquid interface. (b) Mesh configuration. (c) Description of the meshes.
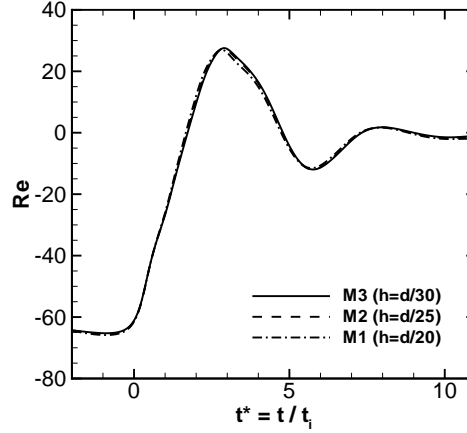
Figure 5.3: Case $\eta_\mu = 0.33$. Grid convergence study for the dimensionless droplet velocity, $Re = \rho_d d \mathbf{v}_{droplet} \cdot \mathbf{e}_z / \mu_d$. Description of the meshes (M_1, M_2 and M_3) is given in Fig. 5.2c.

experiments.

Figs. 5.6-5.7 show a sequence of snapshots of the drop collision for both cases $\eta_\mu = 0.14$ and $\eta_\mu = 0.33$; whereas Figs. 5.8-5.9 illustrate a comparison of the calculated shape profiles of the drops and the interface ($z = 0$) against experimental images reported by [30]. Following the work of [30], the impact time $t/t_i = 0$ is defined as the time when the lower drop surface crosses the quiescent liquid-liquid interface level. Thus, prior to the impact, $t/t_i < 0$ (see Fig. 5.10), both drops have reached steady spheroidal shapes, furthermore, the approach is nearly linear in time until the collision between the drop and liquid-liquid interface is achieved at $t/t_i = 0$. Additionally, just before the collision, the droplets decelerate and their shapes are flattened, moreover, the trapped fluid near the free surface is drained radially outward, while the gap between the drop and the interface is reduced until a thin fluid layer remains. Indeed, coalescence is inhibited by the thin film of continuous fluid trapped between the droplet and the liquid-liquid interface. In experiments reported by [30] a direct analysis of the flow images showed that the film thickness is of order $400\mu m$ when the macroscopic steady state is achieved, which is far smaller than the minimum cell size used in this work. After collision ($t/t_i > 0$), the droplet surfaces are stretched horizontally as they touch the liquid-liquid interface. With time, the remaining inertia inside the drop deflects the interface to a maximum while the drop
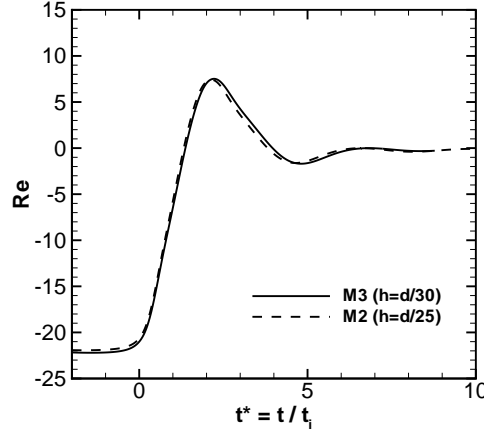
Figure 5.4: Case $\eta_\mu = 0.14$. Grid convergence study for the dimensionless droplet velocity, $Re = \rho_d d \mathbf{v}_{droplet} \cdot \mathbf{e}_z / \mu_d$. Description of the meshes $(M_1, M_2$ and $M_3)$ is given in Fig. 5.2c.

extends vertically at the same time. This large deformation is followed by a rebound occurring at the time $t/t_i = 1.4$ and $t/t_i = 1.8$ for cases $\eta_\mu = 0.14$ and $\eta_\mu = 0.33$, respectively. The drop interfaces continue to deform until they reach a steady state, as can be seen in Figs. 5.8-5.9. In Fig. 5.10, normalized centerline locations of the lower drop surface, upper drop surface, and the underlying liquid-liquid interface (aligned with the vertical axis through the drop center) are shown for both viscosity ratios. Numerical results obtained using the present method match fairly well with experimental data reported by [30]., Similar results were also reported by [11].

Fig. 5.12 and Fig. 5.13 present contour plots of the normalized vertical velocity, $|\mathbf{v} \cdot \mathbf{e}_y|/U_i$, for $\eta_\mu = 0.33$ and $\eta_\mu = 0.14$ respectively. A comparison of the present results against experimental findings reported by [30] is performed in the aforementioned figures. It can be observed that prior to impact $(t/t_i = 0)$ a wake is generated behind each drop, whereas a toroidal shaped region is formed inside them. The dark circles inside the drops in Figs 5.12-5.13 $(t/t_i = 0)$ represent regions where the fluid is moving faster, with a maximum downward velocity of approximately $1.2U_i$. The circles mentioned above suggest the existence of a circulation zone, which is clearly confirmed in Fig. 5.11. Both wakes have similar structure and their width approximates the drop size, however, there is a slower upward velocity in the ambient fluid near the side of the drop for the case $\eta_\mu = 0.33$ (see Figs. 5.6-5.7 at $t/t_i = 0$). Further-
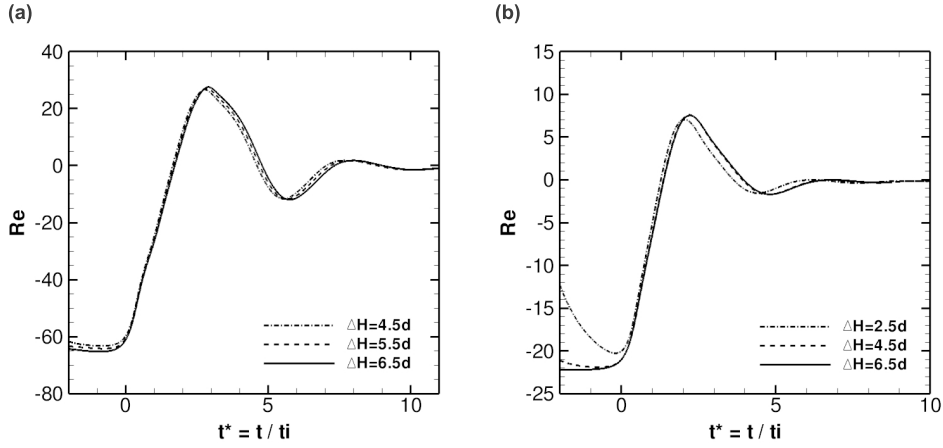
(a)

(b)

Figure 5.5: Time evolution of the dimensionless droplet velocity, $Re(t) = \rho_c d(\mathbf{v}_{droplet}(t) \cdot \mathbf{e}_z)/\mu_c$, as a function of the initial distance between the droplet centroid and the liquid-liquid interface (ΔH). All cases were carried out using the mesh M_3 (see Fig. 5.2c). (a) Case A: $\eta_\mu = 0.33$ (b) case B: $\eta_\mu = 0.14$

more, the presence of the interface bellow, causes an upward movement of the ambient fluid around the drops (see Fig. 5.11). At the time $t/t_i = 0.9$, although the general structure of the wake is conserved the downward velocities have decreased, moreover a thin film is formed between the drop and the liquid-liquid interface while the drop surface is forced to move radially outward. From Figs. 5.12-5.13, it is observed that the aforementioned tendency is maintained as the time advances, and it is more evident for the case where the viscosity ratio is $\eta_\mu = 0.14$. During the rebound, at $t/t_i > 1.4$, the surface tension force is dominant [30], moreover, a sudden change of the upper drop flow structure produces an increase in drop height, which is more pronounced in the case with $\eta_\mu = 0.33$. Finally, at $t/t_i > 3$, the upward velocity of the drop fluid is higher away from the center than at the center. Thus, the time evolution of wake structure is in close agreement, both qualitatively and quantitatively in comparison with experimental findings reported by [31] and numerical results presented in [11]. The small discrepancies observed between numerical and experimental data at Fig. 5.10 can be explained in terms of the viscosity approximation used to solve the momentum equations when two interfaces are at the same control volume. Indeed, a better performance of the numerical method is observed for the case $\eta_\mu = 0.33$, which is closer to $\eta_\mu = 1$, where the simulation does not depend on the continuum approach used to represent the jump conditions. Previous observations are also in
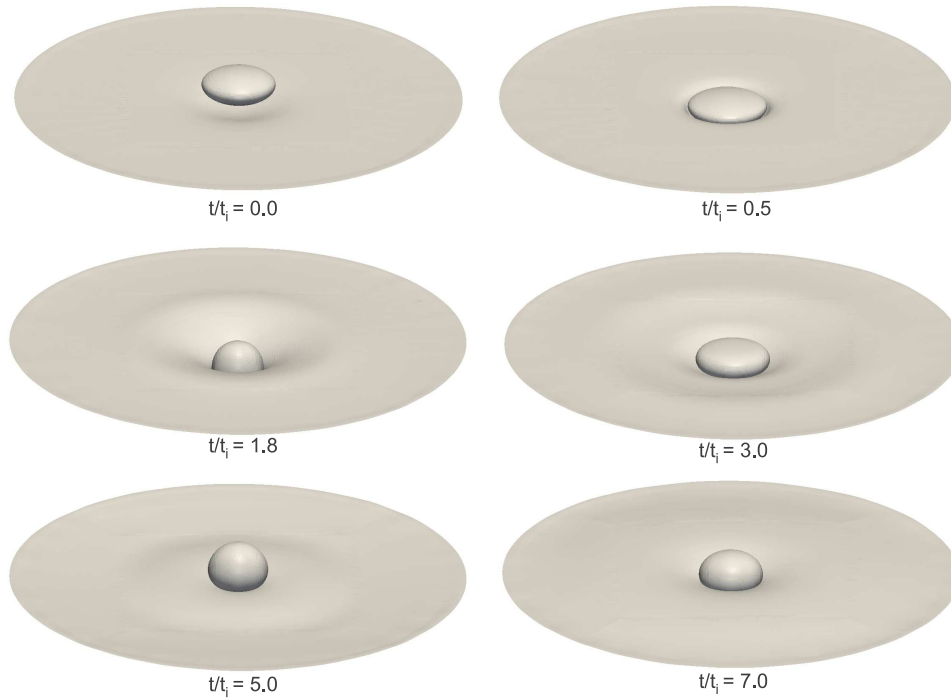
Figure 5.6: Snapshots of the drop impact onto a liquid-liquid interface, $Eo = 6.4$, $M = 8.82 \times 10^{-8}$, $\eta_\rho = 1.189$ and $\eta_\mu = 0.33$.

close agreement with numerical results reported by [11].

In Figs. 5.14-5.15, the normalized vortical contour plots ($\omega_z/(U_i/d)$) obtained by the present numerical method are contrasted against experimental data reported by [30]. At the time of impact, $t/t_i = 0$, two vortices can be observed in the lower half of each drop, which are concentrated near the interface at opposite sides regarding the vertical symmetry axis. At $t/t_i = 0.9$ the magnitude of the vorticity have decreased, moreover, a new pair of vortices can be identified for both cases, which are localized between the drop interfaces and their wakes. The interaction between the above mentioned vortices reduces the drop internal circulation as the time advances, to finally achieve a rest state (see Figs. 5.14-5.15). Thus, regarding the vorticity, present results are also in close agreement with experiments of [30] and numerical simulations reported by [11].
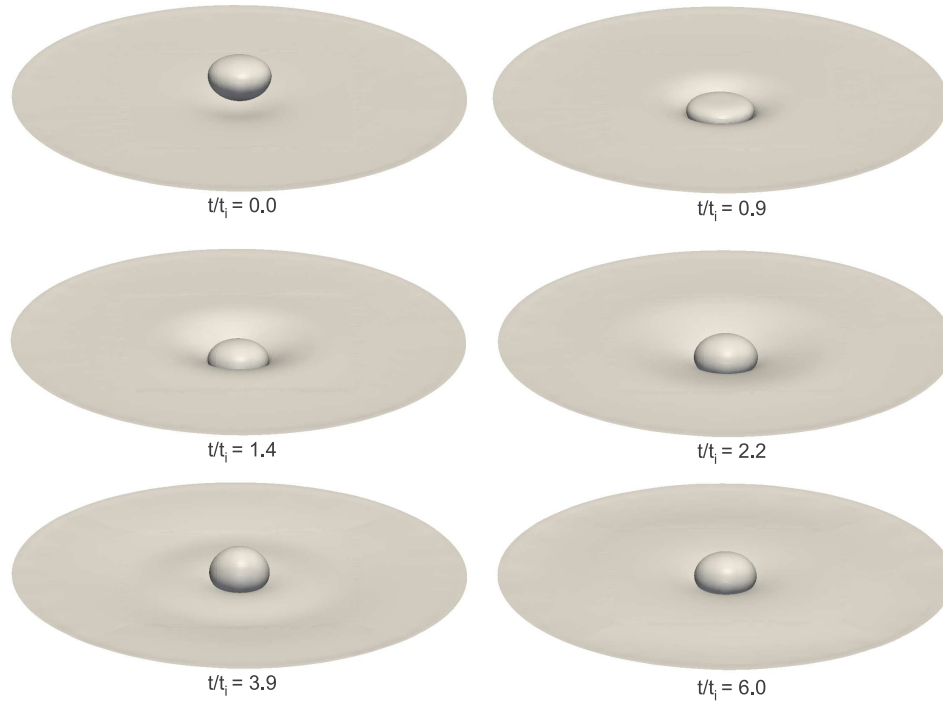
Figure 5.7: Snapshots of the drop impact onto a liquid-liquid interface, $Eo = 6.03$, $M = 1.029 \times 10^{-7}$, $\eta_\rho = 1.18$ and $\eta_\mu = 0.14$.

5.4.2   Binary droplet collision with bouncing outcome

Following experimental studies on binary droplet collision performed by [39], there are four regimes of distinctively different outcomes for hydrocarbon droplets: (I) permanent coalescence after minor droplet deformation, (II) bouncing, (III) permanent coalescence after major droplet deformation, and (IV) coalescence followed by separation and the concomitant production of satellite droplets, as shown in Fig. 5.16. The physical criterion that determines the outcome of the collision (coalescence or bouncing) is the gap size or the trapped gas layer thickness between the droplets, therefore, coalescence may happen when the gas layer thickness reaches a critical value which is within the range of the molecular interaction, where the attractive van der Waals force gradually dominates over other forces and eventually pulls the two interfaces together, otherwise the droplets will bounce. Bouncing regime is difficult
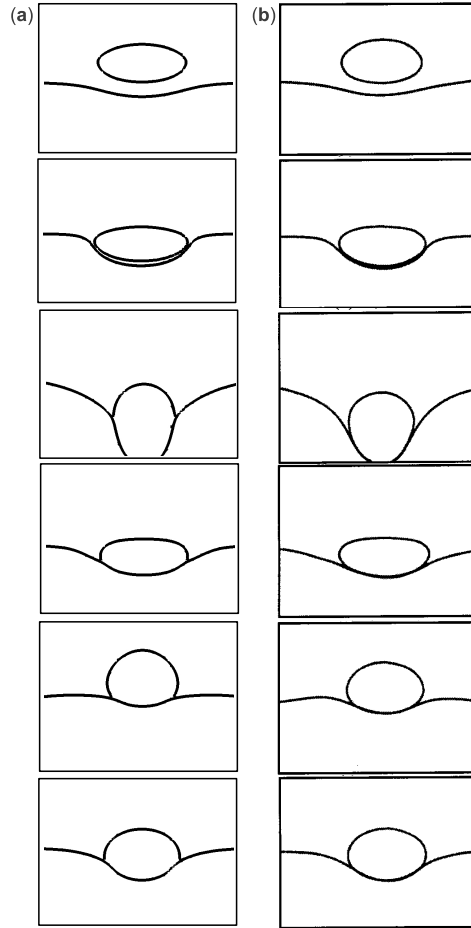
Figure 5.8: Time evolution of the drop shape for $\eta_\mu = 0.33$, $t/t_i = \{0.0, 0.5, 1.8, 3.0, 5.0, 7.0\}$ (a) Present computation (b) Experimental findings of [30]

to handle with classical interface tracking methods (e.g. level-set, volume-of-fluid), because two interfaces will merge automatically whenever they move into adjacent cells. [21] and [26] have studied the droplet collision using a volume-of-fluid method by setting a zero volume-fraction boundary condition on the symmetry plane. In their work, only one droplet, moving toward the symmetry plane, was tracked and
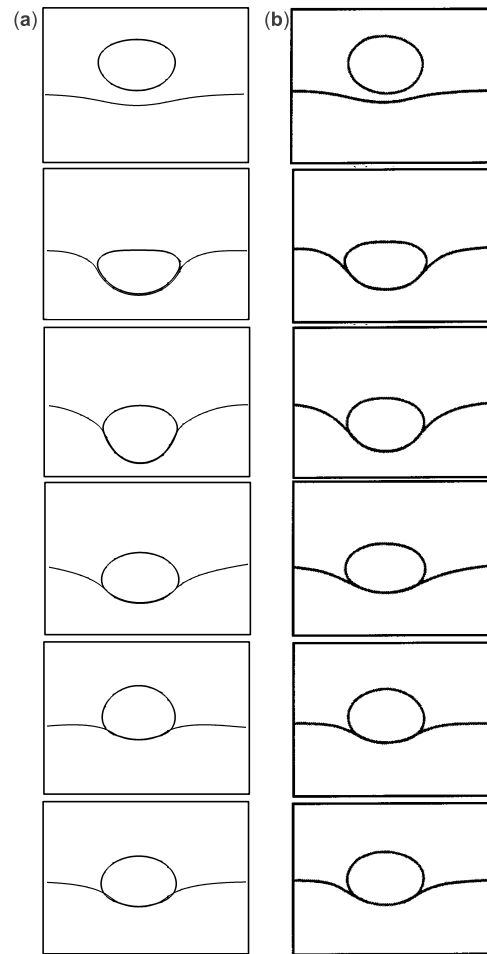
Figure 5.9: Time evolution of the drop shape for $\eta_\mu = 0.14$, $t/t_i = \{0.0, 0.9, 1.4, 2.2, 3.9, 6.0\}$ (a) Present computation (b) Experimental findings of [30]

the zero volume-fraction boundary condition was applied using the ghost cells outside the physical boundaries, avoiding the merge of the droplet with their image. On the other hand [34] and [33] used an interface tracking/finite difference technique to simulate the head-on collision of drops with bouncing outcome. Recently [38]

(a)

(b)

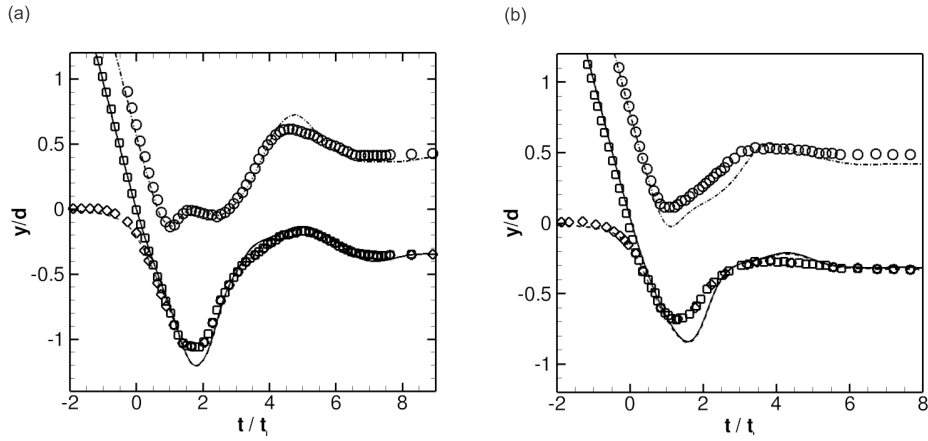

Figure 5.10: Normalized locations of interface, present results $-$, lower drop surface $\square$, upper drop surface $\circ$, liquid-liquid surface $\Diamond$, (a) $\eta_\mu = 0.33$ (b) $\eta_\mu = 0.14$

$\eta_\mu = 0.14$

$\eta_\mu = 0.33$
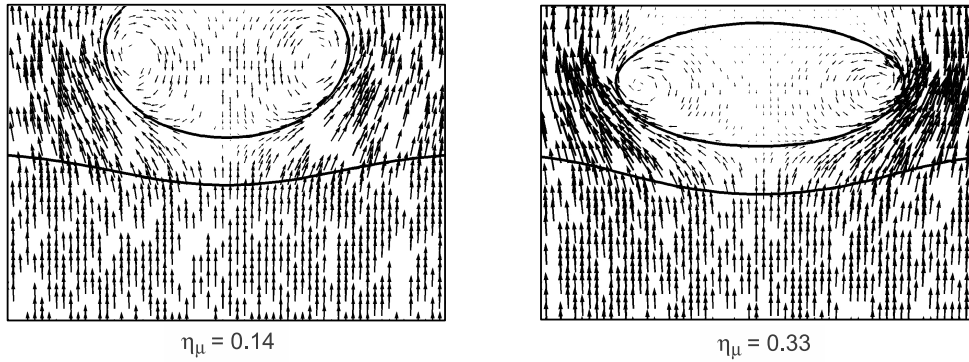
Figure 5.11: Present results of the normalized velocity vector field relative to the drop frame of reference at $t/t_i = 0$

studied the dynamics of head-on collision ($I = 0$) between two identical droplets. They performed experiments and numerical simulations based on the front tracking method, with emphasis on the transitions from merging to bouncing and to merging again, as the Weber number was increased. [23] have also performed numerical simulations of droplet-laden flows using a coupled volume-of-fluid/level-set method

Figure 5.12: Normalized vertical velocity contour for case $\eta_\mu = 0.33$. (a) Numerical results using present MLS method. (b) Experimental results given by [30].
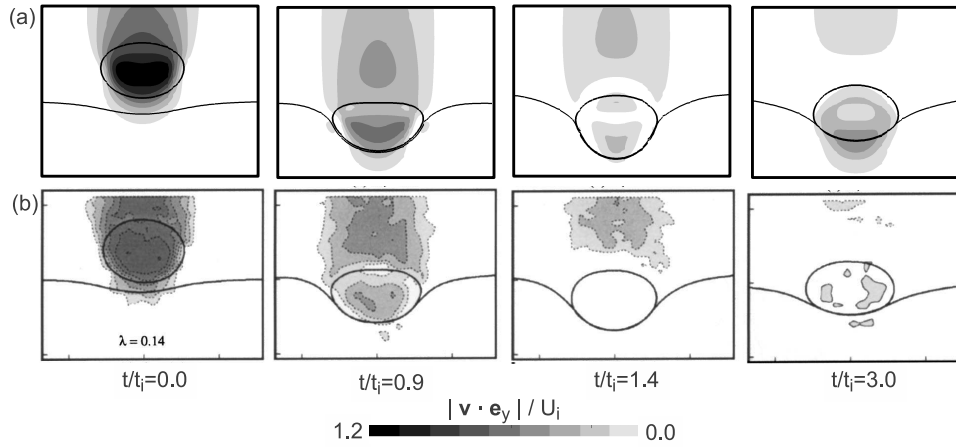
Figure 5.13: Normalized vertical velocity contour for case $\eta_\mu = 0.14$. (a) Numerical results using present MLS method. (b) Experimental results given by [30].

172
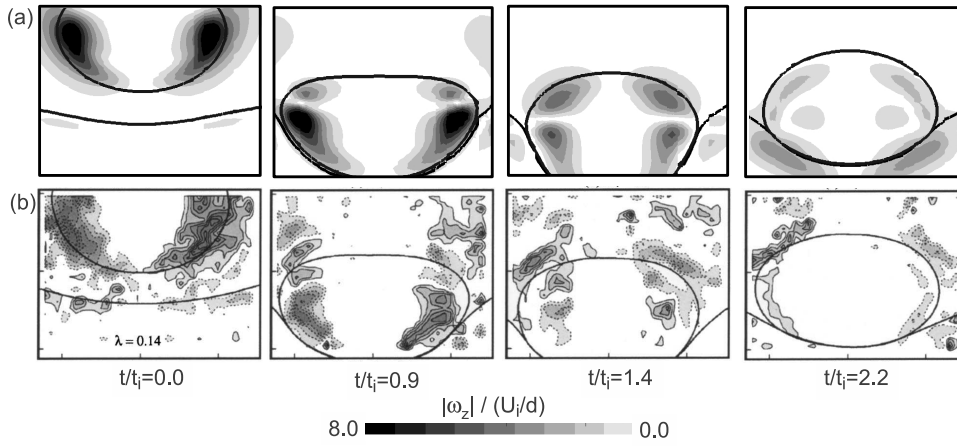
Figure 5.14: Normalized vorticity (ω_z) contour for case $\eta_\mu = 0.14$. (a) Numerical results using present MLS method. (b) Experimental results given by [30].
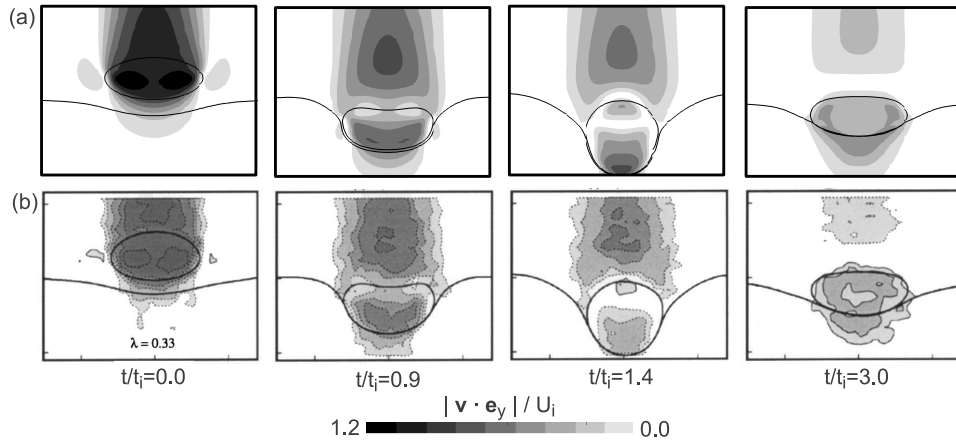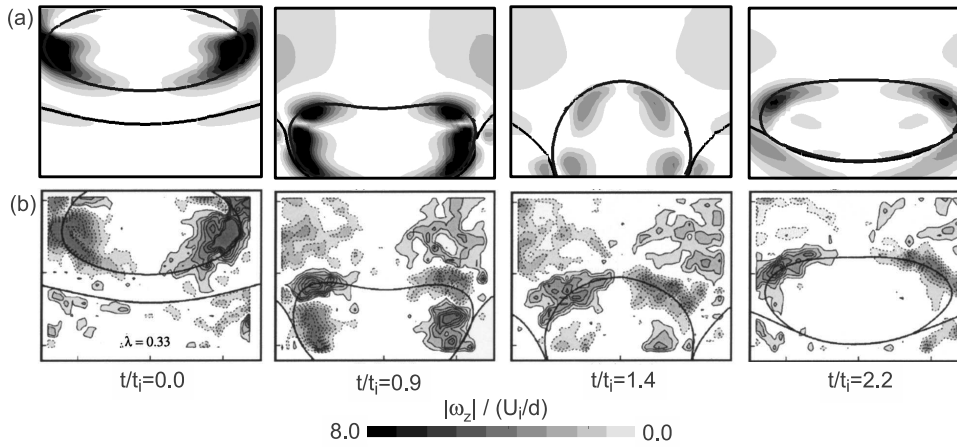

Figure 5.15: Normalized vorticity (ω_z) contour for case $\eta_\mu = 0.33$. (a) Numerical results using present MLS method. (b) Experimental results given by [30].
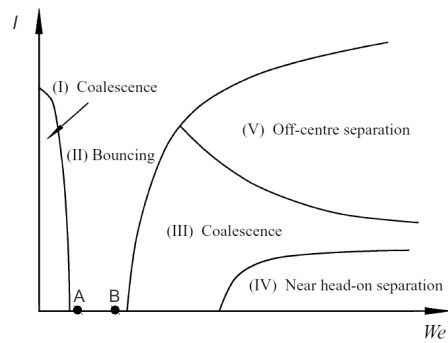
Figure 5.16: Schematic of various collision regimes of hydrocarbon droplets in 1 atm. air, where I is the dimensionless impact parameter (Eq. 5.21) and We is the Weber number (Eq. 5.19). This figure is reproduced from [39]. Simulated cases are indicated with capitals.
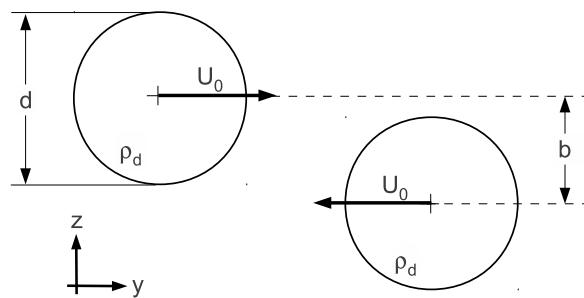
Figure 5.17: Computational domain and initial conditions. The drops are initially $1.4d$ apart.

t=0.000ms

t=0.300ms
(0.361)

t=0.600ms
(0.722)

t=0.700ms
(0.843)

t=0.900ms
(1.083)

Present results   Experimental results

t=1.050ms
(1.264)

t=0.150ms
(1.384)

t=1.250ms
(1.505)

t=1.300ms
(1.565)

t=1.500ms
(1.806)

Present results   Experimental results
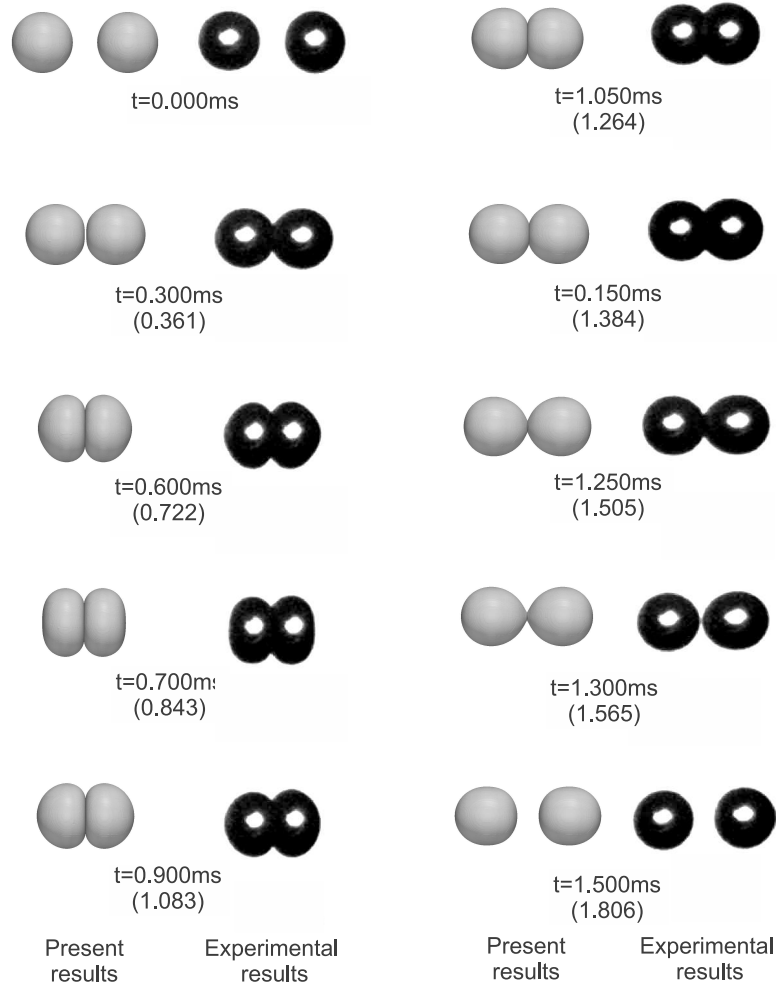
Figure 5.18: Comparison of bouncing collision sequence between present numerical simulation using multi-marker/level-set method and experimental results reported by [38]. Conditions for case A in Table 5.4: Tetradecane in 1 atm. air, $d/2 = 170.6 \mu m$, $We = 2.27$, $Re = 122.2$.

t=0.300ms
(0.370)

t=0.470ms
(0.580)

t=0.500ms
(0.600)

t=0.600ms
(0.740)

t=0.650ms
(0.801)

t=0.700ms
(0.863)

t=0.790ms
(0.974)

t=0.850ms
(1.048)

Present
results

Experimental
results

t=0.905ms
(1.116)

t=0.950ms
(1.172)

t=1.000ms
(1.234)

t=1.050ms
(1.295)

t=1.100ms
(1.357)

t=1.200ms
(1.480)

t=1.285ms
(1.585)

t=1.400ms
(1.727)

Present
results

Experimental
results

Figure 5.19: Comparison of bouncing collision sequence between present numerical simulation using multi-marker/level-set method and experimental results reported by [38]. Conditions for case B in Table 5.4: Tetradecane in 1 atm. air, $d/2 = 167.6\mu m$, $We = 9.33$, $Re = 116.2$.
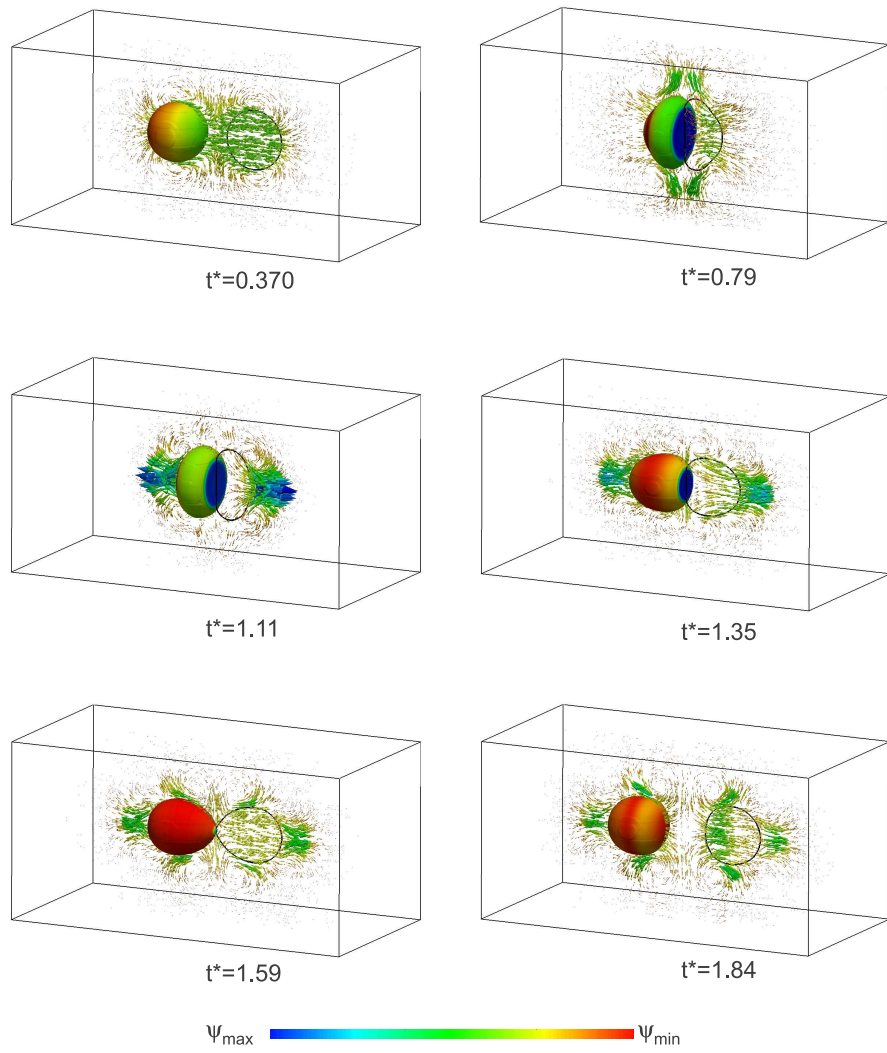
Figure 5.20: Velocity field and pressure evolution for case B (see Table 5.4 and Fig. 5.16). Here $\psi \in \{||\mathbf{v}||, p\}$. Pressure field is represented on the droplet surface.

with a coalescence/breakup model. Their numerical experiments reproduced experimental results reported by [39] and [38]. Thus, with the aim of validating the present multi-marker/level-set method, this section is devoted to perform numerical simulations of head-on collisions between equal sized droplets, with bouncing outcome. Furthermore, numerical results are compared with experimental and numerical data reported by [38] and [23].
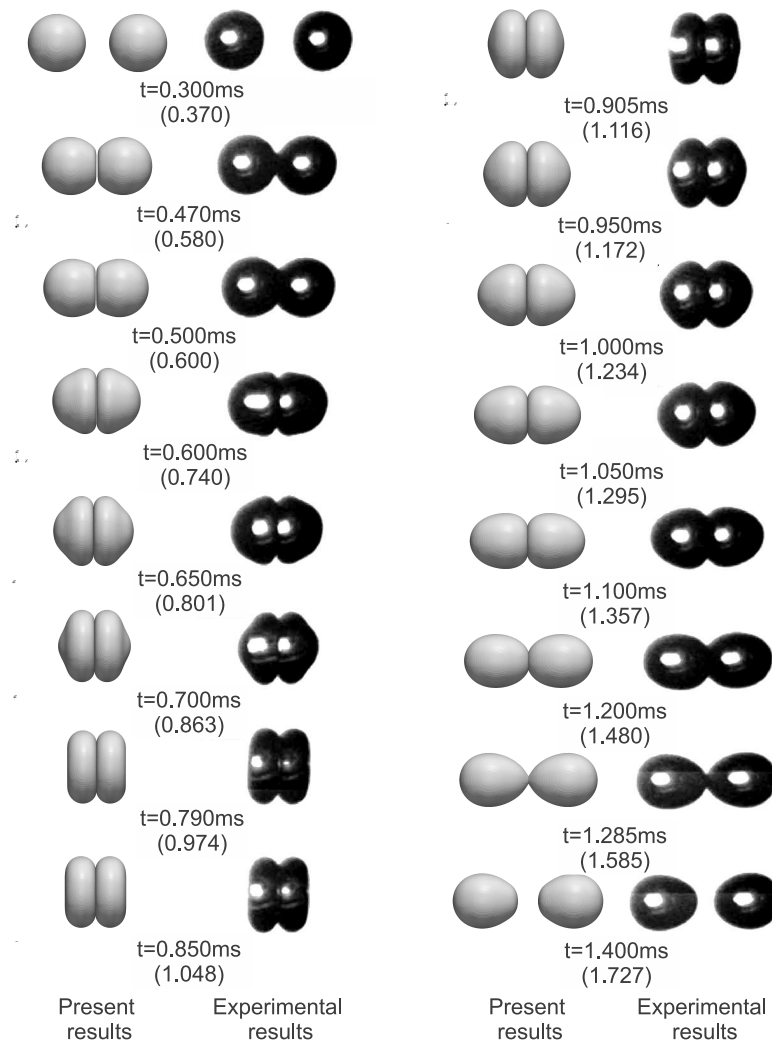
The kinetic and geometric parameters determining the binary droplet collision are shown in Fig. 5.17. The physical parameters of the disperse liquid phase are ρ_d, μ_d and σ. The size of the colliding droplets is d, the relative velocity $2U_0$, and the impact parameter b. Nondimensionalization gives a Weber number

$$We = \frac{\rho_d d U_0^2}{\sigma} \tag{5.19}$$

the Reynolds number

$$Re = \frac{\rho_d U_0 d}{\mu_d} \tag{5.20}$$

and the dimensionless impact parameter

$$I = \frac{b}{d} \tag{5.21}$$

where b is the perpendicular distance between the lines that the droplets move along before collision (see Fig. 5.17). In addition, the density ratio η_ρ and the viscosity ratio η_μ must be specified. Here, the subscript d denotes the fluid in the drop (see Fig. 5.17).

The computational domain is a rectangular box with size $3d \times 6d \times 3d$ where the largest dimension is along the direction of the collision ($y - axis$). Free slip boundary conditions are used on all six sides of the domain. Initially the distance between the droplet centers is $1.4d$ (see Fig. 5.17). An initial velocity field is used, which imposes a uniform velocity of U_0 only on the droplets in opposite directions without any driving force. These conditions were also used by [38] and [23]. A uniform cartesian grid $150 \times 300 \times 150$ is used, therefore, the droplet diameter d is resolved by 50 grid points of dimension h. The dimensionless properties and geometrical parameters used to perform the numerical experiments are summarized in Table 5.5. Such selection of dimensionless parameters corresponds to physical properties of tetradecane droplets in atmospheric air, as shown in Table 5.5. For the sake of comparison with data reported by [38], a dimensionless time t^* is defined as:

$$t^* = \frac{t}{2\pi(\rho_d(d/2)^3/8\sigma)^{1/2}} \tag{5.22}$$

where $2\pi(\rho_d(d/2)^3/8\sigma)^{1/2}$ is the droplet oscillation period, based on inviscid droplet oscillation with small amplitude [25].

Case	We	Re	I	η_ρ	η_μ
A	2.27	122.2	0.0	622	116.5
B	9.33	116.2	0.0	622	116.5

Table 5.4: Dimensionless parameters for the collision of tetradecane droplets in atmospheric air.

Air density	ρ_c	$1.225 kgm^{-3}$
Air viscosity	μ_c	$1.827 \times 10^{-5} Nsm^{-2}$
Tetradecane density	ρ_d	$762 kgm^{-3}$
Tetradecane viscosity	μ_d	$2.128 \times 10^{-3} Nsm^{-2}$
Surface tension	σ	$2.65 \times 10^{-2} Nm^{-1}$

Table 5.5: Physical properties for the collision of tetradecane droplets in atmospheric air.

Fig. 5.18 and 5.19 show a comparison of the present results against experiments reported by [38]. For the parameters here selected the droplets bounce off without coalescence. The droplet sequences illustrate the bouncing collision with increasing Weber number, moreover, the numerical simulations performed by multi-marker/level-set method compare fairly well in terms of the droplet shape and phase. Similar results were reported by [23] using a coupled volume-of-fluid/level-set method. Figure 5.20 shows the pressure and the velocity field as they advance in time. As the drops approach each other the pressure between them builds up, leading to the formation of a dimple (see Fig. 5.20, $t^* = 0.79$). As consequence, the droplets become flatter and the ambient fluid between them is pushed away leaving a thin film of fluid between the droplets, and conversion of the droplet kinetic energy into surface tension energy. The kinetic energy is also partly dissipated through the internal motion within the droplet and, to a much smaller extent, the gas flow inside the gap. Due to the large pressure build up, the drops rebound (see Fig. 5.20, $t^* = 1.11$) and the film resumes its dimpled shape until the drops are almost round (see Fig. 5.20, $t^* = 1.59$). The above results therefore support the adequacy and accuracy of the computational simulation of binary collision with bouncing outcome.

5.4.3 Gravity-driven bubbly flow in a vertical pipe

With the confidence that multi-marker/level-set method has been validated, this section is devoted to explore the gravity-driven bubbly flow in a vertical pipe. The objective of this test-case is to demonstrate the capability of the presented numerical method to perform long-time simulation of bubbly flow in a confined domain

without numerical coalescence. Despite simulations of homogeneous bubbly flows have been reported in the past using the front tracking method or Lattice-Boltzmann method (e.g. [6],[7], [15], [61]), this is the first time that a multiple marker approach is used in the context of the conservative level-set method to perform such simulations.
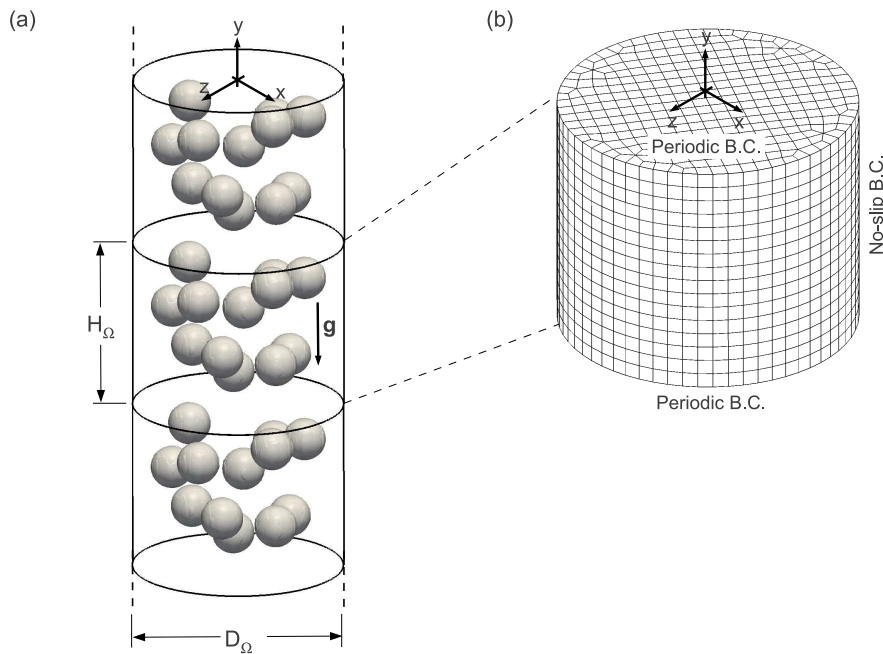
Figure 5.21: Monodisperse gravity-driven bubbly flow. (a) Computational setup and initial condition. Free bubble array. (b) Mesh configuration (hexahedral cells) and boundary conditions. (c) Superimposed mesh (red) used in space-averaging

In this work, the computational set-up is specified as a vertical cylinder bounded by a rigid wall, with gravity in the $-y$ direction. The size of the domain is $(D_\Omega, H_\Omega) = (5d, 4d)$, where d is the initial bubble diameter, D_Ω is the cylinder diameter and H_Ω is the cylinder height, as shown in Fig. 5.21a. Imposed boundary conditions are non-slip at the rigid wall and periodic on the streamwise (y-direction). In this way bubbles go out of the domain on the top side, and they come back in the domain again from the opposite side. The mesh was generated by a constant step extrusion of a two-dimensional unstructured grid of quadrilateral cells along the symmetry
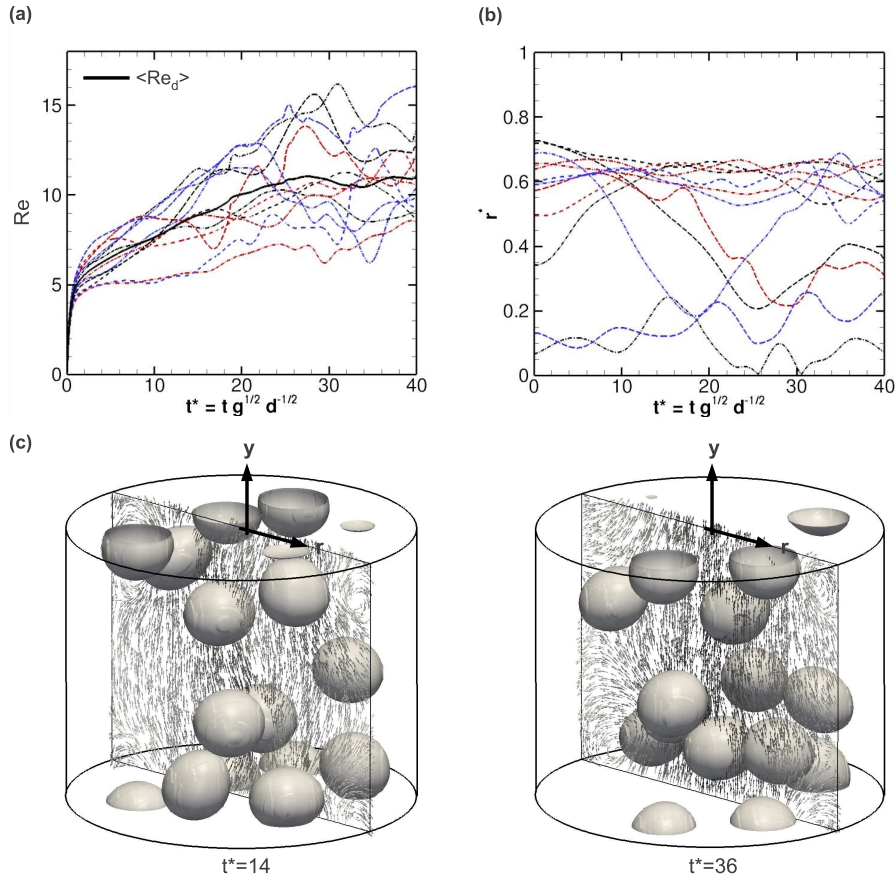
Figure 5.22: Homogeneous bubbly flow at $Eo = 3$, $M = 1 \times 10^{-3}$, $\eta_\rho = 10$ and $\eta_\mu = 10$. (**a**) Time evolution of Reynols number given by Eq. 5.25 and 5.26. (**b**) Time evolution of the dimensionless radial distance for each bubble, $(r^* = 2(x_i^2 + z_i^2)^{1/2} D_\Omega^{-1})$, hence, $r^* = 0$ is on the symmetry axis of the cylindrical domain and $r^* = 1$ is on the cylinder wall. (**c**) Instantaneous bubble distribution and velocity field.

axis of the cylindrical domain, being the step size H_Ω / N_{planes}, where N_{planes} is the number of planes in which the vertical axis is divided; therefore, the tridimensional mesh is conformed by hexahedral volumes as shown in Fig. 5.21b and Table 5.6.
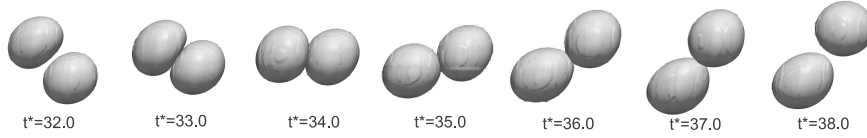
Figure 5.23: Two bubbles from the $Eo = 3$, $M = 1 \times 10^{-3}$, $\eta_\rho = 10$ and $\eta_\mu = 10$.

The gravity-driven bubbly flow is simulated in a vertical column with a stationary free surface, hence, an additional body force was imposed on both fluids to adjust the pressure gradient such that the flow rate of the fluid phase is exactly zero [61]. Following the work of [6] and [61], this force is equivalent to the pressure gradient generated by the base of a flow container which prevents the gravitational force to cause the acceleration of the entire flow field in the downward vertical direction. Indeed, a constant force equal to the space-averaged density times the gravitational acceleration, $\rho_0 \mathbf{g}$ where $\rho_0 = \int_\Omega (\phi_d(\mathbf{x}, 0)\rho_d + (1 - \phi_d(\mathbf{x}, 0))\rho_c)\, dV$, is subtracted from the right hand side of the Navier-Stokes Eq. 5.1 (see [6]). As a consequence, the velocity field of the bubbles in the whole domain will be oriented upwards. Since both fluids are assumed to be incompressible, the overall volumetric fraction of dispersed fluid phase, $\langle \alpha_d \rangle = 2 n_d \pi d^3 / (3 \pi D_\Omega^2 H_\Omega)$, is constant throughout the simulation. A free bubble array of bubbles are initially placed in a quiescent liquid following a random pattern, as shown in Fig. 5.21a. According to the work of [10], the gravity-driven bubble motion in an infinite domain can be characterized by the Eötvos number, the Morton number and the ratios of viscosity and density, which are defined in Eq. (5.17). Physical and geometrical parameters used in this section are summarized in Table 5.6. The accuracy of the present level-set method with respect to simulation of single buoyant bubbles has been shown in [2] and it has been found that about 25 grid points per bubble diameter are sufficient for accurate capturing of bubble dynamics. However, in order to improve the resolution of films formed when bubbles collide, 40 grid points per bubble diameter are used.

The velocity of the bubble centroid is calculated as follows:

$$\langle \mathbf{v}_i \rangle(t) = \frac{\int_\Omega \mathbf{v} \phi_i(\mathbf{x}, t) dV}{\int_\Omega \phi_i(\mathbf{x}, t) dV} \qquad \text{for } i = 1, .., n_d \tag{5.23}$$

whereas the rise velocity of the swarm is computed by:

$$\langle \mathbf{v}_d \rangle(t) = \frac{1}{n_d} \sum_{i=1}^{n_d} \langle \mathbf{v}_i \rangle(t) \tag{5.24}$$
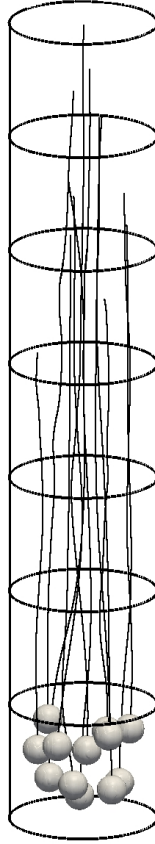
Figure 5.24: Homogeneous bubbly flow at $Eo = 3$, $M = 1 \times 10^{-3}$, $\eta_\rho = 10$ and $\eta_\mu = 10$. Bubbles trajectories.

The bubble rise is characterized by the bubble Reynolds number:

$$\langle Re_i \rangle = \frac{\rho_c d\mathbf{v}_i \cdot \mathbf{e}_y}{\mu_c} \tag{5.25}$$

where $\mathbf{e}_y$ is a unit vector parallel to $+y$ direction. Finally, the average Reynolds number for the swarm of bubbles is calculated as:

$$\langle Re_d \rangle = \frac{1}{n_d} \sum_{i=1}^{n_d} \langle Re_i \rangle \tag{5.26}$$

183
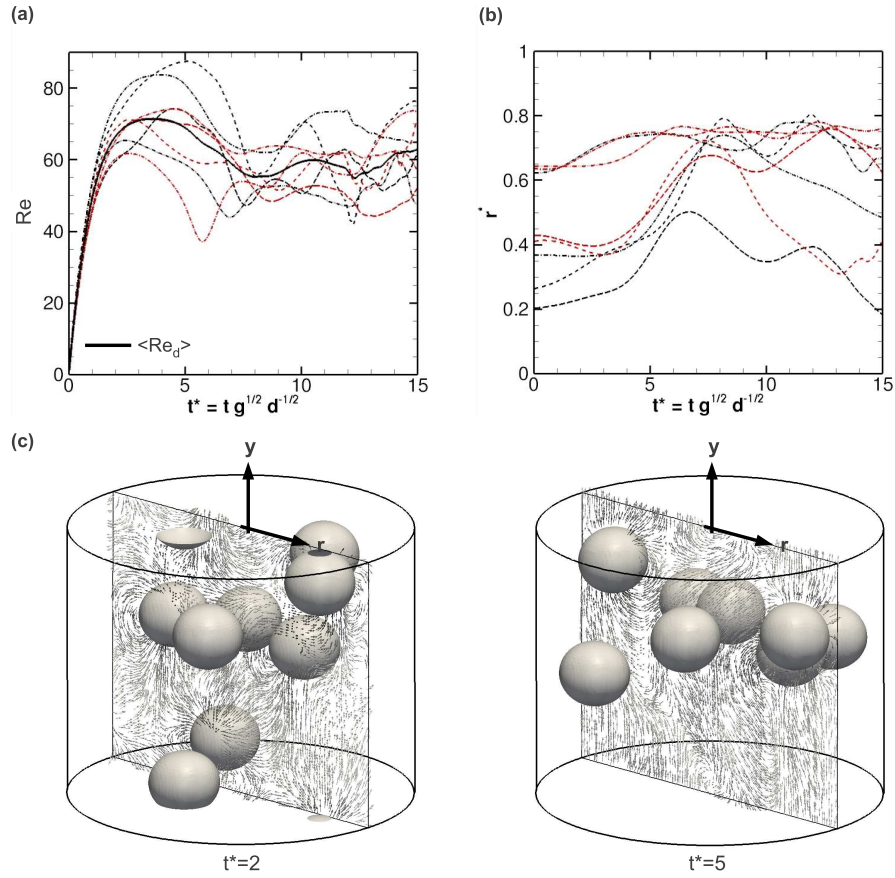
Figure 5.25: Homogeneous bubbly flow at $Eo = 0.5$, $M = 1 \times 10^{-8}$, $\eta_\rho = 10$ and $\eta_\mu = 10$. (**a**) Time evolution of Reynols number given by Eq. 5.25 and 5.26. (**b**) Time evolution of the dimensionless radial distance for each bubble, $(r^* = 2(x_i^2 + z_i^2)^{1/2} D_\Omega^{-1})$, hence, $r^* = 0$ is on the symmetry axis of the cylindrical domain and $r^* = 1$ is on the cylinder wall. (**c**) Instantaneous bubble distribution and velocity field.

Once the velocity of each bubble has been calculated by Eq. 5.23, the trajectory of the
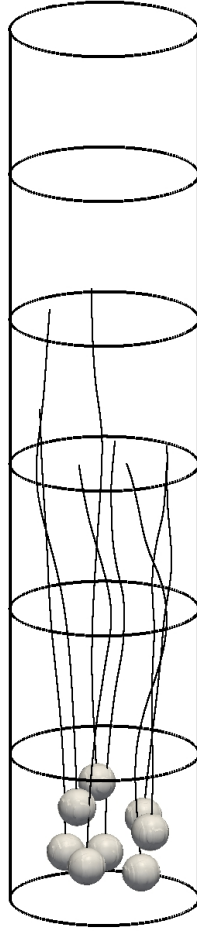
Figure 5.26: Homogeneous bubbly flow at $Eo = 0.5$, $M = 1 \times 10^{-8}$, $\eta_\rho = 10$ and $\eta_\mu = 10$. Bubble trajectories are integrated from Eq. 5.27 from $t^* = [0, 15]$.

bubble can be determined by:

$$\langle \mathbf{x}_i \rangle(t) = \langle \mathbf{x}_i^0 \rangle + \int_0^t \langle \mathbf{v}_i \rangle(t) dt \tag{5.27}$$

where $\langle \mathbf{x}_i^0 \rangle$ is the initial position of the ith bubble centroid.

Case	A	B
Domain size (D_Ω, H_Ω)	$(5d, 4d)$	$(5d, 4d)$
Mesh: cells per plane	31518	31518
Mesh: number of planes	160	160
Mesh: number of cells	5.042×10^6	5.042×10^6
Mesh: cell size (h)	$\approx d/40$	$\approx d/25$
Density ratio	10	10
Viscosity ratio	10	10
Number of bubbles	12	8
Average void fraction $(< \alpha_d >)$	0.032	0.021
Eötvos number	3.0	0.5
Morton number	1×10^{-3}	1×10^{-8}

Table 5.6: Physical and geometrical parameters for gravity-driven bubbly flow in a vertical pipe.

Examining the velocity of each bubble in Fig. 5.22a and Fig. 5.25a, it is clear that the velocity of the center of mass of the bubble swarm reaches a steady state, while each individual bubble does not, furthermore they present oscillating rise velocities. This transient behaviour is produced by the wake interaction of bubbles, moreover, a nonuniform bubble concentration will induce a gradient velocity, which will, in turn generate a lift force on the bubbles that influences the distribution of bubbles. Also, the bubbles near the symmetry axis of the cylinder move faster than the bubbles near the wall. This observation can be confirmed by the bubble trajectories plotted in Fig. 5.24 and Fig. 5.26. It can be seen that the bubbles move, not only in streamwise direction, but also in radial direction, as shown in Fig. 5.22b. These radial movements tend to align bubbles at approximately constant distance from the wall (see Fig. 5.22b and Fig. 5.25b).A typical interaction event of a bubble-pair is illustrated in Fig. 5.23, where one bubble accelerates in the wake of a leading bubble until they collide, after which the trailing bubble pushes the leading bubble aside. A similar sequence of images has been reported in [7], to illustrate the so-called "drafting, kissing and tumbling "process. Therefore, the long-time simulation presented in this section demonstrates the feasibility of using the multiple marker level-set approach to examine the dynamics of homogeneous bubbly flows without numerical coalescence.

5.5 Conclusions

In this chapter we have presented a novel numerical method for interface advection which has the additional ability to handle the interaction of multiple fluid particles without numerical coalescence. The multiple marker level-set method, combines a conservative level-set method on unstructured grids introduced in [2] with a multiple marker approach, where separated fluid regions of the dispersed phase are represented by different level-set functions. Therefore, multiple interfaces can be solved at the same control volume avoiding their numerical merging.

The results of drop impact on a liquid-liquid interface confirm that the multi-marker/level-set method can be used effectively for the simulation of droplets in a liquid, accurately representing the surface tension on the dynamics of the flow. While the multiple marker approach prevents numerical coalescence of interfaces, a better performance of the numerical method was obtained when the viscosity ratio of the fluids is close to unity. A close agreement was found between present numerical results and experiments reported by [30]. Then, numerical predictions of fully three-dimensional collisions of two drops with bouncing outcome were performed. Detailed comparisons with the time-resolved images obtained from the experiments of [38] were used to validate the numerical method. Both qualitative and quantitative agreements were obtained in terms of droplet shape and phase. Finally, the unstructured multiphase solver has been used to perform numerical simulations of gravity-driven bubbly flow in a vertical pipe of monodisperse and noncoalescing bubbles. To the best of the author's knowledge, this is the first time that an interface multi-tracking approach is used in the context of the conservative level-set method, moreover, numerical investigations of bubble swarms on vertical pipes has not been previously reported. Thus, it is demonstrated that the present numerical method is able to capture the dynamics of multiple deformable fluid particles, avoiding the numerical coalescence inherent to standard formulations of level-set methods. One possible extension of this work would be to vary the number of bubbles and flow conditions to obtain bubble concentration and fluid velocity profiles. These profiles can be used for the determination of the wall force and lift force closures as well as appropriate boundary conditions for the averaged two-fuid equations.

References

[1] Aboulhasanzadeh, B., Thomas, S., Taeibi-Rahni, M., Tryggvason, G., 2012. Multiscale computations of mass transfer from buoyant bubbles, Chem. Eng. Sci., 75, 456-467.

[2] Balcázar, N., Jofre, L., Lehmkuhl, O.,Castro, J., Rigola, J., 2014. A finite-volume/level-set method for simulating two-phase flows on unstructured grids, International Journal of Multiphase Flow 64, 55-72.

[3] Biswas, S., Esmaeli, A., Tryggvason, G., 2005. Comparison of results from DNS bubbly flows with a two-fluid model for two dimensional laminar flows, Int. J.Multiphase Flow 31, 1036-1048.

[4] Lu, J., Biswas, S., Tryggvason, G., 2006. A DNS study of laminar bubbly flows in a vertical channel, Int. J.Multiphase Flow 32, 643-660.

[5] Brackbill, J.U., Kothe, D.B., Zemach, C., 1992. A Continuum Method for Modeling Surface Tension, J. Comput. Phys. 100, 335-354.

[6] Bunner, B., Tryggvason, G., 2002. Dynamics of homogeneous bubbly flows Part 1. Rise velocity and microstructure of the bubbles, J. Fluid Mech. 466, 17-52.

[7] Bunner, B., Tryggvason, G., 2003. Effect of bubble deformation on the properties of bubbly flows, J. Fluid Mech. 495, 77-118.

[8] Chorin, A.J., Numerical solution of the Navier-Stokes equations. 1968. Math. Comput. 22, 745-762.

[9] Ceniceros, H., Roma, A.M., Silveira-Neto, A., Villar, M.M., A Robust, Fully Adaptive Hybrid Level-Set/Front-Tracking Method for Two-Phase Flows with an Accurate Surface Tension Computation. 2010. Commun. Comput. Phys. 8, 51-94.

[10] Clift, R., Grace, J.R., Weber, M.E., Bubbles, Drops and Particles. Academic Press, New York, 1978.

[11] Coyajee, E., Boersma, J.B., Numerical simulation of drop impact on a liquid-liquid interface with a multiple marker front-capturing method, 2009, J. Comp. Phys. 228, 4444-4467

[12] Deen, N.G., Van Sint Annaland, M., Kuipers, J.A.M. , 2009. Direct numerical simulation of complex multi-fluid flows using a combined front tracking and immersed boundary method, Chemical Engineering Science 64, 2186-2201.

[13] Dijkhuizen, W., Roghair, I., Van Sint Annaland, M., Kuipers, J.A.M., 2008. DNS of gas bubbles behaviour using an improved 3D front tracking model - Drag force on isolated bubbles and comparison with experiments, Chemical Engineering Science 65, 1415-1426

References

[14] Duineveld, P.C., 1998. Bouncing and coalescence of bubble pairs rising at high Reynolds number in pure water or aqueous surfactant solutions, Appl. Sci. Res. 58, 409-439

[15] Esmaeeli, A., Tryggvason, G., 2005. A DNS study of the buoyant rise of bubbles at O(100) Reynolds number, Physics of Fluids 17, 093303.

[16] Felten, F.N., Lund, T.S., 2006. Kinetic energy conservation issues associated with the collocated mesh scheme for incompressible flow, J. Comput. Phys. 215, 465-484

[17] Focke, C., Kuschel, M., Sommerfeld, M., Bothe, D., 2006. Collision between high and low viscosity droplets: Direct Numerical Simulations and experiments, International Journal of Multiphase Flow 56, 81-92

[18] Gottlieb, S., Chi-Wang, S., 1998. Total Variation Dimishing Runge-Kutta Schemes, Mathematics of Computations 67, 73-85.

[19] Guermond, J.L., Minev, P., Jie, S., 2006. An overview of projection methods for incompressible flows, Comput. Methods Appl. Mech. Engrg. 195, 6011-6045.

[20] Jamet, D., Lebaigue, O., Morel, C., Arcen, B., 2010. Towards a multi-scale approach of two-phase flow modeling in the context of DNB modeling, Nuclear Engineering and Design 240, 2131-2138.

[21] Jiang, X., James, A., 2007. Numerical simulation of the head-on collision of two equal sized drops with van der Waals forces, Journal of Engineering Mathematics 59, 99-121.

[22] Katz, J., Meneveau C., 1996. Wake induced relative motion of bubbles rising in line, Int. J. Multiphase Flow, 22 (2), 239-258.

[23] Kwakkel, M., Breugem, W.P., Boersma, B., 2013. Extension of a CLSVOF method for droplet-laden flows with a coalescence/breakup model, Journal of Computational Physics 253, 166â188.

[24] Lehmkuhl, O., Perez-Segarra, C.D., Soria, M., Oliva, A., 2007, A new Parallel unstructured CFD code for the simulation of turbulent industrial problems on low cost PC cluster, Proceedings of the Parallel CFD 2007 Conference, pp.1-8.

[25] Lamb, H., 1932. Hydrodynamics, Dover, New York, 1932.

[26] Li, X., Fritsching, U., 2011. Numerical investigation of binary droplet collisions in all relevant collision regimes, The Journal of Computational Multiphase Flows 3, 207â224.

[27] Lu, J., Fernández, A., Tryggvason, G., 2005. The effect of bubbles on the wall drag in a turbulent channel flow, Physics of Fluids 17, 095102.

[28] Magnaudet, J., Eames, I., 2000. The Motion of High-Reynolds-Number Bubbles in Inhomogeneous Flows, Annu. Rev. Fluid Mech. 32, 659-708.

[29] Martínez-Mercado, J., Palacios-Morales, C.A., Zenit, R., 2007. Measurement of pseudoturbulence intensity in monodispersed bubbly liquids for $10 < Re < 500$, Physics of fluids 19, 103302.

[30] Mohamed-Kassim, Z., Longmire, E.K., Drop impact on a liquid-liquid interface, 2003. Phys. Fluids 15, 3263-3273.

[31] Mohamed-Kassim, Z., Longmire, E.K., Kim, J.S., Zheng, X., Lowengrub, J., Experiments and Computations on Drop Impact at a Liquid/Liquid Interface, 2004. $5th$ International Conference on Multiphase Flow, Paper 122.

[32] Mudde, R., 2005. Gravity-Driven bubbly flows, Annu. Rev. Fluid Mech. 37, 393-423.

[33] Nobari, M.R., Tryggvason, G., 1996. Numerical Simulations of Three-Dimensional Drop Collisions, AIAA Journal 34, 750-755.

[34] Nobari, M. R. and Jan, Y.âJ. and Tryggvason, G., 1996. Head-on collision of drops-A numerical investigation, Phys. Fluids 8, 29-42.

[35] Olsson, E., Kreiss, G., 2005. A conservative level set method for two phase flow, J. Comput. Phys. 210, 225-246.

[36] Olsson, E., Kreiss, G., 2007. A conservative level set method for two phase flow II, J. Comput. Phys. 225, 785-807.

[37] Osher, S., Sethian, J.A., 1988. Fronts propagating with curvature-dependent speed: Algorithms based on Hamilton-Jacobi formulations, J. Comput. Phys. 79, 175-210.

[38] Pan, K., Law, C.K., Zhou, B., 2008. Experimental and mechanistic description of merging and bouncing in head-on binary droplet collision, Journal of Applied Physics 103, 064901.

[39] Qian, J., Law, C.K., 1997. Regimes of coalescence and separation in droplet collision, Journal of Fluid Mechanics 331, 59-80.

[40] Rhie, C.M., Chow, W.L., 1983. Numerical Study of the Turbulent Flow past an Airfoil with Trailing Edge Separation, AIAA J. 21, 1525-1532.

References

[41] Rodríguez, I., Borrell, R., Lehmkuhl, O., Pérez-Segarra, C.D., Oliva, A., 2011. Direct numerical simulation of the flow over a sphere at Re = 3700, J. Fluids Mech. 679, 263â287.

[42] Roghair, I., Lau, Y.M., Deen, N.G., Slagter, H.M., Baltussen, M.W., Van Sint Annaland, M., Kuipers, J.A.M., 2011. On the drag force of bubbles in bubble swarms at intermediate and high Reynolds numbers. Chemical Engineering Science 66, 3204-3211.

[43] Sanada, T., Sato, A., Shirota, M., Watanabe, M., 2009. Motion and coalescence of a pair of bubbles rising side by side, Chem. Eng. Sci. 64, 2659-2671.

[44] Sankaranarayanan, K., Shan, X., Kevrekidis, I.G., Sundaresan, S., 2002. Analysis of drag and virtual mass forces in bubbly suspensions using an implicit formulation of the lattice Boltzmann method, J. Fluid Mech. 452, 61-96

[45] Scardovelli, R., Zaleski, S., 1999. Direct numerical simulation of free surface and interfacial flow, Annu. Rev. Fluid Mech. 31, 567-603.

[46] Sussman, M., Puckett, E., 2000. A Coupled Level Set and Volume-of-Fluid Method for Computing 3D and Axisymmetric Incompressible Two-Phase Flows, J. Comput. Phys. 162, 301-337.

[47] Sussman, M., Smereka, P., Osher, S., 1994. A Level Set Approach for Computing Solutions to Incompressible Two-Phase Flow, J. Comput. Phys. 144, 146-159.

[48] Smolianski, A., Haario, H., Luukka, P., 2008. Numerical study of dynamics of single bubbles and bubble swarms, Appl. Math. Model. 32, 641-659.

[49] Stewart, C.W., 1995. Bubble Interaction in Low-Viscosity Liquids, Int. J. Multiphase Flow 21, 1037-1046.

[50] Sweby, P.K., 1984. High Resolution Using Flux Limiters for Hyperbolic Conservation Laws, SIAM Journal on Numerical Analysis 21, 995-1011.

[51] Takemura, F., Magnaudet, J., 2003. The transverse force on clean and contaminated bubbles rising near a vertical wall at moderate Reynolds number, Journal of Fluid Mechanics 495, 235-253.

[52] Thomas, S., Esmaeeli, A., Tryggvason, G., 2010. Multiscale computations of thin films in multiphase flows, International Journal of Multiphase Flow 36, 71â77.

[53] Trias, F.X., Lehmkuhl, O., 2011. A Self-Adaptive Strategy for the Time Integration of Navier-Stokes Equations. Numerical Heat Transfer, Part B 60, 116-134.

[54] Tryggvason, G., Dabiri, S., Abouhasanzadeh, B., Jaicai, L., 2013. Multiscale considerations in direct numerical simulations of multiphase flows, Phys. Fluids 25, 031302.

[55] Tryggvason, G., Bunner, B., Esmaeeli, A., Juric, D., Al-Rawahi, N., Tauber, W., Han, J., Nas, S., Jan, Y-J., 2001. A Front-Tracking Method for the Computations of Multiphase Flow, J. Comput. Phys. 169, 708-759.

[56] Tryggvason, G., Thomas, S., Lu, J., Aboulhasanzadeh, B., 2001. A Front-Tracking Method for the Computations of Multiphase Flow, J. Comput. Phys. 169, 708-759.

[57] Unverdi, S., Tryggvason, G., 1992. A front-tracking method for viscous, incompressible, multifluid flows, J. Comput. Phys. 100, 25-37.

[58] Vandewalle, N., Terwagne, D., Mulleners, K., Gilet, T., Dorbolo, S., 2006. Dancing droplets onto liquid surfaces, Physics of fluids 18, 091106.

[59] Van Sint Annaland, M., Deen, N.G., Kuipers, J.A.M., 2005. Numerical Simulation of gas bubbles behaviour using a three-dimensional volume-of-fluid method, Chemical Engineering Science 60, 2999-3011.

[60] Van Wachem, B.G.M., Almstedt, A.E., 2003. Methods for multiphase computational fluid dynamics. Chemical Engineering Journal 96, 81-98.

[61] Yin, X. and Koch, L., 2008. Lattice-Boltzmann simulation of finite Reynolds number buoyancy-driven bubbly flows in periodic and wall domains, Physics of fluids 20, 103304.

[62] Zenit, R., Koch D.L., Sangani, A.S., 2001. Measurements of the average properties of a suspension of bubbles rising in a vertical channel, J. Fluid Mech. 429, 307-342.

[63] Zheng, X., Lowengrub, J., Anderson, A., Cristini, V., 2005. Adaptive unstructured volume remeshing II: Application to two and three dimensional level-set simulations of multiphase flow, Journal of Computational Physics 208, 626-650.

Chapter 6

Conclusions and further work

In this thesis a set of numerical methods based on level-set techniques have been developed for the simulation of multiphase flows with surface tension effects. The focus of this work has been on the simulation of interfacial flows, such as bubble and droplet flows, where interfaces are clearly identified. The numerical methods have been incorporated in an in-house C++ program called TermoFluids [2].

In Chapter 2, a finite-volume/level-set method for simulating incompressible two-phase flows on collocated unstructured grids is presented. Special care is taken to develop an accurate TVD flux limiter formulation to discretize the convective term on unstructured meshes, avoiding unphysical oscillations in the level set function. In order to improve accuracy and robustness, gradients and normals are computed by the least-squares method. Surface tension is introduced through the CSF model. The pressure-velocity decoupling has been solved by using a classical fractional-step method. Such combination of numerical techniques, results in a robust algorithm that allows to simulate virtually all kinds of two-phase flows with moving interphase boundaries (e.g. bubbles, waves, liquid films, etc.).

In chapter 3, the conservative level-set method has been used to study the gravity-driven flow of single and multiple bubbles. The numerical method offers a high degree of accuracy in prediction of terminal Reynolds numbers, drag coefficient and the bubble shape for a wide range of Eo and M numbers. The methodology described is also capable of predicting the hydrodynamic interaction of bubble pairs and bubble swarms. The numerical results showed that bubble shapes, Reynolds numbers and wake patterns predicted by the CLS method agree well with experimental and numerical findings reported in the literature. Numerical results of bubble pair interactions are in good agreement with results reported in the literature. For the conditions selected in this work ($s = 1.5d$, $0° \leqslant \theta \leqslant 90°$), both repulsive and attractive interactions were observed for spherical and ellipsoidal bubbles, depending of the Reynolds number and the initial configuration angle. The present study exhibits some fundamental characteristics of the hydrodynamics of multiple bubbles in a periodic vertical pipe. The performed simulations demonstrates that the CLS method can be employed to deliver useful information on the dynamics of

bubbly flow.

In Chapter 4, a coupled volume-of-fluid/level-set method is presented for simulation of surface-tension-driven interfacial flows. While the volume-of-fluid transport relies on a robust and accurate polyhedral library for interface capturing, geometrical properties of interface (e.g. curvature) are calculated by using a level-set function, which is reconstructed through a geometrical procedure. The method has been validated on 2D and 3D test cases. The simulations reveal that numerical schemes afford accurate results, moreover, conservation properties are shown to be excellent while geometrical accuracy remains even for the most complex flows.

In Chapter 5, we have presented a novel numerical method for interface advection which has the additional ability to handle the interaction of multiple fluid particles without numerical coalescence. The multi-marker/level-set method, combines a conservative level-set method on unstructured grids introduced in [1] with a multiple marker approach to represent separated fluid regions in the dispersed phase. Therefore, multiple interfaces can be solved at the same control volume avoiding their numerical merging. The results of drop impact on a liquid-liquid interface confirm that the multi-marker/level-set method can be used effectively for the simulation of droplets in a liquid, accurately representing the surface tension on the dynamics of the flow. While the multiple marker approach prevents numerical coalescence of interfaces, a better performance of the numerical method was obtained when the viscosity ratio of the fluids is close to unity. A close agreement was found between present numerical results and experiments reported by [4]. Then, numerical predictions of fully three-dimensional collisions of two drops with bouncing outcome were performed. Detailed comparisons with the time-resolved images obtained from the experiments of [5] were used to validate the numerical method. Both qualitative and quantitative agreements were obtained in terms of droplet shape and phase. Finally, the unstructured multiphase solver has been used to perform numerical simulations of gravity-driven bubbly flow in a vertical pipe of monodisperse and noncoalescing bubbles. To the best of the author's knowledge, this is the first time that an interface multi-tracking approach is used in the context of the conservative level-set method, moreover, numerical investigations of bubble swarms on vertical pipes has not been previously reported. Thus, it is demonstrated that the present numerical method is able to capture the dynamics of multiple deformable fluid particles, avoiding the numerical coalescence inherent to standard formulations of level-set methods. One possible extension of this work would be to vary the number of bubbles and flow conditions to obtain bubble concentration and fluid velocity profiles. These profiles can be used for the determination of the wall force and lift force closures as well as appropriate boundary conditions for the averaged two-fluid equations.

Further Work

Regarding the numerical methods and code developed in this work, the main result of the present Ph.D. thesis is an efficient and robust unstructured multiphase solver for simulation of free surface and interfacial flows with surface tension effects, which is based on the conservative level-set method for interface capturing [1]. In addition, a level-set methodology has been coupled with a volume-of-fluid method developed by [3] in order to design an accurate solver for simulating surface-tension-driven interfacial flows. Finally, a novel multiple marker level-set approach has been introduced for simulation of deformable fluid particles without numerical coalescence, which is an artifact inherent to standard formulations of interface capturing methods (e.g. level-set and volume-of-fluid). Therefore, using the aforementioned methodology, now it is possible to perform Direct Numerical Simulations of bubble swarms, which in the past could be simulated only by using the front tracking method [6]. The methodologies developed in this thesis have been tested in several multiphase flows going from more canonical DNS cases to industrial complex configurations using the same CFD code.

Now the numerical methods and code developed in this thesis can be extended to include complex interfacial physics. Additional physics includes heat and mass transfer, phase change such as solidification, boiling, evaporation and condensation, adsorption and desorption, and chemical reactions. In general, additional interfacial physics introduces a wide range of scales and resolving everything becomes a very challenging task. In some cases the only viable approach may be the use of adaptive mesh refinement methodology, with a fine resolution near to the interface where the smaller scales have to be resolved, but allowing to use a coarser mesh size inside each phase to reduce the computational cost[9].

Boiling flows are central to many industrial and natural processes. The high heat transfer rate and the ability of fluids to store large amount of energy in the form of latent heat make boiling particularly important in large-scale energy generation and thermal energy storage. However, although their multiple applications, the evaluation of boiling heat transfer is based mainly on empirical correlations, because DNS methods are not sufficiently well established [8]. Thus, in future research, the DNS techniques proposed in this work can be extended to incorporate an energy equation including phase change phenomena, in order to perform detailed simulations of film boiling and nucleate boiling flows. Moreover, the unstructured formulation of the conservative level-set method could open the possibility to explore new cases including complex geometries.

The presence of surfactants can critically alter the dynamics of interfacial flows by changing the surface tension. Surfactant physics is extremely complicated and computational modeling of surfactants in multiphase flows is a challenging task [7]. The interfacial and bulk surfactant concentration evolution equations have to be solved

fully coupled with the incompressible Navier-Stokes equations, while a non-linear equation of state is used to relate interfacial surface tension to surfactant concentration at the interface. An extension of the conservative level-set method can be used to develop new numerical methods and to examine the effects of surfactants on the migration of bubbles in buoyancy-driven and pressure-driven flows.

Another interesting phenomena is the thermocapillary migration of drops. A non-uniform temperature field in the ambient fluid produces interfacial tension gradients at the fluid interface that, in turn, induces shear stresses acting on the outer fluid by viscous forces, and thus inducing a motion of the drops in the direction of the temperature gradient [10]. This phenomena can play an important role under the microgravity condition in the space as well as in many other scientific and engineering applications. The multiple marker level-set method developed in this thesis can be extended to incorporate the aforementioned thermocapillary effects in order to perform numerical investigations of this kind of flows.

In many problems the interface between the fluid phases can be considered as a free-boundary, which allows for the computation of the flow on the more dense fluid only. Examples of this class of problems are the wave impact on offshore platforms, the water flow on submerged bodies (e.g. submerged hydrofoil) and ship hydrodynamics. In this regard, the conservative level-set method has been adapted to develop a single-phase level set approach, where only the heaviest fluid phase is solved [11]. These results are very promising, and further steps can include the development of new methodologies for the simulation of waves (e.g. [12]).

References

[1] Balcázar, N., Jofre, L., Lehmkhul, O., Castro, J., Rigola, J., 2014. A finite-volume/level-set method for simulating two-phase flows on unstructured grids. International Journal of Multiphase Flow 64, 55-72

[2] Lehmkuhl, O., Perez-Segarra, C.D., Soria, M., Oliva, A., 2007, A new Parallel unstructured CFD code for the simulation of turbulent industrial problems on low cost PC cluster, Proceedings of the Parallel CFD 2007 Conference, pp.1-8.

[3] Jofre, L., Lehmkuhl, O., Castro, J., Oliva, A., 2014. A 3-D Volume-of-Fluid advection method based on cell-vertex velocities, Computers & Fluids 94, 14-29

[4] Mohamed-Kassim, Z., Longmire, E.K., Drop impact on a liquid-liquid interface, 2003. Phys. Fluids 15, 3263-3273.

[5] Pan, K., Law, C.K., Zhou, B., 2008. Experimental and mechanistic description of merging and bouncing in head-on binary droplet collision, Journal of Applied Physics 103, 064901.

References

[6] Tryggvason, G., Bunner, B., Esmaeeli, A., Juric, D., Al-Rawahi, N., Tauber, W., Han, J., Nas, S., Jan, Y-J., 2001. A Front-Tracking Method for the Computations of Multiphase Flow, J. Comput. Phys. 169, 708-759.

[7] Muradoglua, M., Tryggvason, G., 2014. Simulations of soluble surfactants in 3D multiphase flow, Journal of Computational Physics 274, 737â757.

[8] Sato, Y., Niceno, B., 2013. A sharp-interface phase change model for a mass-conservative interface tracking method, Journal of Computational Physics 249, 127â161.

[9] Zuzio, D., Estivalezes, J.L., 2011. An efficient block parallel AMR method for two phase interfacial flow simulations, Computers & Fluids 44, 339â357

[10] Nas, S., Muradoglu, M., Tryggvason, G., 2006. Pattern formation of drops in thermocapillary migration, International Journal of Heat and Mass Transfer 49, 13-14.

[11] Schillaci, E., Balcázar, N., Lehmkuhl, O., Jofre, L., Castro, J., A free surface model for the numerical simulation of oscillating water column systems. In ECFD VI: European Conference on Computational Fluid Dynamics, July 2014

[12] Wang,Z., Yang, J., Koo, B., Stern, F., 2009. A coupled level set and volume-of-fluid method for sharp interface simulation of plunging breaking waves International Journal of Multiphase Flow 35, 227-246

Appendix A

A standard level-set method for simulation of incompressible two-phase flows

A.1 Standard Level-set method

In this appendix, a standard formulation of the level-set method [7, 8] is presented. Level-set methods (LS) are based on the representation of the interface by an isosurface of a smooth function, defined as the signed distance function,

$$d(\mathbf{x}, t) = \begin{cases} -|\mathbf{x} - \mathbf{x}_\Gamma| & \text{if } \mathbf{x} \in \Omega_1 \\ +|\mathbf{x} - \mathbf{x}_\Gamma| & \text{if } \mathbf{x} \in \Omega_2 \end{cases} \tag{A.1}$$

where $\mathbf{x}_\Gamma$ is the closest position vector on the interface to $\mathbf{x}$, Ω_1 is the subdomain occupied by fluid 1, while Ω_2 is occupied by the fluid 2. The evolution of the level-set function is given by,

$$\frac{\partial d}{\partial t} + \mathbf{v} \cdot \nabla d = 0 \tag{A.2}$$

If $\nabla \cdot \mathbf{v} = 0$ the last equation can be written as follows

$$\frac{\partial d}{\partial t} + \nabla \cdot d\mathbf{v} = 0 \tag{A.3}$$

Since d is the signed normal distance from the interface, it should satisfy the constraint

$$||\nabla d|| = 1 \tag{A.4}$$

This is achieved by solving for steady state the re-initialization equation:

$$\frac{\partial d}{\partial \tau} + sign(d)(1 - ||\nabla d||) = 0 \tag{A.5}$$

where τ is a fictitious time and $sign(\cdot)$ is a smoothed sign function,

$$sign(d) = \frac{d}{\sqrt{d^2 + (\varepsilon||\nabla d||)^2}} \tag{A.6}$$

Here $\varepsilon = 1.5h$, while h is the local cell size. For incompressible flows, the mass of each phase is conserved in time, however, the numerical discretization of the level-set formulation does not preserve this property. To overcome this issue, a global mass correction equation [10, 9] is solved for steady state

$$\frac{\partial d}{\partial \bar{\tau}} = \frac{M|_{t=0} - M|_{\bar{\tau}}}{M|_{t=0}} \tag{A.7}$$

where $M|_{\bar{\tau}=0}$ is the initial total mass of the reference phase, while $M_{\bar{\tau}}$ is the total mass at the pseudo-time $\bar{\tau}$. Here, M is computed as

$$M(t) = \int_{\Omega} H_{\varepsilon}(\mathbf{x}, t) dV \tag{A.8}$$

where H_{ε} is a smoothed Heaviside function introduced in [8]

$$H_{\varepsilon}(d(\mathbf{x}, t)) = \begin{cases} 0 \text{ if } d(\mathbf{x}, t) < -\varepsilon \\ \frac{1}{2}\left(1 + \frac{d(\mathbf{x},t)}{\varepsilon} - \frac{1}{\pi}sin\left(\frac{\pi d(\mathbf{x},t)}{\varepsilon}\right)\right) \text{ if } |d(\mathbf{x}_P, t)| \leqslant \varepsilon \\ 1 \text{ if } d(\mathbf{x}, t) > \varepsilon \end{cases} \tag{A.9}$$

where $\varepsilon = 1.5h$ and h is the cell size. From the level-set function, $d(\mathbf{x}, t)$, the curvature κ is obtained by the following equation

$$\kappa = \nabla \cdot \mathbf{n} \tag{A.10}$$

with the interface normal vectors, $\mathbf{n}$, given by

$$\mathbf{n} = \left(\frac{\nabla d}{||\nabla d||}\right) \tag{A.11}$$

Here ∇d is calculated by using the least-squares method [1]. The reader is referred to [1] (or Chapter 2) for details on the finite-volume discretization of Eq. A.10, and the application of the least squares method for gradient evaluation.

The level-set Eqs. A.3 and A.5 are discretized using the finite-volume method according to [1]. Gradients are computed by the least-squares method [1]. The convective term of Eq. A.3 is solved by using a TVD Superbee limiter as proposed in [1], while time integration is performed by a first order Euler method.

A.1. Standard Level-set method

The standard level-set method has been coupled with an unstructured collocated Navier-Stokes solver introduced by [1] (or Chapter 2). In the aforementioned work the velocity-pressure coupling is solved by means of a classical fractional step projection method [3], while the surface tension force in momentum equations (see [1]) is calculated according to the continuum surface force model (CSF) introduced by [2]. In standard level-set methods [8] the CSF model takes the form

$$\sigma \kappa \mathbf{n} \delta_\Gamma = \sigma \kappa \delta_\varepsilon \nabla d \tag{A.12}$$

where ∇d is computed by the least-squares method [1]. The delta function δ_ε is given by

$$\delta_\varepsilon^{cos}(d(\mathbf{x}, t)) = \begin{cases} \frac{1}{2\varepsilon} \left(1 + cos \left(\frac{\pi d(\mathbf{x}, t)}{\varepsilon} \right) \right) & \text{if } |d(\mathbf{x}_P, t)| \leqslant \varepsilon \\ 0 \text{ otherwise} \end{cases} \tag{A.13}$$

with $\varepsilon = 1.5h$ [8]. Physical properties in standard level-set methods [8] are regularized by

$$\rho = \rho_1 H_\varepsilon + \rho_2(1 - H_\varepsilon) \tag{A.14}$$
$$\mu = \mu_1 H_\varepsilon + \mu_2(1 - H_\varepsilon)$$

The reader is referred to [1] (Chapter 2) for technical details on the spatial discretization and temporal discretization of the Navier-Stokes equations on collocated unstructured grids. The solution procedure used in this appendix is summarized as follows:

1. Initialize $\mathbf{v}(\mathbf{x}_P, 0)$, $d(\mathbf{x}_P, 0)$, physical properties and interface geometric properties (κ and $\mathbf{n}$).

2. The time increment Δt, which is limited by the CFL conditions and the stability condition for the capillary force [2], is calculated by

$$\Delta t = C_{\Delta t} min \left(\frac{h}{||\mathbf{v}||}, \frac{\rho h^2}{\mu}, \left(\frac{h}{||\mathbf{g}||} \right)^{1/2}, h^{3/2} \left(\frac{\rho_1 + \rho_2}{4\pi\sigma} \right)^{1/2} \right) \tag{A.15}$$

   where $C_{\Delta t} = 0.1$ for the current LS method, and h is the cell size.

3. The interface is advected by solving Eq. A.3.

4. The signed distance function $d(\mathbf{x}, t)$ is re-initialized by solving Eq. A.5 for steady state.

5. The signed distance function is re-initialized by solving Eq. A.7 for steady state. Thus, the mass conservation error is limited.

6. The curvature is computed by using the Eq. A.10.

7. Physical properties (ρ, μ) are updated by using the Eq. A.14.

8. An intermediate velocity $\mathbf{v}^*$ is evaluated by

$$\frac{\rho \mathbf{v}^* - \rho \mathbf{v}^n}{\Delta t} = -\frac{3}{2}\mathbf{A}_h(\rho \mathbf{v}^n) + \frac{1}{2}\mathbf{A}_h(\rho \mathbf{v}^{n-1}) + \mathbf{D}_h(\mathbf{v}^n) + \rho \mathbf{g} + \sigma \kappa \delta_\varepsilon^{cos} \nabla_h(d) \quad \text{(A.16)}$$

where ∇_h represents the gradient operator, $D_h(\mathbf{v}) = \nabla_h \cdot \mu \left(\nabla_h \mathbf{v} + \nabla_h^T \mathbf{v}\right)$ represents the diffusion operator, and $\mathbf{A}_h(\rho \mathbf{v}) = \nabla_h \cdot (\rho \mathbf{v}\mathbf{v})$ is the convective operator.

9. The pressure field p is computed by the Poisson equation

$$\nabla_h \cdot \left(\frac{1}{\rho}\nabla_h(p^{n+1})\right) = \frac{1}{\Delta t}\nabla_h \cdot (\mathbf{v}^*) \quad \text{(A.17)}$$

Discretization of Eq. A.17 leads to a linear system, which is solved by using a preconditioned conjugate gradient method.

10. The resulting velocity $\mathbf{v}^*$ from Eq. (A.16), does not satisfy the constraint $\nabla \cdot \mathbf{v} = 0$. Therefore it is corrected by

$$\mathbf{v}^{n+1} = \mathbf{v}^* - \frac{\Delta t}{\rho}\nabla_h(p^{n+1}) \quad \text{(A.18)}$$

11. In order to avoid pressure-velocity decoupling when the pressure projection is made on collocated meshes [11, 12], a cell face velocity $\mathbf{v}_f$ is calculated so that $\nabla_h \cdot \mathbf{v} = 0$ at each control volume. Namely in discretized form:

$$\mathbf{v}_f = \sum_{q \in \{P,F\}} \frac{1}{2}\left(\mathbf{v}_q^{n+1} + \frac{\Delta t}{\rho(\phi_q^n)}(\nabla_h p^{n+1})_q\right) - \frac{\Delta t}{\rho_f}(\nabla_h p^{n+1})_f \quad \text{(A.19)}$$

where P and F are denoting the adjacent cell nodes to the face f.

12. Repeat steps 2-11 until time step required.

A.2 Two-dimensional rising bubble

This benchmark problem was selected for code validation in previous chapters. Therefore, the reader is referred to [1] or Chapter 2 of this thesis for a detailed description of the computational setup, initial conditions and boundary conditions. The numerical results are summarized in Figs. A.2 and A.2 for uniform cartesian meshes of different cell size (h). Numerical results are in close agreement with reference data reported by [5, 6].
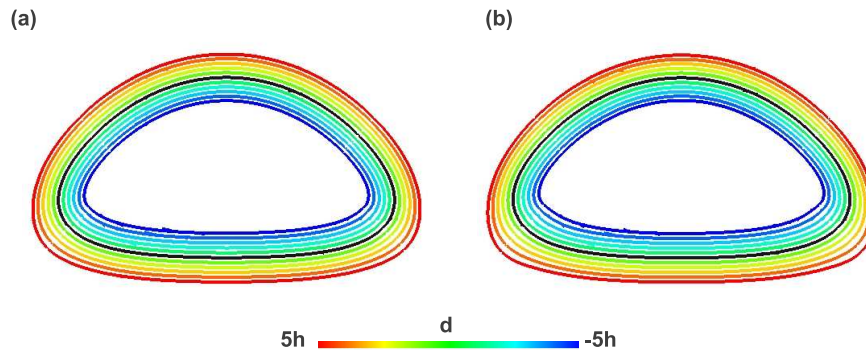
(a) **(b)**

Figure A.1: Comparison of signed distance functions for $(h, t) = (1/160, 3)$. (a) Eq. A.7 is not solved. (b) Eq. A.7 is solved for steady state.

References

[1] Balcázar, N., Jofre, L., Lehmkuhl, O., Castro, J., Rigola, J., 2014. A finite-volume/level-set method for simulating two-phase flows on unstructured grids, International Journal of Multiphase Flow 64, 55-72

[2] Brackbill, J.U., Kothe, D.B., Zemach, C., 1992. A Continuum Method for Modeling Surface Tension, J. Comput. Phys. 100, 335-354.

[3] Chorin, A.J., Numerical solution of the Navier-Stokes equations. 1968. Math. Comput. 22, 745-762.

[4] Lehmkuhl, O., Perez-Segarra, C.D., Soria, M., Oliva, A., 2007, A new Parallel unstructured CFD code for the simulation of turbulent industrial problems on low cost PC cluster, Proceedings of the Parallel CFD 2007 Conference, pp.1-8.

[5] Hysing, S., Turet, S., Kuzmin, D., Parolini, N., Burman, E., Ganesan, S., Tobiska, L., 2009. Quantitative benchmark computations of two-dimensional bubble dynamics, International Journal for Numerical Methods in Fluids 60, 1259-1288.

[6] Hysing, S., 2012. Mixed element FEM level set method for numerical simulation of immiscible fluids, J. Comput. Phys. 231, 2449-2465.

[7] Osher, S., Sethian, J.A., 1988. Fronts propagating with curvature-dependent speed: Algorithms based on Hamilton-Jacobi formulations, J. Comput. Phys. 79, 175-210.
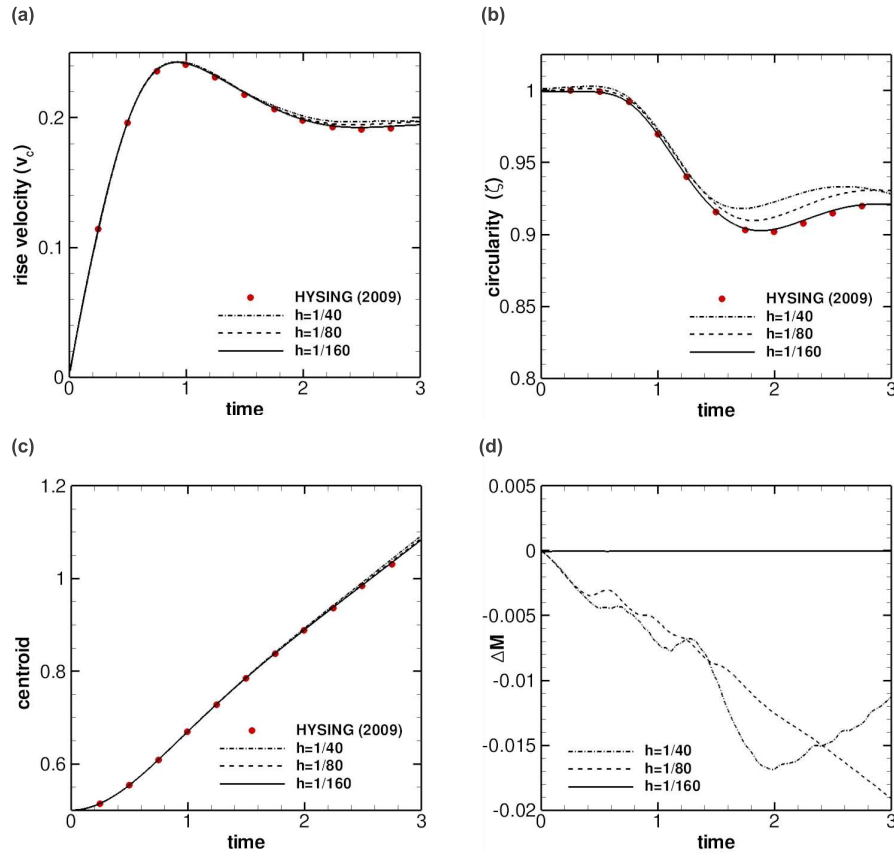
Figure A.2: Two-dimensional rising bubble on uniform cartesian meshes. Here, Eq. A.7 is not solved. (a) rise velocity (b) circularity (c) bubble centroid (d) error in mass conservation $\Delta M = \frac{M(t)-M(0)}{M(0)}$ where $M(t) = \int_\Omega H_\varepsilon(\mathbf{x}, t)dV$.
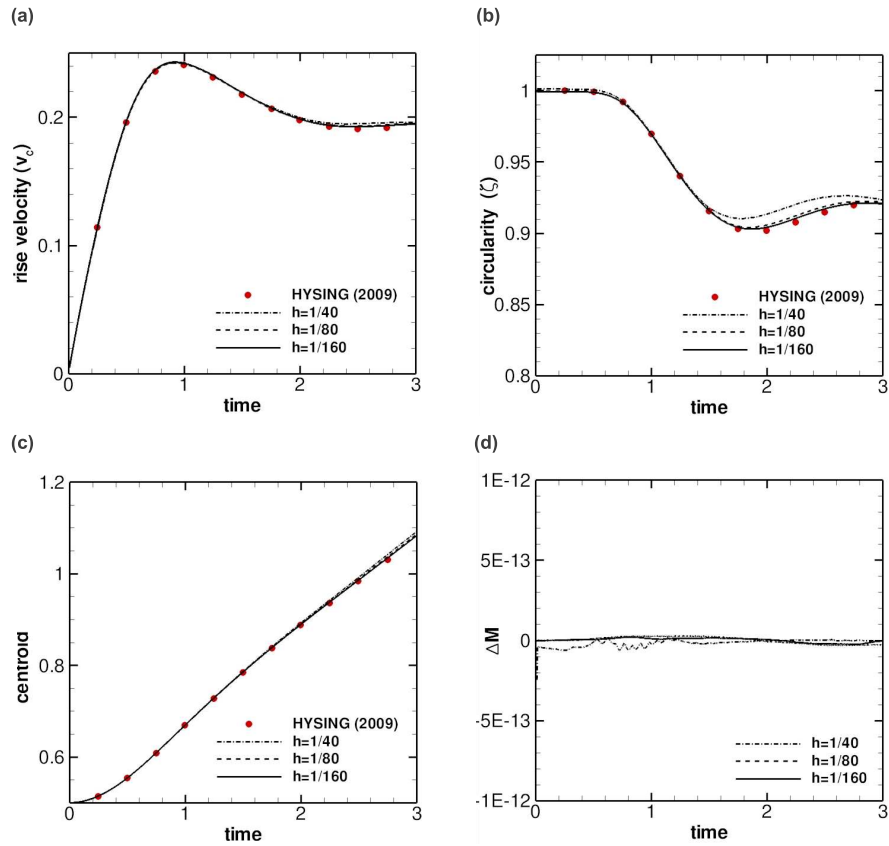
204

Figure A.3: Two-dimensional rising bubble on uniform cartesian meshes. Here, Eq. A.7 is solved for steady state. (a) rise velocity (b) circularity (c) bubble centroid (d) error in mass conservation $\Delta M = \frac{M(t) - M(0)}{M(0)}$ where $M(t) = \int_\Omega H_\varepsilon(\mathbf{x}, t) dV$.

205

[8] Sussman, M., Smereka, P., Osher, S., 1994. A Level Set Approach for Computing Solutions to Incompressible Two-Phase Flow, J. Comput. Phys. 144, 146-159.

[9] Zhang, Y., Zou, Q., Greaves, D., 2010. Numerical simulation of free-surface flow using the level-set method with global mass correction, International Journal for Numerical Methods in Fluids 63, 651-680.

[10] Yap, Y., Chaia, C., Wonga, N., Toha, C., Zhang, Y., 2007. A Global Mass Correction Scheme for the Level-Set Method, Numerical Heat Transfer, Part B: Fundamentals: An International Journal of Computation and Methodology 50, 455-472.

[11] Rhie, C.M., Chow, W.L., 1983. Numerical Study of the Turbulent Flow past an Airfoil with Trailing Edge Separation, AIAA J. 21, 1525-1532.

[12] Felten, F.N., Lund, T.S., 2006. Kinetic energy conservation issues associated with the collocated mesh scheme for incompressible flow, J. Comput. Phys. 215, 465-484.

Appendix B

An industrial application of the CLS method: Oscillating water column

An oscillating water column (OWC) is a wave energy converting system which is partially submerged, open below the water free surface. The device consists of a wave capture chamber, a platform for an air turbine and an air chamber. When waves approach the device, they enter under the partially submerged lip that traps air in a piston type system, forcing the air upwards through the air turbine. This pressure forces the turbine to spin, which is directly coupled to an electrical generator. As the waves retreat, air enters back into the air chamber from the other side of the turbine keeping it spinning. Numerical simulation of the free surface flow in a OWC system, in order to calculate the energy power produced by the turbines, requires the solution and modelling of three main aspects. First, solution of the discrete Navier-Stokes equations to obtain velocity and pressure fields. Second, evaluation of an interface tracking method to follow the free surface as it moves. Third, implementation of a wave generation model to reproduce the typical waves found in open seas.

The main objective of this work is to simulate the free surface flow in an industrial OWC system, hence, numerical methods to be used need to present good accuracy versus computational cost ratio. In this way, the conservative Level-Set method suitable for 3D unstructured meshes introduced in [1] has been chosen, which is fast and accurate enough to deal with problems related to these type of industrial multiphase flows.
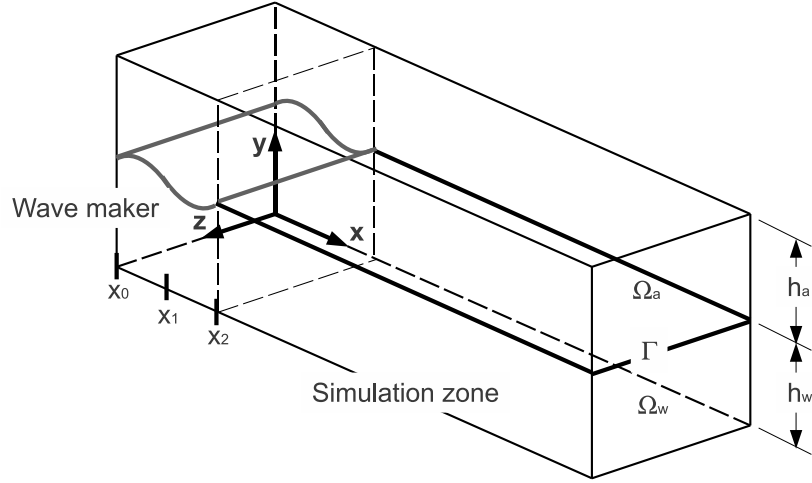
Figure B.1: Schematic diagram of the numerical wave flume. Subdomain Ω_w is filled with water and the outer medium Ω_a is occupied with air.

B.1 Numerical wave generation

Wave maker is implemented by relaxation of analytical [2, 3, 4] and numerical solutions,

$$\psi_{relaxed} = \xi(x)\psi_{analytical} + (1 - \xi(x))\psi_{numerical} \tag{B.1}$$

where $\psi \in \{\mathbf{u}, p, \phi\}$ is a generic variable and $\xi(x)$ is a relaxation function defined as

$$\xi(x) = \begin{cases} 1 & \text{if } x_0 \leqslant x \leqslant x_1 \\ -2\left(1 - \frac{x-x_1}{x_2-x_1}\right)^3 + 3\left(1 - \frac{x-x_1}{x_2-x_1}\right)^2 & \text{if } x_1 < x \leqslant x_2 \\ 0 & \text{if } x > x_2 \end{cases} \tag{B.2}$$

The analytical solution of the two layer potential flow [2, 4, 3] is used for relaxation of ψ in the wave maker zone. The surface elevation, y, of the wave traveling in the x-direction is

$$y = A sin(\kappa x - \omega t) \tag{B.3}$$

208

where $\kappa = 2\pi/\lambda$, $\omega = 2\pi/T$. The velocity components, pressure and level set function in the air are given by

$$\begin{cases} u_x = U - B_a\kappa cAsin(\kappa x - \omega t)cosh(\kappa(y - h_a)), \\ u_y = B_a\kappa cAcos(\kappa x - \omega t)sinh(\kappa(y - h_a)), \\ u_z = 0. \end{cases} \tag{B.4}$$

$$p = -\rho_a(A\kappa c^2 B_a cosh(\kappa(y - h_a))sin(\kappa x - \omega t) + \frac{1}{2}(\mathbf{v} \cdot \mathbf{v}) + \mathbf{g} \cdot \mathbf{e}_y\mathbf{x} \cdot \mathbf{e}_y) \tag{B.5}$$

$$\phi = 0 \tag{B.6}$$

where, U is the wind speed, c is the wave speed, A is the wave amplitude, λ is the wave length, T is the period, h_w is the water depth and h_a is the air depth. In water, they are given by

$$\begin{cases} u_x = B_w\kappa cAsin(\kappa x - \omega t)cosh(\kappa(y + h_w)), \\ u_y = -B_w\kappa cAcos(\kappa x - \omega t)sinh(\kappa(y + h_w)), \\ u_z = 0. \end{cases} \tag{B.7}$$

$$p = -\rho_w(A\kappa c^2 B_w cosh(\kappa(y + h_w))sin(\kappa x - \omega t) + \frac{1}{2}(\mathbf{v} \cdot \mathbf{v}) + \mathbf{g} \cdot \mathbf{e}_y\mathbf{x} \cdot \mathbf{e}_y) \tag{B.8}$$

$$\phi = 1 \tag{B.9}$$

where

$$B_a = \frac{1 - \frac{U}{c}}{sinh(\kappa h_a)} \quad \text{and} \quad B_w = \frac{1}{sinh(\kappa h_w)} \tag{B.10}$$

The dispersion equation takes the following form

$$\rho_w\omega^2 coth(\kappa h_w) + \rho_a(\omega - \kappa U)^2 coth(\kappa h_a) = (\rho_w - \rho_a)g\kappa \tag{B.11}$$

B.2 Numerical simulation of Anortec's OWC system

This appendix is based on a technical report [6] developed as a first approach to assess TermoFluids [5] multiphase capabilities in simulating a oscillating water column (OWC) system proposed by Electric Waves-Anortec. Following the work of [1], the Navier-Stokes equations are solved in a finite-volume basis using a collocated mesh arrangement. The air-water interface is tracked by the conservative Level-Set method [1] and waves are generated by the wave maker introduced in Section B.1.

The free surface flow in Anortec's OWC system is solved using a computational domain of dimensions $[0, 40] \times [0, 25.5] \times [0, 40]$ meters in the x, y and z directions respectively, with vertical symmetry axis of the OWC structure centered at position $(20, 0, 20)$,
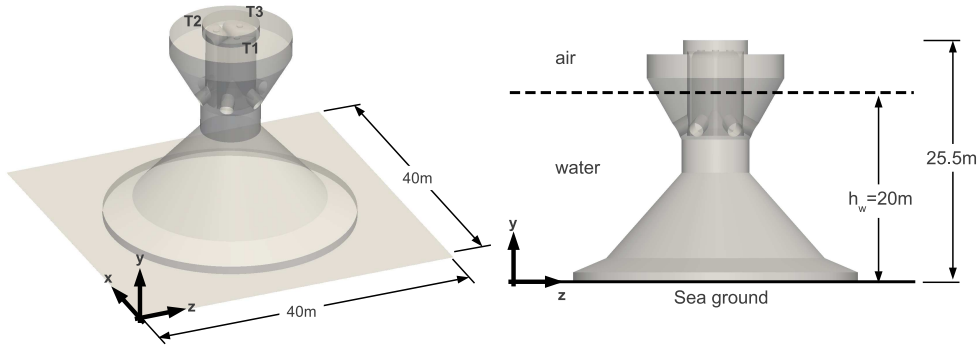
Figure B.2: Computational setup.

as shown in Fig. B.2. The OWC system is composed of three turbines; indicated as $T1$,$T2$ and $T3$, oriented to the incoming wave as shown in Fig. B.2. Neumann boundary condition is imposed at x and z planes, no-slip boundary conditions are prescribed at sea ground ($y = 0$) and surface of the OWC device, a pressure-based condition accounting for atmospheric pressure is used at the air boundary ($y = 25.5$) and a similar one to represent the pressure decay at turbines outlet.

As a first test, a wave of period $T = 3.58s$ seconds, wave length $L = 20m$ and amplitude $a = 1.5m$ is generated by the wave maker. It has been also considered to create waves with period $T = 10s$ seconds but it is not feasible yet, since the relation between period and length for monochromatic waves determines that a wave of length $120m$ is needed. The pressure drop through the turbine and its power are modeled by the following expressions

$$P_T = \frac{Q|Q|}{C_T\pi^2 R_T^3}^2 \tag{B.12}$$

$$Pw_T = a_T Q^2|Q| + b_T Q^2 + c_T|Q| \tag{B.13}$$

where Q stands for air volume flux in $m^3/2$, C_T is a flux coefficient, R_T corresponds to the turbine radius in meters, turbine pressure P_T is calculated in Pa and turbine power Pw_T is given in kW. Please the reader is referred to [6] for the parameters $\{C_T, a_T, b_T, c_T\}$ selected in the present simulations.

The problem is solved up to $t = 100s$ by using an unstructured mesh of $1.2MCVs$ with tetrahedral volumes, partitioned in $128CPUs$. Details of the three-dimensional grid, which has been cutted by different y planes, are shown in Figure B.3. Additionally, the domain decomposition parallelisation utilized is represented by different colors. The cluster JFF of the CTTC was used to carry out these simulations. It is

composed of nodes with 2 AMD Opteron (16 cores per CPU) linked with an infiniband QDR 4X with latencies of $1.07 \mu s$ and a $40 Gbit/s$ bandwidth.

Wave propagation at different time instants are depicted in Figures B.4 and B.5. The waves are created at the wave maker (inlet) and transported through the domain, moreover, they are broken due to the OWC structure. Figure B.6 shows the time evolution of the power for each turbine. As future work three main aspects will be considered. First, validation of the multiphase model will be carried out by comparing numerical results to experimental data provided by Electric Waves- Anortec, and second the maximum theoretical power extracted from the turbines can be calculated by simulating their naked chambers instead of placing them inside. Regarding the first point, a validation work has been performed in [7].

References

[1] Balcázar, N., Jofre, L., Lehmkuhl, O., Castro, J., Rigola, J., 2014. A finite-volume/level-set method for simulating two-phase flows on unstructured grids, International Journal of Multiphase Flow 64, 55-72

[2] Lamb H. Hydrodynamics. Cambridge University Press: Cambridge, 1932.

[3] Milne-Thomson LM. Theoretical Hydrodynamics. Dover Publications Inc.: New York, 1994.

[4] Mei CC. The Applied Dynamics of Ocean Surface Waves. World Scientific: Singapore, 1989.

[5] Lehmkuhl, O., Perez-Segarra, C.D., Soria, M., Oliva, A., 2007, A new Parallel unstructured CFD code for the simulation of turbulent industrial problems on low cost PC cluster, Proceedings of the Parallel CFD 2007 Conference, pp.1-8.

[6] Balcázar, N., Jofre, L., Lehmkuhl, O., 2012, Electric waves - ANORTEC: OWC wave energy extraction, Technical Report.

[7] Schillaci, E., Balcázar, N., Lehmkuhl, O., Jofre, L., Castro, J., A free surface model for the numerical simulation of oscillating water column systems. In ECFD VI: European Conference on Computational Fluid Dynamics, July 2014
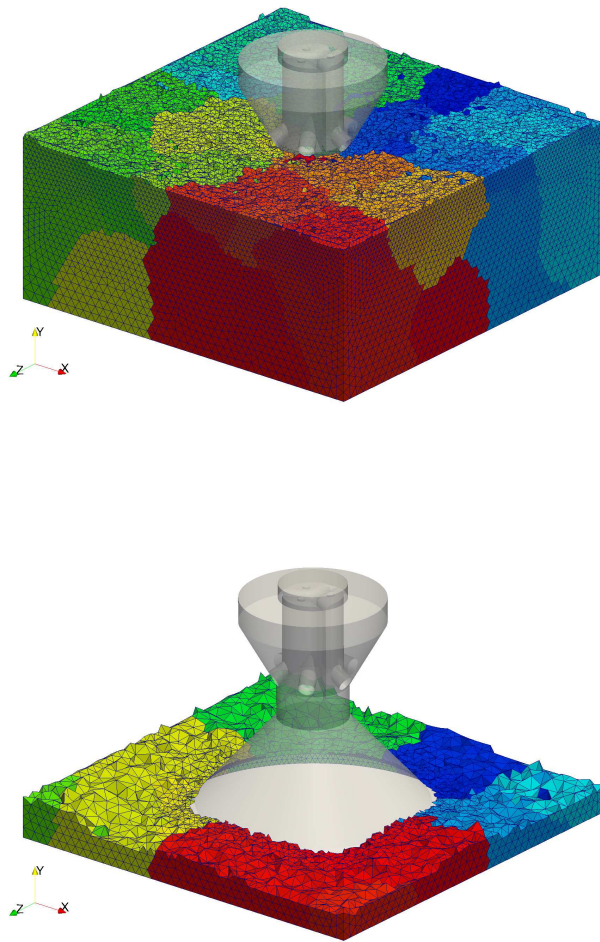
Figure B.3: Mesh configuration: The computationa domain has been divided in 2×10^6 tetrahedral volumes.
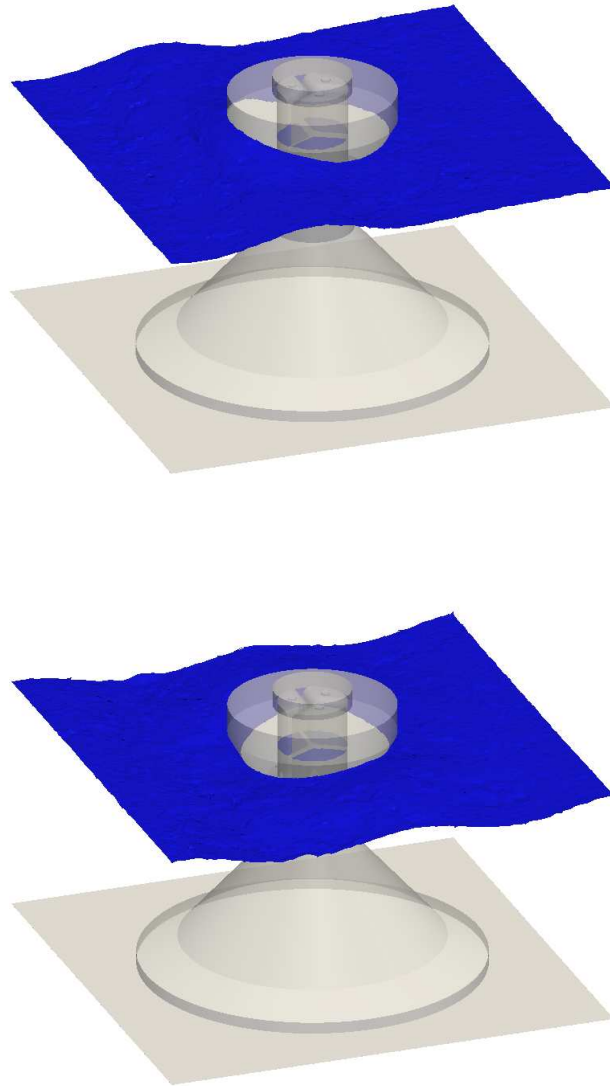
Figure B.4: Snapshots of free surfaces ($t = 10$ above, $t = 20$ bellow) generated by the interaction between waves and the OWC device.
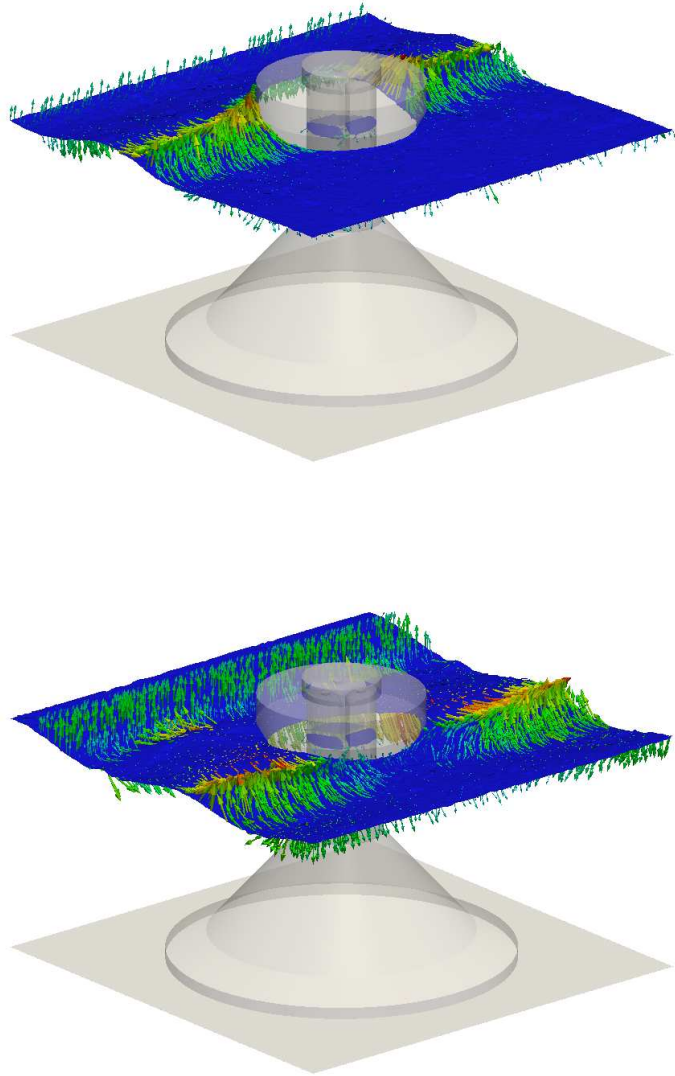
Figure B.5: Snapshots of free surfaces and their velocity vector ($t = 10$ above, $t = 20$ bellow) generated by the interaction between waves and the OWC device.
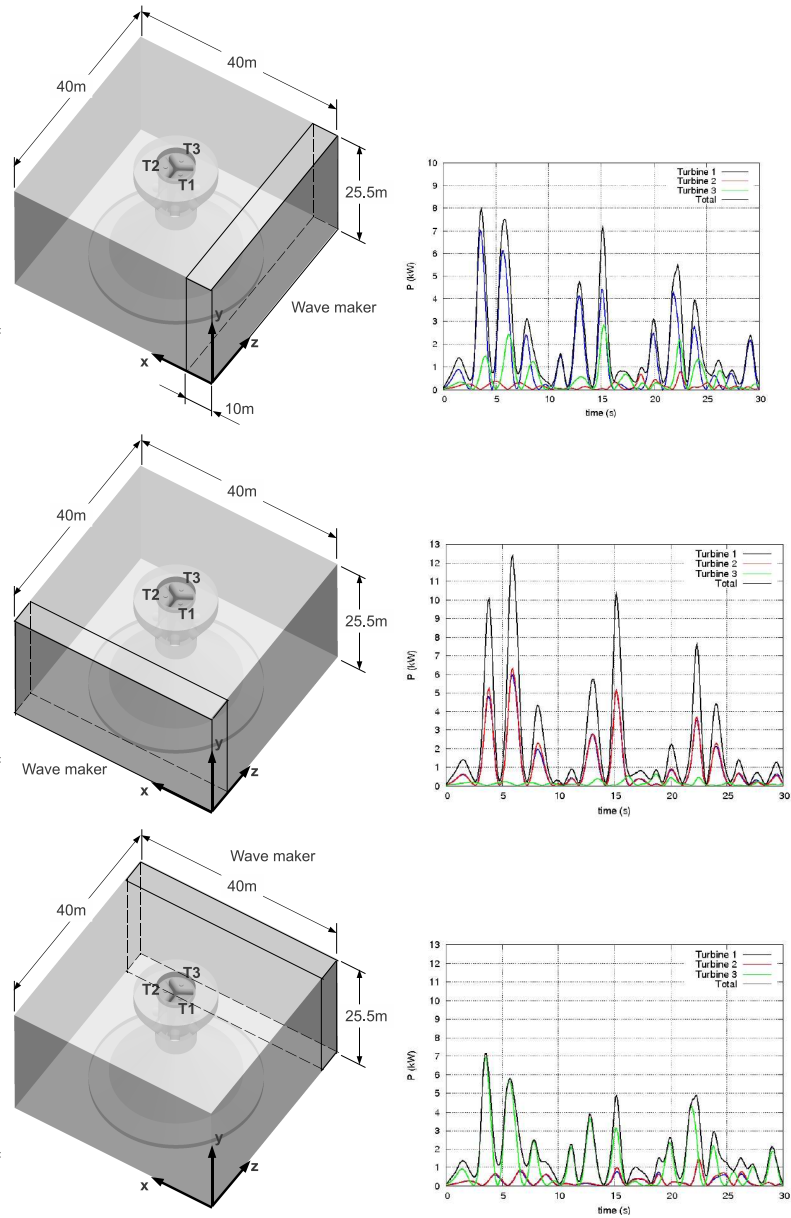
214

Figure B.6: OWC turbines wave power extraction from time simulation 0 to 30 seconds at different incoming waves.

215

References

List of Publications

This is an exhaustive list of publications carried out within the framework of the present thesis.

On International Journals

Balcázar, N., Jofre, L., Lehmkuhl, O., Castro, J., Rigola, J., A finite-volume/level-set method for simulating two-phase flows on unstructured grids. *International Journal of Multiphase Flow*, 64:55–72, 2014.

Balcázar, N., Lehmkuhl, O., Rigola, J., Oliva, A., A multiple marker level-set method for simulation of deformable fluid particles. *International Journal of Multiphase Flow*. Submitted on 1 August, 2014.

Papers in preparation

Balcázar, N. et al., Numerical investigation of single and multiple bubble dynamics using a conservative level-set method (Chapter 3). To be submitted: *Computers & Fluids*.

Balcázar, N., et al., A coupled volume-of-fluid/level-set method for simulation of surface-tension-driven interfacial flows (Chapter 4). To be submitted: *International Journal of Multiphase Flow*.

On Conferences Proceedings

Balcázar, N., Jofre, L., Lehmkuhl, O., Castro, J., Oliva, A., A multiple marker level-set method for simulation of bubbly flows. In ECFD VI: European Conference on Computational Fluid Dynamics, July 2014

Schillaci, E., Balcázar, N., Lehmkuhl, O., Jofre, L., Castro, J., A free surface model for the numerical simulation of oscillating water column systems. In ECFD VI: European Conference on Computational Fluid Dynamics, July 2014

Jofre, L., Balcázar, N., Lehmkuhl, O., Borrell, R., Castro, J., Direct numerical simulation of the flow around a spherical bubble in a turbulent pipe flow. In ECFD VI: European Conference on Computational Fluid Dynamics, July 2014

Balcázar, N., Jofre, L., Lehmkuhl, O., Rigola, J., Castro, J., Oliva, A., A finite-volume/level-set interface capturing method for unstructured grids: simulations of bubbles rising through viscous liquids. In Advances in Fluid Mechanics X, At 283, Volume: 82, June 2014

Jofre, L., Lehmkuhl, O., Balcázar, N., Castro, J., Rigola, J., Oliva, A., Conservative discretization of multiphase flow with high density ratios. In Advances in Fluid Mechanics X, At 153, Volume: 82, June 2014

Balcázar, N., Jofre, L., Lehmkuhl, O., Rigola, J., Castro, J., Numerical simulation of incompressible two-phase flows by Conservative level-set method. In Conference on Modeling Fluid Flow, Budapest, 2012

Jofre, L., Balcázar, N., Lehmkuhl, O., Castro, J., Oliva, A., Numerical study of the incompressible Ritchtmyer-Meshkov instability. Interface tracking on general meshes. In Conference on Modeling Fluid Flow, Budapest, 2012

Supercomputing projects

FI-2013-1-0024: Direct Numerical Simulations of channel flows with regime transition due to coalescence in gas liquid bubbly flows. 800kh at MARENOSTRUM (BSC), from 2013-03-01 to 2013-07-05.

FI-2012-3-0021: Direct Numerical Simulations of channel flows with regime transition due to coalescence in gas liquid bubbly flows. 300kh at MARENOSTRUM (BSC), from 2013-01-11 to 2013-03-01.